



THE HONG KONG
POLYTECHNIC UNIVERSITY

香港理工大學

Pao Yue-kong Library

包玉剛圖書館

Copyright Undertaking

This thesis is protected by copyright, with all rights reserved.

By reading and using the thesis, the reader understands and agrees to the following terms:

1. The reader will abide by the rules and legal ordinances governing copyright regarding the use of the thesis.
2. The reader will use the thesis for the purpose of research or private study only and not for distribution or further reproduction or any other purpose.
3. The reader agrees to indemnify and hold the University harmless from and against any loss, damage, cost, liability or expenses arising from copyright infringement or unauthorized usage.

IMPORTANT

If you have reasons to believe that any materials in this thesis are deemed not suitable to be distributed in this form, or a copyright owner having difficulty with the material being included in our database, please contact lbsys@polyu.edu.hk providing details. The Library will look into your claim and consider taking remedial action upon receipt of the written requests.

**STUDY OF SILK-BASED TRIBOELECTRIC
NANOGENERATORS FOR ENERGY HARVESTING
AND SENSING**

WANG QIAN

PhD

The Hong Kong Polytechnic University

2025

The Hong Kong Polytechnic University

School of Fashion and Textiles

**Study of Silk-based Triboelectric Nanogenerators for
Energy Harvesting and Sensing**

WANG Qian

**A Thesis Submitted in Partial Fulfilment of the
Requirements for the Degree of Doctor of Philosophy**

August 2024

CERTIFICATE OF ORIGINALITY

I hereby declare that this thesis is my own work and that, to the best of my knowledge and belief, it reproduces no material previously published or written, nor material that has been accepted for the award of any other degree or diploma, except where due acknowledgement has been made in the text.

_____ (Signed)

_____ WANG QIAN _____ (Name of student)

Abstract

Triboelectric nanogenerators (TENGs) have emerged as a revolutionary technology for converting mechanical energy into electrical energy through the triboelectric effect and electrostatic induction. For wearable devices, the prioritization of flexible and abundant natural fibers has led to extensive research on silk, which excels owing to its biocompatibility, mechanical strength, and biodegradability. Silk, derived from silkworm cocoon (SC), is a multi-layer composite material composed of a single continuous fiber, with fibroin (SF) being hydrophobic and sericin (SS) being hydrophilic, resulting in a semi-crystalline polymer structure. Traditionally, SS has been removed due to its potential to trigger biological immune responses, resulting in a significant waste of resources. In this thesis, a method has been explored to retain SS in the design of silk-based TENGs without compromising output performance. By incorporating various dopants, the performance of these TENGs has been significantly enhanced beyond their original capabilities, achieving superior efficiency and functionality. This innovative approach provides an efficient energy solution for wearable devices.

Firstly, a kind of silk-based biocompatible TENGs with integrated SS retention was proposed and fabricated for the first time, where three kinds of silkworm cocoon layers (SCLs) endowed with naturally distinct bulge structures were considered as the positive triboelectric materials while Polydimethylsiloxane (PDMS) was used as the negative tribolayer. The novelty of this methodology lies in utilizing the initial layer of the silkworm cocoon as the tribolayer without undergoing the degumming process, thereby achieving a simplified fabrication approach. The triboelectric properties of different SCLs were investigated and analyzed. The working mechanisms and the influence of operational parameters were thoroughly investigated. Its promising potential for wearable energy harvesting and sensing applications has also been demonstrated. This work broadens the material selection by retaining SS to enhance the output performance of TENGs for practical applications.

Subsequently, inspired by the hierarchical structure of silkworm cocoons, silk-based TENGs were designed by retaining SS to leverage the unique properties of both SF and SS. Polyvinyl alcohol (PVA) was utilized as a substrate owing to its excellent film-forming ability and favorable electron-donating ability. The optimal ratio of SS to SF within the PVA matrix was then investigated to achieve the best triboelectric performance. The composite SF/SS/PVA (SFP) membrane serves as the positive tribolayer, while fluoro-nylon (F-Nylon) functions as the negative tribolayer, operating in the contact-separation mode. The surface roughness and secondary structure of the resulting composite films were analyzed to investigate the relationship between triboelectric output performance and structural features. Furthermore, the triboelectric mechanism and output performance were examined to explore potential applications in wearable technology.

Thirdly, a scalable SFP membrane integrated with silver nanowires (AgNWs) was synthesized to form a composite film. When paired with a separate F-Nylon film to construct the TENG device, this design, inspired by the rough surface of silkworm cocoons, features interwoven AgNWs that create a similarly textured surface. The integration of AgNWs, renowned for their exceptional electrical conductivity, enabled our TENG device to attain an ultrahigh power density of 7.6 W/m^2 , surpassing the performance metrics of most recently reported silk-based TENGs. This advancement underscores the potential of silk-based membranes in wearable energy harvesting and sensing applications, highlighting their promise in the development of high-performance protein-based triboelectric materials.

Lastly, a novel two-dimensional material, MXene, was incorporated into the synthesized SFP matrix. MXene exhibits excellent triboelectric properties, and its tendency to aggregate and difficulty in dispersion are effectively mitigated by the significant disaggregation effects of the SS in the substrate, resulting in a uniformly stable composite membrane. Another innovative aspect of this research is the implementation of a single-electrode operation mode, which simplifies and optimizes the structural design. Remarkably, our engineered silk/MXene-based device

demonstrates an exceptionally high instantaneous power density of 35.76 W/m². Furthermore, a comprehensive exploration and analysis of the secondary structure of the silk-MXene composite membrane were conducted. This SS retention-based membrane offers valuable insights into the fabrication of high-performance TENG devices.

In summary, a comprehensive investigation into the hierarchical structure of the silkworm cocoon was conducted, uncovering significant insights that can be used to guide the design of composite membranes based on this unique structure. Inspired by the hierarchical structure of the silkworm cocoon and the specific ratio of SF to SS in individual silk fibers, an SFP membrane has been synthesized. By leveraging the natural properties of silk, our SFP membrane exhibits enhanced electrical performance, making it a promising candidate for advanced technological applications in sustainable energy solutions and sensing detection systems. Additionally, incorporating highly conductive AgNWs into the SFP matrix resulted in rough surface morphology, which facilitated the improved charge transfer and significantly enhanced the overall electrical performance. Moreover, MXene, a two-dimensional material known for its exceptional triboelectric properties but prone to aggregation, was incorporated into the SFP matrix. The resulting silk-based TENGs exhibit enhanced electrical outputs by the disaggregation effects of SS. This research study provides an insight on the rational design and development of silk-based TENG devices with enhanced electrical outputs for applications in energy harvesting and sensing.

Keywords: Triboelectric nanogenerators; Silkworm cocoon; Hierarchical structure; Energy harvesting; MXene

Publications arising from the thesis

Published Journal Paper:

1. **Wang, Q.**; Xu, B.; Huang, J.; Tan, D. (2023). Natural silkworm cocoon-based hierarchically architected composite triboelectric nanogenerators for biomechanical energy harvesting. *ACS Applied Materials & Interfaces*, 15 (7), 9182-9192.
2. **Wang, Q.**; Xu, B.; Tan, D.; Hu, X.; Yang, Y.; Huang, J.; Gao, Y.; Liu, X. (2024). Nature-inspired scalable high-performance triboelectric nanogenerators for energy harvesting and sensing. *Nano Energy*, 121, 109217.
3. Yang, Y., Xu, B., Yin, X., Liu, X., Tan, D., & **Wang, Q.** (2024). Flexible hybrid nanogenerator coupling of triboelectric and photovoltaic effects based on fluoride dielectric regulation for energy harvesting. *Nano Energy*, 126, 109707.
4. Tan, D., Guan, X., Chung, K. Y., Tang, Y., Yang, Y., **Wang, Q.**, ... & Xu, B. (2024). Smart-Adhesive, Breathable and Waterproof Fibrous Electronic Skins. *Advanced Science*, 2405828.
5. Tan, D., Xu, B., Chung, K. Y., Yang, Y., **Wang, Q.**, Gao, Y., & Huang, J. (2024). Self-Adhesive, Detach-on-Demand, and Waterproof Hydrophobic Electronic Skins with Customized Functionality and Wearability. *Advanced Functional Materials*, 34(16), 2311457.
6. Han, J., Li, Z., Fang, C., Liu, X., Yang, Y., **Wang, Q.**, ... & Xu, B. (2024). Hierarchically porous architected stretchable fibrous materials in energy harvesting and self-powered sensing. *Nano Energy*, 129, 110080.
7. Ahmed, T., Gao, Y., So, M. Y., Tan, D., Lu, J., Zhang, J., **Wang, Q.**, ... & Xu, B. (2024). Diamond-Structured Fabric-Based Triboelectric Nanogenerators for Energy Harvesting and Healthcare Application. *Advanced Functional Materials*, 2408680.

Journal Paper under Revision:

Wang Q, Liu X, Han J, Tan D, Yang Y, Zhang J & Bingang Xu*, High-Performance Naturally Crosslinked Silk-Based Triboelectric Nanogenerators for Multimodal Sensing and Energy Harvesting. (Under revision)

Conference Paper:**Oral Presentation**

WANG, Q., & Xu, B. (2024). A Silk-based Hydrogel with High Performance in Triboelectric Nanogenerators for Energy Harvesting and Sensing, 8TH ICMENS, Osaka, 2024.

Acknowledgement

First and foremost, I would like to express my deepest gratitude to my supervisor, Professor Bingang Xu. His unwavering patience, timely feedback, and invaluable guidance have been the cornerstone of my academic journey. His dedication to my progress, coupled with his approachable and kind demeanor, has made this challenging process both manageable and enriching. I am profoundly grateful for his mentorship, which has significantly shaped my research and personal growth.

I am also deeply thankful to my fellow group members and colleagues, including Dr. Zihua Li, Dr. Xiaoyang Guan, Dr. Yun Tang, Dr. Qingjun Yang, Dr. Xiao Yu, Dr. Jian Lu, Dr. Di Tan, Dr. Xin Yin, Dr. Tiandi Chen, Dr. Junxian Huang, Dr. Yujue Yang, Dr. Zhenguo Gao, Dr. Cuiqin Fang, Ms. Jing Han, Mr. Xinlong Liu, Ms. Yuanyuan Gao, Ms. Meiqi Li, Ms. Mei Yi So, Ms. King Yan Chung, Mr. Junze Zhang, Mr. Juyang Wei, and Mr. Taosif, their camaraderie, support, and insightful discussions have been instrumental in fostering a collaborative and stimulating research environment. The shared experiences and collective wisdom of this group have greatly enriched my academic journey.

I would like to extend my special thanks to the technicians at our institution, whose technical expertise and patience have been indispensable. I am particularly grateful to Dr. Chenghao Li, who has been incredibly supportive whenever I encountered difficulties with unfamiliar instruments. He patiently guided me in how to use them and provided valuable suggestions when unexpected issues arose during testing. I also want to express my appreciation to Kevin, who manages the spinning equipment. He took the time to teach me how to operate the machines and offered helpful advice on spinning techniques. Kevin's readiness to assist has been a great support throughout my research.

Additionally, I would like to extend my appreciation to the administrative staff and librarians at The Hong Kong Polytechnic University. Their efficiency and dedication have ensured that I had access to all the resources and support needed to complete my

research. Their behind-the-scenes efforts have not gone unnoticed and are deeply appreciated.

I also want to thank my badminton friends, Ms. Pan Fan, Dr. Wei Wu, Ms. Yingbo Zhang, Ms. Yufan Zuo, Dr. Mengting Fan, Dr. Yunke Luo, Mr. Xin Hu, Mr. Ziwei Chen, Mr. Liwang Lu, Mr. Junkai Meng, and so on. During the most stressful periods of my dissertation writing, our weekly badminton activities provided a much-needed break and helped me maintain a balanced and healthy lifestyle. Their companionship and encouragement have been a source of great comfort and joy.

Lastly, I would like to express my deepest gratitude to my parents, whose unwavering support and encouragement have been the cornerstone of this journey. From the beginning, your faith in my abilities and your endless love have given me the strength and determination to pursue my dreams. To Mr. Lili Lu, being with you is the sincerest declaration of love.

Thank you all for your unwavering support and encouragement. This dissertation would not have been possible without every one of you.

Table of Contents

CERTIFICATE OF ORIGINALITY	I
Abstract.....	II
Publications arising from the thesis	V
Acknowledgement	VII
Table of Contents	IX
List of Figures.....	XVII
List of Tables	XXVIII
List of Abbreviations	XXIX
CHAPTER 1 Introduction	1
1.1 Background	1
1.2 Objectives.....	4
1.3 Research Methodology	5
1.4 Research Significance	8
1.5 Outline of the Thesis	10
CHAPTER 2 Literature Review.....	12
2.1 Fundamentals of Triboelectric Nanogenerators.....	12

2.1.1	Triboelectrification.....	12
2.1.2	Advantages of TENGs.....	12
2.1.3	Working Principles of TENGs	12
2.2	Wearable Natural Fibrous-based TENGs.....	15
2.2.1	Introduction of Natural Fibrous Materials	15
2.2.2	Natural Fibrous-based TENGs	16
2.3	Silk-based TENGs.....	20
2.3.1	Introduction of Silk.....	21
2.3.2	Preparation of Silk-based Materials	25
2.3.3	Membrane-based TENGs.....	29
2.3.4	Electrospinning-based TENGs.....	34
2.3.5	Spraying-based TENGs	38
2.3.6	3D Printing-based TENGs	41
2.3.7	Gel-based TENGs.....	44
2.3.8	Fibrous-based TENGs	47
2.4	Application.....	51
2.4.1	Sensors	51
2.4.2	Energy Harvesters	53

2.5 Summary.....	55
CHAPTER 3 Natural Silkworm Cocoon layer based Hierarchically Architected Composite Triboelectric Nanogenerators for Biomechanical Energy Harvesting	57
3.1 Introduction.....	57
3.2 Experimental Section.....	59
3.2.1 Materials	59
3.2.2 Preparation of SCLs	59
3.2.3 Preparation of PDMS Membrane	60
3.2.4 Fabrication of SCL/PDMS TENGs	60
3.2.5 Characterization	60
3.3 Results and Discussion.....	61
3.3.1 Structural Characteristics of SCLs	61
3.3.2 Working Mechanism of SCL/PDMS TENGs	68
3.3.3 Output Performance of SCL-TENGs.....	70
3.3.4 Mechanical Energy Harvesting by the OL/PDMS-TENG	81
3.3.5 Applications of OL-TENG as Self-powered Wearable Sensors	82
3.4 Conclusion	84
CHAPTER 4 PVA/Silk Composite Membranes for Scalable Triboelectric	

Nanogenerators in Energy Harvesting and Sensing	85
4.1 Introduction.....	85
4.2 Methodology	87
4.2.1 Materials	87
4.2.2 Preparation of SF Solution.....	88
4.2.3 Preparation of SF/SS/PVA (SFP) Membrane	88
4.2.4 Fabrication of SFP/F-TENGs	89
4.2.5 Characterizations	89
4.3 Results and Discussion.....	90
4.3.1 Structure and Working Principle of Fabricated SFP/F-TENGs ..	90
4.3.2 Characterization of the Composite SFP Membranes	92
4.3.3 Electrical Performance	96
4.3.4 Applications of the SFP-S-3.39%/F-TENGs as Energy Harvesters	101
4.3.5 Applications of the SFP/F-TENGs as Sensors	102
4.4 Summary.....	103
CHAPTER 5 High-Performance Triboelectric Nanogenerators for Energy Harvesting and Sensing Based on Silver Nanowires-Enhanced Silk Composite Membranes	105

5.1 Introduction	105
5.2 Methodology	105
5.2.1 Materials	105
5.2.2 Preparation of SF Solution	106
5.2.3 Synthesis of AgNWs	106
5.2.4 Preparation of SF/SS/PVA/AgNWs Membrane (SFPAG)	107
5.2.5 Fabrication of SFPAG/F-TENGs	108
5.2.6 Characterizations	108
5.3 Results and Discussion	109
5.3.1 Structure and Working Principle of Fabricated SFPAG/F-TENGs	109
5.3.2 Characterization of the Composite SFPAG Membrane	111
5.3.3 Electrical Characterization of the SFPAG/F-TENGs	116
5.3.4 Applications of SFPAG/F-TENG as Energy Harvesters	123
5.3.5 Applications of SFPAG/F-TENG as Sensors	124
5.4 Summary	128
 CHAPTER 6 High-Performance Triboelectric Nanogenerators for Energy Harvesting and Sensing Based on MXene-Enhanced Silk Composite Membranes	 130

6.1 Introduction	130
6.2 Experimental Section	133
6.2.1 Materials	133
6.2.2 Preparation of SF Solution	133
6.2.3 Preparation of SF/SS/PVA/MXene (MFS) Membrane	133
6.2.4 Fabrication of MFS/F-TENGs	134
6.2.5 Characterizations	134
6.3 Results and Discussion	135
6.3.1 Structure and Characteristics of MFS Membrane as Friction Layer	135
6.3.2 Mechanism of the MFS/F-SETENGs	146
6.3.3 Electrical Output Performance of MFS/F-SETENGs	148
6.3.4 Application of MFS/F-SETENGs for Energy Harvesting	150
6.3.5 Application of MFS/F-SETENGs for Sensing	152
6.4 Summary	155
CHAPTER 7 Conclusions and Suggestions for Future Research	157
7.1 Conclusions	157
7.2 Limitations of the Study and Suggestions for Future Research	159

Reference	161
------------------------	------------

List of Figures

Fig.2. 1 Four working modes of TENGs: a. Vertical contact-separation mode; b. Lateral-sliding mode; c. Single-electrode mode; d. Freestanding triboelectric-layer mode^{49, 50}

Fig.2. 2 Typical natural fiber-based TENG devices: a. The preparation process of a 3D angle-interlock woven (3DAW) structural wearable TENG; b. The structure schematic of the 3DAW-TENG⁶⁸; c. Schematic diagram to illustrate the fabrication of CPF-pTENG⁶⁹; d. The preparation illustration of a kind of jute-based TENG; e. Digital image of the knitted jute TENG⁷⁰; f. The production flow chart of sisal cellulose paper (SCP) film⁷¹; g. The structural design of wool-based FF-TENG device⁷²; h. A self-power supercapacitor (SPSC) using CSSC and silk/PVA/PVDF-based TENG⁷³

Fig.2. 3 SF-based flexible materials and flexible electronics^{27, 33, 64, 76-88}

Fig.2. 4 The schematic representation of the hierarchical network structures of SF fibers and non-fiber silk materials⁹¹.

Fig.2. 5 Molecular Structure of silk: a. The composition of the amino acid sequence inside silk; b. Illustration of silk structure; c. Schematic of two typical secondary structures: α -helix and β -sheet; d. An anti-parallel arrangement within silk materials⁹²; e. The process of β -sheets from different molecules stacking into β -crystallite; f. The interaction between β -sheets to form β -crystallites⁹³

Fig.2. 6 Examples of different methods to prepare silk-based materials: a. Flowchart illustrating the production process of regenerated SF solution derived from natural *B. mori* cocoons¹⁰⁹; b. Illustration of silk composite membranes¹¹⁰; c. Illustration of preparation of silk-based composites by using 3D electrospinning technology¹¹¹; d. Process schematic of producing silk-based materials by 3D printing method¹⁰⁸; e. Process diagram of making silk-based hydrogels¹¹²; f. process illustration of fabricating modified silk fabric-based materials¹¹³.

Fig.2. 7 Typical structural illustration of pure silk membrane-based TENGs: a. The first silk-film-based TENG⁹⁹; b. Structure diagram of a typical BN-TENG device³⁰; c. Schematic diagram of SF/PTFE TENG¹⁰⁰; d. Schematic demonstration of the silk/PVDF TENG¹⁰¹.

Fig.2. 8 Typical modified composite silk-membrane-based TENGs: a. Schematic of T²ENGs showing the device structure and material system¹¹⁵; b. The schematic view of the CNT-silk mixing layer based TENG¹⁰²; c Structure of silk ring (modified silk and AgNWs) SETENG¹⁰³; d. Structure illustration of SF/Ag/PTFE-TENG³²; e. Schematic diagram of carboxymethyl chitosan and silk (CSF)-TENG¹⁰⁴; f. Schematic diagram of NF-MOF TENG based on the composite film³⁵; g. The schematic diagram of the PVA/SF/Ecoflex TENG device¹¹⁶; h. Device illustration of the proposed alcohol-treated microarchitected SF (AT-MASF)/PTFE-TENG device¹¹⁷; i. Schematic diagram of SF-based composite/Teflon TENG¹¹⁸; j. Schematic photographic images depict the completely packed soft pouch-like CSPCF/PTFE-TENG¹¹⁹.

Fig.2. 9 Typical electrospinning method-based TENGs: a. A regenerated silk nanofiber-based TENG²⁴; b. Schematic diagram of all-fiber hybrid TENG, which consists of two electrodes (conductive fabric) and electrospun silk nanofibers (top) and PVDF nanofibers (bottom) serving as a triboelectric pair²⁷; c. Illustration of a kind of flexible TENG based on an SF fibrous layer and a polycaprolactone (PCL)/GO fibrous layer¹²⁰; d. Schematic illustration of the fabrication of PVA/MXene and silk nanofibers film-based TENG²⁸; e. A high-power and protein-based TENG consisting of electrospun PEO-Silk nanofibers (PEO-Silk-NFs) and poly(vinyl butyral-co-vinyl alcohol-co-vinyl acetate) nanofibers (PVBVA-NFs)¹⁰⁵; f. Schematic of skin-actuated SNF/CNT/SNF E-tattoo energy harvester¹²¹; g. A hybrid nanogenerator integrating TENG and PENG based on electrospun silk fibers¹²²; h. A TENG realized by synchronous electrospinning of styrene-isoprene (SIS) block copolymers and electrospaying of the fluorinated SiO₂ nanoparticles inspired by the sericin-bundled silk¹²³.

Fig.2. 10 Typical illustrations of spraying coating-based silk materials: a. Fabrication steps for the SF/PET/ITO TENG³⁸; b. The TENG energy harvesting system modulating

the mechanical vibration to collect ultralow frequency mechanical energy less than 1 Hz using SF/PET/ITO TENG³⁹; c. Components of the designed self-powered acceleration sensor based on the SF/PET/ITO TENG⁴⁰; d. An electro-spray-etching (ESE) process for fabricating ITO/PET/SF/SiO₂ TENG³⁴; e. Hybrid electrospinning and electro-spray method for fabricating silk-based TENG²⁹; f. A hybrid triboelectric-piezoelectric-electromagnetic generator with PI and SF serving as the tribo-pairs¹²⁷.

Fig.2. 11 Typical 3D printing method-based TENGs: a. Schematic showing the fabrication process of the silk protein-based strain sensor and the TENG³⁶; b. Illustration of the proposed wearable PS-TENG and its electric performance³⁷; c. Schematic illustration showing the 3D printing process using a coaxial spinneret¹³¹

Fig.2. 12 Typical gel-based TENGs: a. Schematic illustration to show the mechanism of artificial EG-skin using silk hydrogel¹³⁷; b. Fabrication and characterization of the PAM/SF/GO/PEDOT: PSS (PSGP) hydrogel-based TENGs⁴²; c. a double-network silk-based hydrogel with high mechanical properties for energy harvesting and sensing¹³⁸; d. A composite silk-coated carbon nanotube aerogel TENG¹³⁹; e. Schematic illustration of the structure of silk aerogel-based TENG¹³⁴; f. A kind of SF/CNF scaffold TENG¹⁴⁰.

Fig.2. 13 Typical silk Fibrous-based TENGs: a. A Fe@TiO₂/PDMS textile and silk cloths TENG¹⁴²; b. A silk-based corrugated Textile TENG¹⁴³; c. A washable silk-based E-textile TENG¹⁴⁴; d. Mechanism description of the Liquid-metal/polymer core/shell fibers/silk fabric device under vertical contact-separation mode¹⁴⁵; e. The commercial woven fabrics silk deposited electrospun nanofibers (nylon 66) and PVDF-coated PET woven fabric as tribolayers for fabricating TENG device¹⁴⁶; f. The commercial silk-based combined fabric TENG device structure for sound energy harvesting¹⁴¹; g. A kind of fluorinated silk-based TENG¹⁴⁷; h. The 3D structural schematic of the rotor made by mulberry silk in MS-TENG¹⁴⁸; i and j: A silk-based crown twill structure TENG⁴⁴; k. The energy transport schematic of the EHSS system and the structure design⁴³; l. The SF/SSF yarns and PTFEF/SSF yarns fabricated by co-wrapping spinning apparatus¹⁴⁹; m. A double silk-based TENG by stacking a cyanoalkylated siloxane grafted fabric with a fluor alkylated siloxane grafted fabric¹⁵⁰.

Fig.2. 14 Applications of silk-based TENG for sensing: a. The SPSM-based STENG as a self-powered sensor for gesture monitoring¹²³; b. A silk-based TENG for detecting different bending angles of fingers¹²¹; c. An SF/PVDF-HFP-based TENG used for abdominal respiratory monitoring¹⁵⁴: i. at a low respiratory rate; ii: at a normal respiratory rate; iii: at a high respiratory rate; d The schematic illustration of letter ‘K’ recognition and identification process by CSF-TENG-based HMI¹⁰⁴; f: Silk/PET TENG as acceleration sensors; g and h: Detection of a human body sitting down vibration intensity⁴⁰

Fig.2. 15 Applications of silk-based TENG for energy harvesting: a. Equivalent circuit model of the bridge rectifier to convert the AC signals of AT-MASF-TENG into DC to power the portable electronic equipment via commercial capacitors¹¹⁷; b. Charging and discharging curve of 47 μF capacitor while it was employed to power LCD through the rectified electrical output of CSPCF-TENG¹⁵⁵; c. Voltage accumulated across the capacitors with the capacitances of 0.47, 4.7, 10, 22, and 47 μF ¹¹⁷; d. AT-MASF-TENG as energy harvesters to power some 52 commercial LEDs¹⁵⁵ and some electronics, such as e. Timer¹⁵⁵, f. LCD screen¹¹⁷, and g. Wristwatch¹⁵⁵; h. Silk-based TENG for powering 4 white bulbs⁴³

Fig.3. 1 Schematic of preparation of hierarchical SCLs

Fig.3. 2 SS content of three SCLs

Fig.3. 3 SEM for surface morphology of a. IL; b. ML; c. OL; Bonding length of silk fibers in d. IL; e. ML; f. OL

Fig.3. 4 The analytical characterization of three SCLs: a. UV–vis spectrum; b. Reflection of three kinds of SCLs; c. Secondary structure and d. The content of different SCLs

Fig.3. 5 The contact angles of three kinds of SCLs

Fig.3. 6 Tensile properties of SCLs: a. Tensile curves of SCLs; b. Tensile strength of

SCLs

Fig.3. 7 TGA curves of SCLs

Fig.3. 8 Working principles of SCL/PDMS Contact-separation TENGs: a Working principle of SCL/PDMS TENGs; b Dielectric constant of PDMS membrane and SCLs; c The COMSOL simulation results of the OL/PDMS-TENG

Fig.3. 9 Evaluation of electrical outputs of SCL/PDMS TENGs: a-c The Voc, Isc, and Qsc of three different SCL/PDMS TENGs

Fig.3. 10 a. Secondary structure inside SCL without applied pressure; b. Secondary structure inside SCL with external load

Fig.3. 11 Electron affinity of three silkworm cocoon layers (SCLs): a. Electron affinity between OL (positive) and IL (negative); b. Electron affinity between OL (positive) and ML (negative); c. Electron affinity between ML (positive) and IL (negative); Electron flow between d. OL and IL; e. OL and ML; f. ML and IL

Fig.3. 12 Evaluation of electrical outputs of the thickness of PDMS-based TENG with the fixed thickness of 0.2 mm of silkworm cocoons: a-c. The Voc, Isc, and Qsc

Fig.3. 13 Stacked effect of SCL/PDMS TENGs: a-c. The Voc, Isc, and Qsc

Fig.3. 14 a. Open-circuit voltage, b. Short-circuit current, and c. Charge of the OL/PDMS-TENG with different working areas.

Fig.3. 14 a. Open-circuit voltage, b. Short-circuit current, and c. Charge of the OL/PDMS-TENG with different working areas.

Fig.3. 15 a. Charging curves of various capacitors by OL/PDMS TENG; b. Output voltage and power density of OL/PDMS TENG at a series of external loads

Fig.3. 16 a. The mechanical stability of OL/PDMS TENG; b. The recovery state of

device housing after 30,000 cycles

Fig.3. 17 Comparison of the voltage density reported in recent years^{1, 24, 32, 38, 42, 118, 122, 202, 203}

Fig.3. 18 Output performance of OL/PDMS TENG: a-c. The Voc, Isc, and Qsc of three kinds of SCL/PDMS-TENGs under different pressure; d-f. The Voc, Isc, and Qsc of three kinds of SCL/PDMS TENGs under different frequencies.

Fig.3. 19 Demonstrations of OL/PDMS TENG for energy harvesting: a. The equivalent circuit for charging/discharging of electronics; b. Charging and discharging process of a capacitor of 22 μF to power an electric watch; c. Powering a small calculator with a capacitor of 4.7 μF ; d. Lighting up 44 LEDs by OL/PDMS TENG

Fig.3. 20 Applications of OL/PDMS TENG as self-powered wearable sensors: a Monitoring of wrist bending angles by fixing OL/PDMS TENG on the wrist; b Monitoring of walking gestures by fixing OL/PDMS TENG under the shoes

Fig.3. 20 Applications of OL/PDMS TENG as self-powered wearable sensors: a Monitoring of wrist bending angles by fixing OL/PDMS TENG on the wrist; b Monitoring of walking gestures by fixing OL/PDMS TENG under the shoes

Fig.4. 1 Design and fabrication of the SFP and SFPAG membrane: a. Illustration of the hierarchical structure of silkworm cocoon; b. Synthesis process of the SFP membrane

Fig.4. 2 Working principles of the fabricated SFP/F-TENGs

Fig.4. 3 Dielectric constant of SFP membranes

Fig.4. 4 Illustration of the flexibility of SFP membranes. a PVA/SF; b SFP-S-0.87%; c SFP-S-1.72%; d SFP-S-2.56%; e SFP-S-3.39%; f SFP-S-4.20%; g SFP-S-5.00%; h SFP-S-5.79%; i SFP-S-6.56%; j SFP-S-7.32%

Fig.4. 5 Surface morphology of the composite SFP membranes. SEM Surface morphology of a. PVA/SF; b. SFP-S-0.87%; c. SFP-S-1.72%; d. SFP-S-2.56%; e. SFP-S-3.39%; f. SFP-S-4.20%; g. SFP-S-5.00%; h. SFP-S-5.79%; i. SFP-S-6.56%; j. SFP-S-7.32%; Surface roughness of (a') PVA/SF; (b') SFP-S-0.87%; (c') SFP-S-1.72%; (d') SFP-S-2.56%; (e') SFP-S-3.39%; (f') SFP-S-4.20%; (g') SFP-S-5.00%; (h') SFP-S-5.79%; (i') SFP-S-6.56%; (j') SFP-S-7.32%

Fig.4. 6 Deconvolution of the amide I region (1600~1700) of FTIR spectra of SFP membranes. a PVA/SF; b SFP-S-0.87%; c SFP-S-1.72%; d SFP-S-2.56%; e SFP-S-3.39%; f SFP-S-4.20%; g SFP-S-5.00%; h SFP-S-5.79%; i SFP-S-6.56%; j SFP-S-7.32%

Fig.4. 7 Electrical performances of SFP/F TENGs under different SS concentrations. a V_{oc} and b I_{sc} of SFP/F-TENGs; c Illustration of the interaction between PVA with SF and SS

Fig.4. 8 Electrical output performance of the SFP/F-TENGs: a. Current, b. Voltage, and c. Charge of the SFP-S-3.39%/F-TENGs under a fixed applied force of 5 N; d. Current, e. Voltage, and f. Charge of the SFP-S-3.39%/F-TENGs under fixed frequencies of 3 Hz; g. Durability and stability test of MFS/F-SETENGs for 10,000 cycles

Fig.4. 9 Application of the SFP-S-3.39%/F-TENGs considered as an energy harvester: a. Power density of SFP-S-3.39%/F-TENG with different external load resistance; b. The powering and charging curves; c. The SFP-S-3.39%/F-TENGs charges a small calculator; d. A diagram that the SFP-S-3.39%/F-TENG powering a clock; e and f: the SFP-S-3.39%/F-TENG can power different LED lights

Fig.4. 10 The applications of SFP-S-3.39%/F-TENG as a self-powered wearable sensor for human motion monitoring: Pressure sensor of different fingers: a. One finger pressure; b. Two fingers pressure; Wrist motion detection at different angles: c. Small angles; d. Large angles; e. Schematic diagram of bending fingers; f. Electrical signals of bending fingers

Fig.5. 1 Synthesis process of the SFPAG membranes

Fig.5. 2 Schematic illustration of the working mechanism of the designed SFPAG/F-TENG: a. Working mechanisms of SFPAG/F-TENG; b. COMSOL simulation results of the potential distribution on dielectric layers

Fig.5. 3 Dielectric constant values of SFPAG membranes

Fig.5. 4 Characterization of SFPAG membranes. a SEM images of SFPAG membranes; b The KPFM images and measured surface potentials of the SFPAG-Ag-0.57%; c XRD patterns of the composite SFPAG films; d Deconvolution of the amide I region (1,580~1,720) of FTIR spectra of SFPAG-Ag-0.57%; e Stress-strain curves of different SFPAG films; f Elongations at break and their vibration of different SFPAG membranes; g Young's modulus of different SFPAG films; h Hydrophilic properties of SFPAG membranes; i TGA results of SFPAG membranes

Fig.5. 5 EDS mapping of elemental a C; b N; c O; d Ag

Fig.5. 6 a. KPFM images of SFP-S-3.39% membrane and b. Surface potential of SFP-S-3.39% membrane.

Fig.5. 7 Deconvolution of the amide I region (1580~1720) of FTIR spectra. a SFPAG-Ag-0.21%; b SFPAG-Ag-0.37%; c SFPAG-Ag-0.48%; d SFPAG-Ag-0.64%

Fig.5. 8 Parametric analysis and design optimization of SFPAG/F-TENG: a. V_{oc} ; b. I_{sc} ; c. Q_{sc} ; d. V_{oc} of SFPAG/F-TENG with different pressures; e. V_{oc} of SFPAG/F-TENG with different frequencies; f. The SFPAG/F-TENG device with the respective triboelectric materials; g. Power density of the SFPAG/F-TENG; h. Electrical performance comparison with silk-based TENGs previously reported^{1, 24, 27-30, 33-38, 118, 122, 133, 134}. Detailed data are provided in Table 5. 3; i. The durability of SFPAG/F-TENG within 30,000 cycles

Fig.5. 9 V_{oc} of SFPAG/F-TENG with different thickness

Fig.5. 10 The applications of SFPAG/F-TENG are energy harvesters. a The equivalent electrical circuit of the SFPAG/F-TENG; b Illustration of SFPAG/F-TENG drives a calculator with a 10 μ F capacitor; c and d The illustration of charging and powering a calculator for calculation and a sports watch with a 10 μ F capacitor ($2 \times 2 \text{ cm}^2$); e Images of the TENG lighting up 240 LEDs with an applied force of 5 N at 3 Hz; f Charging curves of various capacitors by the SFPAG/F-TENG

Fig.5. 11 The application of SFPAG/F-TENG being smart sensors. a SFPAG/F-TENG being pressure sensors for finger pressing; b Monitoring of elbow bending angles by pasting SFPAG/F-TENG on the elbow; c Knee-related activities monitoring by attaching SFPAG/F-TENG to the knee joint; d Foot-related activities detecting by placing SFPAG/F-TENG in the shoes; e Humidity resistance of the fabricated SFPAG/F-TENG

Fig.5. 12 Time sensitivity and response duration

Fig.6. 1 Preparation process of the MFS membrane

Fig.6. 2 Concept, fabrication, and characteristics of MFS films: a. Schematic illustration of the structure of the hierarchical porous MFS film; b. surface morphology of MFS-0.25% film; c. EDS of the MFS-0.25% film including C, N, O, and Ti element; d and e. Cross-sectional morphologies of the MFS-0.25% film; f. Digital photos of the fabricated MFS membranes with contrasting MXene content; g. XRD spectra of the MFS membranes; h. FTIR of diverse MFS membranes

Fig.6. 3 Sectional view and surface morphologies of the MFS membranes: a. The sectional view of PVA/SF/SS membrane; a1. Partial enlargement of the sectional view of PVA/SF/SS membrane; a2. Surface morphology of PVA/SF/SS membrane; b. The sectional view of the MFS-0.08% membrane; b1. Partial enlargement of the sectional view of the MFS-0.08% membrane; b2. Surface morphology of the MFS-0.08% membrane; c. The sectional view of the MFS-0.17% membrane; c1. Partial enlargement of the sectional view of the MFS-0.17% membrane; c2. Surface morphology of the

MFS-0.17% membrane; d. The sectional view of the MFS-0.34% membrane; d1. Partial enlargement of the sectional view of the MFS-0.34% membrane; d2. Surface morphology of the MFS-0.34% membrane; e. The sectional view of the MFS-0.42% membrane; e1. Partial enlargement of the sectional view of the MFS-0.42% membrane; e2. Surface morphology of the MFS-0.42% membrane.

Fig.6. 4 a. SEM of MXene nanosheets; b. EDS of the MFS-0.08% membrane for the sectional view.

Fig.6. 5 UV Transmission of the MFS membranes

Fig.6. 6 Deconvolution of the amide I region (1580~1720) of FTIR spectra of MSF membranes. a PVA/SF/SS; b MFS-0.08%; c MFS-0.17%; d MFS-0.25%; e MFS-0.34%; f MFS-0.42%

Fig.6. 7 Structural characteristics of the MFS membranes: a. Representative stress-strain curve of different MFS films; b. Summary of stress and strain of varied MFS membranes; c. The surface morphology of the MFS-0.25% membrane after the tensile fracture; d. The potential self-assembly process of the MFS membranes; e. The surface potential difference of the SFP membrane; f. The surface potential difference of the MFS-0.25% film; g. The roughness of the SFP membrane; h. The roughness of MFS-0.25% membrane; i. The work function of SFP membrane and MFS-0.25% membrane; j. Diagram of the work function changes for SFP membrane and MFS-0.25% membrane

Fig.6. 8 Surface morphology of the MFS membranes after the tensile fracture: a and a1: the surface morphology of the PVA/SF/SS membrane after the tensile fracture; b and b1: the surface morphology of the MFS-0.08% membrane after the tensile fracture; c and c1: the surface morphology of the MFS-0.17% membrane after the tensile fracture; d and d1: the surface morphology of the MFS-0.25% membrane after the tensile fracture; e and e1: the surface morphology of the MFS-0.34% membrane after the tensile fracture; f and f1: the surface morphology of the MFS-0.42% membrane after the tensile fracture.

Fig.6. 9 a. Contact angles of the MFS membranes; b. TGA results of the MFS membranes.

Fig.6. 10 CPD of the Au

Fig.6. 11 The working mechanism of the MFS/F-SETENGs: a. The illustration of the electricity transferring process in a full cycle of the TENG; b. COMSOL simulation on the potential distribution in the TENG; c. The dielectric constant of different MFS membranes

Fig.6. 12 Electrical output performance of the MFS/F-SETENGs: a. Current, b. Voltage, and c. Charge of the MFS/F-SETENGs under fixed frequencies of 3 Hz and applied force of 5 N; d. The voltage of the MFS-0.25% film applied different forces (3 N~11 N) with a fixed frequency of 3 Hz; e. Voltage of the MFS-0.25% film in various frequencies (1 Hz~5 Hz) with a fixed force of 5 N; f. Voltage of the MFS-0.25% film based on different areas (1, 4, 6, 9 cm²); g. Durability and stability test of MFS/F-SETENGs for 15,000 cycles. The insets exhibit detailed signals during the test cycles

Fig.6. 13 Application of MFS/F-SETENGs considered as an energy harvester: a. Power density of MFS-0.25%/F-SETENG with different external load resistance; b. Comparison of the power density of our fabricated MFS-0.25%/F-SETENG with silk-based double-electrode TENGs^{24, 29, 30, 33-35, 38, 117, 118, 122, 133, 134, 141, 142, 146, 147, 155, 229, 279, 280}, and the inset is the comparison with other silk-based SETENGs^{1, 36, 37, 123, 278}; c. The MFS-0.25%/F-SETENG charging capacitors of different capacities, and the inset is the equivalent electrical circuit of MFS-0.25%/F-SETENG when working as a power supplier; Charging and powering small electronics of MFS-0.25%/F-SETENG: d. A calculator; e. A timer; and f. A clock

Fig.6. 14 The applications of MFS/F-SETENG as a self-powered wearable sensor for human motion monitoring: Wrist motion detection at different angles: a. 30°; b. 45°; c. 90°; Finger bending detection at varying angle d. 30°; e. 45°; f. 90°; The MFS/F-SETENG is applied for the detection of g. Walking; h. Running detection; i. Jumping

Fig.6. 15 Practical applications of the MFS/F-SETENG in self-powered sensing: a. The Bluetooth signal transmission system by tapping the MFS/F-SETENG; b. The schematic diagram of the pressure-sensing system includes the optical and schematic diagram with 3×3 channels, multichannel acquisition, real-time sensing, and statistic results; c. Real-time output voltage signals in tapping different pixels in the order of 1, 2, 3, 4, 5, 6, 7, 8, and 9; d. Real-time output voltage signals in tapping different channels in the order of 47, 12, 28, 37, and 13; e. Enlarged output voltage signals of 13 pixels; f. Pressure distribution of the MFS/F-SETENG sensor in sensing different letter located in the sensing arrays

List of Tables

- Table 2. 1 Comparison of electrical outputs of silk-based TENGs in recent years
- Table 3. 1 Basic parameters of cocoon layers
- Table 3. 2 UPF of different silkworm cocoon layers
- Table 3. 3 Comparison of output performance of silk-based TENGs
- Table 4. 1 Composition and thickness of the SFP membranes
- Table 4. 2 Relative contents of secondary structures through FTIR test
- Table 5. 1 Composition and thickness of the SFPAG membranes
- Table 5. 2 Relative contents of SFPAG membrane's secondary structures
- Table 5. 3 Electrical performance comparison of previously reported silk-based TENGs
- Table 5. 4 Comparison of the electrical performance of cellulose-TENGs
- Table 6. 1 Specific parameters and proportion of each component inside the MFS membranes
- Table 6. 2 Relative contents of secondary structures through FTIR test

List of Abbreviations

TENGs	Triboelectric nanogenerators
SC	Silkworm cocoon
SF	Silk fibroin
SS	Sericin
SCL	Silkworm cocoon layer
PDMS	Polydimethylsiloxane
PVA	Polyvinyl alcohol
SFP	Fibroin/Sericin/Polyvinyl alcohol
F-Nylon	Fluoro-nylon
AgNWs	Silver nanowires
EMG	Electromagnetic generator
CS	Contact-separation
SETENG	single-electrode triboelectric nanogenerator
LSTENG	Lateral-sliding TENG
3DAW	3D angle-interlock woven
SPSC	Self-power supercapacitor
Na ₂ CO ₃	Sodium carbonate
LiBr	Lithium bromide
CSF	Carboxymethyl chitosan and silk
AT-MASF	Alcohol-treated microarchitected SF
CNT	Carbon nanotube
SMPs	Silk microparticles
PCB	Printed circuit board
AT-MASF	Alcohol-treated microarchitected silk fibroin
CSPCF	Silk microparticles loaded PVA composite film
ESE	Electrospray-etching
ESD	Electrospray deposition
SNR	Silk nanoribbon
SNRF	Nascent SNR film

RSFF	Regenerative silk fibroin film
PD	Power density
MOFs	Metal-organic frameworks
LEDs	Light-emitting diodes
RH	Relative humidity
STENG	Silk aerogel-based TENG
CSPCF	Silk microparticles loaded PVA composite film
CNF	Copper-nickel conductive fabric
UPF	Ultraviolet protection factor
OL	Outermost layer
ML	Middle layer
IL	Innermost layer
EA	Electron affinity
IoT	Internet of Things
SFPAG	Fibroin/sericin/Polyvinyl alcohol/AgNWs
MFS	SF/SS/PVA/MXene

CHAPTER 1 Introduction

1.1 Background

In recent decades, fossil fuel consumption has caused severe environmental pollution and resource shortages, which are expected to become increasingly troublesome problems in the coming years. Researchers are actively seeking new solutions to replace traditional resources. At the same time, significant efforts have been directed towards developing flexible electronics, such as electronic skins¹⁻³, flexible sensors^{4, 5}, and energy supply systems^{6, 7}, as well as expanding applications in fields like smart cities monitoring⁸, touchpad⁹, and healthcare¹⁰. Moreover, the rapid advancement of smart electronics and wearable textiles is driving an increasing demand for flexible fiber sensors and sustainable energy solutions. In response, there is an urgent need for convenient and lightweight energy sources that can seamlessly integrate with these technologies.

Triboelectric nanogenerators (TENGs), as an emerging branch of energy conversion technologies, were first proposed by Wang's group in 2012¹¹, which is based on the coupling effect of triboelectrification and electrostatic induction¹². To date, four kinds of working modes have been developed, namely contact-separation (CS) mode, freestanding mode, lateral sliding mode, and single electrode mode¹³, in which CS mode is the primary electrification mechanism for polymer-based TENGs with the principle of vertical charge polarization. In addition, many endeavors have been devoted to broadening the application scopes of TENGs, such as wearable electronic devices^{6, 14, 15}, artificial skin¹⁶⁻¹⁸, and energy harvesting¹⁹⁻²², etc. However, various fabricated materials employed in TENGs pose potential issues of concern. For instance, using poisonous organic solvents may cause environmental problems and harm human bodies if exposed to such conditions for a long time. Therefore, from a sustainability point of view, eco-friendly materials should be considered with a higher priority. Accordingly, the materials selected for TENGs are preferably biodegradable, biocompatible, easily fabricated, eco-friendly, and low-cost.

Natural fibers have garnered significant attention in the design of TENGs owing to their inherent advantages, aligning well with the growing demand for sustainable and eco-friendly energy solutions. Derived from renewable resources, natural fibers such as cotton, silk, and wool offer remarkable biodegradability and biocompatibility, reducing the environmental impact of electronic devices. Their fibrous structures provide a high surface area, which is beneficial for enhancing the triboelectric effect. The intrinsic flexibility and mechanical strength of these fibers also contribute to the durability and adaptability of TENGs in various applications such as wearable electronics and environmental sensors. Furthermore, the diverse chemical compositions of natural fibers allow for surface modifications to optimize their electrical properties, thereby improving energy conversion efficiency. By integrating natural fibers into TENG designs, researchers aim to develop devices that are not only efficient and cost-effective but also harmonious in integrating with the natural ecosystem, offering a promising pathway toward greener technology innovations.

Among natural fibers, silk stands out as a natural protein fiber produced by the larvae of the silkworm moth, *Bombyx mori* (*B. mori*), during the construction of their cocoons. Surprisingly, SC possesses a hierarchical structure with a random surface morphology like a nonwoven structure consisting of a continuous silk thread. Single silk comprises intertwining fibroin fibers (SF) of high molecular weight, which are bonded together by a glue-like protein known as sericin (SS), creating a structure reminiscent of a core-shell model²³⁻²⁵. This intricate architecture is formed through a spinning process that occurs over several hours as the larva extrudes a continuous silk thread from labial glands in its head in a figure-of-eight or 'S' pattern. Owing to the presence of various amino acids, silk exhibits excellent electron-donating abilities²⁶. This characteristic, combined with its natural abundance, biodegradability, and mechanical flexibility, positions silk as a good material for developing sustainable energy technologies and advanced electronic applications.

As a result, numerous SF-based TENGs have been developed by employing different fabrication techniques such as electrospinning^{24, 27-29}, membranes³⁰⁻³⁵, 3D printing^{36, 37},

spraying³⁸⁻⁴⁰, gel formation^{41, 42}, and fibrous modifications^{43, 44}. These innovations highlight the versatility and potential of silk for advancing energy-harvesting technologies. Power density is a critical parameter for evaluating the performance of triboelectric devices, as it directly impacts the capability of TENGs to power electronic devices, extending from small sensors in wearable technology to larger systems in renewable energy applications. In the past decade, significant attention has been devoted to enhancing the performance of silk-based TENGs to expand their application areas. Although the output performance of these devices has improved since 2016, several critical issues remain to be addressed: (1) Some silk-based materials utilize highly volatile organic solvents that pose significant environmental hazards and are toxic, with prolonged exposure potentially leading to carcinogenic effects. Consequently, the design of silk-based composites should prioritize the selection of biodegradable, environmentally benign, and non-toxic materials; (2) Power density is a critical factor in determining the potential applications of TENGs. However, the power density of many current devices remains insufficient to serve as energy harvesters for powering small electronic devices. Some researchers have pursued high power density by integrating many devices and employing costly and complex electrospay techniques. Therefore, it is essential to explore facile and effective methods to achieve high power density in silk-based TENGs; (3) In the development of silk-based TENGs, researchers often remove SS to focus exclusively on SF, rendering sericin a waste byproduct. This degumming process is not only complex but also resource-intensive. By integrating SS into the design of silk-based TENGs, it is possible to eliminate the need for this complicated procedure while simultaneously reducing the water contamination associated with SS disposal.

Given the current challenges and gaps in research, this thesis seeks to design and fabricate innovative silk-based TENGs with customized functionalities via facile and effective methods. Firstly, a comprehensive investigation into the hierarchical structure of the silkworm cocoon was conducted, uncovering significant insights that can be used to guide the design of composite membranes based on this unique structure. Inspired by the hierarchical structure of the silkworm cocoon and the specific ratio of SF to SS

in individual silk fibers, an SFP membrane has been synthesized. By leveraging the natural properties of silk, the SFP membrane-based TENG device exhibits enhanced electrical performance, making it a promising candidate for advanced technological applications in sustainable energy solutions and sensing detection systems. Additionally, incorporating highly conductive AgNWs into the SFP matrix resulted in a rough surface morphology, which facilitated the improved charge transfer and significantly enhanced the overall electrical performance. Moreover, MXene was incorporated into the SFP matrix, a two-dimensional material known for its exceptional triboelectric properties but prone to aggregation. The resultant silk-based TENGs exhibit enhanced electrical outputs by the disaggregation effects of SS. This research study provides insight into the rational design and development of silk-based TENG devices with enhanced electrical outputs for energy harvesting and sensing applications.

1.2 Objectives

This research focuses on designing and exploring facile and effective methods to fabricate high-performance silk-based TENGs for energy harvesting and multichannel sensing. The detailed objectives of this research are listed as follows:

- (1) To design and investigate TENGs based on silkworm cocoon layers through a facile and effective approach to gain deep insights into the structure of silkworm cocoons, facilitating subsequent biomimetic design and enabling efficient energy harvesting and sensing.
- (2) To develop a biomimetic silkworm cocoon layer that imitates the original 3D architecture of silkworm cocoons, enabling the fabrication of TENGs for efficient energy harvesting.
- (3) To construct silk-based composite membrane TENGs by incorporating conductive metal materials to achieve high-performance TENGs suitable for practical applications in various scenarios.

(4) To fabricate high-performance silk-based single-electrode TENGs by incorporating two-dimensional materials to realize multichannel sensing and energy harvesting.

1.3 Research Methodology

Following the objectives mentioned above, my research study focuses on designing and fabricating silk-based TENGs with improved performance using facile, low-cost, and controllable methods. The strategies being addressed in this research are listed below:

(1) Investigation of Silkworm Cocoon Layers as Tribolayers for Energy Harvesting and Sensing Applications

Silkworm cocoon layers were initially peeled from the middle section of pristine cocoons. Next, the middle part was exfoliated into multiple layers. Three distinct layers were selected: the outermost layer, middle layer, and innermost layer, each having unique architecture and sericin content while maintaining consistent thickness. These layers were then used to fabricate SCLs/PDMS double-electrode TENGs. Structural characterization and triboelectric performance measurements were then conducted.

(2) Study of Silk-Based Composite Membranes Inspired by Silkworm Cocoon Structure as Tribolayers in Energy Harvesting and Sensing Applications

Firstly, one gram of water-soluble PVA precursor was added to ten milliliters of SF solution. The mixture was heated and stirred at ninety degrees Celsius for forty minutes before being cooled to sixty degrees Celsius. Subsequently, different proportions of SS powders were mixed into the SF/PVA solution to form various membranes, which were designated as PVA/SF, SFP-S-0.87%, SFP-S-1.72%, SFP-S-2.56%, SFP-S-3.39%, SFP-S-4.20%, SFP-S-5.00%, SFP-S-5.79%, SFP-S-6.56%, and SFP-S-7.32%, respectively. The SFP/F-TENG was then fabricated using the SFP membrane as the positive friction layer and commercial fluoro-nylon as the negative layer. Systematic structural characterization and triboelectric performance measurements were subsequently conducted.

(3) Exploration of AgNWs-Enhanced Conductive Silk Membranes as Tribolayers for Energy harvesting and Sensing

Firstly, the AgNWs were synthesized by the following steps: ethylene glycol (45 milliliters) was preheated in a boiling flask-3-neck in an oil bath at one hundred fifty degrees Celsius for around one hour with continuous magnetic stirring. Then, two milliliters of FeCl_3 solution (0.004 moles per liter) were added to the flask. After fifteen minutes, fifteen milliliters of AgNO_3 solution (0.5 moles per liter) were injected into the flask using a syringe pump. Then, forty-five milliliters of PVP solution (0.147 moles per liter) were added to the flask and left for six hours. Afterward, the reaction was cooled down to room temperature with a water bath. For the purification step, the synthesized AgNWs were dispersed in ethanol and acetone and centrifuged for three times. Finally, the purified AgNWs were dispersed in ethanol (ten milligrams per milliliter) for use in TENG fabrication in the next step. After the synthesis of AgNWs, different percentages of AgNWs were incorporated into the SPF matrix to form the SFPAG membranes as the positive tribolayer inside the TENG while F-Nylon is considered the negative tribolayer to form a double-electrode TENG device. Based on the addition of AgNWs content, the membranes are named SFPAG-Ag-0.21%, SFPAG-Ag-0.37%, SFPAG-Ag-0.48%, SFPAG-Ag-0.57%, and SFPAG-Ag-0.64%, respectively. Structural characterization and triboelectric performance measurements were then conducted.

(4) Analysis of MXene-Enhanced Conductive Silk Membranes for Designing Single-Electrode Triboelectric Nanogenerators in Energy Harvesting and Sensing Applications

Initially, a two-dimensional material, MXene, was incorporated into the SFP matrix and heated at 60 degrees Celsius for one hour to facilitate preliminary dispersion. After heating, the mixture was subject to ultrasonic treatment, with agitation every 10 minutes to prevent MXene aggregation. This process was repeated approximately for 10 times until MXene was fully dispersed within the SFP matrix. The solution was then allowed to stand undisturbed for 6 to 8 hours to eliminate any entrapped air bubbles. Subsequently, the mixture was transferred to a Petri dish and dried at 50 degrees Celsius

to form a film. The formed MFS membranes are named SFP, MFS-0.08%, MFS-0.17%, MFS-0.25%, MFS-0.34%, and MFS-0.42%, respectively. The as-prepared MFS films were tailored into a square shape with a dimension of 2.0 cm × 2.0 cm as the positive tribolayers while the Fluoro-nylon as the negative one with the copper wire connecting to the ground working as a single electrode MFS/F-TENGs. Structural characterization and triboelectric performance measurements were then conducted.

(5) Materials characterization and performance measurement

Field Emission Scanning Electron Microscope (SEM, Tescan MIRA) was used to characterize the morphology of membranes operating at an accelerating voltage of 10 kV. Energy Disperse Spectroscopy (EDS) data was acquired on an SEM (Tescan VEGA3) operating at 10 kV. Fourier Transform Infrared Spectrometer (FTIR) (PerkinElmer FTIR Spectrum 100 + Autoimage IR Microscope) was utilized to analyze the crystalline characteristics of the composite membranes. A thermogravimetric analyzer (TGA) (Perkinelmer TGA 4000 System 100–240 V/50–60 Hz) was used to evaluate the thermal stability of the composited membranes. To investigate the tensile strength of the membranes, a universal material testing machine (3365, Instron, USA) was employed under constant temperature and humidity (20 °C, R.H. 65%). X-ray Diffractometer (XRD, Rigaku SmartLab 9kW) was used to detect the additives into the silk-based matrix at the 2θ ranging from 5° to 80° (4°/min). UV–vis (Hitachi UH5300) was used to measure the UV-visible absorption spectrum of MFS membranes. Contact angle (SDC-350, Dynetech, Inc., China) was utilized to confirm the water repellency of films. AFM (Germany, Bruker Dimension Icon) was used to measure the surface roughness, the surface potential difference, and the work functions of the membranes. Electrical performance: The dielectric constant was tested by an LCR meter (E4980A, Keysight). The short-circuit currents (I_{sc}) and transferred charge (Q_{sc}) of the MFS/F TENGs were investigated by an electrometer (Keithley 6514 system) and the open-circuit voltages (V_{oc}) were measured by an oscilloscope.

1.4 Research Significance

Sustainability is becoming increasingly critical in bioelectronics, particularly given its global adoption across medical industries, from wearable technologies to implantable systems. Although the miniaturization of biomedical devices has provided logistical and cost benefits, it has not been well achieved sustainably. The continued reliance on non-renewable materials and batteries contributes significantly to global waste, highlighting the need for more stringent resource management and eco-friendly disposal practices to ensure a sustainable future. My research presents four configurations of TENGs using materials that are eco-friendly, sustainable, biocompatible, biodegradable, and easy to fabricate. The thesis has delivered the following positive outcomes:

(1) The design of electronic products utilizing natural materials has consistently been pursued by researchers owing to their environmental compatibility and skin-friendly properties. In this context, a pristine silkworm cocoon layer/Polydimethylsiloxane (SCLs/PDMS) TENG was introduced, marking the first proposal of a silkworm cocoon layer serving as the tribolayer. The proposed SCLs/PDMS-TENG demonstrates a novel architecture resembling a nonwoven structure, achieved through a straightforward and effective peeling method. Benefiting from the natural structure disparities of the silkworm cocoon, the SCLs/PDMS devices exhibit diverse electrical performance, with the OL/PDMS-TENG attaining a voltage of 126 V. Furthermore, the proposed SCLs/PDMS-TENG maintain stable output voltage after 10,500 cycles. This facile and efficient approach forms the foundation for the development of hierarchical electronic designs inspired by the silkworm cocoon structure.

(2) Bionics is an interdisciplinary field that is continually enriched and advanced by the progress of modern science and technology. Its contributions to and impact on materials science have become increasingly significant. Drawing inspiration from the natural ratio of SF to SS inside the silkworm cocoons, a PVA/SF/SS (SFP) membrane was synthesized to preliminarily emulate the structure of silkworm cocoons. The resulting

SFP/F-Nylon-TENG exhibited enhanced electrical output by adjusting the SS proportion, achieving an impressive voltage of 494.47 V. The optimal SF to SS ratio of 3:1 was evaluated and discussed. These SFP membranes demonstrated an improved crystalline structure. The proposed SFP/F-Nylon-TENG offers valuable insights for the fabrication of biodegradable and biocompatible high-performance TENGs.

(3) Researchers have continually sought to enhance the output performance of TENGs to fulfill the diverse power requirements of various applications. Benefiting from the superior conductivity of AgNWs, the composite PVA/SF/SS/AgNWs (SFPAG) membranes, formed by incorporating AgNWs into the SFP matrix, exhibited improved electrical performance, achieving a voltage of 745 V and an instantaneous power density of 7.6 W/m². The tensile strain of the fabricated SFPAG membrane reached 132 %, conferring exceptional stretchability to the film. Additionally, all SFPAG membranes demonstrated hydrophilic properties, which facilitate excellent breathability, enhanced biocompatibility, and increased comfort in wearable applications. The proposed SFPAG/F-Nylon-TENG offers valuable insights into the development of TENGs with enhanced electrical properties.

(4) Power density is a critical parameter for assessing the performance of triboelectric devices, as it directly influences the ability of TENGs to power electronic systems, from small sensors used in wearable technology to larger systems in renewable energy applications. By incorporating the two-dimensional material MXene into the SFP substrate and leveraging the benefits of structural simplicity and optimized configuration, an SFP/MXene (MFS)/F-Nylon single-electrode TENG was developed. This resulted in a voltage output of 745 V and an instantaneous power density of 35.76 W/m², significantly surpassing those achieved by more complex configurations. The MFS membranes exhibited a decreased work function and enhanced coarse surface morphologies, elucidating the MXene-enhanced triboelectric performance mechanism. The optimized SETENG offers capabilities for multichannel sensing and energy harvesting, providing valuable insights for the fabrication of silk-based TENGs with enhanced electrical performance.

1.5 Outline of the Thesis

This thesis consists of seven chapters organized as follows:

Chapter 1 briefly introduces the research background of this project, the existing challenges in this field, the expected research objectives, the research methodology, and the significance and values of this research.

Chapter 2 presents a comprehensive literature review on silk-based TENGs. To introduce silk-based TENGs, an overview of natural fibrous-based TENG is provided, followed by an in-depth examination of silk's structure, the preparation method for fabricating silk-based TENG, and the diverse configurations of TENGs derived from silk, including those based on pure silk membranes and composite silk membranes, as well as methods like silk electrospinning, spraying, 3D printing, gel formation, and fibrous techniques. Finally, the applications of silk-based TENGs are summarized, which encompass energy harvesters and sensors.

Chapter 3 introduces a novel silk-based TENG design that employs an SCL as the tribolayer through a facile and effective process. The characteristics of three distinct SCLs, each with unique SS content and diverse surface morphologies, are meticulously measured and analyzed. The electrical performance of the fabricated SCL/PDMS-TENGs is systematically evaluated.

Chapter 4 develops a silk-based membrane TENG that incorporates PVA, SF, and SS powders, a discarded silk byproduct material inspired by the structural composition of silkworm cocoons. The resultant SFP membranes show an improved and customized performance by changing the proportion of SS powders. The SFP/F-Nylon-TENG is further constructed for energy harvesting and sensing applications.

Chapter 5 designs an advanced SFPAG/F-Nylon TENG that introduces AgNWs into the SFP matrix to significantly enhance conductivity. The fabricated SFPAG film demonstrates improved crystalline structure and increased stretchability. The

performance-optimized SFPAG/F-Nylon TENG is extensively investigated for its applications in moisture sensing and energy harvesting.

Chapter 6 introduces a novel single-electrode silk-based TENG with enhanced electrical performance by integrating MXene into the SFP substrate. Comprehensive characterizations of the MFS membranes are conducted, focusing on work functions, surface potential, and secondary structure analysis, which provide deep insight into the architectural properties of the MFS membranes. The electrical performance is thoroughly evaluated and compared. Moreover, the potential applications of MFS/F-Nylon SETENGs in energy harvesting and sensing are investigated.

Chapter 7 summarizes the results of the whole research work, indicates the limitations of the study, and provides suggestions for future studies on fabricating high-performance silk-based TENGs.

CHAPTER 2 Literature Review

2.1 Fundamentals of Triboelectric Nanogenerators

2.1.1 Triboelectrification

When two materials come into contact or are rubbed together, electric charge is typically transferred from one material to the other. This phenomenon has been commonly referred to as 'frictional electrification' although this term can be misleading; actual rubbing is not always required, as mere contact is adequate to facilitate the considerate charge transferring. If one of the materials is a strong insulator, allowing the charge to remain on its surface for an extended period, the consequences of the charge transfer become evident. Sparks may appear, and lightweight objects may become strongly polarized by the field, leading them to be attracted to the charged insulator. Contact electrification is often thought of as a phenomenon associated with insulators⁴⁵.

2.1.2 Advantages of TENGs

TENGs emerge as a significant energy technology akin to conventional electromagnetic generators (EMG) for converting mechanical energy into electricity. It features a simple structure, high power density, and low operational frequency. Furthermore, TENGs surpass other cutting-edge electronics in terms of portability, ease of fabrication, efficient energy conservation, eco-friendliness, and the ability to harness energy from low frequency wasted mechanical energy. Noteworthy is that certain TENGs are crafted from affordable waste materials, underscoring their cost-effectiveness and recyclability^{46, 47}.

2.1.3 Working Principles of TENGs

Depending on the structural design and the motion profile of the triboelectric layers in a TENG, four fundamental modes of operation have been defined: vertical contact-

separation, lateral-sliding, single-electrode, and freestanding triboelectric-layer modes⁴⁸, as represented in Fig.2. 1.

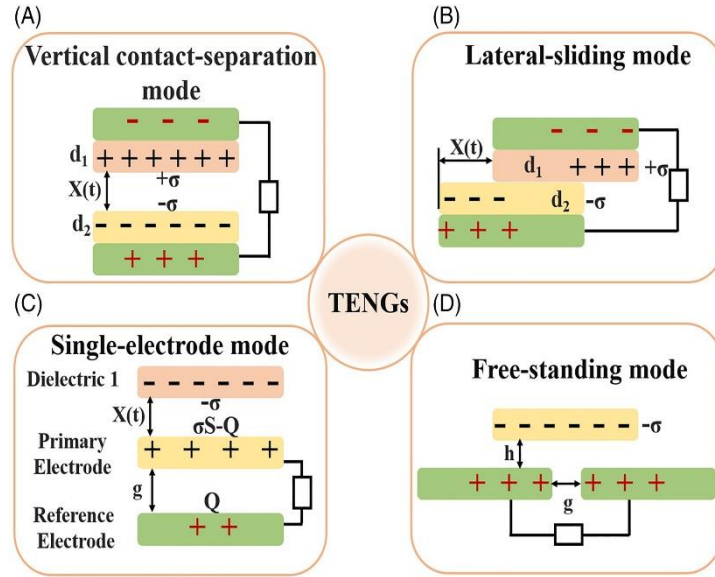


Fig.2. 1 Four working modes of TENGs: a. Vertical contact-separation mode; b. Lateral-sliding mode; c. Single-electrode mode; d. Freestanding triboelectric-layer mode^{49, 50}

(1) Vertical contact-separation mode (CS)

TENGs operating in the contact-separation (CS) mode rely on mechanical sources that generate discontinuous outputs, such as intermittent impacts or shocks. As a result, the CS mode is particularly suited for harvesting energy from activities like human walking⁵¹. Within this mode, two categories of TENGs can be constructed based on the nature of the triboelectric materials: dielectric/dielectric (Fig.2. 1a) and dielectric/conductor.

The operational mechanism of a dielectric/dielectric CSTENG involves the following process: when an external mechanical force causes the triboelectric layers to make contact, through actions such as bending or pressing, triboelectric charges develop as each material acquires opposing charges. Upon the separation of the two materials, a potential difference is electrostatically induced between the electrodes, prompting electrons to flow from the top to the bottom electrode (as shown in Fig.2. 1a)^{52, 53}. Once

the maximum separation distance is achieved, the induced charge on each electrode peaks, halting the current flow. When a compressive mechanical force reduces the distance between the surfaces again, electrons flow from the bottom to the top electrode to balance the potential difference. Through repeated contact and separation, this cyclical process generates alternating current outputs. In the dielectric/conductor configuration, the mechanism is similar, but the conductor surface serves as both the triboelectric surface and the electrode. The working principles of other TENG operation modes are fundamentally similar and thus will not be elaborated upon in this paper. Readers interested in a comprehensive explanation of each mode are directed to existing reviews.

(3) Single-electrode mode (SE)

The single-electrode TENG (SETENG) is classified into two subcategories: contact–separation SETENG (Fig.2. 1c) and sliding SETENG. Each subcategory can function through two types of triboelectric layer interactions: dielectric/conductor and dielectric/dielectric. A key advantage of SETENGs compared to the previously discussed designs is that the top triboelectric layer does not require a connection to an external circuit, enhancing the versatility and applicability of devices⁵⁴. However, due to the electrostatic shielding effect of the primary electrode, SETENGs can achieve only up to 50% of the maximum transferred charge efficiency compared to an equivalent CSTENG or LSTENG, thus affecting their overall performance.

(4) Freestanding mode (FS)

freestanding triboelectric-layer TENGs (FSTENGs) are categorized into two configurations: contact-mode FSTENG and sliding-mode FSTENG (Fig.2. 1d). Each configuration can utilize a dielectric or metal as the freestanding triboelectric layer. FSTENGs offer several advantages, including higher energy conversion efficiency, long-term stability, and reduced surface wear. A notable advantage of sliding-mode FSTENGs over LSTENGs is the lack of required direct physical contact between triboelectric surfaces, which reduces heat generation and material wear during

operation⁵⁵. However, sliding-mode FSTENGs necessitate pre-charging of the tribomaterial for proper functionality. This model boasts additional benefits, such as improved energy conversion efficiency and exceptional robustness.

2.2 Wearable Natural Fibrous-based TENGs

2.2.1 Introduction of Natural Fibrous Materials

a. Cotton

Cotton is a plant-based natural fiber with the formula (C₆H₁₀O₅) known for its environment-friendliness, biocompatibility, and versatility in textiles owing to its unique structure. The primary component of cotton fibers is cellulose, a complex polysaccharide comprising long chains of glucose units. Cellulose accounts for about 90% of the cotton fiber composition, providing strength and durability^{56, 57}. Within the cotton fiber cell wall, cellulose microfibrils are aligned parallel to the fiber axis. These microfibrils are held together by hydrogen bonds and other intermolecular forces, contributing to the strength of the fiber. Commonly, cotton is classified as a positively charged triboelectric material owing to -OH groups to lost electrons. Generally, the cotton-based TENGs displayed an increased output by the effective contact area with their fluffy, porous, and deformable structure⁵⁸.

b. Jute

Jute is a natural fiber obtained from the outer stem and skin of the jute plant. It is primarily composed of cellulose and lignin, giving it a combination of strength, durability, and flexibility. Jute fibers are long, soft, and shiny with a golden hue, making them versatile for various applications. Owing to its eco-friendly and biodegradable nature, jute is widely used in textile production, packaging, and even in designing eco-friendly composite materials. Its affordability, sustainability, and biodegradability render jute a potential choice in industries aiming for environmentally conscious alternatives.

c. Wool

Wool is a natural fiber sourced from the fleece of sheep or other animals like goats, llamas, or rabbits. It is known for its softness, warmth, and resilience. Wool fibers have natural crimp and elasticity, which make them excellent at trapping heat and providing insulation. Wool is also breathable and moisture-wicking, making it comfortable to wear in various climates. Additionally, wool is naturally flame-resistant and tends to be more durable than many synthetic fibers. Wool plays a significant role in the realm of TENGs^{59, 60}. The complex surface texture and the friction between fibers render wool an excellent triboelectric material because of the large contact area from the naturally rough surface. Therefore, wool-based TENGs enable the efficient conversion of mechanical energy into electrical energy, offering a convenient and sustainable method for energy harvesting in renewable energy^{61, 62}.

d. Silk

SF is derived from natural silk fibers produced by insects like silkworms and spiders, comprising glycine-rich proteins. Within *B. mori* cocoons, SF constitutes 70-80 wt% of the cocoon, while SS makes up 25-30 wt%. It is important to note that SS is typically eliminated during preparation due to its potential to trigger immune responses⁶³. SF is structured with α -helices, β -sheet crystals, and random coils, organized through repetitive amino acid sequences involving hydrogen bonds, hydrophobic interactions, and van der Waals forces^{64, 65}. Various forms of silk such as regenerated silk film, spun silk membranes, silk solutions for spray coating, silk fabrics, and fibers, as well as intermediary states like silk hydrogel, aerogel, scaffold, and sponges, have been applied in the design of different types of TENG.

2.2.2 Natural Fibrous-based TENGs

Natural fibers or fabrics show considerable advantages for designing wearable electronics, such as inexpensive, easy to access, abundant, biocompatible, and biodegradable features^{66, 67}. Regarding their structure, natural fibers are composed of

hydrogen interactions weaker than covalent, ionic, and metallic bonds found in inorganic and petroleum-derived materials, which may bring about dissolution and deformation. Therefore, from an environmental perspective, natural fiber is a promising candidate to construct small electronics for energy harvesting and sensing. Herein, 6 representative studies are selected to introduce the natural fibrous-based TENGs including cotton-based TENGs, jute-based TENGs, wool-based TENGs, and silk-based TENGs.

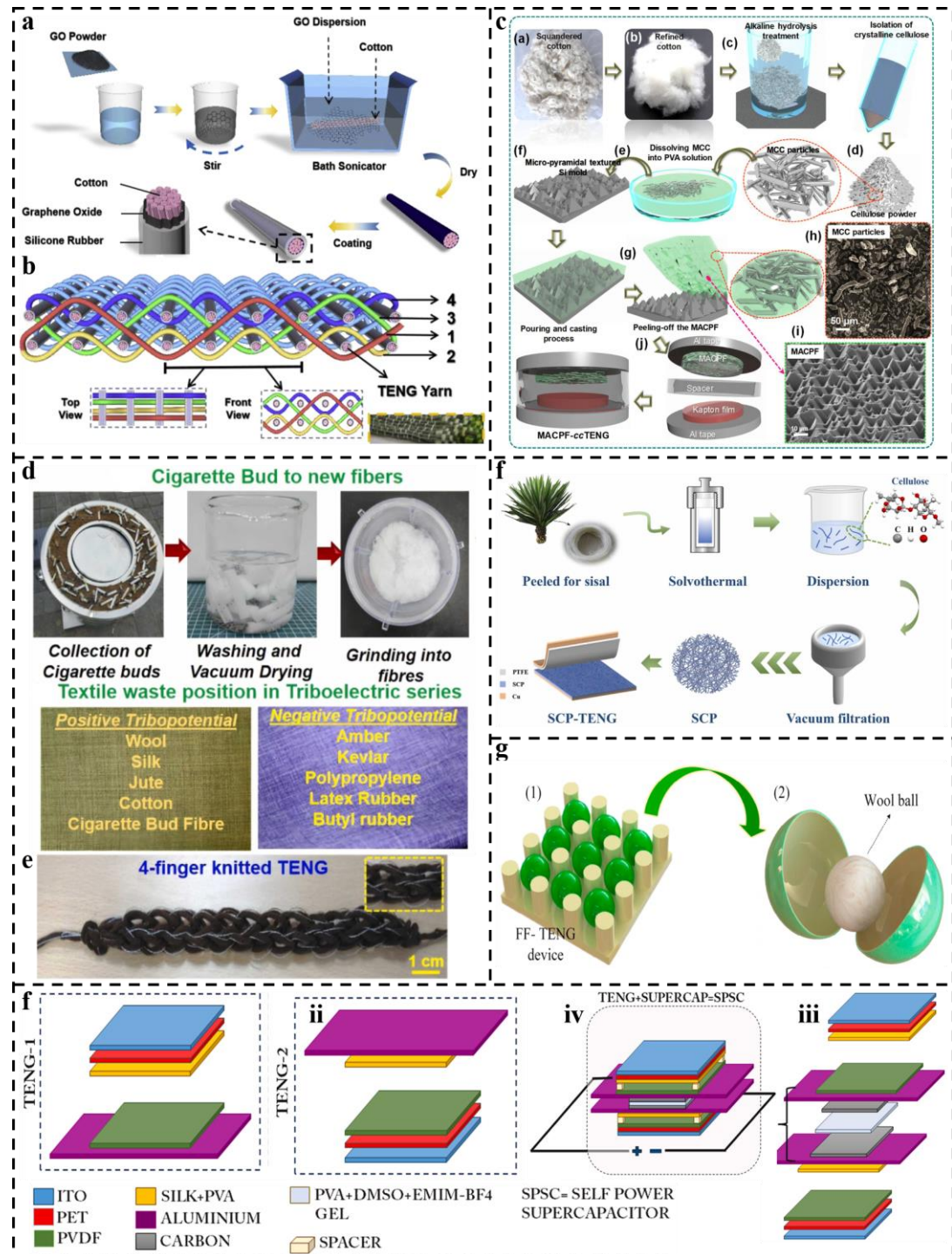


Fig.2. 2 Typical natural fiber-based TENG devices: a. The preparation process of a 3D angle-interlock woven (3DAW) structural wearable TENG; b. The structure schematic of the 3DAW-TENG⁶⁸; c. Schematic diagram to illustrate the fabrication of CPF-pTENG⁶⁹; d. The preparation illustration of a kind of jute-based TENG; e. Digital image

of the knitted jute TENG⁷⁰; f. The production flow chart of sisal cellulose paper (SCP) film⁷¹; g. The structural design of wool-based FF-TENG device⁷²; h. A self-power supercapacitor (SPSC) using CSSC and silk/PVA/PVDF-based TENG⁷³

Cotton containing polar functional groups is frequently chosen as the primary material for creating composite conductive fibers owing to its high porosity, excellent wrinkle resistance, and strong durability^{74, 75}. In a research study⁶⁸, He and his colleagues proposed a 3D angle-interlock woven (3DAW) structure. In this structure, cotton acts as the core fiber, initially immersed in graphene oxide (GO) and subsequently enveloped with silicon fiber, as displayed in Fig.2. 2a. The resulting 3DAW-TENG (see Fig.2. 2b) demonstrates an output power of 0.225 W/m², outperforming both the 2D plain structure and the 3D double-layer plain structure. The regenerated cotton film is another impactful method for designing cotton-based TENGs. With the growing demand in the textile industry, the disposal of waste cotton has become a significant environmental concern. In response to this issue, Graham et al.⁶⁹ transformed waste cotton into a biocompatible film combined with PVA to serve as the positive triboelectric layer. This film was then used to create a coin-cell type TENG, where Kapton functions as the negative material, as shown in Fig.2. 2c.

Jute is another type of natural fiber that is generally insoluble in water. To utilize jute in the design of TENGs, researchers generally modify it through methods such as coating, immersion, carbonization treatment, and composite material preparation. Here, a research study focused on fabricating jute-based TENGs is presented. Manisha et al.⁷⁰ recommend a design of TENG by collecting worn-out textiles from the waste bin, as illustrated in Fig.2. 2d. In addition, Fig.2. 2e depicts a schematic of the deformation of a single knitted loop using conductive rubber and wool weaving. The special TENG can be employed to harness various sports energy, such as dribbling the ball, running, and stretching exercises. In another work, the researchers used a vacuum filtration methodology to attain a regenerated sisal cellulose membrane for energy harvesting, as described in Fig.2. 2f.

Wool exhibits outstanding positive triboelectric properties and is lightweight, which

imparts excellent wave-following characteristics in ocean environments. Recognizing this advantage, Xia et al.⁷² proposed a wool-based TENG for harnessing ocean energy, where a wool ball enclosed within a sphere functions as the positively charged triboelectric component, as depicted in Fig.2. 2g. Because of its mobile feature, the wool-based TENG can effectively convert rolling mechanical energy into triboelectric energy.

Silk is commonly employed to enhance the immediate performance of TENG devices, with the silk-PVDF combination showing significant promise. To enhance this composite, Sarkar et al. proposed a self-powered supercapacitor comprising two TENG units, each utilizing a mixture of naturally available silk with PVA and PVDF as triboelectric elements. Due to its substantial electron affinity, the silk-based TENG configuration achieved an impressive instantaneous output power density of 5980 W/m².

Natural fibers generally demonstrate positive friction properties, with silk being particularly versatile owing to its stable structure and adjustability. As a result, our research is primarily centered on designing and developing silk-based TENGs. In the following sections, a detailed exploration of the current advancements in silk-based TENGs will be provided.

2.3 Silk-based TENGs

SF is characterized by numerous outstanding attributes, such as exceptional biocompatibility, controllable biodegradability, water solubility, high optical transparency, and robust mechanical strength. Furthermore, SF can be processed into diverse forms including fibers, films, sponges, and hydrogels. As a result, it is extensively employed as a key material in fabricating biocompatible wearable and implantable electronic devices, as well as functional elements for energy harvesters, sensors, filters, lenses, memristors, and other applications^{27, 33, 76-88}.

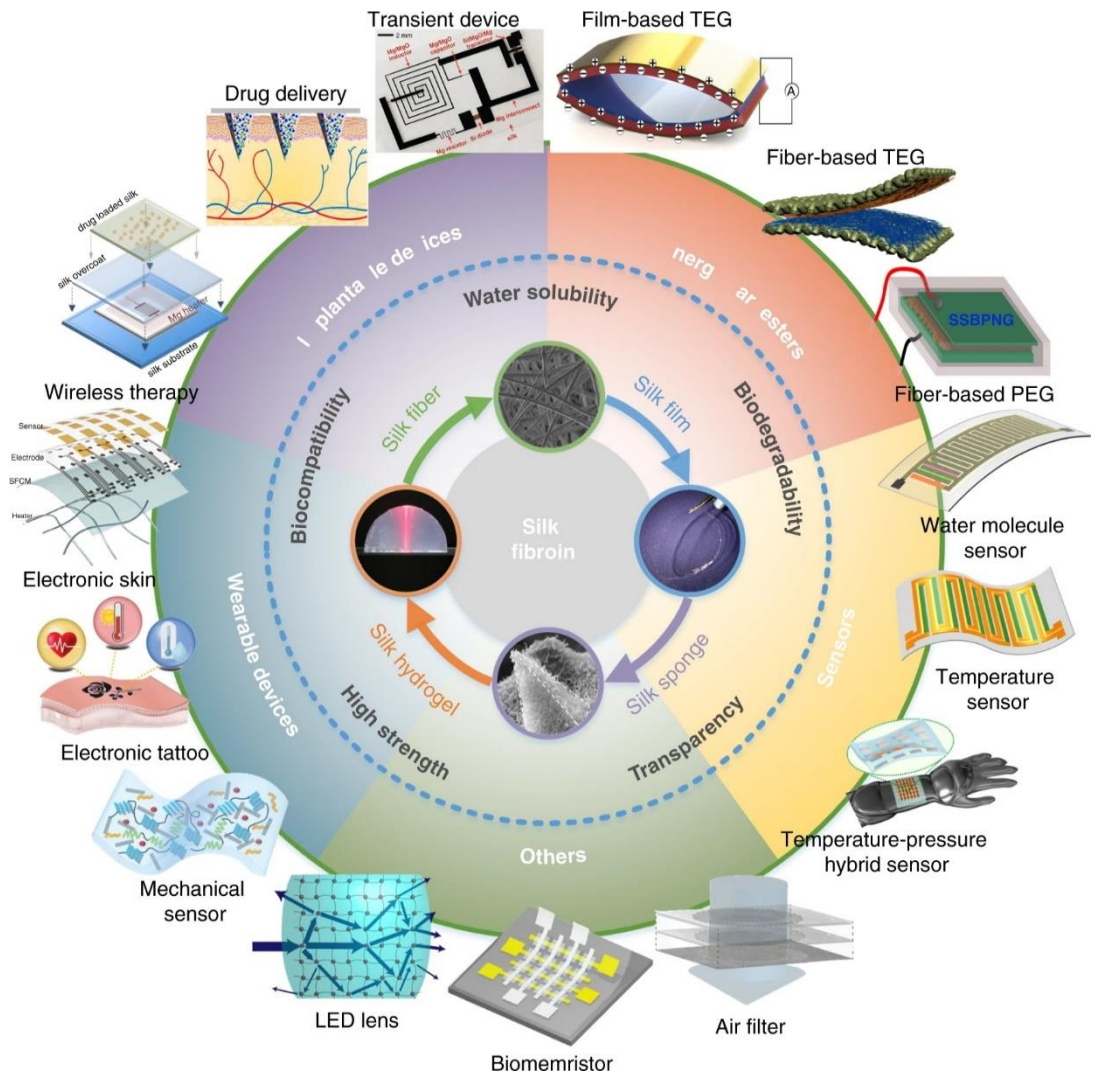


Fig.2. 3 SF-based flexible materials and flexible electronics^{27, 33, 64, 76-88}

2.3.1 Introduction of Silk

Silk is derived from *B. mori* silkworm cocoons and possesses a hierarchical structure^{89, 90}. In this discussion, the hierarchical structure of silk and its characteristics at the molecular level are explored.

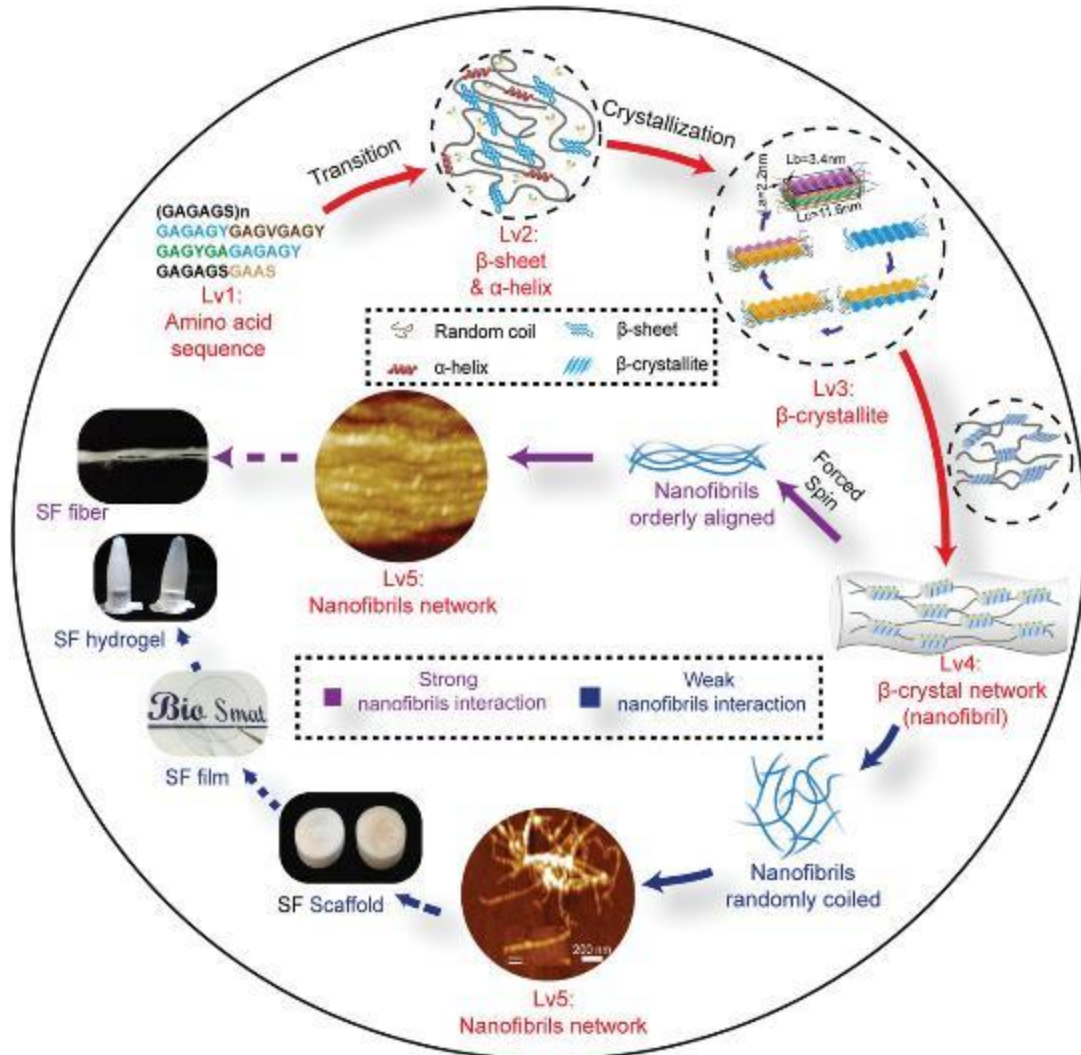


Fig.2. 4 The schematic representation of the hierarchical network structures of SF fibers and non-fiber silk materials⁹¹.

Based on the analysis of the structure of silk materials, the superior performance of *B. mori* silk materials can be attributed to a hierarchical network structure consisting of five levels, as illustrated in Fig.2. 4. The five levels are amino acid sequence (Lv1), secondary structure (Lv2), β -crystallites (Lv3), crystal networks or nanofibrils (Lv4), and nanofibrils networks (Lv5).

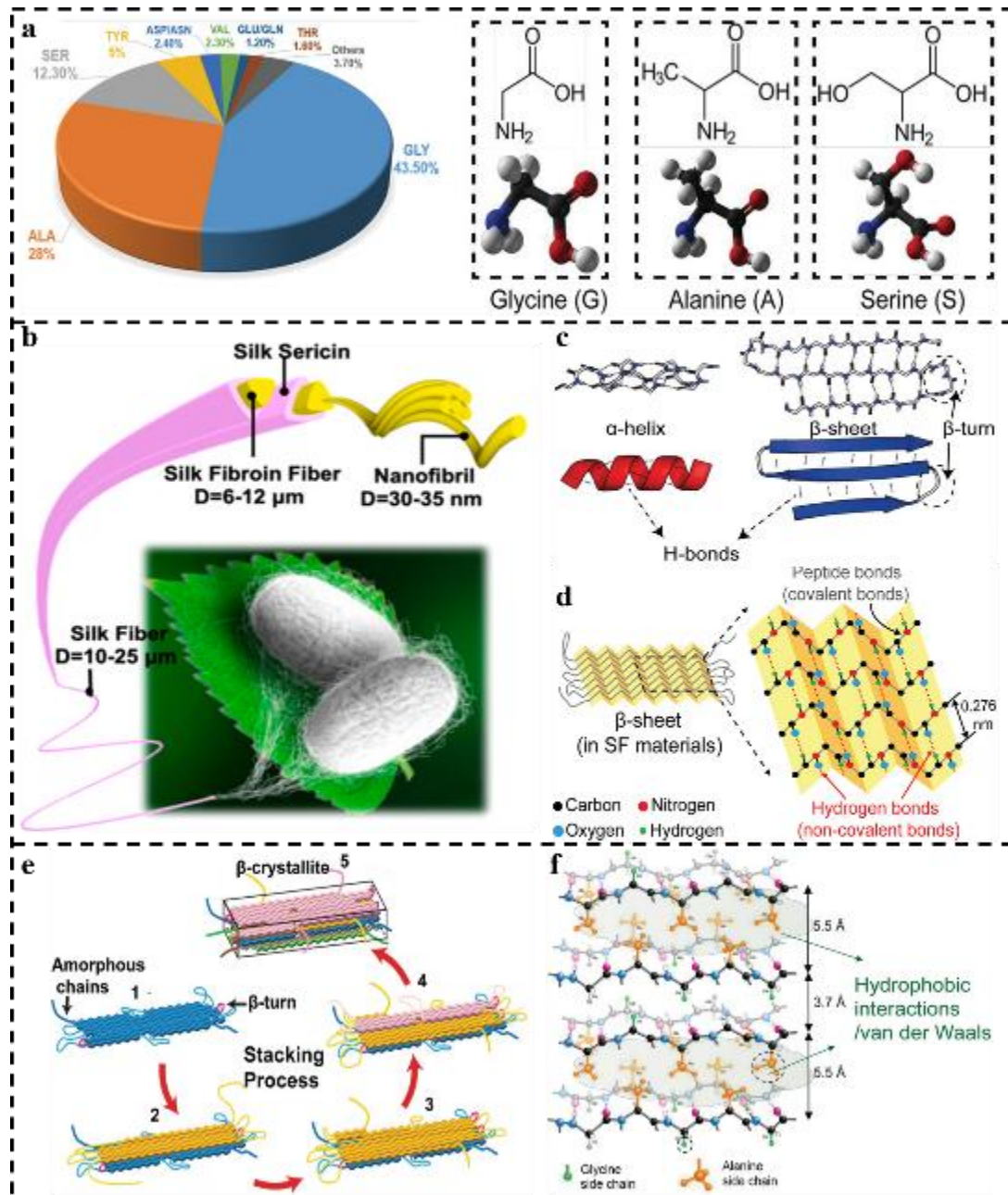


Fig.2. 5 Molecular Structure of silk: a. The composition of the amino acid sequence inside silk; b. Illustration of silk structure; c. Schematic of two typical secondary structures: α -helix and β -sheet; d. An anti-parallel arrangement within silk materials⁹²; e. The process of β -sheets from different molecules stacking into β -crystallite; f. The interaction between β -sheets to form β -crystallites⁹³

The fundamental building block of silk is the amino acid, with silk primarily consisting

of glycine (approximately 43%), alanine (approximately 30%), serine (approximately 12%), tyrosine (approximately 5%), and valine (approximately 2%). Among these, glycine, alanine, and serine are the most prevalent components within silk⁹⁴, as presented in Fig.2. 5a. A single silk fiber is composed of two parallel SF filaments, which account for approximately 75% of its total weight, and these filaments are encased in an SS adhesive. SS, a water-soluble globular protein, acts as a binder to achieve structural integration. Typically, SF has a highly crystalline structure that is rich in β -sheets and β -crystallites⁹⁵. In contrast, SS exhibits a more random structure with an abundance of random coils, α -helices, and β -turns, and a lower content of β -sheets, as presented in Fig.2. 5b.

Regarding α -helices, hydrogen bonds form between the oxygen atom of the C=O group of each peptide bond in the strand and the hydrogen atom of the N-H group of the peptide bond located four amino acids below it in the helix. This arrangement causes the hydrogen bonds to run roughly parallel to the α -helices, contributing significantly to the stability of this secondary structure. Conversely, hydrogen bonds in β -sheets form between different strands (interstrand) rather than within a single strand (intrastrand). In β -sheets, the carbonyl oxygens in one strand form hydrogen bonds with the amino hydrogens of the adjacent strand (Fig.2. 5c). The orientation of β -sheets within silk is a subject of debate among researchers, with discussions addressing both parallel and antiparallel arrangements. However, after extensive consideration, the most widely accepted view is that the β -sheets in silk materials are arranged in an antiparallel version. The likely reason for this preference is that the linear hydrogen bonds (measuring 2.76 Å) between antiparallel β -strands are shorter than the non-linear hydrogen bonds (measuring 2.97 Å) between parallel β -strands⁹¹. This shorter bond length in antiparallel arrangements results in greater β -sheet stability, as illustrated in Fig.2. 5d.

Typically, multiple secondary structural elements combine to create a highly compact and organized three-dimensional protein structure, known as the tertiary structure. Concerning silk materials, the tertiary structure is characterized by intermolecular β -crystals (Fig.2. 5e). Specifically, β -crystallites consist of multiple adjacent β -sheets

from different molecules. Hydrogen bonds, hydrophobic interactions, and van der Waals forces are essential in maintaining the stability and organization of these β -sheets, as revealed in Fig.2. 5f. Generally, β -sheets are viewed as two-dimensional crystals, whereas β -crystallites are considered more stable three-dimensional crystals. The content of β -sheets is usually higher than that of β -crystallites because β -sheets exhibit two types of polymorphism: intramolecular 2D β -sheets and intermolecular 3D β -crystallites. The intramolecular β -sheet content can be determined by subtracting the content of intermolecular 3D β -crystallites (measured using XRD) from the total β -conformation content (measured by FTIR or Raman)^{64, 96}.

2.3.2 Preparation of Silk-based Materials

a. Preparation of SF solution

The preparation process of SF solution involves a meticulous and multi-step process to ensure high purity and functionality^{65, 97, 98}, as depicted in Fig.2. 6a. Firstly, silk cocoons are cut into small fragments and subjected to a degumming process using a 5 g/L sodium carbonate (Na_2CO_3) solution, which effectively removes SS. After degumming, the SF fibers are thoroughly rinsed and dried to eliminate residual chemicals and moisture. Secondly, the dried SF fibers are dissolved in a 9.3 M lithium bromide (LiBr) solution at 60 °C for 6 h. The resulting solution is then subjected to dialysis for three days against deionized water to remove excess LiBr and other small molecular weight impurities. It is important to note that the dialysis cassette should have sufficient margin to prevent rupture due to water absorption, and the DI water must be replaced five times during the dialysis process. Thirdly, following dialysis, the SF solution undergoes centrifugation to remove any remaining insoluble particles and aggregates, yielding a highly purified SF solution. Finally, the purified SF solution is stored at 4°C to maintain stability and prevent gelation.

b. Preparation of silk film and composite

After preparing the silk solution, a pure silk membrane is formed via template by

adjusting the concentration of the silk solution^{30, 99-101}. Generally, a 4 % silk solution makes it hard to produce a flexible and stretchable film that can be applied to various conditions. Therefore, a concentration exceeding 4% should be employed to fabricate pure silk films. In addition, to enhance the functionalities of silk materials under certain circumstances and leverage their desired processing properties, the SF solution can be blended with other materials to form composite solutions, which are then processed into solid SF materials¹⁰²⁻¹⁰⁴, as shown in Fig.2. 6b.

c. Preparation of electrospinning silk fibers

Electrospinning is a method used to prepare fibers in a strong electric field and is commonly employed to process SF solution into uniformly distributed silk fibers^{24, 105}. The preparation process generally involves four steps. Firstly, to improve the viscosity and spinnability of the SF solution, a suitable quantity of a high-viscosity organic solvent is introduced and gently stirred to create a uniform blended solution. Secondly, the composite solution is carefully drawn and then sprayed onto a collector to form a composite fiber using a syringe with a needle. The flow rate of the composite solution, the voltage applied, and the distance between the needle tip and the collector are critical parameters that greatly influence the diameter and morphology of the electrospun silk-based fibers¹⁰⁶. Thirdly, the resulting silk-based composite fiber undergoes post-treatment processes such as water vapor annealing or alcohol (methanol or ethanol) annealing. These annealing techniques are commonly used to induce β -sheet crystallization in SF¹⁰⁷. Finally, the post-treated silk-based composite fiber is immersed in deionized water and agitated overnight using a reciprocating shaker to remove the extra organic solvents.

d. Preparation of 3D-printed silk materials

In recent years, Printing techniques such as inkjet printing, contact printing, screen printing, stenciling, nanoimprinting, and 3D printing have been developed to create silk materials with diverse structures, thereby expanding the potential applications of silk in flexible electronics. The 3D printing process can be described as follows: A printer

designed for printing silk solution consists of a syringe pump, a standing moving rail, and a substrate (Fig.2. 6d), primarily constructed from 0.25-inch acrylic plates machined by a laser cutter. The printer's x, y, and z movements are controlled by stepper motors, ball screws, and a CNC board, all managed via Mach3 software and G-code generated by a Matlab script. The system has a theoretical motion resolution of 20 μm , with actual printing resolution dependent on the viscosity of the silk solution and the hydrophobicity of the substrate. In printing a silk strain gauge, the resolution is constrained by the syringe tip's inner diameter (0.64 mm), the shear force required, and silk clogging issues. Using the current setup, line spacing can be as narrow as 500 μm , achieving X-Y resolutions up to 1 mm¹⁰⁸.

e. Preparation of silk hydrogels

The gelation process is driven by intermolecular and intramolecular interactions, such as hydrogen bonding and hydrophobic interactions, among the macromolecular protein chains in SF. These interactions lead to the physical cross-linking of the protein chains. Consequently, SF solution exhibits gelation even under normal conditions; however, due to the lengthy process and low quality, it is not typically used for preparing SF hydrogels. When external factors such as ultrasound, electric fields, ultraviolet (UV) irradiation, rotating water flow, and acids are applied to the SF solution, they promote interactions among the protein chains, leading to rapid physical cross-linking, resulting in the formation of SF hydrogels. Here, a detailed process is provided to fabricate the silk hydrogel as exhibited in Fig.2. 6e. After obtaining the SF solution mentioned in 2.3.2a, 6 ml of GMA were gradually added and stirred at 60 °C and 300 rpm for 4 h. The solution was dialyzed for 4 days using a dialysis bag with a 12-14 kDa cut-off, with the deionized water being replaced daily. Finally, the SilMA solution was freeze-dried and stored at -20 °C until use. The silk-based hydrogel will be formed through photo-crosslinking.

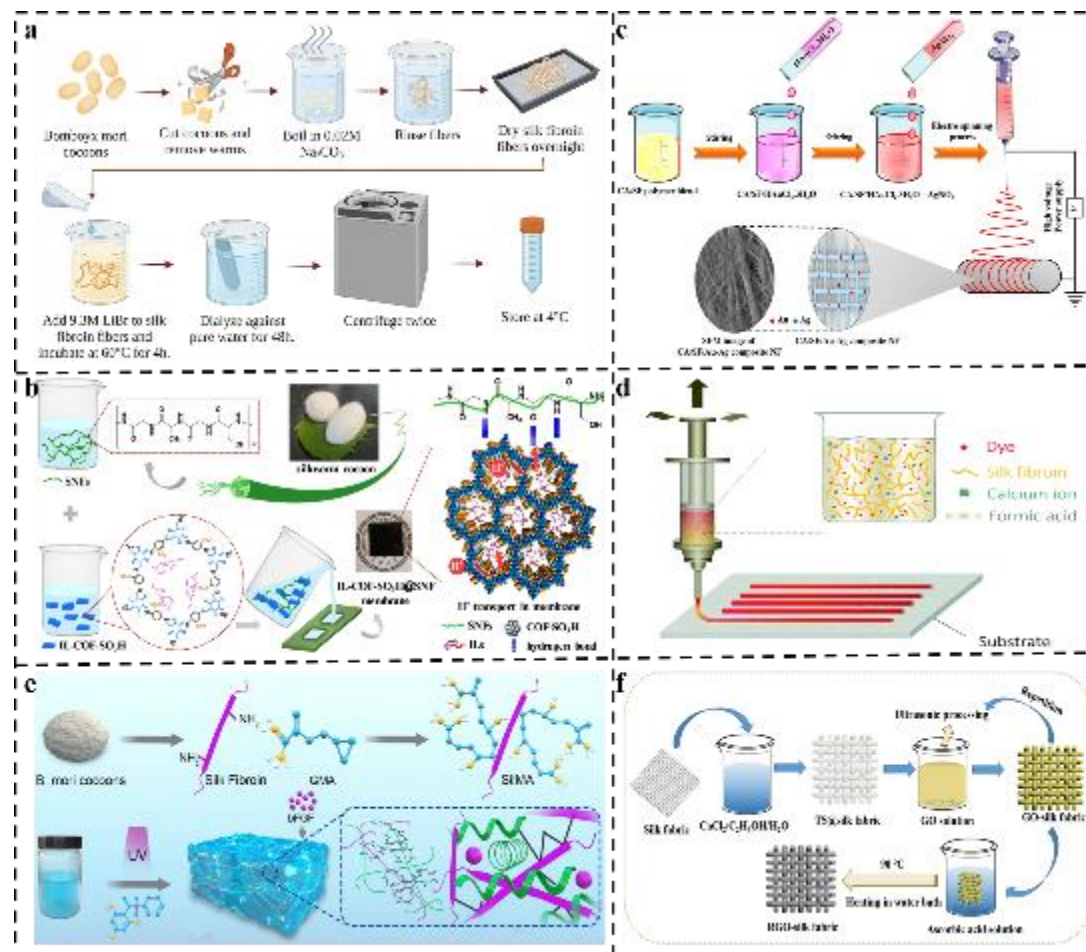


Fig.2. 6 Examples of different methods to prepare silk-based materials: a. Flowchart illustrating the production process of regenerated SF solution derived from natural *B. mori* cocoons¹⁰⁹; b. Illustration of silk composite membranes¹¹⁰; c. Illustration of preparation of silk-based composites by using 3D electrospinning technology¹¹¹; d. Process schematic of producing silk-based materials by 3D printing method¹⁰⁸; e. Process diagram of making silk-based hydrogels¹¹²; f. process illustration of fabricating modified silk fabric-based materials¹¹³.

f. Preparation of modified silk fabric-based materials

Silk fabric is subjected to ultrasonic treatment to remove impurities, after which chemical agents are typically employed to modify it or utilized in coating processes to impart multifunctionality to fibers or textiles. As depicted in Fig.2. 6f, GO is used to

immerse the silk-based textiles for physical modification, enhancing conductivity for various applications.

2.3.3 Membrane-based TENGs

a. Silk film as a tribolayer

In certain instances, researchers seek to alter the properties of the negative triboelectric layer through modifications, opting for a straightforward positive triboelectric layer. Under these conditions, a pure silk membrane emerges as a promising candidate for the positive triboelectric layer owing to its superior electron-losing capability. In this context, four noteworthy studies are presented that offer comprehensive illustrations of pure silk membrane-based TENGs.

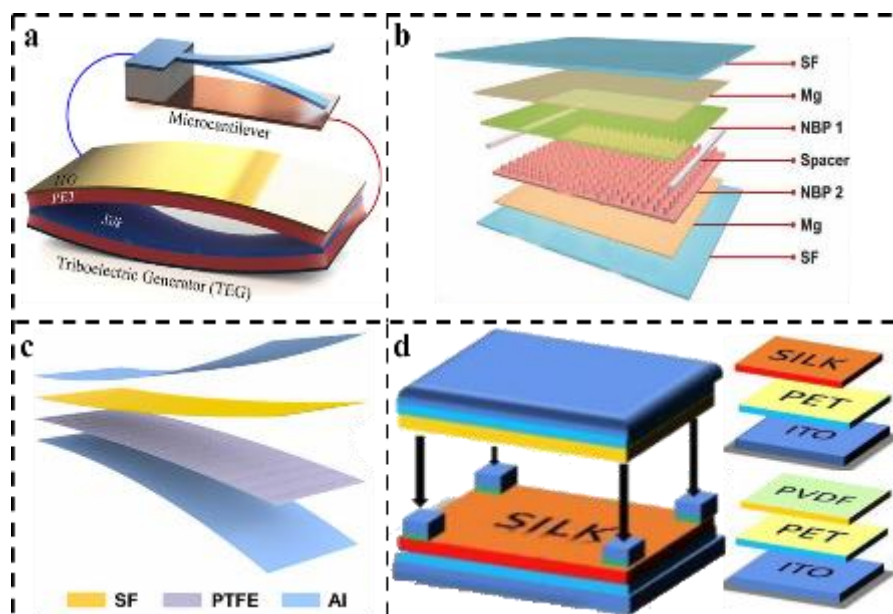


Fig.2. 7 Typical structural illustration of pure silk membrane-based TENGs: a. The first silk-film-based TENG⁹⁹; b. Structure diagram of a typical BN-TENG device³⁰; c. Schematic diagram of SF/PTFE TENG¹⁰⁰; d. Schematic demonstration of the silk/PVDF TENG¹⁰¹.

The development and optimization of SF membrane-based TENGs have seen

significant advances since their inception. As demonstrated in Fig. 2.8a, Zhang et al.³³ pioneered utilizing SF as a triboelectric layer with a polyethylene terephthalate (PET) tribo-pair to design SF membrane-based TENGs in 2016. These SF-TENGs exhibited stable output power with a maximum voltage of 40 V and were modified via an oxygen plasma process to improve the interfacial energy, achieving a substantial increase in performance with a maximum voltage of 268 V, current of 5.78 μA , and power density of 1.93 W/m^2 . In contrast, a year later, Jiang et al.³⁰ proposed a TENG based entirely on natural fiber materials to provide a basic material selection principle, as presented in Fig.2. 7b. By adjusting a single material and their pairwise combinations, including SF, cellulose, chitin, egg white, and rice paper, the maximum voltage, current, and power density reach up to 55 V, 0.6 μA , and 0.0216 W/m^2 , respectively. In this research, SF was employed both as an encapsulation material and as one of the functional dielectric components for sensing applications, while biodegradable Mg functioned as the electrode. Moreover, Li and his cooperators¹⁰⁰ developed a simple and cost-effective polishing technique to fabricate the microstructured SF and PTFE tribolayers using sandpapers with different meshes (Fig.2. 7c). Through this facile method, the maximum voltage and short-circuit current of the silk-based TENGs can reach 238 V and 12.6 μA , and the peak power density denotes 0.2635 W/m^2 . Additionally, Sarkar et al.¹⁰¹ proposed a TENG device to convert the mechanical energy from the rolling of vehicles into electric pulses with PVDF and single silk film based on the satisfying position of the PVDF-silk triboelectric pair in the triboelectric series¹¹⁴, as illustrated in Fig.2. 7d. Collectively, these studies highlight the versatile tribopairs and evolving strategies in optimizing SF-based TENGs for enhanced energy harvesting capabilities.

b. Compositing silk membrane as a tribolayer

Single silk film has disadvantages due to its brittleness, difficulty in forming film (depending on the concentration of silk solution), and uncontrollable versatile functionalities, thereby researchers usually tried to add fillers to adjust the properties of silk film, rendering it functional. Fig.2. 8 represents ten published works, which are selected to give explanations about compositing SF membrane-based TENGs.

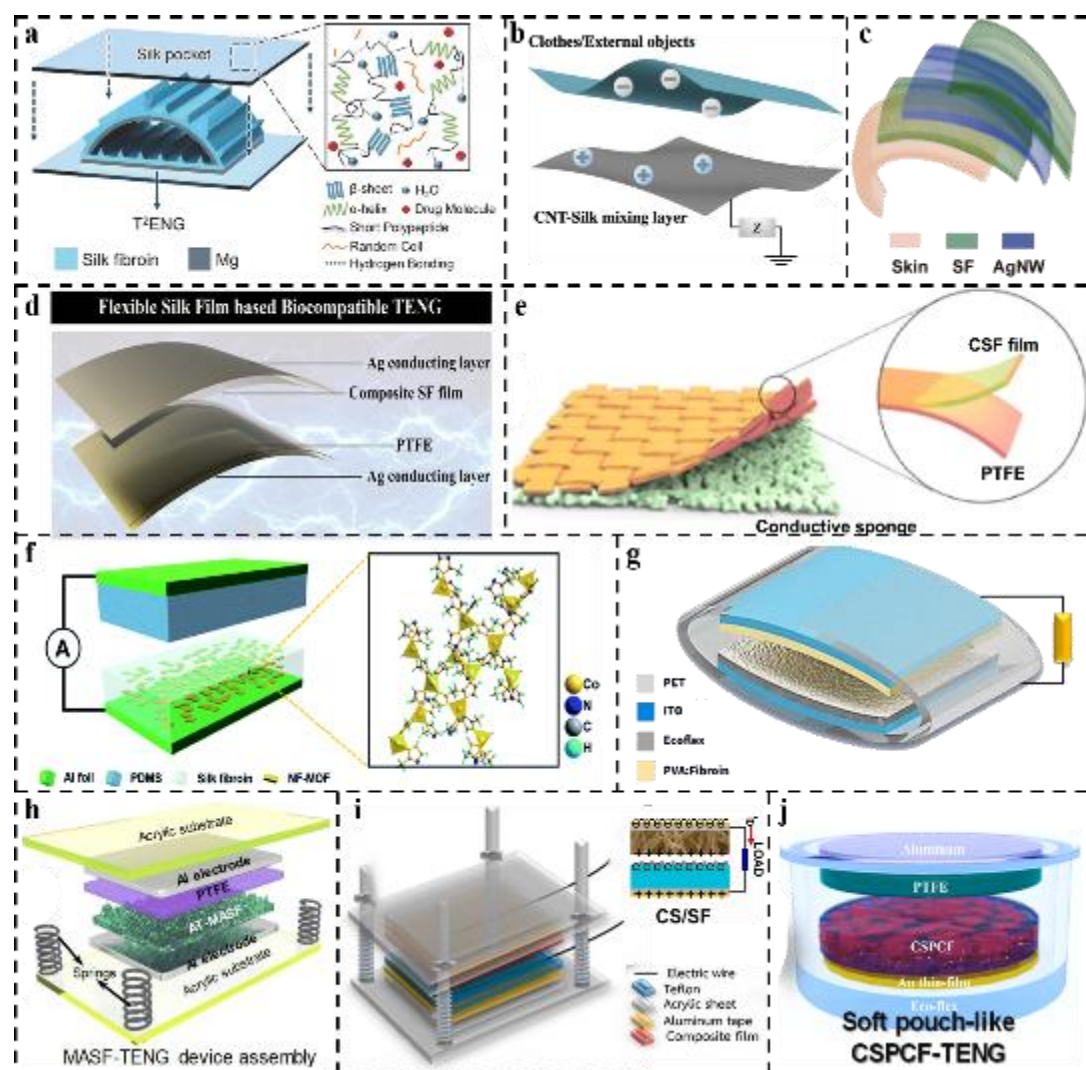


Fig.2. 8 Typical modified composite silk-membrane-based TENGs: a. Schematic of T²ENGs showing the device structure and material system¹¹⁵; b. The schematic view of the CNT-silk mixing layer based TENG¹⁰²; c. Structure of silk ring (modified silk and AgNWs) SETENG¹⁰³; d. Structure illustration of SF/Ag/PTFE-TENG³²; e. Schematic diagram of carboxymethyl chitosan and silk (CSF)-TENG¹⁰⁴; f. Schematic diagram of NF-MOF TENG based on the composite film³⁵; g. The schematic diagram of the PVA/SF/Ecoflex TENG device¹¹⁶; h. Device illustration of the proposed alcohol-treated microarchitected SF (AT-MASF)/PTFE-TENG device¹¹⁷; i. Schematic diagram of SF-based composite/Teflon TENG¹¹⁸; j. Schematic photographic images depict the completely packed soft pouch-like CSPCF/PTFE-TENG¹¹⁹.

In recent advancements, a transient T²ENG for self-powered epilepsy treatment was proposed by Zhang et al.¹¹⁵ (Fig.2. 8a). This innovative device employed fully biodegradable silk as encapsulation layers and Mg as the electrode. The SF was modified using micro gratings to control surface morphologies, allowing for optical observation of the entire device through special diffractive patterns with noninvasive laser illumination. Consequently, the T²ENG exhibited enhanced electrical performance, achieving a maximum voltage output of approximately 60 V and a current output of about 1.0 μ A. Although some researchers have fabricated TENG devices using complex configurations and advanced techniques, simpler structures have demonstrated unexpectedly effective results. For instance, Su et al.¹⁰² introduced a straightforward TENG incorporating a mixed silk and carbon nanotube (CNT) membrane in a single-electrode working mode, as shown in Fig.2. 8b. This design attained voltage, current, and power density values of 262 V, 8.73 μ A, and 2.86 W/m², respectively. Furthermore, Liu and his team¹⁰³ developed a next-generation keyboard utilizing ultra-thin SF film rings, highlighted for their excellent biocompatibility, air permeability, and conformability, making them suitable for long-term finger wear (Fig.2. 8c). These silk rings enable keyboard communication through a printed circuit board (PCB) and a Wi-Fi module, indicating promising applications in future human-computer interactions, the Internet of Things, and virtual reality scenarios.

To enhance the mechanical properties of the SF membrane and better apply it to the wearable field, Xu et al.³² proposed a regenerated SF solution with PU embedded as one tribo-layer and PTFE with silver as the other tribo-layer (see Fig.2. 8d). The designed SF-TENGs show significant improvements in mechanical flexibility (approximately 250% stretchability and 1000 bending cycles) and chemical stability. Similarly, a TENG device proposed by Shen et al.¹⁰⁴ used a biodegradable and conductive carboxymethyl chitosan-silk fibroin (CSF) film as the tribopositive layer and PTFE as the negative tribolayer (Fig.2. 8e). The addition of carboxymethyl chitosan enabled the CSF film to form numerous lacunae within the network and enlarged pore size. Based on this principle, Chen et al.³⁵ synthesized 2D metal-organic frameworks nanoflakes (NF-MOF) and embedded them in SF to fabricate composite film for TENG,

as demonstrated in Fig.2. 8f. In-plane aligning MOF nanoflakes obtained a maximum instantaneous power density of 2.63 W/m^2 in the SF matrix. Following that, a compatible SF/PVA/Ecoflex TENG was constructed by incorporating PVA into SF to fabricate a PVA/SF composite membrane (Fig.2. 8g), as indicated by Candido and his coauthors¹¹⁶. This TENG device is transparent and flexible with output performance of voltage, current, and power density of 172 V, 8.5 μA , and 1.304 W/m^2 , respectively.

Dudem et al.³⁸ fabricated SF-based TENGs with a very high output power density of 22 W/m^2 (Fig.2. 8h). In this study, RSF solution was coated on a micro-grooved PDMS mold and then was dried to form a composite film. Subsequently, the prepared RSFF underwent a spray coating with alcohol, followed by an annealing process. In this SF-based TENG, RSFF and PTFE served as the positive and negative friction layers, respectively. The construction of micro-nano patterns and the polarity differences between these friction layers significantly contributed to the enhanced output performance. Based on chitosan (CS), by incorporating protein-based compounds as fillers, Charoonsuk et al.¹¹⁸ proposed highly efficient biopolymer TENGs (Fig.2. 8i). Specifically, they incorporated eggshell membrane (ESM) and SF as natural fillers into the CS matrix to develop a CS/protein-based composite TENG. Among various additives tested, the inclusion of SF yielded the highest output voltage and current. The fabricated CS/protein composite TENG achieved approximately 77 V in open-circuit voltage and 13 μA in short-circuit current with a 10% SF additive. Notably, its maximum output power density reached approximately 0.224 W/m^2 , which is six times higher than that of the pristine CS TENG. Further investigation into the amino acid content revealed that high levels of glycine, alanine, and serine enhance the output signal by providing additional charges through molecular polarizations. This finding could stimulate significant interest in using biodegradable materials for TENG applications.

Humidity and temperature are two key factors in deciding TENG's electrical outputs. Therefore, it is significant to maximize the surface charge density across triboelectric layers while protecting it from humidity. To reduce the effect of humidity on TENGs,

Dudem et al.¹¹⁹, for the first time, proposed the utility of crystalline silk microparticles (SMPs) embedding into PVA (Fig.2. 8j) to improve the surface charge density and realize its applicability for TENG devices as well as fully packaged silicone rubber device to protect it from humidity. As a result, the designed SMPs/PVA TENG exhibits maximum output voltage, current, and charge of ~280 V, 17.3 μ A, and 32.5 nC, respectively, creating a highly competitive energy harvester that can conform to the rigorous needs of wearables and mobile applications. More importantly, from an environmentally friendly point of view, they utilized waste materials by incorporating these composites with counter-materials made from discarded PTFE plastic cups and demonstrated the potential for recycling and sustainable reuse.

2.3.4 Electrospinning-based TENGs

Electrospinning as an electrostatic fiber manufacturing process has attracted more interest and attention in recent years due to its versatility and potential for applications in various fields, especially for designing TENGs owing to its high surface-to-volume ratio, specific surface area, tunable porosity with uniform pores distribution, and the ability of desired chemical functionalization for various applications¹⁰⁷.

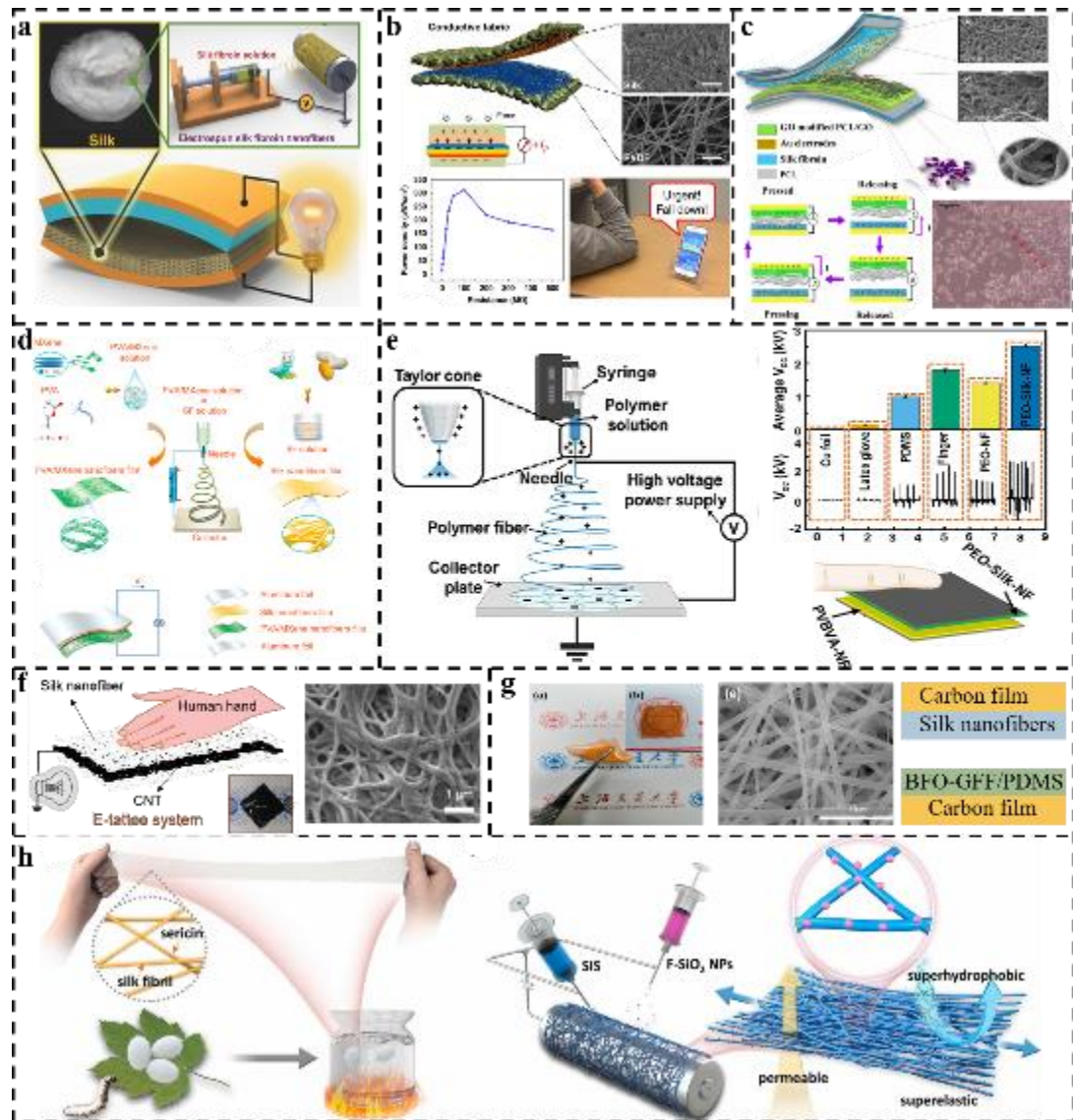


Fig.2. 9 Typical electrospinning method-based TENGs: a. A regenerated silk nanofiber-based TENG²⁴; b. Schematic diagram of all-fiber hybrid TENG, which consists of two electrodes (conductive fabric) and electrospun silk nanofibers (top) and PVDF nanofibers (bottom) serving as a triboelectric pair²⁷; c. Illustration of a kind of flexible TENG based on an SF fibrous layer and a polycaprolactone (PCL)/GO fibrous layer¹²⁰; d. Schematic illustration of the fabrication of PVA/MXene and silk nanofibers film-based TENG²⁸; e. A high-power and protein-based TENG consisting of electrospun PEO-Silk nanofibers (PEO-Silk-NFs) and poly(vinyl butyral-co-vinyl alcohol-co-vinyl acetate) nanofibers (PVBVA-NFs)¹⁰⁵; f. Schematic of skin-actuated SNF/CNT/SNF E-tattoo energy harvester¹²¹; g. A hybrid nanogenerator integrating TENG and PENG

based on electrospun silk fibers¹²²; h. A TENG realized by synchronous electrospinning of styrene-isoprene (SIS) block copolymers and electrospaying of the fluorinated SiO₂ nanoparticles inspired by the sericin-bundled silk¹²³.

In 2016, regenerated SNFs prepared by electrospinning to design an environmentally friendly bio-TENG were first proposed by Kim et al.²⁴, as presented in Fig.2. 9a. In this study, the two triboelectric layers consisted of regenerated nano SF fibers and a polyimide (PI) membrane. The voltage output of the fabricated electrospun silk bio-TENG was nearly 1.5 times greater than that of the cast silk-TENG. This work is significant as it represents one of the earliest demonstrations of the potential to incorporate silk into TENGs. Similarly, a subsequent study by Guo et al.²⁷ proposed one kind of all fiber-based TENGs with PVDF fibers and SF operating in CS mode to connect both TENGs and PENGs in 2018, as illustrated in Fig.2. 9b. Unlike Kim's work, this approach employed entirely electrospun fibers for the two triboelectric layers. This design retains the advantages of traditional fabrics, such as flexibility and good air permeability, making it easily integrated into clothing of any desired size and shape. The large specific surface area of the nanofibers, coupled with the exceptional electron donation capability of SF in triboelectrification, endows the hybrid nanogenerator with outstanding electrical performance, achieving a power density of 3.1 W/m².

Similarly, an eco-friendly bio-TENG was proposed by S Parandeh et al¹²⁰ based on an SF layer and a PCL/GO fibrous layer, as depicted in Fig.2. 9c. Besides, by optimizing the surface morphology of the GO layer, the developed TENG obtains a voltage of 100 V, which is 4 times greater than that of the pristine TENG. This improvement is attributed to the enhanced contact area and the presence of nanopores that serve as electron-trapping sites. Furthermore, the bio-TENG can be applied for electrical stimulation of PC12 cells and the results prove to promote the attachment and proliferation of PC12 cells. Another eco-friendly material, Mxenes, comprises a class of two-dimensional inorganic compounds. These materials consist of atomically thin layers of transition metal carbides, nitrides, or carbonitrides, making them highly suitable for smart electronics owing to their metallic electrical conductivity and

abundant functional groups^{120, 124-126}. A study by Jiang et al.²⁸, shown in Fig.2. 9d, illustrated a fully electrospun TENG with a highly electronegative and conductive MXene nanosheet integrated with PVA in an electrospun nanofiber film. The fully electrospun TENG supports an instantaneous maximum peak power density of 1.087 mW/m² with a load resistance of 5.0 MΩ.

Apart from applying electrospinning silk to act as a single tribolayer, researchers attempt to fabricate silk composite as a tribopositive layer. For example, Joshi et al.¹⁰⁵ introduce a novel strategy to develop a high-output and protein-based TENG consisting of electrospun PEO-Silk nanofibers (PEO-Silk-NFs) and poly (vinyl butyral-co-vinyl alcohol-co-vinyl acetate) nanofibers (PVBVA-NFs), This configuration achieves a remarkable voltage of 2.1 kV, attributed to the large surface areas and electrical affinity differences between the two types of nanofibers (Fig.2. 9e). Similarly, Gogurla et al.¹²¹ present an innovative E-tattoo composed of carbon nanotubes and silk nanofibers, designed to be substrate-free, skin-compatible, and capable of generating triboelectric signals upon contact with skin (Fig.2. 9f). In addition, many researchers have sought to integrate PENG with TENG to obtain hybrid NGs. For instance, Liu and his co-researchers¹²² introduce such a hybrid NG using electrospinning silk fiber covering carbon film as the tribopositive layer and interconnected inorganic ferroelectric material BFO-GFF/PDMS as the tribonegative layer, as shown in Fig.2. 9g. The silk nanofiber exhibits reticular morphologies, rendering an enhanced connected area with the BFO-GFF/PDMS to facilitate the charge separation after friction. By optimizing the experimental conditions, the hybrid NG device can realize a voltage of 110 V, a current of 3.67 μA/cm², and a power density of 1.51 W/m².

Silk is composed of robust SF and soft SS that is endowed with providential binder ability. Inspired by such an interlocked structure between SF and SS, Li and co-workers¹²³ proposed a microfiber membrane by synchronous electrospinning of styrene-isoprene (SIS) block copolymers and electrospaying of the fluorinated SiO₂ nanoparticles to grant the composited membrane with omnidirectional superelasticity, permeability, and superhydrophobicity (Fig.2. 9h). The bionic SIS membrane shows

extraordinary stretchability with ultimate elongation of over 3600%, superelasticity (recovery from 2000% strain), and permeability (over 90% of cotton). The innovative design of the co-solvent method revealed success in gaining superior electrical conductivity and endurance than that of the traditional sputtered gold electrode.

2.3.5 Spraying-based TENGs

The spraying technique has emerged as a transformative method in the fabrication of TENGs, offering unique advantages in terms of material distribution and device scalability. By employing a spraying process, SF solutions can be uniformly deposited onto substrates, facilitating the formation of highly efficient and uniform triboelectric layers^{38, 39}. This method not only enhances the mechanical robustness and adaptability of the TENGs but also allows for precise control over the thickness and surface morphology of the active layers. The versatility of spraying techniques enables the integration of TENGs into various form factors, paving the way for innovative applications in wearable electronics and other flexible energy-harvesting devices. This introduction explores the role of the spraying method in advancing the performance of silk-based TENGs and its potential to drive future innovations in sustainable energy technologies.

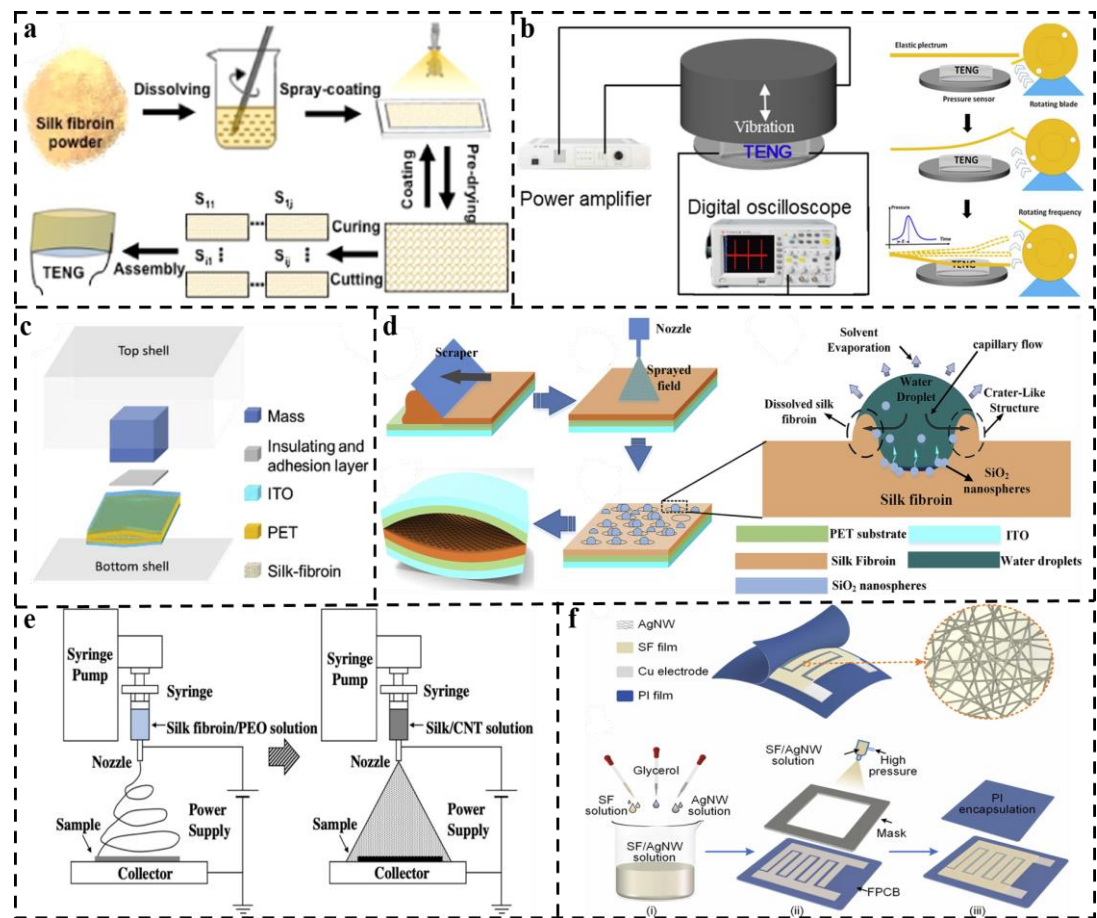


Fig.2. 10 Typical illustrations of spraying coating-based silk materials: a. Fabrication steps for the SF/PET/ITO TENG³⁸; b. The TENG energy harvesting system modulating the mechanical vibration to collect ultralow frequency mechanical energy less than 1 Hz using SF/PET/ITO TENG³⁹; c. Components of the designed self-powered acceleration sensor based on the SF/PET/ITO TENG⁴⁰; d. An electro-spray-etching (ESE) process for fabricating ITO/PET/SF/SiO₂ TENG³⁴; e. Hybrid electrospinning and electro-spray method for fabricating silk-based TENG²⁹; f. A hybrid triboelectric-piezoelectric-electromagnetic generator with PI and SF serving as the tribo-pairs¹²⁷.

Liu and his coauthors³⁸ developed a TENG using the spraying coating method, employing SF and PET TENG to create an SF/PET/ITO TENG noted for its exceptional transparency and hydrophobicity, as shown in Fig.2. 10a. The as-fabricated SF-based TENG device can obtain a voltage of 213.9 V and power density of 0.068 W/m² because of the excellent ability to lose electrons and rough surface rendered by the SF. Later,

this research group³⁹ integrated this fabricated TENG with a theoretical model to collect ultralow frequency mechanical energy less than 1 Hz by controlling vibration waveforms and contact-release time, as illustrated in Fig.2. 10b. The results confirm that reducing the contact-release time significantly enhances the collection efficiency of TENGs, promoting the design of TENGs capable of harvesting various forms of mechanical energy across a wide frequency range. In addition, this research group⁴⁰ reported a novel V-Q-a theoretical model based on the proposed TENG in Fig.2. 10a. As shown in Fig.2. 10c, this TENG device can be used as a self-powered accelerometer, and by adjusting the speed of the accelerometer, a high-power density of 0.372 W/m² is achieved.

Electrospray-etching is a specialized technique used in material processing to create fine patterns and structures on a surface at the micro and nanoscale. Recently, researchers have begun integrating this technology into TENG fabrication. For instance, Luo et al.³⁴ proposed an ITO/PET/SF/SiO₂ TENG using the water electrospray-etching (ESE) process to produce micro/nanostructured SF film as the positive tribolayer (Fig.2. 10d). The etched crater-like structures result in quasi-periodic and porous features with enhanced surface roughness. This leads to a significant performance improvement, with the maximum voltage of the porous-based TENG increasing by 180% compared to a planar device, achieving a power density of 1.615 W/m².

In 2020, Su et al²⁹ used a hybrid strategy of electrospinning and electrospray to produce a three-layer membrane. The bottom layer is the silk fiber membrane fabricated by electrospinning that comes into contact with human skin, the top layer is the CNT-silk blended film fabricated by electrospray on the top surface, and the middle interlacing layer in which the top part of the sprayed blended layer was wrapped around the electrospun fibers on the surface of the silk layer (see Fig.2. 10e). This study also overcame the technical bottleneck of spraying a highly conductive blending solution onto a non-conductive silk fiber substrate while ensuring stability and uniformity. The power generation capacity of the designed silk-based TENG is 1.41 W/m² when shaken and 3.17 W/m² when tapped by hand. Later, a hybrid triboelectric-piezoelectric-

electromagnetic hybrid generator was proposed by Wen and his collaborators¹²⁷ with PI and SF being the tribo-pairs (see Fig.2. 10f). The maximum power density is 189.6 W/m³, which represents an improvement over previously reported triboelectric-piezoelectric-electromagnetic hybrid devices and other thermoelectric-based devices operating at the same frequency.

2.3.6 3D Printing-based TENGs

3D printing involves constructing a three-dimensional object from a CAD or digital 3D model. This process can occur through various methods where the material is applied, assembled, or solidified under computer control, typically by adding material, such as plastics, liquids, or powder grains that are fused, layer by layer¹²⁸. In recent years, 3D-printing technology has been utilized to fabricate TENGs^{129, 130}. Here, three silk-based 3D TENGs are introduced to enhance the understanding of how 3D printing technology can be applied in TENG fabrication.

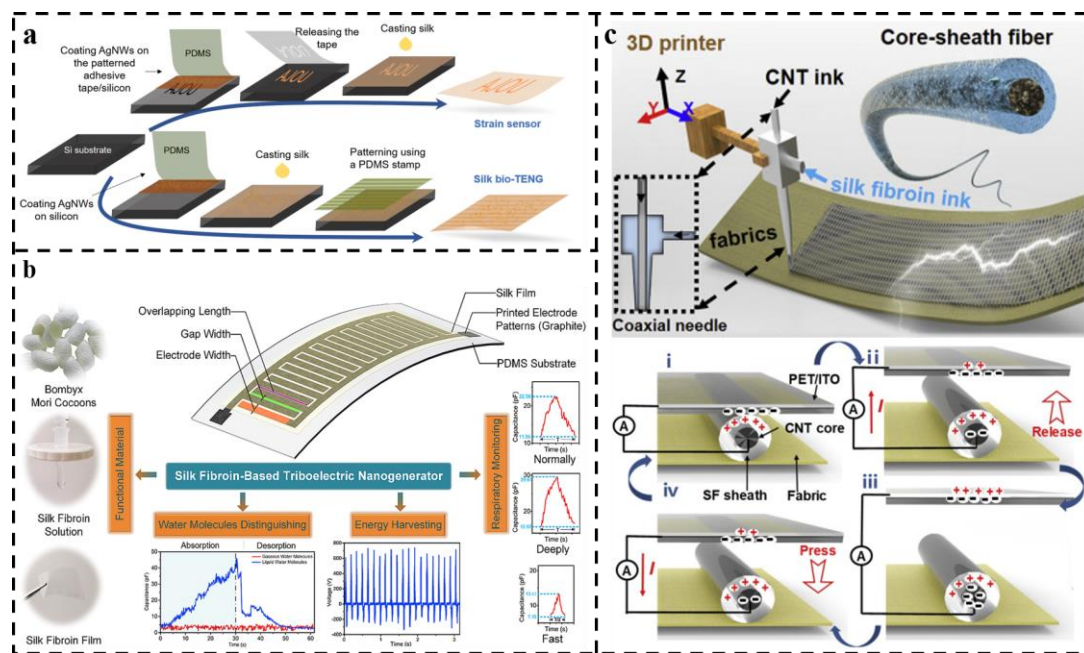


Fig.2. 11 Typical 3D printing method-based TENGs: a. Schematic showing the fabrication process of the silk protein-based strain sensor and the TENG³⁶; b. Illustration of the proposed wearable PS-TENG and its electric performance³⁷; c.

Schematic illustration showing the 3D printing process using a coaxial spinneret¹³¹

As shown in Fig. 2. 11a, Gogurla et al.³⁶ developed a nanostructured silk protein and embedded AgNWs within the silk nanostructure to create an efficient, flexible, transparent, and skin- or textile-compatible TENG and strain sensor for biomechanical energy harvesting and motion sensing. The devised bio-TENG, when positioned on the skin for gesture monitoring, showcases exceptional qualities of optical transparency and flexibility. Paired with the environmentally sustainable attributes of a biodegradable and biocompatible silk protein, the bio-TENG embodies a fully eco-friendly solution. This innovative device is capable of generating an open-circuit voltage reaching up to 90 V (with a maximum potential of ~110 V), delivering a short-circuit current of 0.06 μA (peaking at around 0.1 μA), and achieving a noteworthy maximum power density of 0.002 W/m^2 . Remarkably, it can concurrently power five commercially available light-emitting diodes (LEDs) with seamless functionality, even under a single-electrode configuration.

To improve the output performance of silk-based 3D TENGs, Wen et al.³⁷ used industrial techniques like screen printing to create micro-scale graphite patterns on a flexible polymer base, forming interdigitated electrodes. They covered the surface with an SF layer to create the PS-TENG (see Fig. 2. 11b). The 3DP-TENG enhanced performance by introducing conductive elements like graphite, achieving voltage, current, and power density levels of 666 V, 174.6 μA , and 4.12 W/m^2 , surpassing reference values of most silk-based TENG devices in recent years, as illustrated in Table 2. 1.

It is essential to carefully adjust and optimize several material parameters to achieve stable composite patterns with uniform or gradient structures, including rheology and density, nozzle diameter and the gap between the nozzle and the build platform, extrusion rate, and printing speed¹³². Additionally, squeeze-based printing is influenced by the design of the print head. Specifically, coaxial nozzles can be used to fabricate core-shell structures, directly serving as single-electrode TENGs. Typically, conductive materials are utilized as the core electrodes, while dielectric materials serve as the

external protective and friction layers. Zhang et al.¹³¹ developed core-shell fibers, employing carbon nanotubes as the conductive core and SF as the dielectric sheath for smart textile applications, as depicted in Fig.2. 11c.

Table 2. 1 Comparison of electrical outputs of silk-based TENGs in recent years

Electrode	Triboelectric materials	Pressure (N)	frequency (Hz)	Area(cm ²)	Voltage (V)	Current(μ A)	Power density (μ W/cm ²)	Ref
CS D	Bio-silk/polyimide film/Al	16.8	3	28	15	2.5	0.43	24
CS D	e-silk/BiFeO ₃ -glass fiber fabric-PDMS	-	1	2 × 3	110	22.02	151.42	122
CS D	PET-SF (Spray-coating)	6	5	4 × 6	213.9	-	6.8	38
CS S	AgNW/e-silk	6	5	2 × 1.8	90	0.06	0.2	36
CS S	SF/PDMS+ graphite	Hand pressure	7	6 × 3	666	174.6	412	37
CS D	regenerative SF film/silk nanoribbons+Mg	50	5	2 × 1	41.64	0.5	8.67	133
CS D	PTFE/alcohol-treated SF	3	5	2 × 2	395	35.6	2205	117
CS D	Silk aerogels/PTFE	-	5	2 × 1	52.8	5.2	37	134
CS S	Silk hydrogel/PDMS	15.9 kPa	1	2 × 2	12	0.2	-	42
CS D	SF+Ag/PTFE+ Ag	20	1	2 × 2	50	1.5	-	32
CS D	Chitosan/albumin, egg-shell membrane (ESM) and silk fiber	250	1.5	3 × 3	77	13	22.4	118
CS D	Silk/PET	-	5	2 × 4	268	5.78	193.6	33
CS D	PTFE/PVA+silk particles+AU	5	5	2 × 2	280	17.3	1440	119
CS D	PVA/MXene+Electrospinning silk	10	10	3.14	118.4	-	108.76	28
CS D	PET/SF(electrospray-etching)+SiO ₂	18	1	2 × 2	260	6.2	161.5	34
CS D	MOFs+SF/PDMS	10	2	2 × 2.5	107.5	10	263	35
CS D	SF+CNT/PET	14	7	2 × 4	200	8	140.99	29
CS D	SF+PVDF	25.7	2	2 × 4	500	12	310	27

CS D	SF+Mg/bioresorbable polymers	/	1	1 × 2	55	0.6	2.16	30
CS S	PDMS/Ag NFs+SFF	/	1	1 × 1	13	0.4 μA	80	1

2.3.7 Gel-based TENGs

Hydrogels are a hot topic for designing smart electronics due to many ionics for reaction and recombination, making them a possible candidate for stretchable, transparent, and highly conductive electrodes. However, hydrogels have two major drawbacks: low water retention ability and a narrow application temperature range for applications¹³⁵. For example, ionic hydrogels easily dehydrate and rapidly lose their stability when kept in a dry (30 °C) environment with a relative humidity (RH) of 26%. To solve the problem, ionogels are one of the possible candidates to improve the current issues owing to their good mechanical properties, transparency, and wide operating temperature range¹³⁶. Here, six studies on silk gel-based TENGs are exhibited.

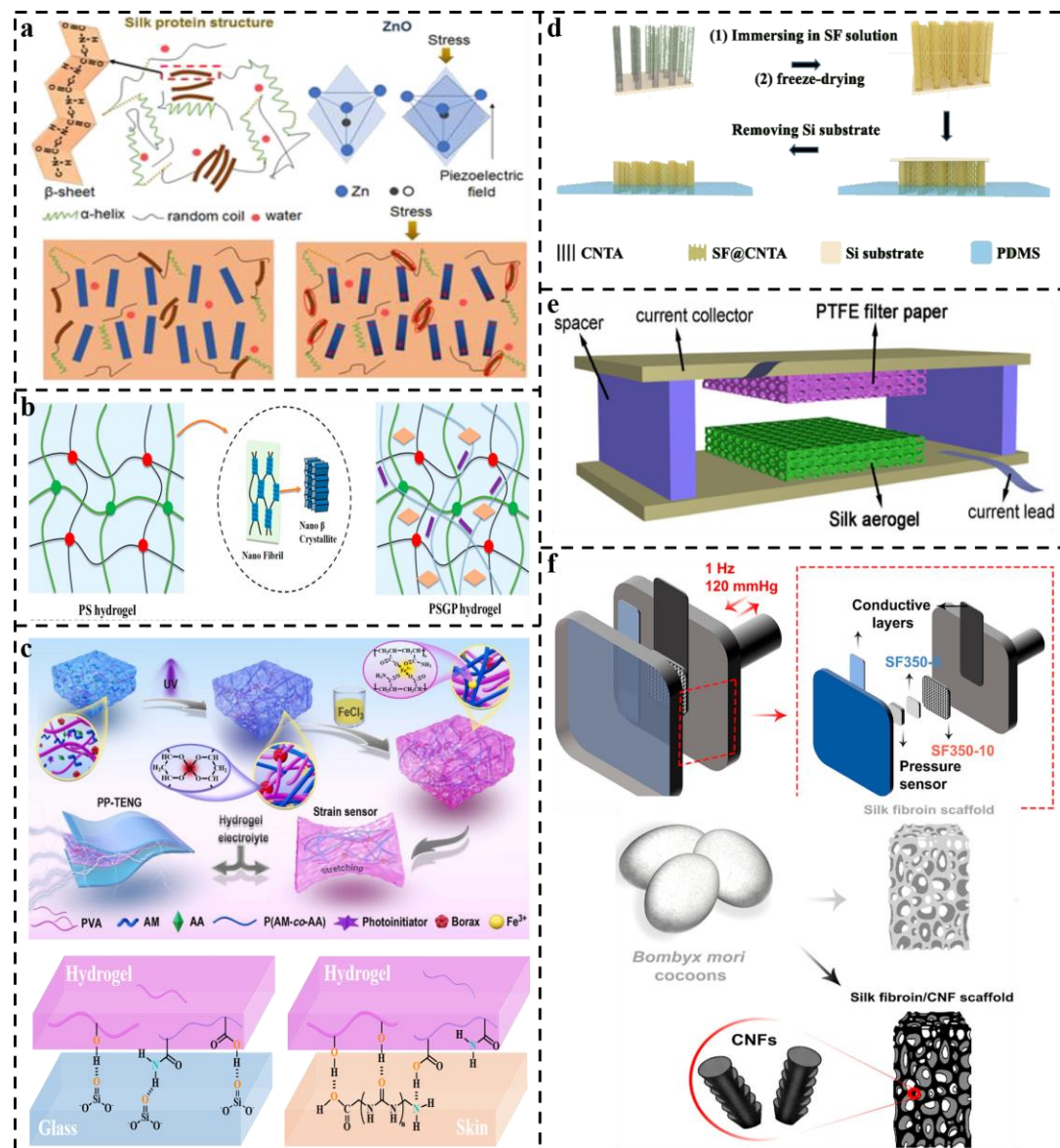


Fig.2. 12 Typical gel-based TENGs: a. Schematic illustration to show the mechanism of artificial EG-skin using silk hydrogel¹³⁷; b. Fabrication and characterization of the PAM/SF/GO/PEDOT: PSS (PSGP) hydrogel-based TENGs⁴²; c. a double-network silk-based hydrogel with high mechanical properties for energy harvesting and sensing¹³⁸; d. A composite silk-coated carbon nanotube aerogel TENG¹³⁹; e. Schematic illustration of the structure of silk aerogel-based TENG¹³⁴; f. A kind of SF/CNF scaffold TENG¹⁴⁰.

Bioinspired artificial electronic skins (E-skins) are attractive for a wide range of applications while fabricating e-skins endowed softness, deformability, and

biocompatibility remains a challenge. Silk is a promising candidate to meet the requirements of these features. Gogurla et al.¹³⁷ proposed a kind of silk protein hydrogel-based electronic skin that simultaneously meets triboelectric and piezoelectric performance requirements, as seen in Fig.2. 12a. Due to the combined effects of triboelectricity and piezoelectricity, encapsulating the ZnO nanorods in an SF layer may potentially double its electrical response, generating a power density of 10 W/m². Simultaneously, a kind of soft conductive hydrogel rationally designed by He et al. has considerable stretchability and compressibility, which enables it to be assembled into a strain/pressure sensor with a wide sensing range (strain, 2%–600%; pressure, 0.5-119.4 kPa) and reliable stability⁴². SF, polyacrylamide, graphene oxide, and poly(3,4ethylenedioxythiophene) are used in the preparation of the hydrogel TENG (Fig.2. 12b). This composite enables the monitoring functionality, such as tracking a series of physical signals of the human body (e.g., joint movements, facial gestures, pulse, respiration, etc.).

Generally, hydrogels exhibit poor mechanical properties, falling short of the requirements for TENG devices, which need to demonstrate strong durability for long-term use. Dual network (DN) gels with fully chemical or mixed chemical-physical crosslinking lack self-recovery properties due to the presence of irreversible covalent bonds. In contrast, DN gels with fully physical crosslinking exhibit excellent self-recovery and mechanical properties, significantly extending the lifespan of hydrogels in flexible wearable electronics. Under this circumstance, Luo et al.¹³⁸ developed a double-network hydrogel based on a fully physical-crosslinked method, including borax-crosslinked PVA as the first network and Fe³⁺-crosslinked P(AM-co-AA) (P(AM-co-AA)-Fe³⁺) as the second network (Fig.2. 12c). The unique dual network (DN) structure and Fe³⁺ coordination endow the resulting hydrogels with excellent mechanical properties and outstanding ionic conductivity, obtaining a maximum power density of 0.27 W/m².

In addition to silk-based hydrogels being used as triboelectric layers, other forms such as aerogels and scaffolds have also been studied as triboelectric layers. For example,

Xiong et al.¹³⁴ developed a porous SF-coated carbon nanotube array, which boasts a high specific surface area and achieves a power density of 5.8 W/m², as depicted in Fig. 2. 12d. Based on ionogels, Mi et al.¹³⁴ proposed a highly porous silk aerogel-based TENG (STENG) with high output performance using SF extracted from silk cocoons (Fig. 2. 12e). The composite aerogel, comprising 2% SF with a nano-fibrillated porous structure and the highest surface area, significantly enhances the triboelectric output performance of the STENG. The developed STENG achieved an open-circuit voltage of 52.8 V, a short-circuit current of 5.2 μ A, and reached a maximum power density of 0.37 W/m² with a 1 M Ω external resistor. A scaffold is a three-dimensional framework that facilitates the assembly of molecules or molecular complexes. Leveraging this structural framework, Tu and his collaborators¹⁴⁰ engineered SF-based porous scaffolds to replicate the mechanical and physical characteristics of cardiac tissue (Fig. 2. 12f). The incorporation of cellulose nanofibers (CNF) resulted in tightly interlocking SF/CNF composite scaffolds, boosting their elastic modulus and ultimately achieving a maximum power output of 0.37×10^{-6} W/m².

2.3.8 Fibrous-based TENGs

In the past couple of years, SF materials have become increasingly popular in designing TENGs. The fibrous structure of silk provides a high surface area and excellent flexibility, enhancing the efficiency of energy capture and conversion. Additionally, silk fibers are naturally robust and biocompatible, making them well-suited for applications that require direct contact with the skin or integration into wearable devices. This method allows for the creation of lightweight, durable, and environmentally friendly TENGs, highlighting their potential in advancing sustainable energy solutions^{44, 141}. Herein, 12 studies of silk fibrous-based TENGs reported recently were selected.

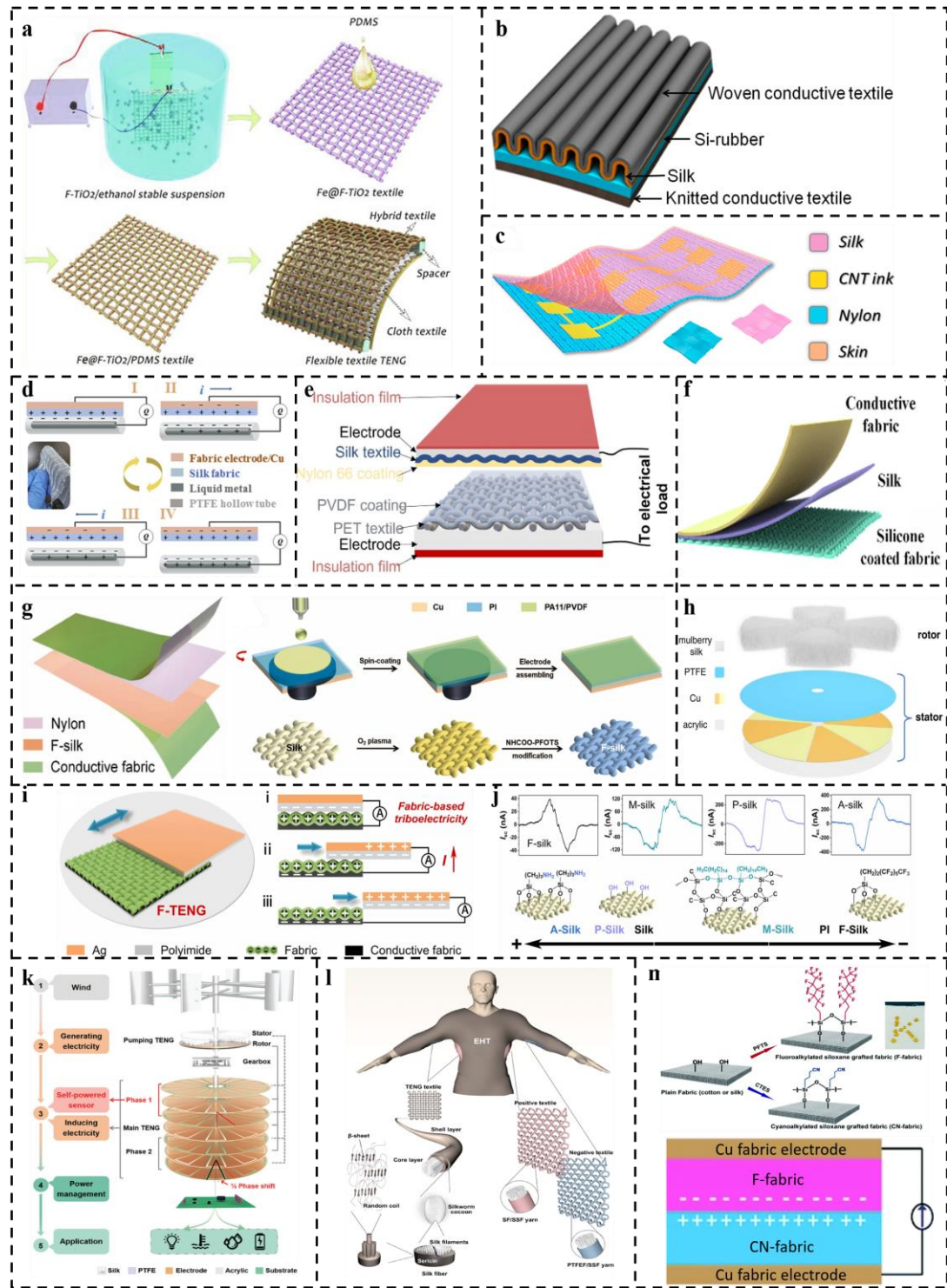


Fig.2. 13 Typical silk Fibrous-based TENGs: a. A Fe@TiO₂/PDMS textile and silk cloths TENG¹⁴²; b. A silk-based corrugated Textile TENG¹⁴³; c. A washable silk-based E-textile TENG¹⁴⁴; d. Mechanism description of the Liquid-metal/polymer core/shell

fibers/silk fabric device under vertical contact-separation mode¹⁴⁵; e. The commercial woven fabrics silk deposited electrospun nanofibers (nylon 66) and PVDF-coated PET woven fabric as tribolayers for fabricating TENG device¹⁴⁶; f. The commercial silk-based combined fabric TENG device structure for sound energy harvesting¹⁴¹; g. A kind of fluorinated silk-based TENG¹⁴⁷; h. The 3D structural schematic of the rotor made by mulberry silk in MS-TENG¹⁴⁸; i and j: A silk-based crown twill structure TENG⁴⁴; k. The energy transport schematic of the EHSS system and the structure design⁴³; l. The SF/SSF yarns and PTFEF/SSF yarns fabricated by co-wrapping spinning apparatus¹⁴⁹; m. A double silk-based TENG by stacking a cyanoalkylated siloxane grafted fabric with a fluor alkylated siloxane grafted fabric¹⁵⁰.

Silk has an excellent electron-donating ability, making it an ideal material for the positive triboelectric layer. Typically, silk fabric is used as a substrate that can be modified to enhance the overall conductivity of the silk-based composite. For instance, Jian et al.¹⁴² enhanced the output performance of silk textile-based tTEFS (triboelectric fiber energy harvesting systems) by depositing flower-like TiO₂ particles onto stainless steel textiles (Fig.2. 13a). This improvement is attributed to the increased surface area and dielectric constant resulting from the flower-like TiO₂ particles. Although this combined method effectively boosts the output performance of tTEFS, the complex structural design and multiple processing steps introduce challenges and elevated costs, thereby limiting its practical application in production. Adjusting the structure of fabric is also a good way to achieve high electrical outputs. As shown in Fig.2. 13b, Choi et al.¹⁴³ proposed a corrugated textile-based TENG that can generate energy by pressing, rubbing, and stretching, effectively leveraging the flexibility and wearability of textiles. Washability is another important advantage of textiles. Utilizing conductive carbon nanotubes (CNTs) and screen-printing technology, Cao et al.¹⁴⁴ fabricated E-textiles with electrode pattern designs that address common concerns such as air permeability, satisfactory washability, and the potential for mass production (Fig.2. 13c). Apart from these merits, a silk textile based TENG proposed by wang et al.¹⁴⁵ show excellent acid and alkali resistance and high friction durability as shown in Fig.2. 13d. In addition, the hollow fiber utilized can be substituted with any other functional fiber, enabling large-

scale production.

As demonstrated by Bairagi et al.¹⁴⁶, coating silk fabric with a more positively charged electrospun nylon can significantly enhance the tribo-positive performance of silk, resulting in output levels approximately 17 times higher than the silk/PET baseline (Fig.2. 13e). Similarly, Cao et al.¹⁴¹ used two electrodes to enhance output: one made from commercial silk fabric and the other from conductive fabric, both functioning together as the positive triboelectric layer, as illustrated in Fig.2. 13f. As a result, a maximum instantaneous power density of 19.4 mW/m² can be achieved. Fluorination is commonly employed to endow textile materials with functional properties such as chemical resistance, thermal and weather resistance, and self-cleaning capabilities. Building on these advantages, fluorinated silk and nylon fabrics have been developed by Feng et al.¹⁴⁷ to create functional textiles that are highly washable, durable, and self-cleaning, as seen in Fig.2. 13g. Moreover, the electrical performance is significantly enhanced due to the formation of long-chain molecules within the silk and the introduction of fluorine atoms with strong electron-accepting abilities. Initial mulberry silk can also be effectively used to fabricate TENGs with high triboelectric performance. As demonstrated by He et al.¹⁴⁸, the mulberry-silk-based TENG exhibits excellent humidity resistance and high output characteristics, attributed to its fluffy structure, as shown in Fig.2. 13h.

Researchers frequently use the contact-separation mode to fabricate fabric-based TENGs, leveraging their unique structure and high friction coefficients. However, the lateral sliding mode has also proven effective in designing fibrous-based TENGs. For instance, Feng et al.⁴⁴ developed a reciprocating tribometer coupled with triboelectric testing instruments, using amino-group-modified silk as one of the triboelectric layers (Fig.2. 13i and j). Although the output was relatively low, with a current of 382.2 nA, this approach provides valuable insights into the underlying mechanism of triboelectric charging and suggests extended applications for TENGs.

Individual TENG units face challenges in achieving multifunctionality. Researchers have, instead, developed an integrated system comprising a non-contact electricity-

induced constant-voltage TENG⁴³. This system maintains a steady output by combining two distinct phases and including a parasitic sensing module within one phase. In this setup, silk serves as the positive triboelectric layer, interacting with a negatively charged material to optimize the selection of the triboelectric material pair for the pumping TENG, as presented in Fig.2. 13k. Combining yarns is an effective method for achieving multi-scale functionalities. A hierarchical yarn composed of silk fiber, polytetrafluoroethylene fiber (PTFEF), and stainless steel fiber (SSF) materials is spun to enhance mechanical and triboelectric performance¹⁴⁹, as demonstrated in Fig.2. 13l. Stacking is another technique to create composited fabric. As displayed in Fig.2. 13m, Sangkhun et al.¹⁵⁰ fabricated a natural silk-based TENG by stacking a cyanoalkylated siloxane grafted fabric with a fluor alkylated siloxane grafted fabric. Consequently, the double-stacked TENG displayed an improved output current.

2.4 Application

2.4.1 Sensors

Silk-based TENGs offer a promising solution for sensor applications. Their unique properties, such as flexibility, biocompatibility, and high sensitivity, make them ideal for detecting various physical stimuli^{40, 151}. These TENGs can effectively convert mechanical energy from movements into electrical signals, enabling precise and reliable sensing capabilities in a wide range of fields, including healthcare, environmental monitoring, and wearable technology^{152, 153}.

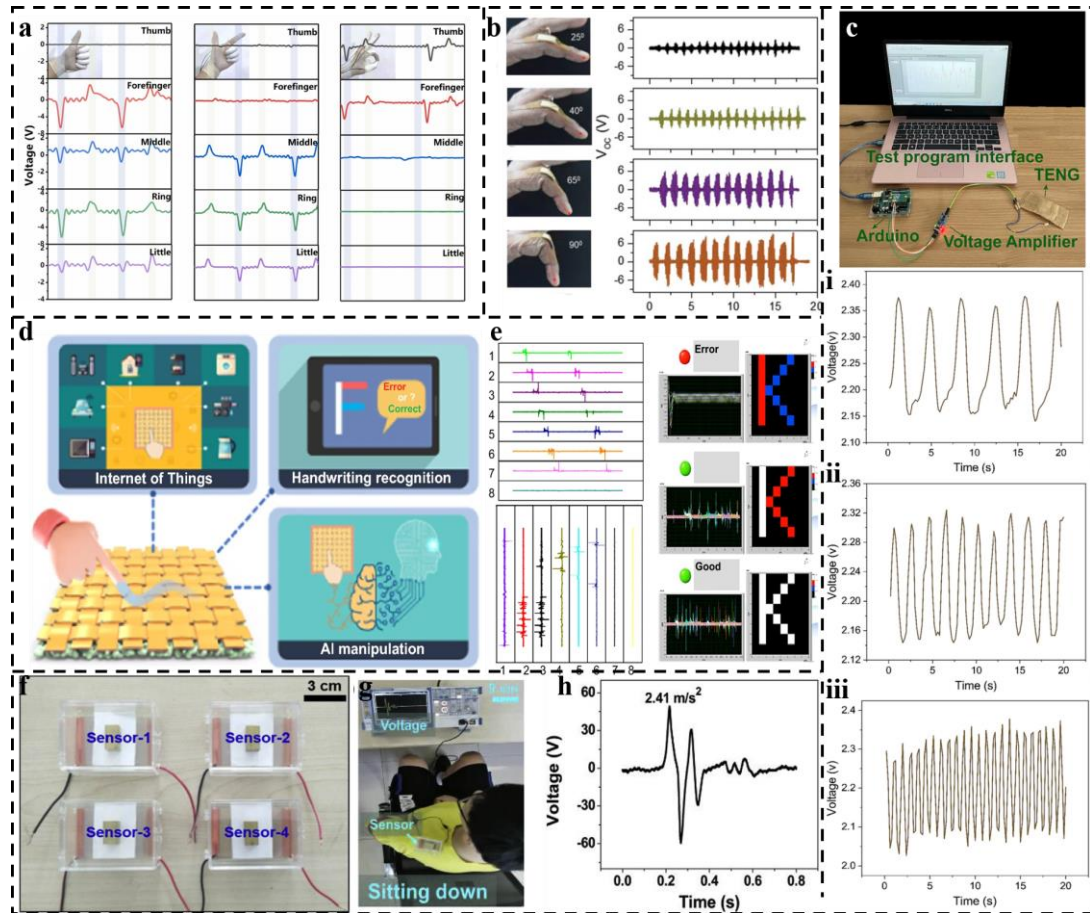


Fig.2. 14 Applications of silk-based TENG for sensing: a. The SPSM-based STENG as a self-powered sensor for gesture monitoring¹²³; b. A silk-based TENG for detecting different bending angles of fingers¹²¹; c. An SF/PVDF-HFP-based TENG used for abdominal respiratory monitoring¹⁵⁴: i. at a low respiratory rate; ii: at a normal respiratory rate; iii: at a high respiratory rate; d The schematic illustration of letter 'K' recognition and identification process by CSF-TENG-based HMI¹⁰⁴; f: Silk/PET TENG as acceleration sensors; g and h: Detection of a human body sitting down vibration intensity⁴⁰

The silk-based TENG serves as self-powered sensors for monitoring various hand gestures. For instance, Li et al.¹²³ engineered a silk-based TENG capable of distinguishing gestures like "praise," "okay," and "check" using the synchronized signals from five STENGs, illustrated in Fig.2. 14a. The operational concept involves the bent fingers activating the STENG to produce a voltage signal, allowing

differentiation of gestures, whereas extended fingers yield no electrical output. In addition, in another research work¹²¹, the silk-based TENG can also differentiate varying bending angles of hands (25°~90°), as illustrated in Fig.2. 14b. As the contact area between the electronic tattoo and the fingers increases, the Voc value significantly increases with the bending angle.

Silk-based TENGs can be applied to the medical field, for example, detecting the abdominal respiratory¹⁵⁴. While maintaining a relatively consistent breathing depth, the signal response period of the system is shorter when the breathing rate is higher than during normal breathing. Conversely, the signal response period is longer when the breathing rate is lower. The amplitude of signal changes does not vary significantly across different breathing rates. By analyzing the signal response period and the amplitude of signal changes during different breathing rates, it becomes easy to distinguish between slow, normal, and fast breathing, as shown in Fig.2. 14c.

TENGs can be effectively integrated with human-machine interfaces (HMIs) to create innovative and energy-efficient systems. By harnessing the mechanical energy from human movements, TENGs can generate electrical power to operate various HMI devices. This integration not only enhances the sustainability of HMI technologies but also improves their responsiveness and sensitivity. For example, Shen et al.¹⁰⁴ connect CSF-TENG with HMI technology to write 'K' perfectly and respond immediately, resulting in high rearrangement and correction accuracies, as displayed in Fig.2. 14d. Additionally, silk-based TENG devices can be utilized as acceleration sensors. For instance, Liu et al.⁴⁰ developed a silk/PET TENG using a spray coating method and employed the device to detect acceleration. Moreover, this device can be used to guide human activities, such as sitting down (see Fig.2. 14f-h).

2.4.2 Energy Harvesters

Silk-based TENGs offer an effective solution for energy harvesting. By incorporating a rectifier bridge, the alternating current (AC) generated by the TENG can be converted into direct current (DC), enabling it to power various small electronic devices. This

simple addition greatly enhances the practicality and versatility of silk-based TENGs, making them an ideal choice for sustainable and efficient energy generation in applications such as wearable electronics and energy harvesters.

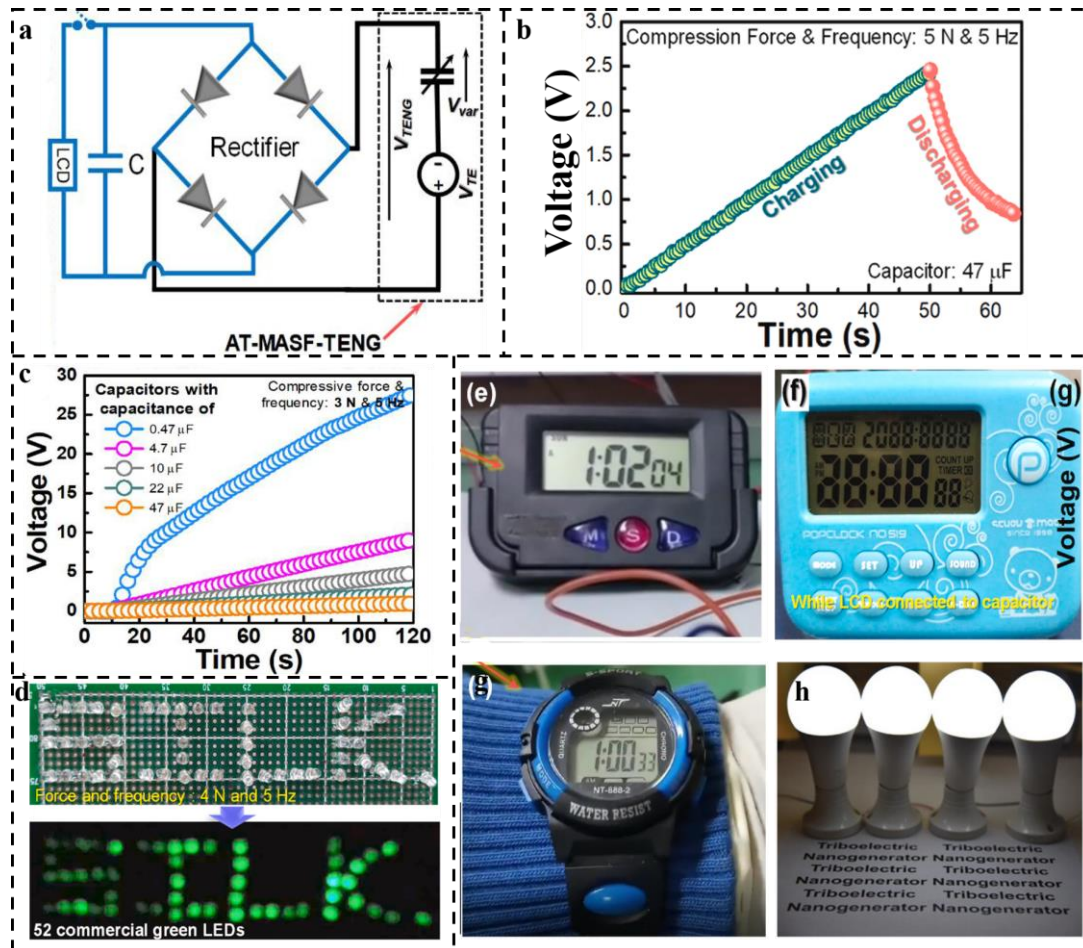


Fig.2. 15 Applications of silk-based TENG for energy harvesting: a. Equivalent circuit model of the bridge rectifier to convert the AC signals of AT-MASF-TENG into DC to power the portable electronic equipment via commercial capacitors¹¹⁷; b. Charging and discharging curve of 47 μF capacitor while it was employed to power LCD through the rectified electrical output of CSPCF-TENG¹⁵⁵; c. Voltage accumulated across the capacitors with the capacitances of 0.47, 4.7, 10, 22, and 47 μF¹¹⁷; d. AT-MASF-TENG as energy harvesters to power some 52 commercial LEDs¹⁵⁵ and some electronics, such as e. Timer¹⁵⁵, f. LCD screen¹¹⁷, and g. Wristwatch¹⁵⁵; h. Silk-based TENG for powering 4 white bulbs⁴³

The electrical output generated by TENG is an alternating current (AC) signal, which is not suitable for directly powering and operating portable electronic devices. Therefore, the AC signal produced by AT-MASF-TENG is first converted into a direct current (DC) signal using a full-bridge rectifier and then used to charge commercial capacitors. Finally, the stored energy in the capacitors is used to operate various portable electronic devices, such as timers and watches. Fig.2. 15a illustrates the equivalent circuit model of AT-MASF-TENG, indicating how it charges the capacitors through the rectifier and then provides power to the portable electronic devices. By using the rectifier, the silk-based TENG device can effectively charge and discharge the capacitors of varying capacitance, as manifested in Fig.2. 15b. Fig.2. 15c demonstrated that a capacitor with low capacitance (i.e., 0.47 μF) charges instantly within a few seconds and reaches a high voltage of 27V, while a capacitor with higher capacitance takes significantly longer to reach a high voltage.

In addition, the silk-based TENG device can power LED lights, as shown in Fig.2. 15d. The LED lights illuminate when pressure is applied to the silk-based TENG device. However, the 52 LED lights turn off once the pressure is released due to the alternating current (AC) generated by the silk-based device. For continuous powering, the AC from the silk-based TENG device can be converted into direct current (DC) to enable long-term operation. For instance, the TENG device can sustainably power low-power electronics such as a timer (Fig.2. 15e), an LED screen (Fig.2. 15f), and a wristwatch (Fig.2. 15g). More importantly, by Unifying a single TENG device into a combined TENG device, the electrical outputs can be improved significantly, further to Drive high-power electronics, like white bulbs, as manifested in Fig.2. 15h.

2.5 Summary

This chapter briefly introduced the basic concept of TENGs, including the triboelectrification, advantages of TENGs, and four working modes of TENGs, especially a detailed working principle of the CSTENGs. To introduce silk-based TENGs, an overview of natural fibrous-based TENGs was first provided. Subsequently,

an in-depth examination of silk's structure was conducted, the preparation method for fabricating silk-based TENG, and the diverse configurations of TENGs derived from silk, including those based on pure silk membranes and composite silk membranes, as well as methods like silk electrospinning, spraying, 3D printing, gel formation, and fibrous techniques. Finally, the applications of silk-based TENGs were summarized, which encompass energy harvesters and sensors.

CHAPTER 3 Natural Silkworm Cocoon layer based Hierarchically Architected Composite Triboelectric Nanogenerators for Biomechanical Energy Harvesting

3.1 Introduction

TENGs, as an emerging branch of energy conversion technologies, is first proposed by Wang's group in 2012¹⁵⁶, which is based on the coupling effect of triboelectrification and electrostatic induction¹⁵⁷. To date, four kinds of working modes have been developed, namely contact-separation (CS) mode, freestanding mode, lateral sliding mode, and single electrode mode¹³, in which CS mode is the main electrification mechanism for polymer-based TENGs in the principle of vertical charge polarization. Many endeavors have been devoted to broadening the application scopes of TENGs, such as wearable electronic devices¹⁵⁸⁻¹⁶⁰, artificial skin¹⁶¹⁻¹⁶³, and energy harvesting¹⁶⁴⁻¹⁶⁷, etc. However, some fabricated materials applied to TENGs have some potential concerns, for instance, the usage of poisonous organic solvents may cause environmental concerns and be harmful to human bodies if exposed to such conditions for a long time. From a sustainable point of view, eco-friendly materials should be considered with a higher priority. Accordingly, TENG material selections are preferably biodegradable, biocompatible, easy to fabricate, eco-friendly and low-cost.

Silkworm cocoon (SC), derived from the *domesticated* silkworm, with a natural protein-fiber composite structure, is composed of twining SF with high molecular weight conglutinated by glue-like sericin (SS) similar to a core-shell model¹⁶⁸⁻¹⁷⁰. SC is formed by a spinning process, which takes place over several hours as the larva draws a continuous silk thread from labial glands in its head in a figure-of-eight or 'S' fashion. Surprisingly, SC has a hierarchical structure with a random surface morphology like a nonwoven structure. Many SF-based TENGs have been developed yet. Most of them are fabricated in the form of electro-spun mat^{27, 29, 169, 171}, membrane^{29, 172-177}, 3D printing^{36, 178}, gel^{134, 179} and other treatments^{155, 180, 181}. For example, Kim et al.¹⁶⁹ first

reported an SF nanofiber net-worked bio-TENG using the electrospinning method. The designed bio-TENG has high output power because of the ultrahigh surface-to-volume ratio, which is the merit of random arrangement based on electrospinning. However, electrospinning is a cumbersome process and the bio-TENG only generated a low output signal of 15 V. Later, Xu et al.¹⁷⁴ developed an SF-based TENG by adding silver (Ag) and polyurethane (PU) into the SF film as the triboelectric layer. The designed device can be attached to the fingers to intelligently control the electrochromic function of rearview mirrors. However, Ag as an additive may increase the cost of designing portable devices from a long-term perspective. Some other designed TENGs may have high energy harnessing performance whereas not proper in terms of sustainability, such as injecting conductive ink and graphite that can cause environmental concerns.

SS is a good binder and is regarded as a bridge connecting intra-SF and inter-SCLs in composites¹⁸². Nevertheless, most researchers designing silk-based TENGs remove the SS component due to their weak mechanical properties as a single component as well as immunoreaction responding as implantation *in vivo* by a complicated degumming, rehydration, and dialysis process¹⁸³. However, compared with single SF fiber, SS is rich in α -helix or random coil in the amorphous region, resulting in a polarization enhancement between α -helix and β -sheet in crystallization regions when subject to external pressure¹⁸⁴. Research has demonstrated that the applied compressive force on the ordered and highly aligned protein fibers creates rubbing of α -helices crystalline fibers on each other which are associated through intramolecular polypeptide-CONH, H-bonding chains¹⁸⁴. Generally, SS is mostly discarded in wastewater, which generates a high chemical and biological oxygen demand as well as contamination of water. Hence, making use of SS for fabricating TENGs through proper methods would be beneficial and sustainable for our environment.

Cocoons possess three distinct and intriguing structural features conducive to integrated sericin (SS) retention: (1) the outermost layer (OL), characterized by the highest SS content, a low-density arrangement, and an abundance of wrinkles; (2) the middle layers (ML), noted for their optimal silk quality and the presence of several wavy bulges;

and (3) the innermost layer (IL), which exhibits a high-density arrangement and a relatively smooth surface¹⁸⁵. Given the advantageous properties of SS for the design of TENGs, as well as the unique hierarchical structures within the SC, it is of significant interest to explore the development of SCL-based TENGs with integrated SS retention.

In this study, the use of biocompatible SCL-based hierarchical composites as TENGs for the scavenging and harvesting of biomechanical energy is presented for the first time. The exfoliated SC layers, serving as triboelectric interfaces, include the outermost, middle, and innermost layers, resulting in the designation of the fabricated TENGs as OL/PDMS TENG, ML/PDMS TENG, and IL/PDMS TENG, respectively. Initially, the triboelectric properties of these three SCLs in contact with a PDMS membrane are examined. Subsequently, the triboelectric properties resulting from the layered stacking of SCLs are assessed. Finally, the effects of varied frequencies and localized pressures between the SCLs and the PDMS membrane are explored. The designed device demonstrates robust real-time biomechanical energy harvesting capabilities, suitable for charging commercial capacitors, powering electronic calculators, and monitoring human gestures.

3.2 Experimental Section

3.2.1 Materials

Domesticated *B. mori*. silkworm cocoons selected in the present research were purchased from the market. Moreover, these silkworm cocoons were received with the pupa removed. PDMS (SYLGARDTM 184 Silicone Elastomer kit) was obtained from Dow Corning Co., Ltd. Sodium carbonate (Na₂CO₃) was purchased from Dieckmann company. All the materials were used as received without further purification.

3.2.2 Preparation of SCLs

The middle part of SCs firstly was cut off from the pristine cocoons. Next, the middle part was exfoliated into multiple layers. Finally, the outermost layer, the innermost layer,

and one of the middle layers were chosen as the positive triboelectric electrode.

3.2.3 Preparation of PDMS Membrane

PDMS solution was prepared at first which was contained from the elastomer and the curing agent in a mass ratio of 10:1. The prepared PDMS solution was standing still to remove the bubble inside the mixed solution using a Vacuum drying oven and then placed in the oven for drying at 60 °C to obtain a PDMS membrane.

3.2.4 Fabrication of SCL/PDMS TENGs

Double-electrode TENGs with the contact/separation working mode were fabricated. The PDMS membrane and different SCLs were utilized as the negative and the positive tribo-materials, respectively. The sizes of the active tribo-layer were both 2 cm × 2 cm. Copper-nickel conductive fabric (CNF) was used as the electrode for triboelectric layers (PDMS and SCLs).

3.2.5 Characterization

Three basic physical parameters, area, thickness, and bonding length for three kinds of SCLs when applicable, were measured. The thickness was measured by a micrometer with the range of 0–25 and averaged with at least five positions for every sample. The bonding length of a single silk fiber which refers to the width of two SFs bonded with sericin was measured and analyzed for 100 times on SEM micrographs via image analysis software (Image J). The SS was calculated with the formula: $W_{SS} = (1 - W_{SF} / W_C) \times 100\%$. Where W_{SS} means the percentage of SS at selected layers, W_{SF} refers to the dry weight of SF at the selected cocoon layer, and W_C is the weight of the initial cocoon before degumming at selected layers. The degummed SF was dried in the oven and then weighed on the electronic balance.

The surface morphologies of the innermost layer, middle layer, and outermost layer of SCs were captured by scanning electron microscopy (SEM, TESCAN VEGA3). The

transmission of UV-A radiation was measured according to AS/NZS4399:1996 standard procedure. The tensile property tests were carried out using a universal tensile testing machine (Instron Co., Ltd.) at a 5 mm/min loading rate. TGA was used to monitor the removal of bound water molecules in the SC layer samples. The heating rate was set as 20 °C/ min, and the temperature ranged from 30°C to 650°C. Electrical output measurement: Open-circuit voltage and short-circuit current were measured using an electrometer (Keithley 6514). The dielectric constant was captured using a precision LCR meter (Keysight E4980A).

3.3 Results and Discussion

3.3.1 Structural Characteristics of SCLs

As conceptually diagramed in Fig.3. 1a, the formation of SCs experiences three stages: firstly, the caterpillar is fed with mulberry leaves for a period. Secondly, the caterpillar would proceed with the spinning process. At last, the multi-layer SC is formed. SC has a special multiple hierarchical structure with approximately nine layers. The multiple layers can be easily separated. The possible reason is that the inter-layer bonding is much weaker than the intra-layer bonding, indicating that individual SCL can be obtained¹⁸⁶. The SC has a vividly hierarchical structure and three unique structures as illustrated in Fig.3. 1a.

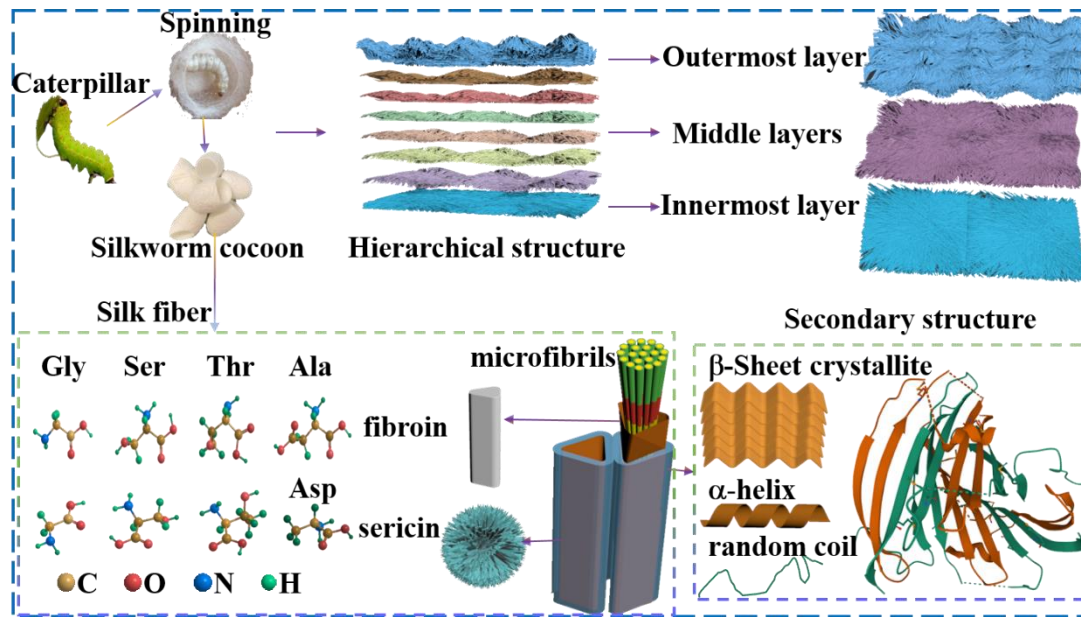


Fig.3. 1 Schematic of preparation of hierarchical SCLs

The basic parameters of SCLs are illustrated in Table 3. 1. With a uniform thickness, the bonding length of the middle layer is higher than that of the inner layer and the subsequent outer layer. The results are consistent with research studies^{25, 186} and it has been explained by the spinning method.

Table 3. 1 Basic parameters of cocoon layers

Cocoon layer	Area(cm ²)	Thickness(mm)	Bonding length(μm)
inner	2×2	0.18±0.08	33.16±0.52
middle	2×2	0.21±0.02	41.57±0.33
outer	2×2	0.22±0.09	30.93±0.86

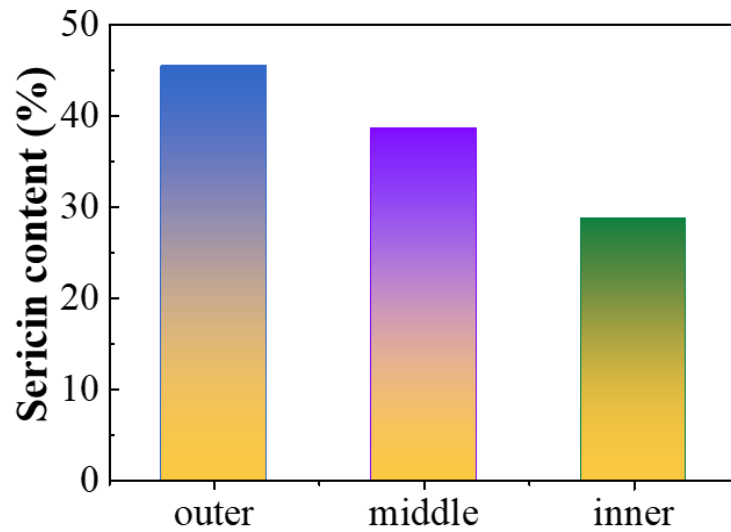


Fig.3. 2 SS content of three SCLs

SS, acting as a binder, plays an imperative role in deciding the properties of composites. Fig.3. 2 presents the SS content of different SCLs. As illustrated in Fig.3. 2, the outer layer has the highest SS content while the inner layer is endowed with the lowest content, consistent with previous research¹⁸⁶. It can be explained that continuous movement of *B. mori* head during spinning also acts on the orientation of protein molecules in the silk thread, and as the silk proteins aggregate and crystallize, more amorphous regions are distributed in the outer surface form at first¹⁸⁷.

To further explore the structure of three kinds of cocoon layers clearly, SEM was adopted for characterization, as shown in Fig.3. 3 a-c.

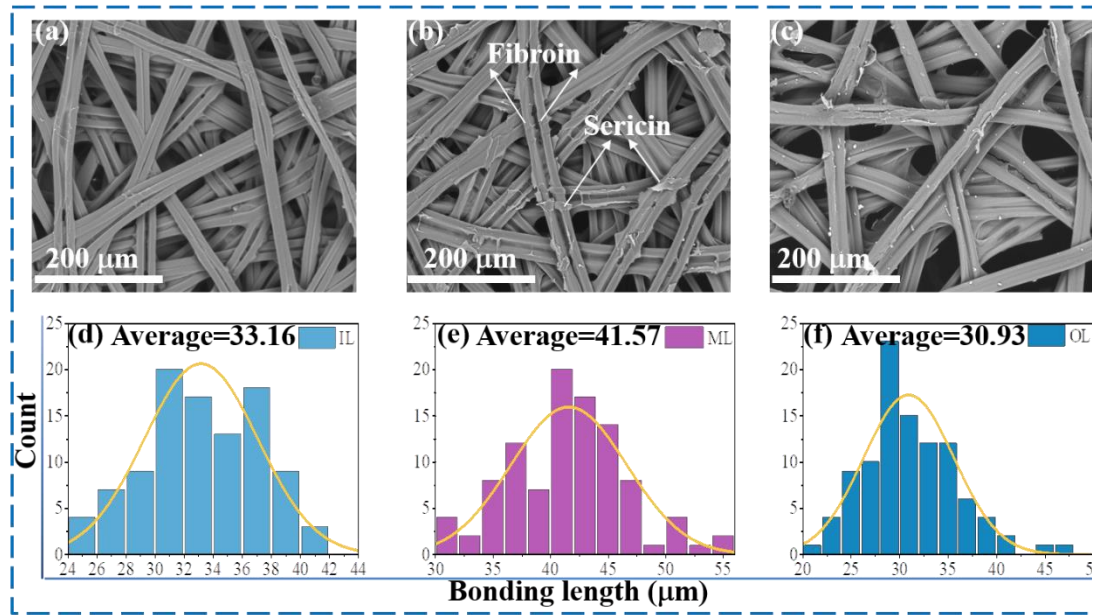


Fig.3. 3 SEM for surface morphology of a. IL; b. ML; c. OL; Bonding length of silk fibers in d. IL; e. ML; f. OL

The graded morphologies of cocoon components in different layers throughout the thickness of a cocoon wall are well depicted in Fig.3. 3. It is obvious that the inner surface (Fig.3. 3a) is smooth enough with covering compact SS on the SF efficiently to form a highly bonded network. As for the middle layer Fig.3. 3b, the SS bonding tends to fail. Notably, the silk fibers behave curved in the outer layer as manifested in Fig.3. 3c. Furthermore, the SS coating on the outer surface does not interconnect the SF fibers as clear cracks can be seen, leading to a loose structure in the outer layer. Fig.3. 3d-f show the bonding length of three kinds of SCLs, which behaves that the middle layer exhibits the largest, and the trade-off of silk quality may be accounted for this.

Before studying electric properties of SCLs as triboelectric positive materials, it is necessary to characterize and evaluate the performance of SCLs.

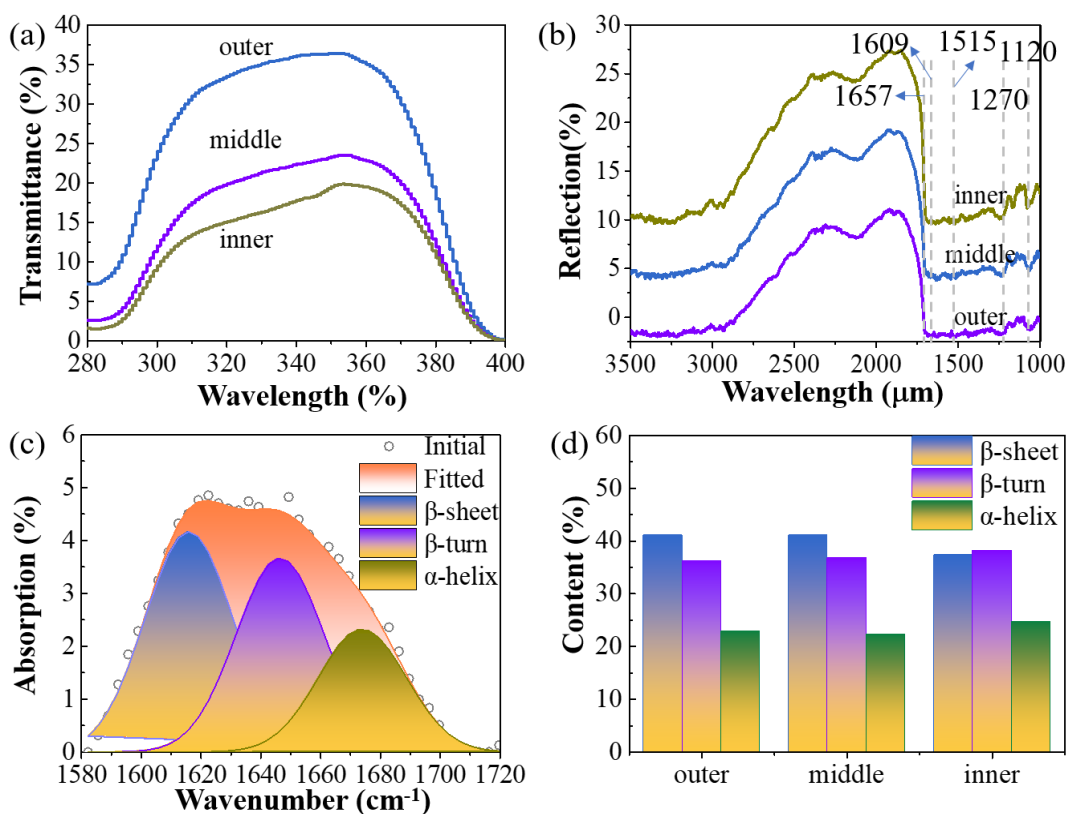


Fig.3. 4 The analytical characterization of three SCLs: a. UV–vis spectrum; b. Reflection of three kinds of SCLs; c. Secondary structure and d. The content of different SCLs

Table 3. 2 UPF of different silkworm cocoon layers

Sample	UPF	UVA Av (%)		
		315nm-400nm	290nm-315nm	290nm-400nm
OL	3.42±0.16	26.25±1.44	24.39±1.27	25.49±1.24
ML	6.17±0.47	16.38±0.96	12.74±1.13	15.32±0.98
IL	7.59±0.89	14.03±1.37	10.29±1.17	13.00±1.30

The UV–vis diffuse reflection of three SCLs is shown in Fig.3. 4a, ultraviolet protection factor (UPF) is defined as the ratio of the average effect of ultraviolet radiation calculated when the skin is unprotected and the average effect of ultraviolet radiation calculated when the skin is protected, The higher the UPF value, the better the UV protection function. Table 3. 2 shows an increasing trend from the outer layer (3.42) to the inner layer (7.59), which means a gradient structure has the advantage of UV

protection.

Fig.3. 4b exhibits the FT-IR spectra of three kinds of SCLs at the range of $3500\text{ cm}^{-1}\sim 1,720\text{ cm}^{-1}$. As illustrated in Fig.3. 4b, the occurrence of extensive peaks from $3,500\text{ cm}^{-1}$ to $3,100\text{ cm}^{-1}$ is mainly due to the bending vibration and OH stretching in the molecule. In addition, peak at $1,609\text{ cm}^{-1}$ corresponds to amide I (C = O stretching vibration directly related to the backbone conformation), peak at $1,515\text{ cm}^{-1}$ corresponds to amide II (out of phase combination of the C–N stretching and N–H bending), and peak at $1,270\text{ cm}^{-1}$ corresponds to amide III (in-phase combination of the C–N stretching and the N–H bending). Peaks amide I ($1,657\text{ cm}^{-1}$), amide II ($1,515\text{ cm}^{-1}$), and amide III ($1,270\text{ cm}^{-1}$) were assigned to the β -sheet conformation¹⁸⁸.

Silk is a natural protein material, and due to specific interactions among their amino acid side-chains, various secondary structures such as β -sheets, β -turn, random coils, or α -helix are formed. Silk fibers exhibit a sophisticated hierarchical structure, in which highly organized antiparallel β -sheet nanocrystals are loosely aligned with the fiber axis and dispersed within a semi-amorphous matrix consisting of helices and β -turns¹⁸⁹. By conducting Deconvolution, the secondary structure can be obtained and revealed in Fig.3. 4c and d, indicating that the outer layer has similar content of β -sheet and α -helix.

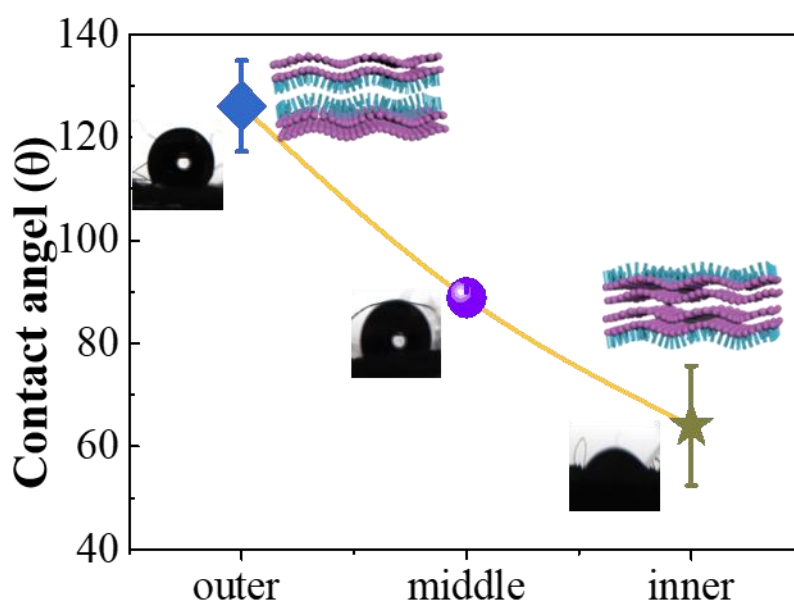


Fig.3. 5 The contact angles of three kinds of SCLs

The photographs of dynamic contact angle tests of the three different SCLs are shown in Fig.3. 5, wherein deionized water is employed as the test liquid. Notably, the outer layer is hydrophobic while the inner layer is hydrophilic as seen in Fig.3. 5.

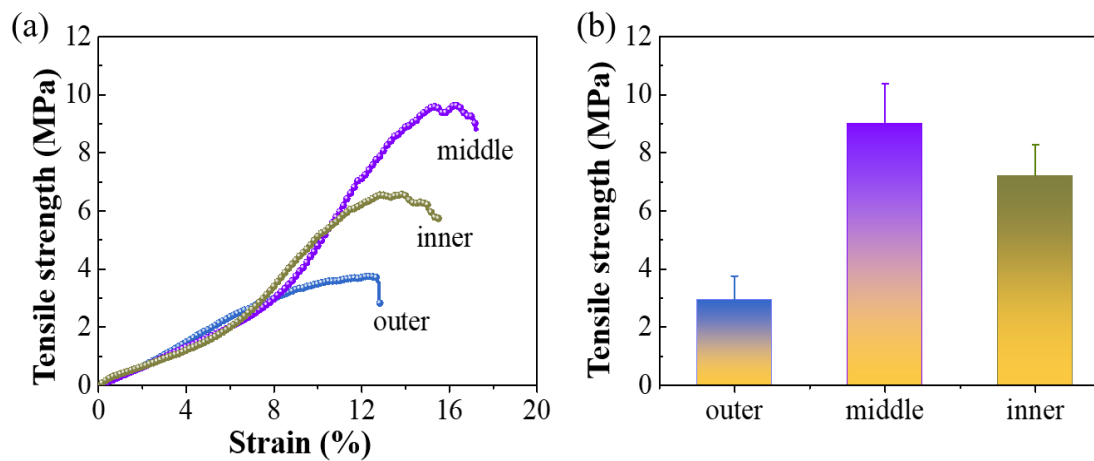


Fig.3. 6 Tensile properties of SCLs: a. Tensile curves of SCLs; b. Tensile strength of SCLs

Fig.3. 6a and b show the tensile properties of three kinds of SCLs and results reveal that the strength of different SCLs ranges from 3 MPa in the outer layer to 9 MPa in the middle layer, which is due to the trade-off between the spinning method and remaining materials inside the puma in the middle layers, a better alignment of β -crystallites¹⁹⁰. Initial *B. mori* cocoons exhibit excellent intrinsic mechanical strength of 54 MPa, with an estimated 6~18 times as a single layer, in accordance with the calculative total layers in the *B. mori* cocoons¹⁸⁶.

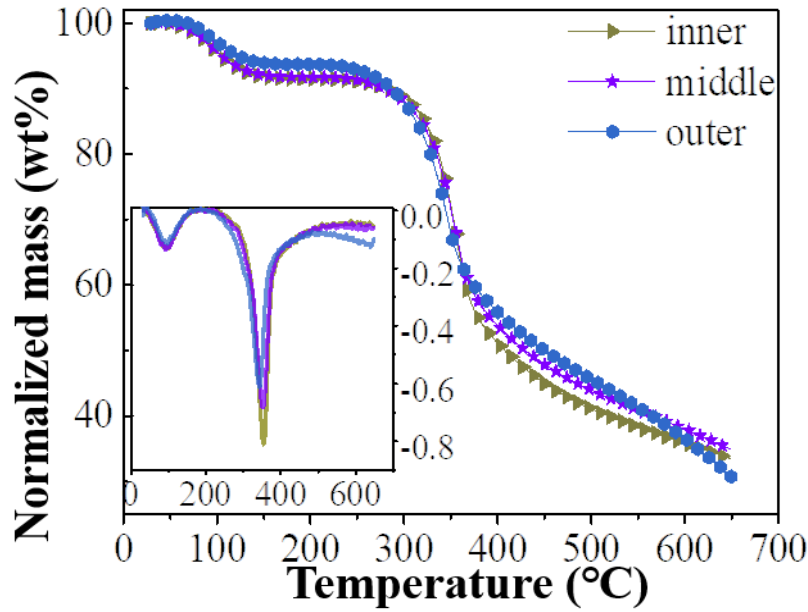


Fig.3. 7 TGA curves of SCLs

To evaluate the thermal stability of SCL-TENG positive materials, the normalized mass of three different SCLs is described in Fig.3. 7. The inflection point of TGA curves means Maximum weight loss rate, and it is notable that the maximum ‘inflection point’ represents the data of the inner layer, while the minimum is that of the outer layer and the middle layer exhibits the medium. For a deeper explanation, it is noted that the outer layer would lose a small percentage of quality over time, indicating that the outer layer has better thermal stability compared to the middle layer and the subsequent inner layer. This stability serves to protect the larva or pupa from external surroundings, parasitism, or natural predators, thereby supporting the internal metabolic activity^{25, 186}.

3.3.2 Working Mechanism of SCL/PDMS TENGs

The working mechanism of the SCL/PDMS TENGs is schematically depicted in Fig.3. 8a, which works in the principle of contact triboelectrification and electrostatic induction^{191, 192}. Based on the triboelectric series¹⁹³, silk exhibits relatively low electronegativity, easy to lose electronic to act as the positive material. Conversely, PDMS is regarded as an excellent triboelectrically negative material because of its relatively high electronegativity, prone to gaining electronic¹⁹⁴.

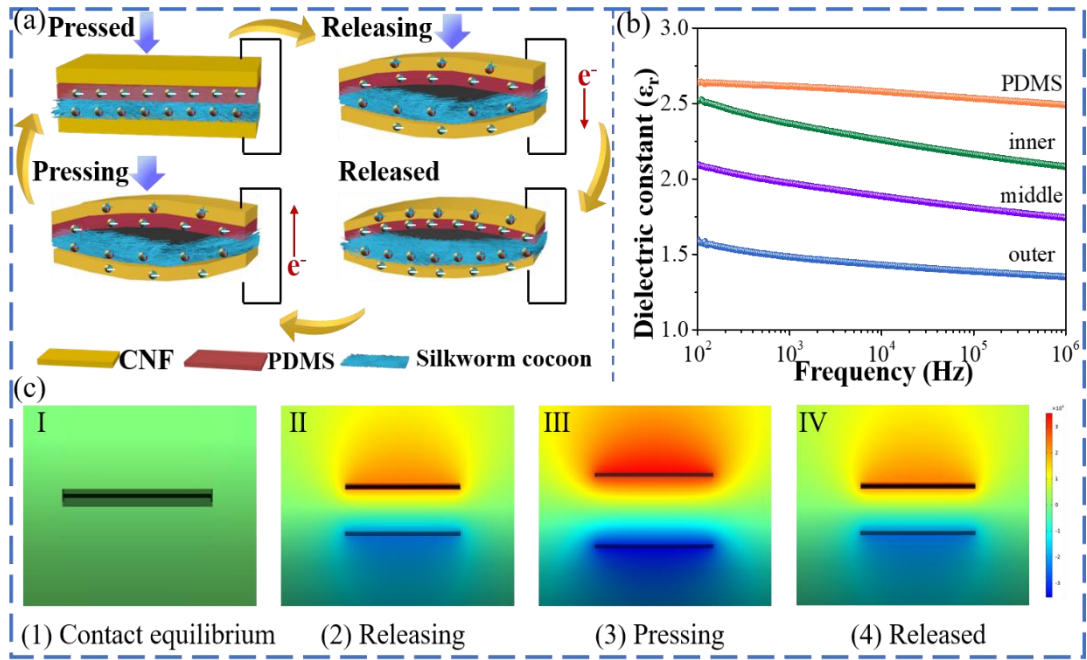


Fig.3. 8 Working principles of SCL/PDMS Contact-separation TENGs: a Working principle of SCL/PDMS TENGs; b Dielectric constant of PDMS membrane and SCLs; c The COMSOL simulation results of the OL/PDMS-TENG

At the first stage, equivalent charges with opposite polarities are generated on the PDMS membrane and SCL surface due to the electrification with an electroneutral circuit under the external load. The PDMS membrane is negatively charged meanwhile the SCL is positively charged. At the time of external force withdraw, the PDMS membrane is separated from the SCL membrane, and electrons on triboelectric layers would flow to the electrodes to achieve the trade-off through an external circuit, emerging an electrical signal. In this process, the electrons generated on each side of the triboelectric layer gradually decrease due to the discharging effect, which probably is attributed to drift, diffusion, air breakdown, and charge recombination. In contrast, the electrical signal is strengthened due to more activated electrons in the circuit^{195, 196}. When the gap distance increases to the maximum value after separating, the whole circuit is well-balanced because of an interrupted circuit. The dipole moment gradually decreases when the compressive force is reapplied to the triboelectric layers. Then, the potential difference almost diminishes, leading to the generation of electron flow in a

reverse direction, from the bottom electrode to the top electrode. Repeated contact and separation between the PDMS membrane and the SCLs can generate recurrent current signals.

The dielectric constant is important in determining the electric performance of the TENGs, and the dielectric constant of three kinds of SCLs is illustrated in Fig.3. 8b. The principle of measuring the dielectric constant is on the condition of a parallel-plate capacitor, and the following equation can obtain the dielectric constant:

$$C = \frac{\epsilon_r S}{4\pi k d} \quad (3-1)$$

Where C means capacitance; ϵ_r represents dielectric constant; k is the electrostatic force constant ($k=8.9880 \times 10^9$ Nm/C); d is the distance between two electrode plates; S means an effective area of electrode plates.

As depicted in Fig.3. 8b, the dielectric constant of the inner layer is larger than that of the middle layer and outer layer, implying that the surface charge density of the inner layer is the largest while the outer layer has the smallest charge density. The empirical results show that the inner layer can be excited with more electrons based on CS working mode. Furthermore, Fig.3. 8c illustrated the simulation results of COMSOL with contact electrification caused by separation and contact movements to understand the power generation process better.

3.3.3 Output Performance of SCL-TENGs

Based on the different mechanical properties and surface morphology and whereas same composition, we suppose that three kinds of SCL/PDMS TENGs present other triboelectric performances. In addition, given that triboelectrification is one type of surface effect and that friction materials and surface morphology can decisively determine the output of TENGs, we further suppose that the OL/PDMS TENG covered with a large amount of wrinkles would exhibit the best triboelectric performance¹⁹⁵.

Therefore, the electrical output properties of three kinds of SCL/PDMS TENGs were measured and compared in Fig.3. 9a-c.

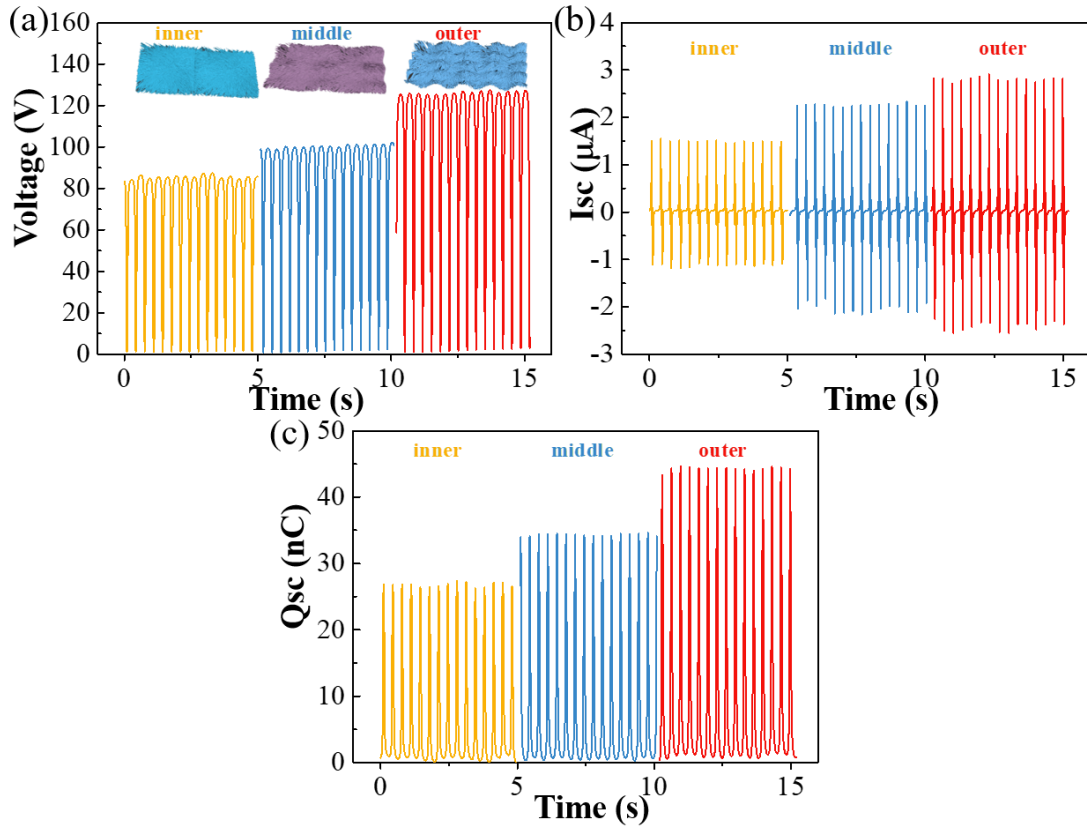


Fig.3. 9 Evaluation of electrical outputs of SCL/PDMS TENGs: a-c The Voc, Isc, and Qsc of three different SCL/PDMS TENGs

The frequency and pressure are fixed for all the measurements at 3 Hz and 5 N, respectively. Fig.3. 9 a-c reveals out that the OL/PDMS TENG exhibits optimal electric performance, and more specifically, Voc, Isc, and Qsc of OL/PDMS TENG reach the maximum value of 126.5 V, 2.91 μA, and 45.41 nC, which are 1.25, 1.25, and 1.28 times higher than ML/PDMS TENG, respectively. Firstly, the reasons can be accounted for by the fact that OL is endowed with lots of wrinkles, enhancing the triboelectric effect and providing channel for electronic transferring.

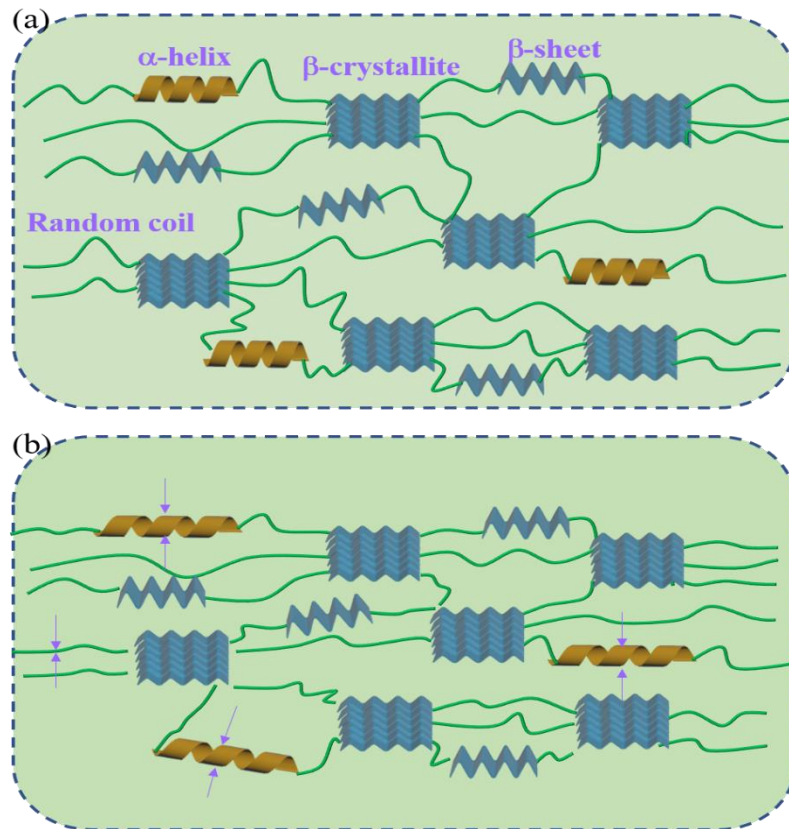


Fig.3. 10 a. Secondary structure inside SCL without applied pressure; b. Secondary structure inside SCL with external load

Secondly, as shown in Fig.3. 2, the content of SS in the outer layer is slightly higher than that of the middle layer and much higher than that of the inner layer, indicating that the outer layer is distributed with more amorphous regions and less crystalline regions as compared to that of the inner layer. While research has demonstrated that the applied compressive force on the ordered and highly aligned protein fibers creates rubbing of α -helices crystalline fibers on each other, which are associated through intramolecular polypeptide-CONH, H-bonding chains¹⁹⁷, as demonstrated in Fig.3. 10 a and b. In addition, compared with single SF fiber, the retention of SS may enhance the polarization effect. These electric dipoles are generated owing to the deformation of the triple helical structure in crystalline collagen-based biomaterials⁵¹. These effects were amplified here through developed intramolecular polypeptide-CONH, H-bonding chains in the highly aligned crystalline collagen fibers⁵¹. Therefore, the triboelectric

output performance of outer layer outperforms that of middle layer and inner layer due to the highest content of SS as illustrated in Fig.3. 2 a.

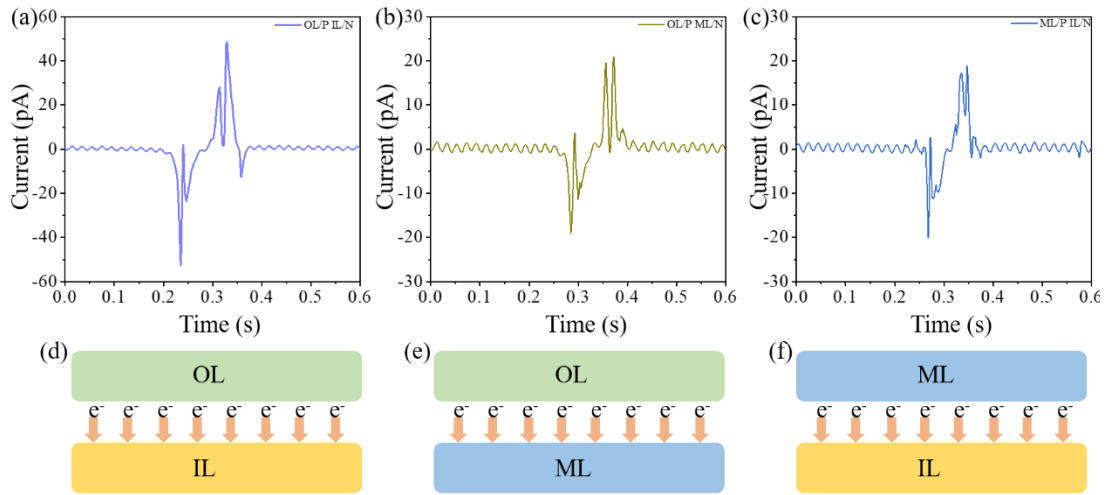


Fig.3. 11 Electron affinity of three silkworm cocoon layers (SCLs): a. Electron affinity between OL (positive) and IL (negative); b. Electron affinity between OL (positive) and ML (negative); c. Electron affinity between ML (positive) and IL (negative); Electron flow between d. OL and IL; e. OL and ML; f. ML and IL

What's more, according to the relationship between the direction of electron flow and current, it is the opposite between the direction of electron flow and current. As Fig.3. 11 shows, when the OL is in contact with IL, the current is negative, indicating the electron flow is from OL to IL, which further implied the OL is easier to lose electrons as compared with IL. Similarly, the OL is easier to lose electrons as compared with ML and the ML is easier to lose electrons as compared with IL. Overall, the results based on electron affinity show that three SCLs can be ranked as follows: $IL < ML < OL$, indicating the polarity between PDMS and OL is larger than that of PDMS/ML and subsequent PMDS/IL, which further confirms that the OL/PDMS TENG generates higher electrical outputs as compared with that of ML/PDMS TENG and next IL/PDMS TENG.

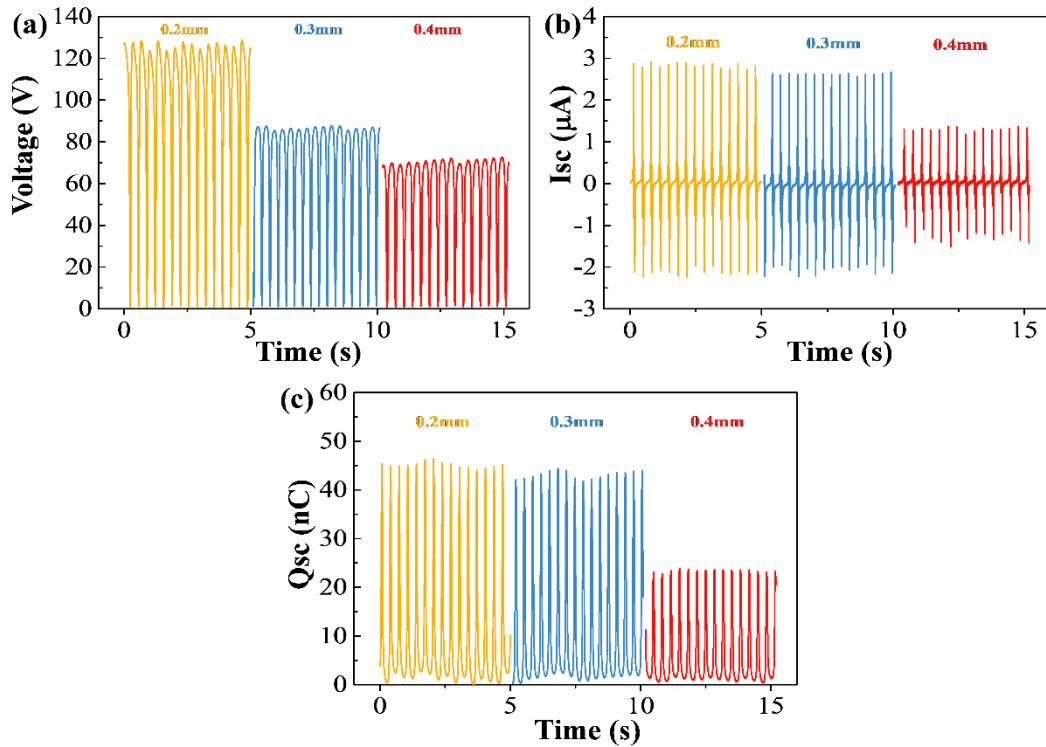


Fig.3. 12 Evaluation of electrical outputs of the thickness of PDMS-based TENG with the fixed thickness of 0.2 mm of silkworm cocoons: a-c. The Voc, Isc, and Qsc

It is worth mentioning that the IL/PDMS TENG behaves with the poorest output performance as the value of Voc, Isc, and Qsc are 86.33 V, 1.55 μ A, and 27.47 nC relatively due to the smooth surface depicted in Fig.3. 1a. Interestingly, some slight fluctuations after saturation can be noticed, which is probably due to the static discharge between orderless silk fibers on the cocoon surface and PDMS membrane¹⁹⁸. The thickness of PDMS was set as 0.2mm, and the reason is explained in Fig.3. 12. Specially, with the increased thickness of PDMS membranes from 0.2 mm to 0.4 mm, the electric performance of OL/PDMS TENG gradually weakens, and that is the reason why the thickness of PDMS film is set as 0.2 mm.

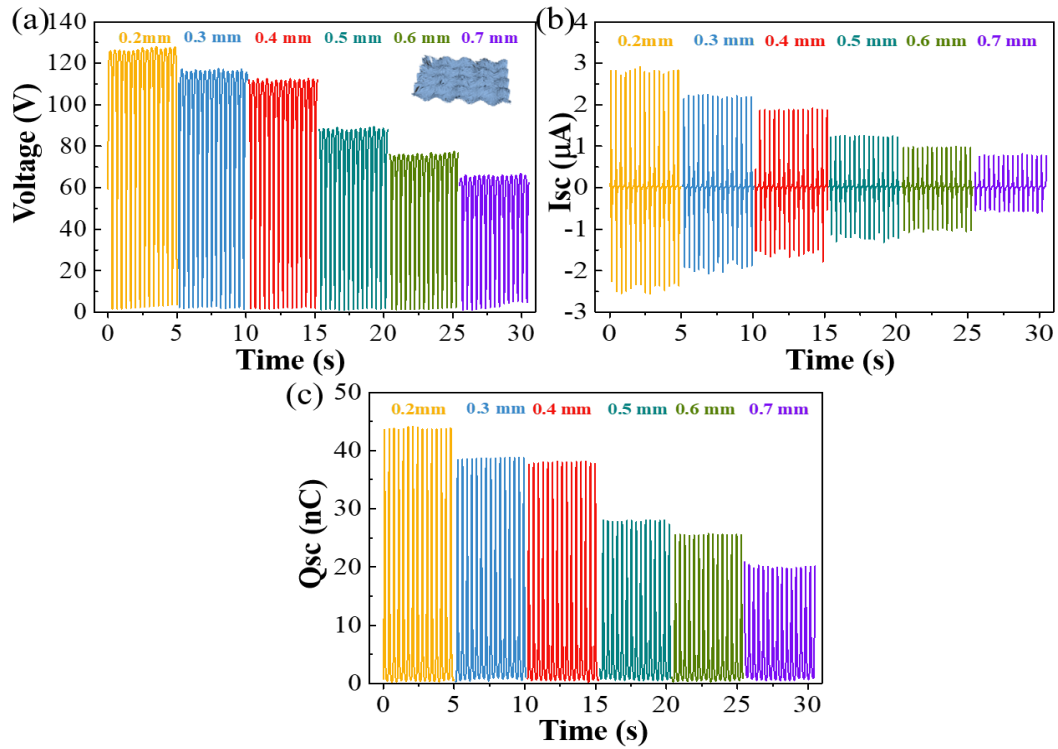


Fig.3. 13 Stacked effect of SCL/PDMS TENGs: a-c. The Voc, Isc, and Qsc

To evaluate the effect of hierarchical structure towards TENG, the stacked effect was investigated, as shown in Fig.3. 13a-c. The optimal outer wrinkled structure is reserved. As demonstrated in Fig.3. 13a, with the increasingly stacked layers, the Voc shows a downward trend, indicating that layers of stack can block the flow of electrons, to some extent. The tendencies of Isc (Fig.3. 13b), and Qsc (Fig.3. 13c) are similar to that of the Voc. Therefore, the amplitude of the peak voltage of 126.5 V regarding 0.2 mm SCL/PDMS TENG is perceived, which is almost 2 times as that of 0.7 mm (65V).

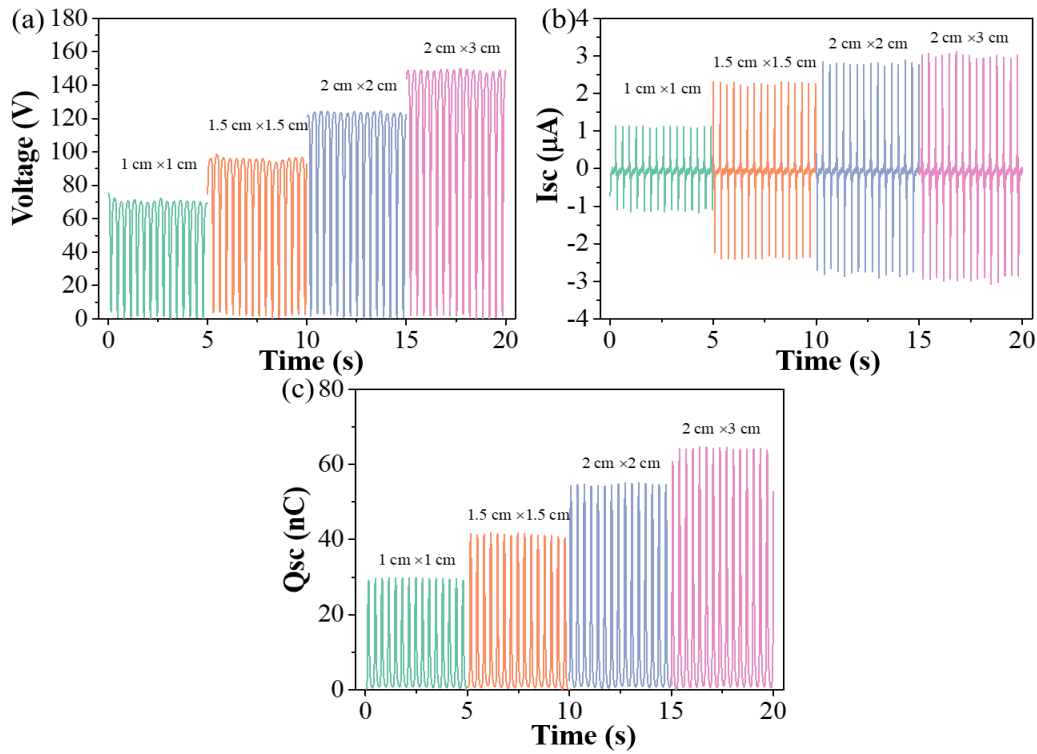


Fig.3. 14 a. Open-circuit voltage, b. Short-circuit current, and c. Charge of the OL/PDMS-TENG with different working areas.

In addition, Fig.3. 14 illustrates the relationship between affective area and electric outputs. Under a given impact force of 5 N and a frequency of 3 Hz, increasing Voc of 70V, 100V, 126V, and 150 V can be obtained as the size increases from 1×1 , 1.5×1.5 , 2×2 , to 2×3 cm² (Fig.3. 14 a). Similarly, Isc of the OL/PDMS-TENG also increased gradually from 1.2 μA, 2.4 μA, 2.91 μA to 3.3 μA, by increasing the size from 1×1 cm² to 2×3 cm² (Fig.3. 14 b). In addition, the Qsc of the OL/PDMS-TENG was changed from 30 nC (1×1 cm²) to 65 nC (2×3 cm²). The reason might be attributed to the larger contact areas with larger size, which could produce more charges with larger outputs.

Fiber diameter is considered a significant factor in determining the electric outputs. As shown in Fig.3. 3, OL has the smallest fiber diameter, while the ML has the largest fiber diameter. When SCL has a smaller fiber diameter, more silk fibers will be embedded into the deep SCL upon contact, which means that a larger affective will be produced.

As a result, the electrical output of the prepared OCL/PDMS-TENG is significantly superior to that of IL/PDMS-TENG and ML/PDMS-TENG. However, the IL has a smaller fiber diameter than that of ML, instead of higher electric outputs, which is attributed to the surface morphology of SCLs¹⁹⁹. Due to the deformation of protruding surface structures, the effective contact area is sensitive to the contact force²⁰⁰. IL and ML have different surface morphology, for instance, IL has a smooth surface while ML has a rough surface. Research has demonstrated plasma etching (rough surface ML) brings much more micro pillars as compared with smooth surface (IL), which own large surface area and easy to deform when compressed, then the larger contact area is achieved which provides more space for charge storage and hence strengthen the contact electric effect²⁰¹.

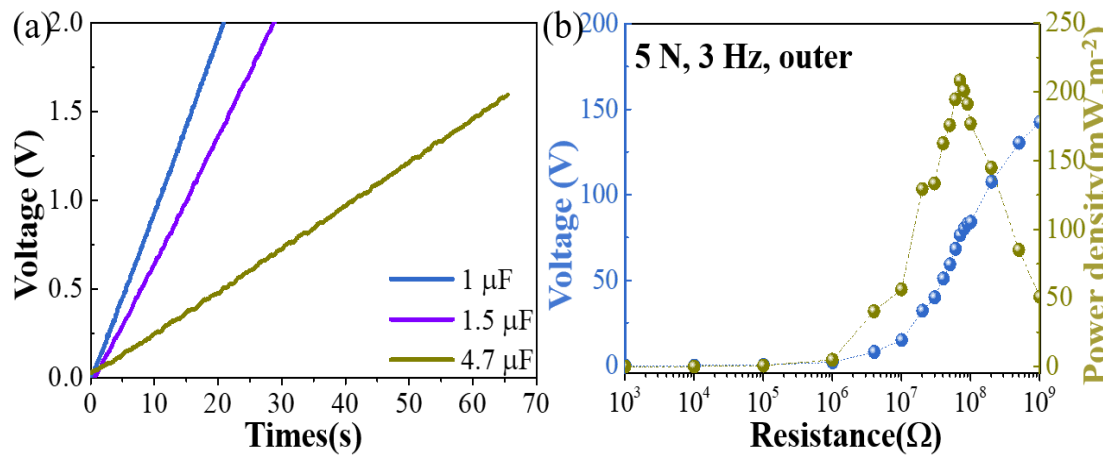


Fig.3. 15 a. Charging curves of various capacitors by OL/PDMS TENG; b. Output voltage and power density of OL/PDMS TENG at a series of external loads

To explore the practicability of OL/PDMS TENG for energy harvesting, the charging capacity of OL-TENG was investigated by charging different capacitors (1, 1.5, 4.7 μF), as illustrated in Fig.3. 15a. Notably, a capacitor of 1, 1.5, and 4.7 μF can be quickly charged continuously to 1.5 V within 15, 23, and 65 s, proving that the device has great potential as a reliable power source. Fig.3. 15b provides the instantaneous power density of OL/PDMS TENG on different external loads from 0.001 MΩ to 3 GΩ, achieving the maximum power density of 216 mW/m² at the resistance of 70 MΩ.

Based on the parallel circuit, the voltage tends to increase with ascending applied load resistance, while the power density rises at first and then shows a downward trend.

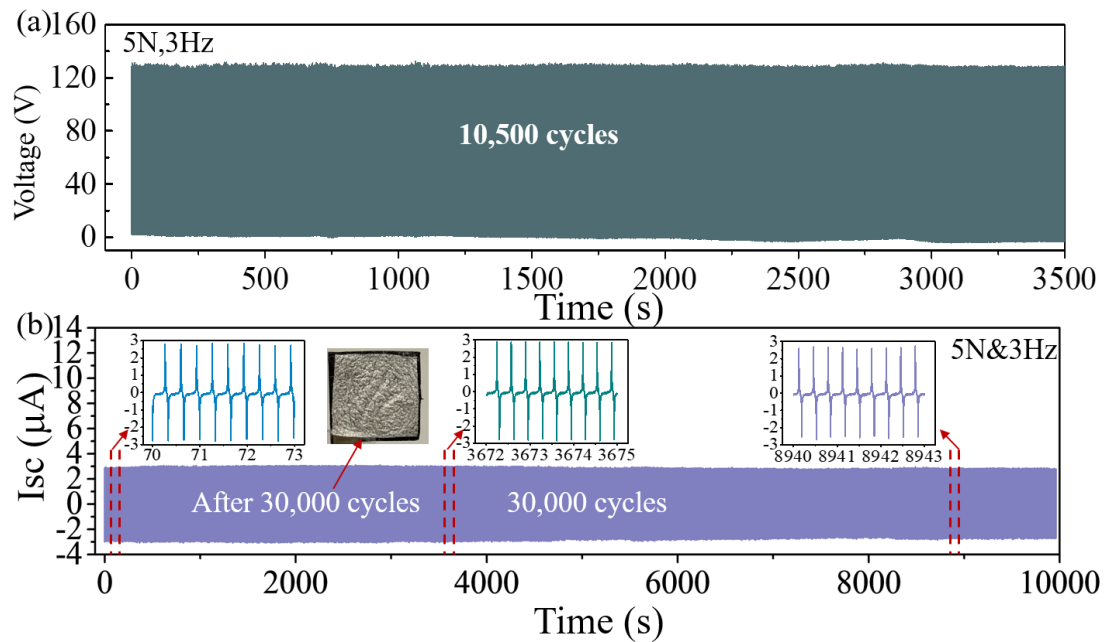


Fig.3. 16 a. The mechanical stability of OL/PDMS TENG; b. The recovery state of device housing after 30,000 cycles

Fig.3. 16a exhibits the stability and durability properties of the OL/PDMS TENGs under cycled compressive force of 5 N and frequency of 3 Hz. It is obviously seen that the output voltage does not seem to change significantly after 10,500 cycles. This result reveals the fabricated TENGs have the robustness and mechanical durability for a practical application. In addition, the recovery state of device housing after 30,000 cycles is also provided in Fig.3. 16b to illustrate the mechanical stability of the designed OL/PDMS TENG.

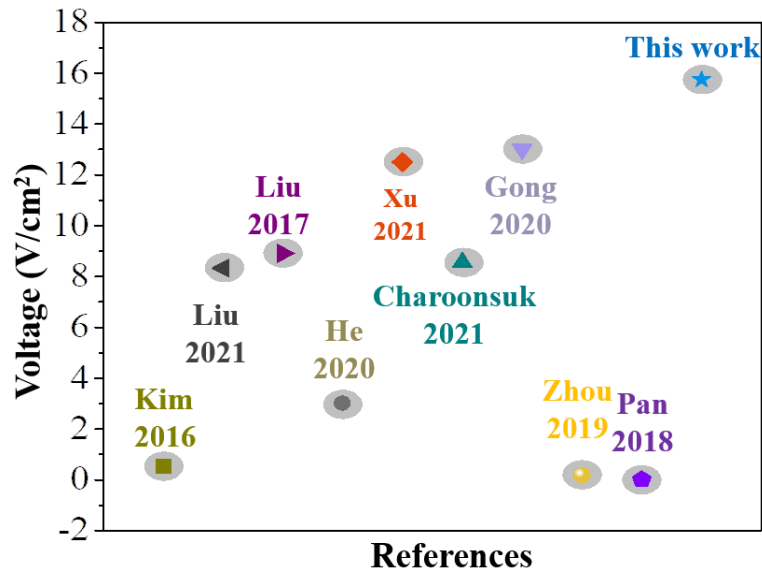


Fig.3. 17 Comparison of the voltage density reported in recent years^{1, 24, 32, 38, 42, 118, 122, 202, 203}

Fig.3. 17 provides a comparison of the V_{OC} densities of silk-based TENGs in recent years, and Table 3. 3 gives a detailed comparison of silk-based TENGs developed recently, from which it is seen that the V_{OC} density of this work exhibits better performance.

Table 3. 3 Comparison of output performance of silk-based TENGs

Mode	Triboelectric materials	Pressure (N)	frequency (Hz)	Area (cm ²)	Voltage (V)	Current (μ A)	Power (mW/m ²)	Ref.
CS D	Bio-silk/polyimide film/Al	16.8	3	28	15	2.5	4.3	24
CS S	AgNW/e-silk	6	5	3.6	90	0.06	2	36
CS D	silk nanoribbons/Mg	50	5	2	41.64	0.5	86.7	133
CS S	Silk hydrogel/PDMS	15.9 kPa	1	4	12	0.2	-	42
CS D	SF+ Ag/PTFE+ Ag	20	1	4	50	1.5	-	32
CS D	SF+Mg/bioresorbable polymers	/	1	2	55	0.6	21.6	30
CS D	PET+ITO/SF+CNT	/	2	81	15	1.4	18	202
CS D	Spider silk+PET	Self-vibration	4	7	0.0407	0.105	59.5 pW	203
CS D	SCLs/PDMS	5	3	4	63	3	216	This work

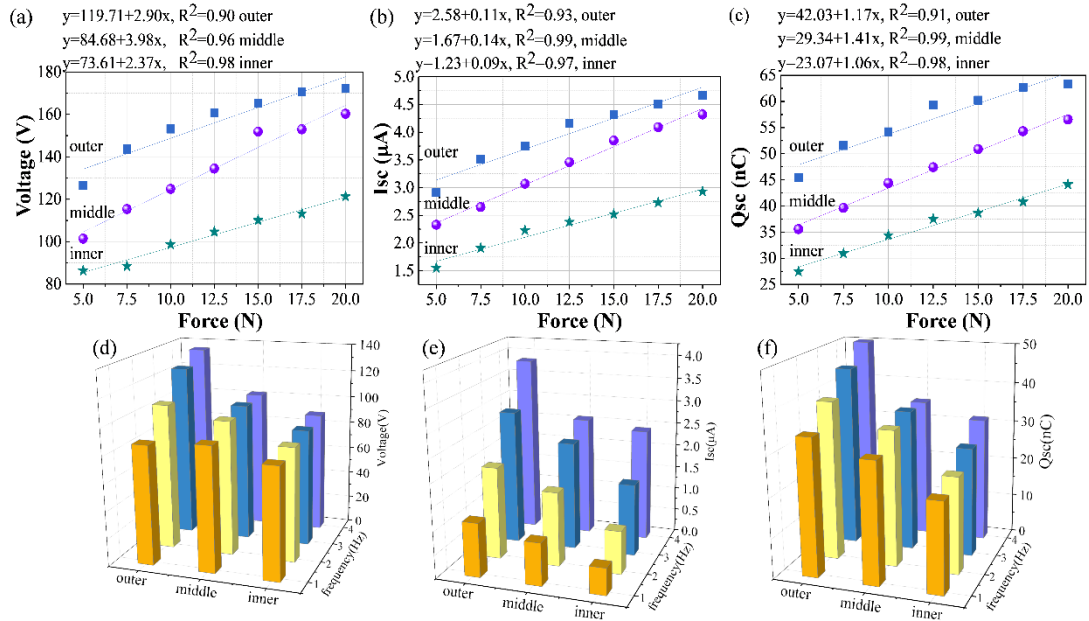


Fig.3. 18 Output performance of OL/PDMS TENG: a-c. The Voc, Isc, and Qsc of three kinds of SCL/PDMS-TENGs under different pressure; d-f. The Voc, Isc, and Qsc of three kinds of SCL/PDMS TENGs under different frequencies.

Considering that different magnitudes of impact forces can be applied to the SCL/PDMS TENGs in real life, it is meaningful to investigate the influence of frequency and pressure on the performance of three kinds of SCL/PDMS TENGs. The range of pressure (5-20 N) and frequency (1-4 Hz) are chosen as illustrated in Fig.3. 18. It is notable that the outputs exhibit an increasing trend all the time with increased frequency, ranging from 126.5 V at 5 N to 172.27 V at 20N. Meanwhile, the Isc and Qsc show a similar trend, which is rising from 2.91 μA and 45.41 nC (5 N) to 4.51 μA and 63.28 nC (20 N). Such enhancements could be attributed to the more intimate contact between the PDMS film and OL at a larger magnitude of applied impact force. When the applied force changes from 12.5 N to 20 N, variation of output voltage is almost negligible and becomes stable which implies crystal deformation inside microfibrils is almost saturated²⁰⁴.

Fig.3. 18 a-c evaluates the external force and frequency impart on three kinds of TENGs.

Surprisingly, the outputs of the three kinds of TENGs almost linearly rise and the Linear regression function of the three kinds of TENGs are different. The ML/PDMS TENG shows a more sensitive reflection towards the external force as depicted in Fig.3. 18 a-c in comparison with the other two types of TENGs, which can be attributed to the balanced silk quality in the ML. Once exposed to the external force, balanced SCL can make quicker reaction with charge excitation as compared with the other ones. Fig.3. 18 d-f shows the output voltage and current as well as the charge increased with enhanced frequency applied for three kinds of TENGs due to the gradually accumulated tribo-charges on the SCL surface²⁰⁵.

3.3.4 Mechanical Energy Harvesting by the OL/PDMS-TENG

Fig.3. 19 a depicted the equivalent circuit of a self-powered system of OL/PDMS TENG where a capacitor of 22 μF was connected in parallel with a high-voltage diode rectifier, which can drive a commercial electronic watch to operate normally. For example, in Fig.3. 19 b, the capacitor of 22 μF was continuously charged to 3.7 V within 750 s and then powered the small calculator. After the discharging process, the TENG device was self-charged again under a compressive force of 5 N with a working frequency of 3 Hz, thus a periodical working curve formed. Small types of electronics were powered to continuously work, such as a watch (Fig.3. 19 b) and a calculator depicted in Fig.3. 19 c. Additionally, the OL/PDMS TENG can serve as a sustainable power supply and directly light up 44 green LEDs (Fig.3. 19 d). The results demonstrated our OL/PDMS TENG is promising as an efficient and clean power source.

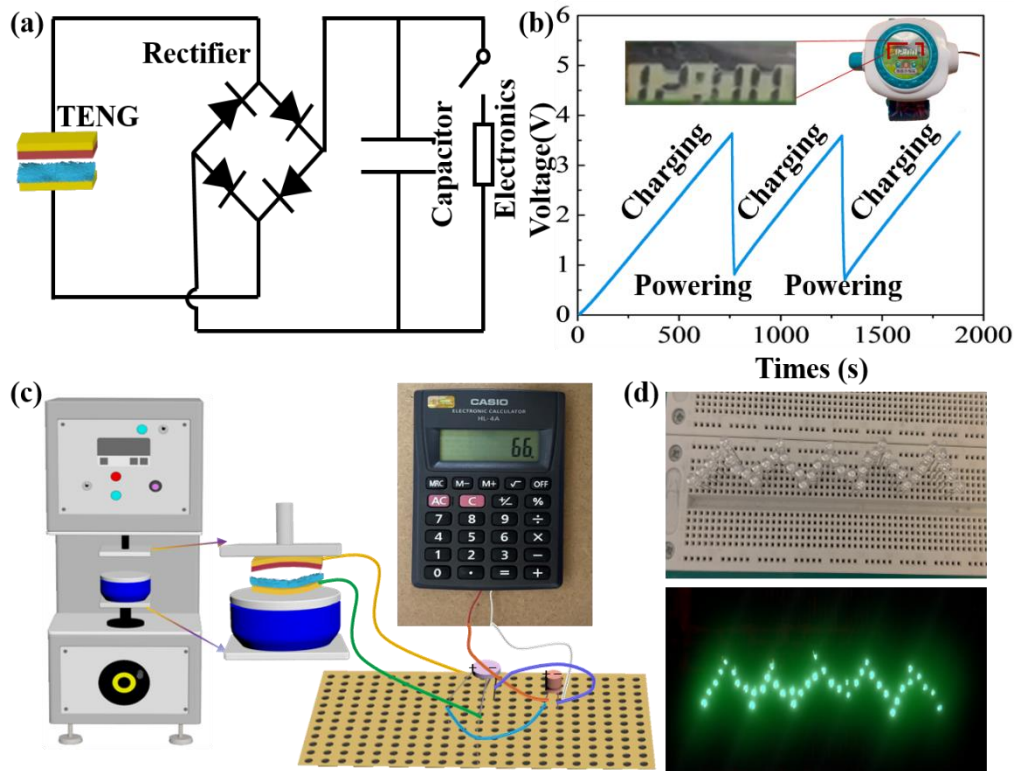


Fig.3. 19 Demonstrations of OL/PDMS TENG for energy harvesting: a. The equivalent circuit for charging/discharging of electronics; b. Charging and discharging process of a capacitor of 22 μF to power an electric watch; c. Powering a small calculator with a capacitor of 4.7 μF ; d. Lighting up 44 LEDs by OL/PDMS TENG

3.3.5 Applications of OL-TENG as Self-powered Wearable Sensors

Based on the flexible properties, the designed OL/PDMS TENG can also act as sensors for monitoring human body activities in a real-time and sensitive way.

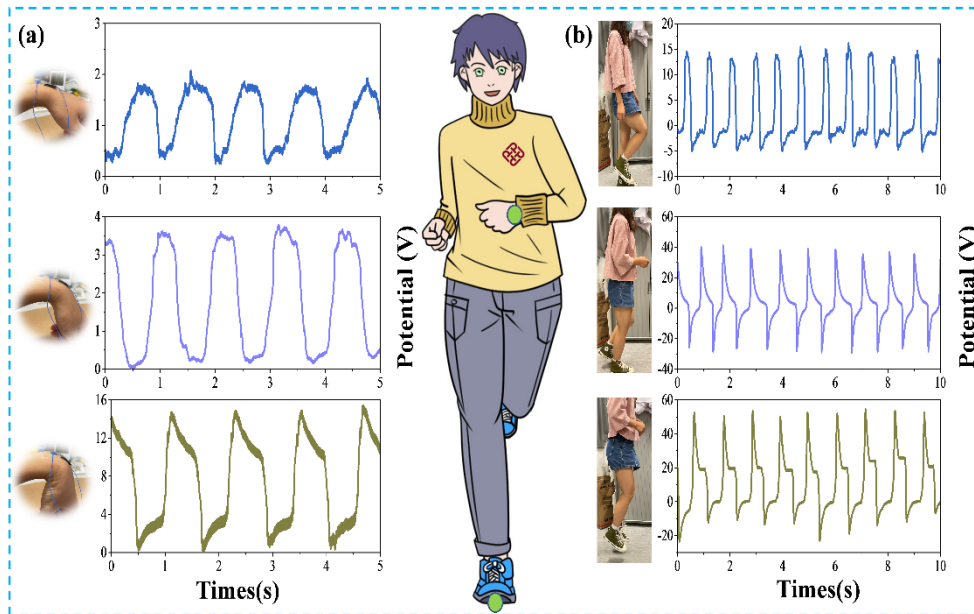


Fig.3. 20 Applications of OL/PDMS TENG as self-powered wearable sensors: a Monitoring of wrist bending angles by fixing OL/PDMS TENG on the wrist; b Monitoring of walking gestures by fixing OL/PDMS TENG under the shoes

For example, it has a good response to major joint motions as illustrated in Fig.3. 20a. By attaching the OL/PDMS TENG on the wrist, it can detect different wrist bending angles from 30° to 90° . With the increase of bending angle, the voltage output of OL/PDMS TENG has a gradual enhancement, which is ascribed to the increase in the contact area between the wrist and OL/PDMS TENG. It is notable that three kinds of signals are different, in which the 90° between the wrist and the OL/PDMS TENG is relatively sharper while the 30° of that are slightly broader. Reasons can be accounted by the fact that sharper force can cause stress concentration, leading a steeper signal on the 90° as compared with other angles. Meanwhile, the fabricated OL/PDMS TENG has great potential to distinguish walking gestures, such as walking, running or jumping shown in Fig.3. 20 b. As expected, similar voltage characteristic peaks can be found on each diagram curve when repeating the same walking mode, while the different walking modes are generating different voltage characteristic signals. It is noteworthy that jumping has the largest output electric performance among the three human movements, which is attributed to a more straightforward and strong contact-separate process,

making the characteristic peaks shaper and higher^{206, 207}.

3.4 Conclusion

In summary, three kinds of silkworm cocoon layer (SCL)/PDMS-TENGs naturally endowed with unique bulge structures have been successfully fabricated for the first time with great potential for self-powered energy harvesting and sensing for monitoring human movements. SS, considered as a waste due to immunological responses as implantation in vivo, remained intact on the SCL for the first time when fabricating silk-based TENGs. The proposed materials for designing TENGs are biodegradable and low-cost without any environmental concerns. Under the contact-separation mode, the peak open-voltage and short-current of OL/PDMS TENG with a size of $2 \times 2 \text{ cm}^2$ is 126 V and $3 \mu\text{A}$, respectively, almost 1.5-fold as that of IL/PDMS TENG and 1.2 times that of ML/PDMS TENG. The optimized OL/PDMS TENG could deliver an instantaneous power density of 216 mW/m^2 at a force of only 5 N at 3 Hz, surpassing many silk-based TENGs reported yet. Moreover, results demonstrated that the stacked effect of the SCL may block the transfer of electrostatic charges. In addition, frequency and applied pressure have been explored to better apply TENGs to daily scenarios. After 10,500 cyclic tests, it can still possess high and stable electric output performances, exhibiting good mechanical durability. By means of virtues such as great mechanical durability, the designed OL/PDMS TENG is further applied to power some low-power electronic devices, such as calculators and watches without extra power sources. Based on the flexibility of polymers, the OL/PDMS TENGs can be also viewed as good sensors to realize the full-range monitoring of physiological signals and joint motions in a rapid, real-time, and noninvasive manner. Therefore, the SCL/PDMS-TENGs will have great potential in bio-integrated areas, such as wearable biomedical devices and thermal control and simultaneously widen the selection of the materials for designing silk-based TENGs with intact SS retention.

CHAPTER 4 PVA/Silk Composite Membranes for Scalable Triboelectric Nanogenerators in Energy Harvesting and Sensing

4.1 Introduction

In the Internet of Things (IoT) era, green and sustainable energy demand has become increasingly significant in society accompanied by the dwindling reserves of fossil fuels²⁰⁸⁻²¹². TENG is deemed a burgeoning method for converting ubiquitous low-frequency mechanical energy into electrical energy with principles of triboelectrification and electrostatic induction^{12, 213-216}. By the emerging energy conversion technology of TENGs, silk has been gradually regarded as a promising and hot candidate applied to the fabrication of smart electronics owing to its excellent mechanical robustness, attractive air permeability, adaptable biodegradability, and ease of modification²¹⁷.

Silk, which is composed of SF enwreathed by a glue-like sericin (SS) in the form of a hierarchical structure with an estimated 18 layers (Fig.4. 1a), is derived from the silkworm cocoon, *B. mori*^{186, 218}. Interestingly, the hierarchical network structure embodies two aspects: (1) Multi-layers for the whole cocoon architecture: owing to the failure of SS, a silkworm cocoon could be peeled into a component layer followed by disparate content of SS and porosity, resulting in differentiated surface morphology and properties; (2) Graded structure for single silk: silk materials are semi-crystalline polymers composed of ordered domains containing crystallites in the majority of SFs interspersed with disordered amorphous domains mainly consisting of SSs. Notably, SF embraces countless nanofibrils while SS is typically composed of five layers displaying a differentiation of hydrophilic properties as a consequence of five levels embodied in the hierarchical network structures: 1) amino acid sequence, 2) secondary structure, 3) β -crystallites, 4) crystal networks or nanofibrils, and 5) nanofibril networks^{91, 219}. The hierarchical structure of silk materials is considered a multidomain

network containing a collection of single-domain networks²²⁰. However, silk sericin has been ignored and discarded as a waste from the textile industry, causing environmental pollution and a waste of natural resources. Silk sericin is a green adhesive and dispersant²²¹ and its abundant functional groups from variable amino acids composition allow sericin to be chemically modified and cross-linked to form versatile constructs. Recently, sericin has been widely used for biomedical applications, however, its applications in electronics are very limited^{221, 222}.

Based on the advantages of silk, considerable effort has been put into the exploration of high-output silk-based TENGs, such as silk-based electrospinning²⁴, membranes³², 3D-printing²²³, and hydrogels^{42, 134}, *etc.* For example, the electrospinning method by Kim *et al.*²⁴ and Jiang *et al.*²⁸ has been considered for design of silk fiber-based TENGs. Kim demonstrated the use of SF electrospun nanofiber-networked film as one tribolayer statically inducted with polyimide membrane. However, the power density of these SF nanofiber-based TENGs is 0.43 and 108.76 $\mu\text{W}/\text{cm}^2$, respectively, far from the requirements in actual applications. Meanwhile, silk-based membrane TENGs have been systematically explored, such as using regenerative SF film (RSFF) as one tribolayer³⁴, embedding conductive materials into regenerative SF solution to form a composite silk-based membrane^{32, 35, 224}, and incorporating silk-based powders into other matrix^{38, 118}, *etc.*, whose maximum instantaneous power density is approximately 300 $\mu\text{W}/\text{cm}^2$. Even though it presents higher power density over electrospinning silk-based TENG, the silk-based membrane TENGs still need further improvement, expanding their subsequent applications in various scenarios. Advanced fabrication technologies, such as 3D printing, have enabled the development of silk-based TENGs. A printed PS-TENG, for example, possessed a power density of 412 $\mu\text{W}/\text{cm}^2$ by integrating graphite-based interdigital electrodes into a thin layer of SF covered by a PDMS substrate³⁷. However, the low efficiency of 3D printing technology obstructs large-scale expansion from a sustainability perspective. Accordingly, easy approaches to constituent materials and the composite structure for silk-based TENGs need to be proposed and tailored to meet actual power requirements.

In general, the ability or inclination to attract or donate electrons is closely linked to the electron affinity (EA) of surface atoms. Halogen atoms are the most electronegative, having a high EA to accommodate additional electrons, particularly high-EA compounds of fluorine, including polyvinylidene fluoride (PVDF)²²⁵, fluorinated ethylene propylene (FEP)²⁰⁸, and polytetrafluoroethylene (PTFE)²²⁶. Despite being overlooked, fluoro-nylon materials display high flexibility and an appealing electron affinity. PVA has film-forming capacity owing to abundant hydroxyl functional groups, which donate electrons with high dielectric constant to form more tribo-positive surface polarity²²⁷.

Herein, silk-doped composite membranes were fabricated using one-pot method triboelectric with commercial fluoro-nylon film to prepare the enhanced TENG device, which is inspired by the hierarchical structure of silkworm cocoons. Specifically, PVA acted as an adhesive to combine the SF and SS is utilized to enhance the surface polarity. Sericin functions as a friendly binder is considered to tune the flexibility of the synthetic membrane. This preparation method is simple, scalable, facile, and cost-effective. The optimization process of the silk-based composite membrane was systematically examined. Moreover, the electric performance of the developed TENG was comprehensively investigated. This study provides a new idea for the development and utilization of high-performance protein-based triboelectric materials and offers promising prospects for the application of wearable electronics.

4.2 Methodology

4.2.1 Materials

Silkworm cocoons were purchased from the market. Silk sericin powder ($\geq 99.5\%$) was purchased from Macklin Co., Ltd. Copper/nickel-coated polyester fabric (CNF) was bought from the 3 M company. PVA (1788) was purchased from Dieckmann. Na_2CO_3 (99%, AR) and LiBr (99%) were purchased from Macklin Co., Ltd. Polydimethylsiloxane (PDMS) precursors consisting of a PDMS-based elastomer and

a curing agent was from Dow Corning (Sylgard 184). Dialysis membrane (MD77-14000) was purchased from Nantong Supin Equipment Co., Ltd. Fluoro-nylon was purchased from Shenma Group Co., Ltd., China (0.2 mm). Deionized (DI) water was used in all experiments. All reagents and materials were commercially available without further purification.

4.2.2 Preparation of SF Solution

SF solution was prepared through the methods previously reported²²⁸. Silkworm cocoons were first cut into pieces and then degummed in 5 g/L sodium carbonate at 120 °C for 1.5 h to remove the binding SS. Then, the obtained degummed SF fibers were rinsed with DI water and dried under ambient conditions. Next, the degummed SF fibers were dissolved in 9.3 M lithium bromide (LiBr) solution at 60 °C for 6 h. The LiBr-SF mixture was then purified by dialysis against DI water with a dialysis membrane for 72 h to remove LiBr and obtain the preliminary SF solution. Finally, the SF solution was purified through microfiltration and stored at 4 °C before use. The whole process was conducted in room temperature (28 ~33 °C, summer, Hong Kong), the humidity was 70 %~90 % with a low-pressure area, and the air circulation is excellent in the chemistry lab. In addition, the prepared solution was immediately encapsulated without any dust particles.

4.2.3 Preparation of SF/SS/PVA (SFP) Membrane

To fabricate the SFP membrane, 1 g of water-soluble PVA precursor was added to 10 mL of SF solution. The mixture was heated and stirred at 90 °C for 40 min before cooling down to 60 °C. Different proportions of SS powders were then mixed into the SF/PVA solution to form the membranes shown in Fig.4. 1b. The membranes are named PVA/SF, SFP-S-0.87%, SFP-S-1.72%, SFP-S-2.56%, SFP-S-3.39%, SFP-S-4.20%, SFP-S-5.00%, SFP-S-5.79%, SFP-S-6.56%, and SFP-S-7.32%, respectively.

Table 4. 1 Composition and thickness of the SFP membranes

membrane	SS (%/g)	SF (%/g)	PVA (%/g)	Water (%/g)	Thickness (mm)
----------	-------------	-------------	--------------	----------------	-------------------

PVA/SF	0(0)	3.51(0.4)	8.77(1)	87.72(10)	0.169±0.004
SFP-S-0.87%	0.87(0.1)	3.47(0.4)	9.00(1)	86.66(10)	0.179±0.001
SFP-S-1.72%	1.72(0.2)	3.45(0.4)	8.62(1)	86.21(10)	0.178±0.003
SFP-S-2.56%	2.56(0.3)	3.42(0.4)	8.55(1)	85.47(10)	0.189±0.004
SFP-S-3.39%	3.39(0.4)	3.39(0.4)	8.47(1)	84.75(10)	0.175±0.000
SFP-S-4.20%	4.20(0.5)	3.36(0.4)	8.40(1)	84.03(10)	0.183±0.007
SFP-S-5.00%	5.00(0.6)	3.33(0.4)	8.33(1)	83.33(10)	0.188±0.009
SFP-S-5.79%	5.79(0.7)	3.31(0.4)	8.26(1)	82.64(10)	0.198±0.003
SFP-S-6.56%	6.56(0.8)	3.28(0.4)	8.20(1)	81.97(10)	0.173±0.003
SFP-S-7.32%	7.32(0.9)	3.25(0.4)	8.13(1)	81.31(10)	0.201±0.001

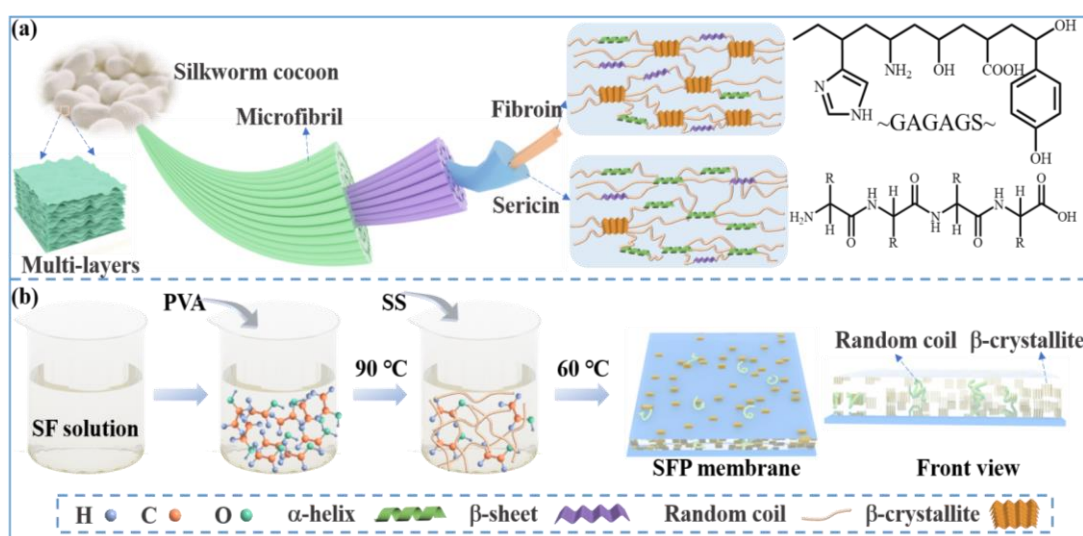


Fig.4. 1 Design and fabrication of the SFP and SFPAG membrane: a. Illustration of the hierarchical structure of silkworm cocoon; b. Synthesis process of the SFP membrane

4.2.4 Fabrication of SFP/F-TENGs

The SFP/F-TENG was fabricated using the SFP membrane as the negative friction layer and commercial fluoro-nylon as the positive one. Both tribolayers were then cut into 2 cm × 2 cm dimensions for optimal effectiveness.

4.2.5 Characterizations

Field Emission Scanning Electron Microscope (SEM, Tescan MIRA) was used to

characterize the morphology of SFP membranes operating at an accelerating voltage of 5 kV. The rough surface morphology of SFP membranes was conducted by the 3D Laser Scanning Microscope (KEYENCE VK-X200). X-ray diffraction (XRD) pattern (Rigaku SmartLab) was used to identify the crystalline phase in the SF fibril samples with scanning from 5 to 80° (2 θ) at a speed of 0.04°/s (λ = 0.154 nm). The simulation was conducted with COMSOL software. The dielectric constant was measured using a precision LCR meter (Keysight E4980A). The short-circuit current and short-circuit charge transfer were recorded on the electrometer (Keithley 6514, Tektronix). The output voltage was measured by an oscilloscope (Keysight InfiniiVision DSOX3024T).

4.3 Results and Discussion

4.3.1 Structure and Working Principle of Fabricated SFP/F-TENGs

The working principles of the fabricated SFP/F-TENG are based on contact triboelectrification and electrostatic induction¹². Four working modes have been developed including vertical contact-separation mode, single-electrode mode, lateral-sliding mode, and freestanding layer mode²⁰⁸. SFP/F-TENGs work in the form of the vertical contact-separation mode. In the first stage, two tribolayers are forced to be in contact with each other accompanied by the generation of equal electrons due to their different electron affinities, without electrons flowing because of contact equilibrium. The surfaces of fluoro-nylon and the composite membrane become excited by opposite static charges obtaining electrons on fluoro-nylon and losing electrons on the composite membrane. For the second stage, the two triboelectric layers begin to separate from each other, inducing a voltage potential (V) between the two friction layers with increased distance. Electrons flow through the external circuit, and the current increasingly reaches a peak value at the proper distance, then drops with the increase of distance²²⁹. In the third stage, when the applied force is completely released, the transferred charges reach an equilibrium state again without current in the external circuit. At the final stage, when they are pressed together again, the electrostatically induced charge flows back through the external load to compensate for the voltage

potential, generating a converse current. This iterative process continuously generates the alternating current (AC) signal, as depicted in Fig.4. 2.

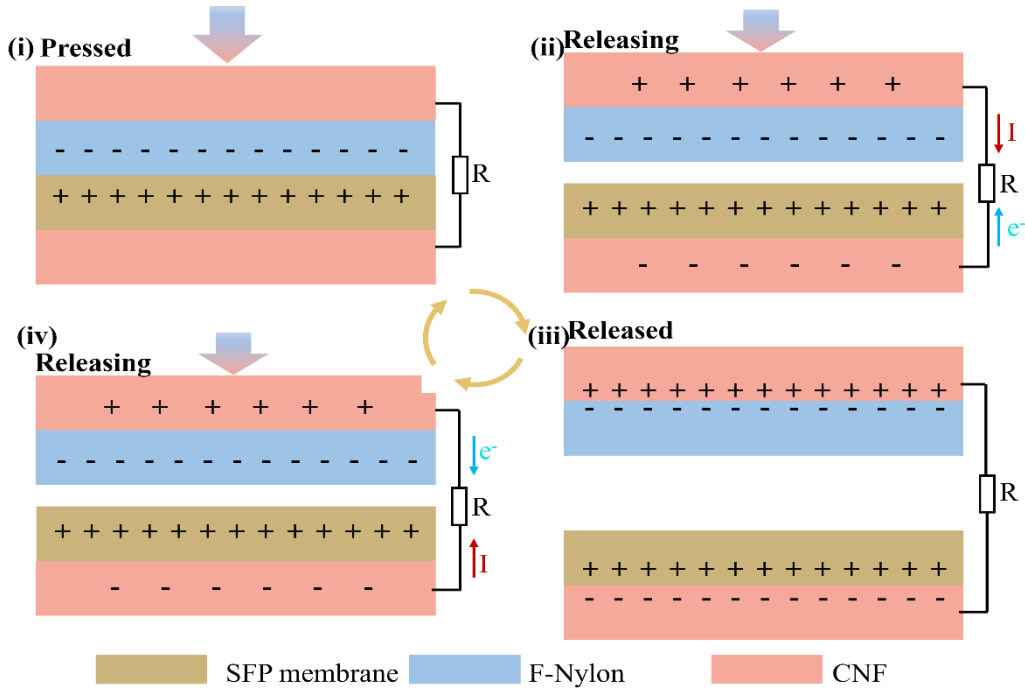


Fig.4. 2 Working principles of the fabricated SFP/F-TENGs

Fig.4. 3 shows the relationship of the dielectric constant regarding SFP membranes endowed with different SS contents. The calculation of the dielectric constant is based on the formula:

$$C = \frac{\epsilon S}{4\pi k d} \quad (4-1)$$

The PVA/SF membrane without SS has an estimated dielectric constant value of 2, which is much lower than those with SS powders added. It is obvious that the dielectric constant significantly increases when the ratio of SS changes from 0.87% to 3.39%. However, when an excessive amount of SS powders is added to the composite membrane from 4.2% to 7.32%, the dielectric constant dramatically decreases. This is attributed to the fact that the SF maintains its crystal structure, while the blending of SS and PVA facilitates the formation of the hydrogen bonds network between the hydroxyl

groups of PVA and the polar amino acid residues of sericin, which further form a highly integrated net structure²³⁰. However, redundant SS powders retard the crystallization of the SF solution²³¹, corresponding to the reduction of the dielectric constant.

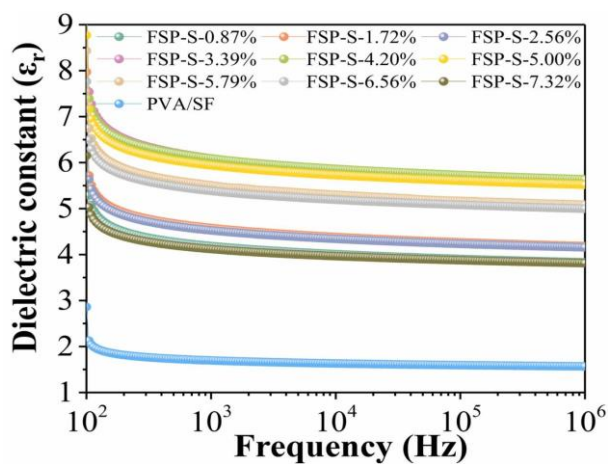


Fig.4. 3 Dielectric constant of SFP membranes

4.3.2 Characterization of the Composite SFP Membranes

The high flexibility of in-plane SFPs was clearly demonstrated under an exogenous force, as shown in Fig.4. 4.

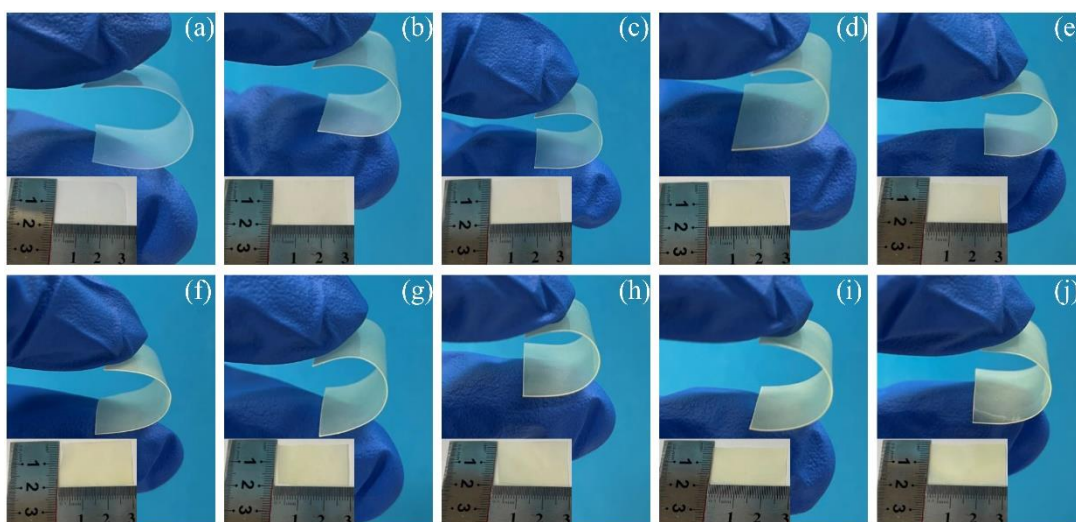


Fig.4. 4 Illustration of the flexibility of SFP membranes. a PVA/SF; b SFP-S-0.87%; c SFP-S-1.72%; d SFP-S-2.56%; e SFP-S-3.39%; f SFP-S-4.20%; g SFP-S-5.00%; h SFP-S-5.79%; i SFP-S-6.56%; j SFP-S-7.32%

SFP-S-5.79%; i SFP-S-6.56%; j SFP-S-7.32%

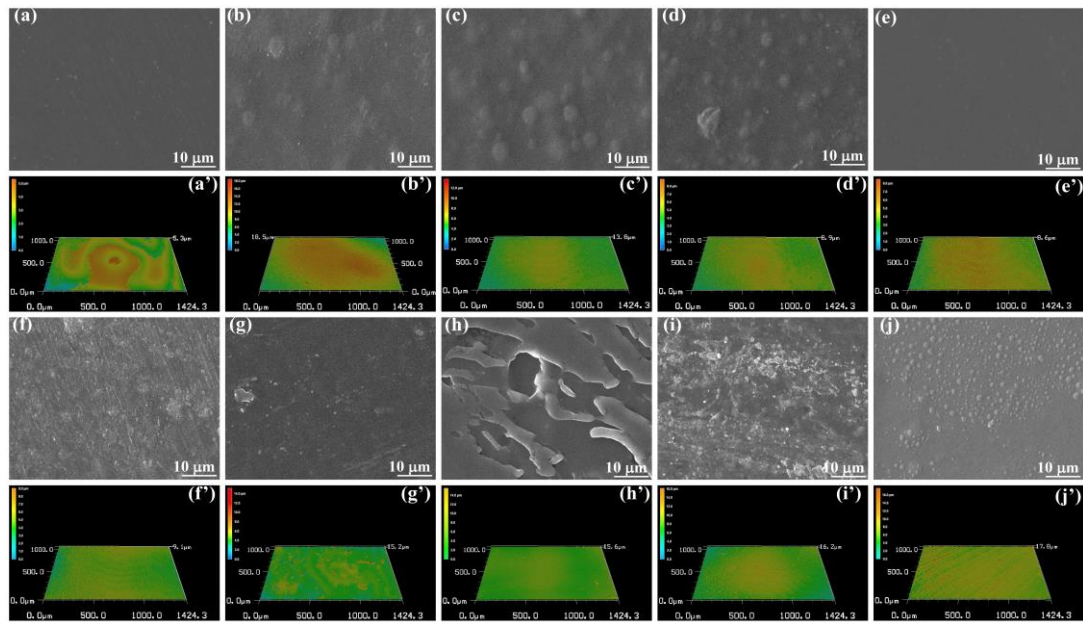


Fig.4. 5 Surface morphology of the composite SFP membranes. SEM Surface morphology of a. PVA/SF; b. SFP-S-0.87%; c. SFP-S-1.72%; d. SFP-S-2.56%; e. SFP-S-3.39%; f. SFP-S-4.20%; g. SFP-S-5.00%; h. SFP-S-5.79%; i. SFP-S-6.56%; j. SFP-S-7.32%; Surface roughness of (a') PVA/SF; (b') SFP-S-0.87%; (c') SFP-S-1.72%; (d') SFP-S-2.56%; (e') SFP-S-3.39%; (f') SFP-S-4.20%; (g') SFP-S-5.00%; (h') SFP-S-5.79%; (i') SFP-S-6.56%; (j') SFP-S-7.32%

SEM analysis was utilized to confirm the differentiated morphologies of the formed SFP membrane. Fig.4. 5 illustrated the surface morphologies of the SFP membrane, where noticeable variations in the structure were observed among the different levels of SS content. The surface morphology of the SFP substrate without any coating of SS appears relatively flat (Fig.4. 5a). By adding SS powders, the surface morphology changes significantly and becomes rougher with irregular and non-uniform SS bulges, as illustrated in Fig. 4.5 b-d, which is possibly attributed to the incomplete dispersion of globulin¹¹⁸. Further addition of SS powders like the SFP-S-3.39% membrane (Fig.4. 5e) shows relatively regular and uniform protrusions, indicating an improvement in the dispersion of SS particles within the PVA/SF matrix. However, adding more SS

powders may disrupt the equilibrium, leading to the reformation of non-homogeneous and irregularly shaped protrusions (Fig.4. 5f-i). When excessive amounts of SS powders are incorporated, extensive molecular aggregation and clustering may occur (Fig.4. 5j). To further elaborate the relationship between the surface morphology and SS powder content, a surface roughness test was conducted in Fig.4. 5a'~ j'. Notably, all modified SFP membranes show a rougher surface than the PVA/SF membrane. With the addition of SS powders (0~3.39%), the surface roughness decreased owing to the enhanced dispersion inside the PVA/SF matrix. However, when the SS particles increased from 4.20% to 7.32%, the roughness started to increase due to the agglomeration on the surface caused by an excessive quantity of sericin that needs to be dispersed.

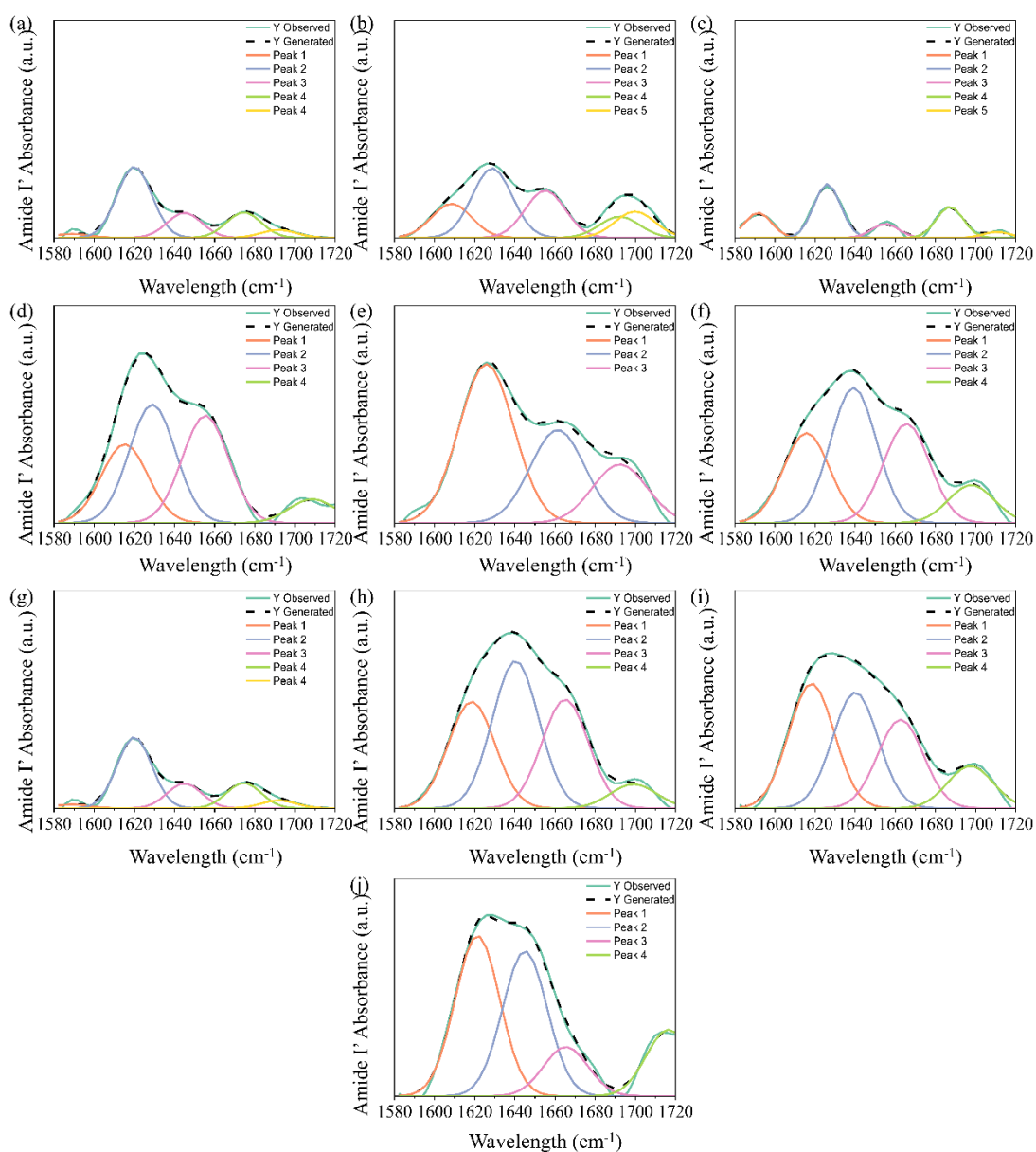


Fig.4. 6 Deconvolution of the amide I region (1600~1700) of FTIR spectra of SFP membranes. a PVA/SF; b SFP-S-0.87%; c SFP-S-1.72%; d SFP-S-2.56%; e SFP-S-3.39%; f SFP-S-4.20%; g SFP-S-5.00%; h SFP-S-5.79%; i SFP-S-6.56%; j SFP-S-7.32%

Table 4. 2 Relative contents of secondary structures through FTIR test

Membrane	Random coil	β -sheet	β -turn	Others
PVA/SF	18.73	53.31 wa	25.06	2.90
SFP-S-0.87%	23.85	35 sb/13.26 wa	10.72	17.17
SFP-S-1.72%	10.77	41.43 sb	23.90	23.90
SFP-S-2.56%	32.66	36.06 sb/23.98 wa	0	7.29

SFP-S-3.39%	29.94	51.18 sa	18.88	0
SFP-S-4.20%	37.31	35.32 wa	27.37	0
SFP-S-5.00%	40.09	44.97 wa	14.94	0
SFP-S-5.79%	38.08	33.79 wa	28.13	0
SFP-S-6.56%	31.18	44.95 wa	23.87	0
SFP-S-7.32%	34.43	38.09 wa	11.68	15.8

wa: Weak Intermolecular beta-sheets; sb: Strong Intramolecular beta-sheets

In addition, the secondary structure of SFP membranes is obtained by deconvolution in FTIR (Fig.4. 6), and then we can get the content of random coil, β -sheet, β -turn, and others in Table 4. ²³². FTIR data show peaks at 1616–1621 (aggregate beta-strand/weak intermolecular β -sheets), at 1622–1627 (strong intermolecular β -sheets), at 1628–1637 (strong intramolecular β -sheets), at 1647–1655 (random coils), at 1663–1696 (β -turn), and 1697–1703 (weak intermolecular β -sheets), respectively²³². The PVA/SF membrane only has weak intermolecular beta-sheets, which are formed through hydrogen bonding between the peptide chains of adjacent protein molecules. However, with the addition of SS from 0.87% to 2.56%, strong intramolecular beta-sheets start to form through hydrogen bonding between different regions of the same protein chain, along with a certain amount of weak intermolecular beta-sheets. The presence of weak intramolecular β -sheets alongside strong intermolecular β -sheets suggests a less ordered and less densely packed arrangement of protein chains. It is noteworthy that when the SS content is 3.39%, 51.18 % of strong intermolecular β -sheets form, indicating a highly organized and tightly packed arrangement of the silk protein chains, which results in a high degree of structural order and crystallinity within the material. With continuous addition of SS powders from 4.2% to 7.32 %, only weak intermolecular beta-sheets are formed, and the possible reason is that redundant SS powders retard the crystallization of the SF solution²³¹.

4.3.3 Electrical Performance

Firstly, a comparatively electrical performance of SFP/F TENG was investigated with an applied force of 5 N at a fixed 3 Hz. It is noted that as the concentration of SS

increases from 0.87% to SF: SS=7.32%, the voltage of SFP/F-TENG gradually rise from around 300 V (0.87%) to 494.47 V (3.39%), before falling to 350 V at 7.32%, as displayed in Fig.4. 7a. Similarly, an increase in current from 5 μ A (0.87%) to 7.8 μ A (3.39%) is observed. However, if the SS concentration is continuously increased to reach a ratio of 3.39%, the current shows a declining trend, as presented in Fig.4. 7b. These results consistently indicate that the proposed SFP/F-TENG has the highest charge transfer in the ratio of 3.39%. Additionally, all SFP/F-TENGs show enhanced outputs compared to SF/PVA-TENG.

Our surmise will be further elucidated as follows. Firstly, the idea of incorporating SS into the SF solution is based on the natural hierarchical structure of silkworm cocoons¹⁸⁶. Silkworm cocoons are composed of multiple layers, where the two parallel SF fibers are enclosed by SS coating in both the inter-layer and intra-layer²⁵. Typically, SF makes up about 70–80 wt % of the cocoon, while SS accounts for 20-30 %, resulting in an ideal SF: SS ratio of 3:1 during the formation of natural silkworm cocoons, which has been refined over time. However, However, the best electrical performance is achieved with a 1:1 (3:3) ratio of SF to SS as illustrated in Table 4. 1, which is higher than the natural SF: SS ratio of 3:1. This is because SF possesses a high ordered crystalline structure with predominantly non-polar amino acid, while SS has an amorphous structure with 75 % polar amino acids and 25 % non-polar amino acids in the side chain R group. When PVA, a water-soluble synthetic polymer containing hydroxyl, is mixed into the SF matrix, it interacts slightly with the carboxyl and amino group present in the SF solution and extensively with the polar amino acid residues of SS. This allows a highly organized and tightly packed arrangement of the silk protein chains (SFP-S-3.39%), which results in a high degree of structural order and crystallinity within the material²³⁰, indicating an improved piezoelectric effect, as illustrated in Fig.4. 7c and Table 4. 2.

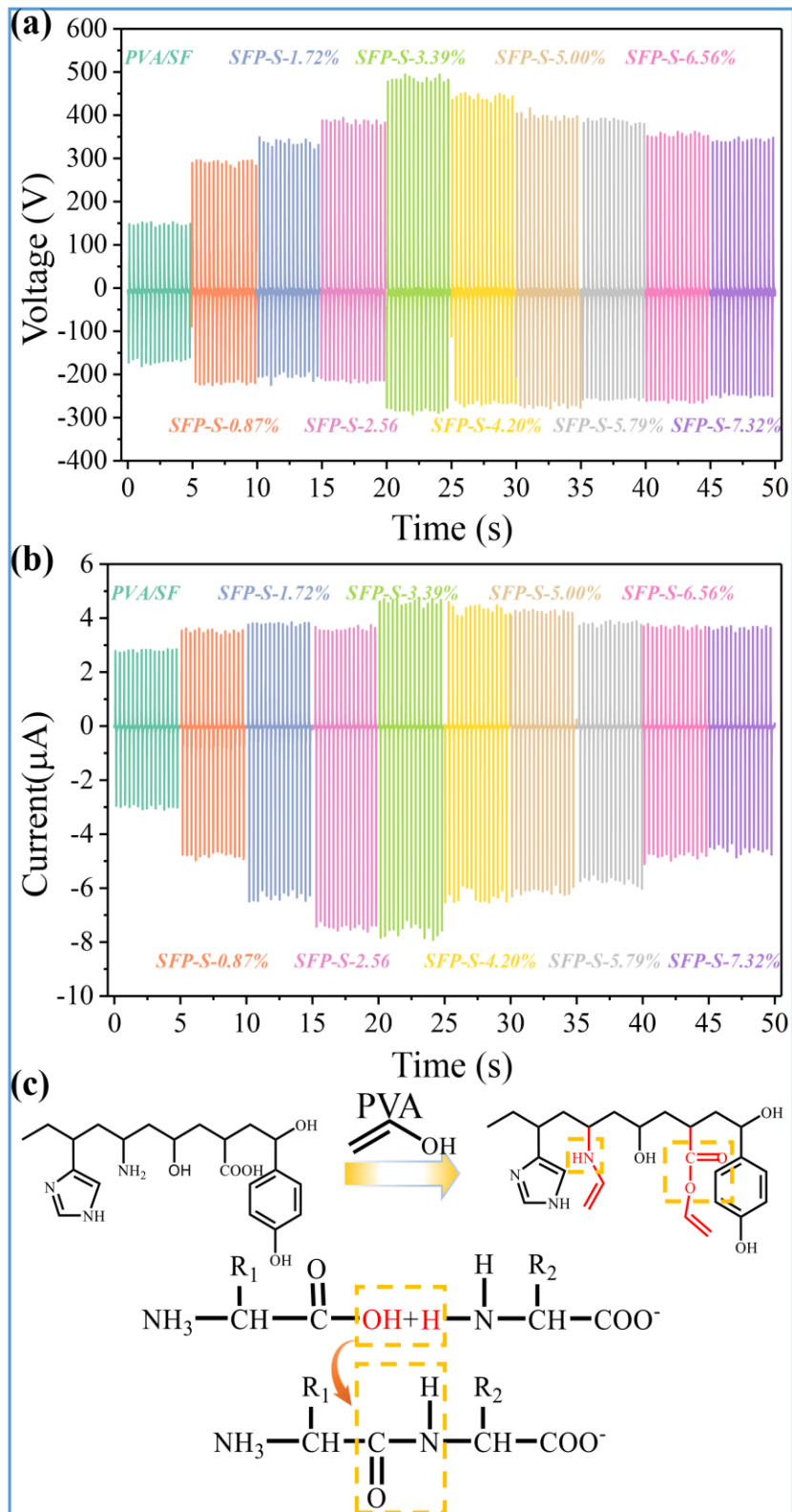


Fig.4. 7 Electrical performances of SFP/F TENGs under different SS concentrations. a

V_{oc} and b I_{sc} of SFP/F-TENGs; c Illustration of the interaction between PVA with SF and SS

Furthermore, based on the results displayed in Fig.4. 5, it can be observed that the surface morphology of the SFP-S-3.39% film appears small and regular protrusions, which may enhance triboelectric properties by reducing the resistance of charge transport by providing a large surface area for electron transferring or minimizing the distance between two friction layers. However, if the bulges are too large or irregular (Fig.4. 5b-d, f-j), it may create non-uniformities in surface morphology that would impede electron transfer.

Considering the optimized triboelectrification and dielectric properties, the operational conditions were examined, specifically the applied force and frequency, to enhance the output performance further. The current values of the SFP-S-3.39%/F-TENGs increased with the frequency rising from 1 Hz to 4 Hz, ranging from 1 μ A to 13 μ A, as illustrated in Fig.4. 8a. Similarly, the voltage increased from 88 V to 650 V, and the charge rose from 36 nC to 45 nC. The enhanced electrical voltage can be attributed to three primary factors. First, the acceleration of external electron flow occurs as increased frequency and applied force intensify the triboelectric interactions, resulting in a more rapid electron exchange across interfaces. This acceleration ensures a more substantial separation of charge and consequently elevates the voltage output. Second, the incomplete neutralization of surface charges results from disparities in work functions between materials, leading to persistent residual charges that amplify the electric field strength between surfaces. This incomplete neutralization maintains high voltage levels, enhancing the efficiency of energy conversion. Finally, the facilitation of charge transfer combined with the reduction in peak current duration optimizes charge migration pathways at the interface. These factors collectively contribute to a significant augmentation in electrical output magnitude²³³. Similarly, the current, voltage and charge values surged as the applied force increased from 1 N to 10 N (Fig.4. 8d, e, and f). This increase in voltage can be explained by enhanced induction electrification, which occurs due to the closer proximity of the friction layer induced by

the greater force. However, it is noteworthy that when the applied force reaches 20 N, the current, voltage, and charge remain nearly constant. This phenomenon is likely attributable to the saturation of electrons within the system.

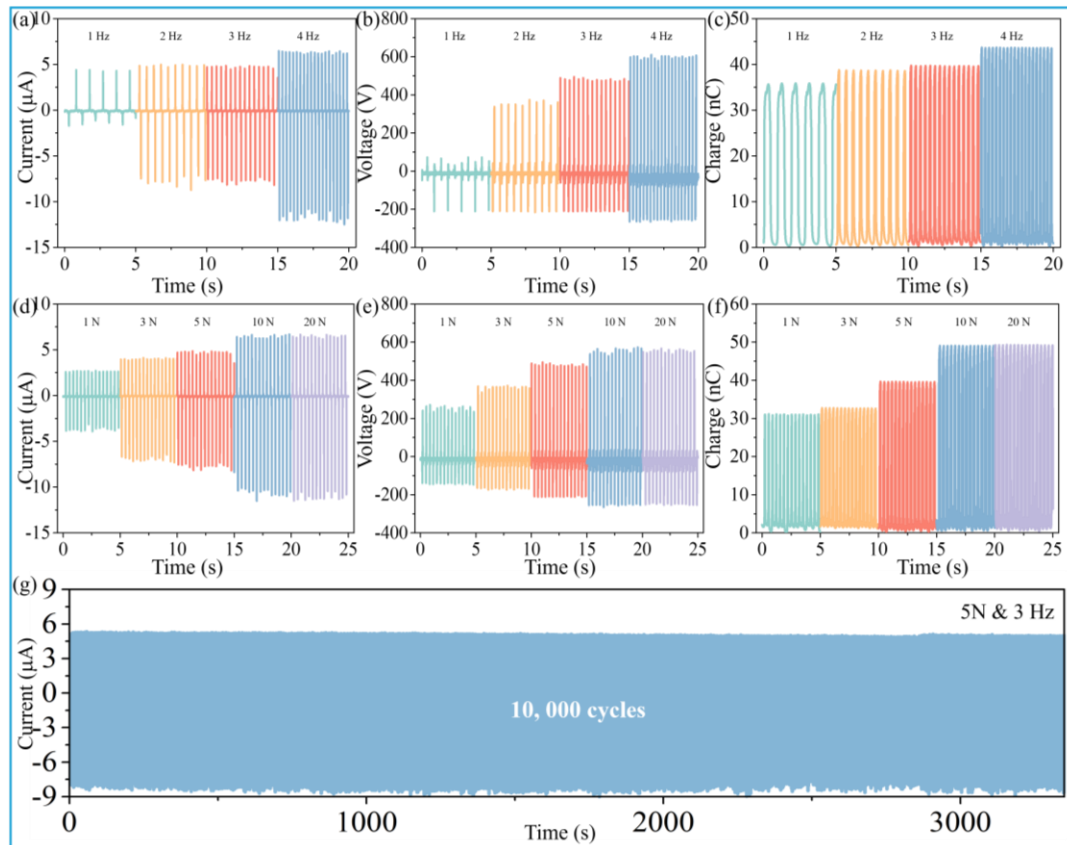


Fig.4. 8 Electrical output performance of the SFP/F-TENGs: a. Current, b. Voltage, and c. Charge of the SFP-S-3.39%/F-TENGs under a fixed applied force of 5 N; d. Current, e. Voltage, and f. Charge of the SFP-S-3.39%/F-TENGs under fixed frequencies of 3 Hz; g. Durability and stability test of MFS/F-SETENGs for 10,000 cycles

Durability is critical for ensuring the adaptability and suitability of applications across various scenarios. A durability test, as depicted in Fig.4. 8g, demonstrated that the voltage output of the SFP-S-3.39%/F-TENGs remained remarkably stable after 10,000 cycles of testing, indicating good wear resistance. This robustness highlights its potential for long-term application in practical scenarios.

4.3.4 Applications of the SFP-S-3.39%/F-TENGs as Energy Harvesters

The effectiveness of SFP-S-3.39%/F-TENG as a power source was evaluated. Power density is a critical parameter for assessing the performance of TENG devices in energy harvesting applications. By connecting the SETENG to various external loads ranging from 0.1 MΩ to 1,000 MΩ, an instantaneous power density of 7.4 W/m² was achieved, calculated using the formula $P=U^2/RA$ at an optimal resistance of 50 MΩ, as shown in Fig.4. 9a, where U represents the output voltage, R denotes the external load resistance, and S indicates the effective contact area.

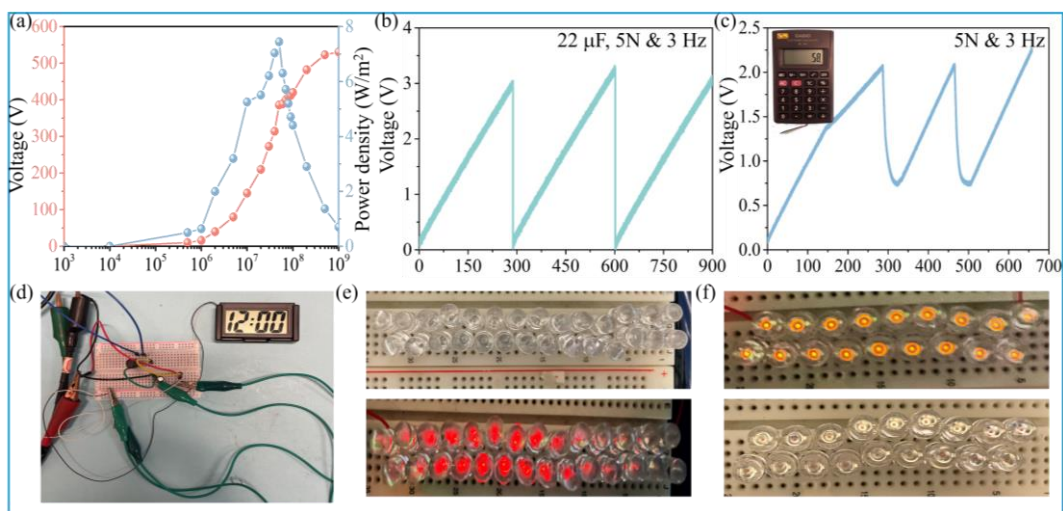


Fig.4. 9 Application of the SFP-S-3.39%/F-TENGs considered as an energy harvester: a. Power density of SFP-S-3.39%/F-TENG with different external load resistance; b. The powering and charging curves; c. The SFP-S-3.39%/F-TENGs charges a small calculator; d. A diagram that the SFP-S-3.39%/F-TENG powering a clock; e and f: the SFP-S-3.39%/F-TENG can power different LED lights

With high power density, capacitors were charged via a rectifier, converting the AC generated by the TENG into DC for powering electronic devices. Fig.4. 9b presents the powering and discharging curves of the SFP-S-3.39%/F-TENG. Notably, the device can rapidly reach 3 V within 280 seconds, and the stored energy can be promptly released when connected with metals. As demonstrated in Fig.4. 9c, SFP-S-3.39%/F-TENG can charge a 22 μF capacitor to 2.2 V in just 300 seconds. Additionally, the

converted direct current can power a variety of electronic devices, such as an electronic calculator (Fig.4. 9c) and a digital timer (Fig.4. 9d). The detailed working conditions and wiring are illustrated in Fig.4. 9d. Furthermore, by directly connecting the SFP-S-3.39%/F-TENG, various types of LED lights can be powered (Fig.4. 9e and f), demonstrating their adaptability in different environments. These findings underscore the significant potential of our TENG for sustainable self-powered systems in wearable electronics.

4.3.5 Applications of the SFP/F-TENGs as Sensors

Owing to its excellent flexibility and extensibility, our SFP/F-TENGs are well-suited for monitoring a diverse range of hand gestures. Primarily, they function as pressure sensors. These sensors operate on the principles of triboelectrification and electrostatic induction, where mechanical stress applied by the fingers facilitates charge transfer between the electrodes. When pressure is applied or released, variations in the contact area and separation distance between the triboelectric layers generate an alternating current. The resulting output voltage signals are directly proportional to the magnitude of the applied pressure, enabling the TENG to effectively convert mechanical stimuli into electrical signals. As illustrated in Fig.4. 10a and b, the application of pressure using two fingers results in higher voltage outputs, demonstrating the sensor's sensitivity and effectiveness in capturing dynamic pressure changes.

By fixing the SFP/F-TENGs at the wrist, different bending angles of the wrist will generate distinct voltage signals, which can be used to monitor the wrist's flexion at various degrees, such as small angles and large angles (Fig.4. 10c and d). Specifically, a bending angle of a small angle produces a voltage of 40 V and large bending angle generates a voltage of 60 V. Notably, the voltage peak at small angle is relatively broad. At the same time, the signal becomes increasingly sharper as the bending angle increases. This capability arises from the changes in bending angles, which affect the signal amplitude and shape.

Our designed SFP/F-TENGs can be applied to various parts of the human body,

including fingers, as illustrated in Fig.4. 10e and f. When attached to fingers, the bending motion generates a voltage signal, similar to the detection mechanism for wrist movements. This occurs because the bending of the fingers causes changes in the contact area and separation distance between the triboelectric layers, producing an electrical signal that corresponds to the motion. This capability highlights the versatility of our TENGs in effectively capturing and translating different types of mechanical movements into electrical signals for practical applications in motion detection and wearable technology.

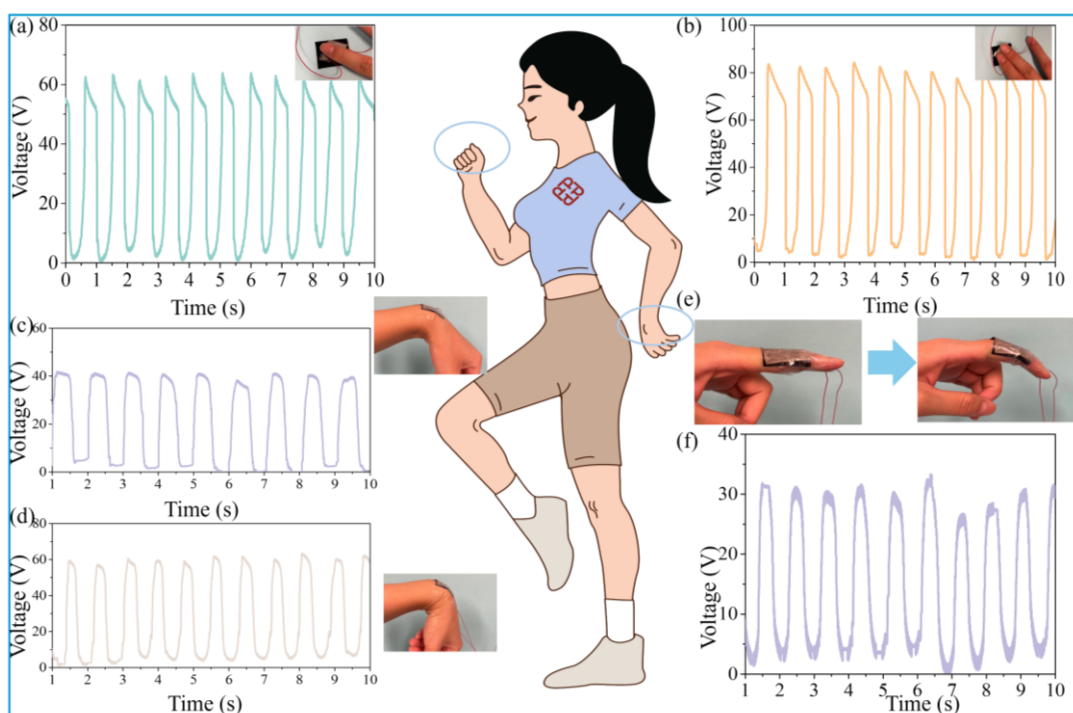


Fig.4. 10 The applications of SFP-S-3.39%/F-TENG as a self-powered wearable sensor for human motion monitoring: Pressure sensor of different fingers: a. One finger pressure; b. Two fingers pressure; Wrist motion detection at different angles: c. Small angles; d. Large angles; e. Schematic diagram of bending fingers; f. Electrical signals of bending fingers

4.4 Summary

In summary, this chapter has demonstrated the successful design and fabrication of silk-

doped composite membranes (SFP) using a straightforward and cost-effective one-pot method that utilizes triboelectric interactions with commercial fluoro-nylon film to create an enhanced TENG device. Inspired by the hierarchical structure of silkworm cocoons, the study employed PVA as an adhesive to integrate SF, while SS enhanced surface polarity and tuned the membrane's flexibility. The examination of the optimization process and electric performance of the TENG device underscores the potential of high-performance, protein-based triboelectric materials. This research offers innovative pathways for the development of wearable electronics, broadening the prospects for sustainable and efficient energy solutions in this field.

CHAPTER 5 High-Performance Triboelectric Nanogenerators for Energy Harvesting and Sensing Based on Silver Nanowires-Enhanced Silk Composite Membranes

5.1 Introduction

Silk has recently demonstrated a promising application potential in wearable electronic devices owing to its attractive electron affinity. However, natural silk possesses poor extensibility, and fabricating high-performance silk-based TENGs remains a challenge.

In this chapter, a facial method is proposed to construct the SF/sericin (SS)/PVA/AgNWs/fluoro-nylon-TENG (SFPAG/F-TENG), which simultaneously achieves high electric outputs and remarkable flexibility with long-lasting durability. By employing SS rich in the amorphous domain and AgNWs with high electric conductivity, our proposed SFPAG/F-TENG can achieve a maximum voltage of 745 V and a current of 22.5 μA with a size of $2\times 2\text{ cm}^2$ at a load of 5 N at 3 Hz. This results in an ultrahigh power density of 760 $\mu\text{W}/\text{cm}^2$, which exceeds most silk-based TENGs reported recently. The potential mechanism of enhanced electrical outputs was also analyzed. The constructed device not only demonstrates desirable mechanical performance like excellent flexibility, extensibility, and wear resistance after 30,000 cycles but also possesses self-sensing capabilities, making it an intelligent device for monitoring human gestures and powering various commercial electronics.

5.2 Methodology

5.2.1 Materials

Silkworm cocoons were purchased from the market. Silk sericin powder ($\geq 99.5\%$) was purchased from Macklin Co., Ltd. Copper/nickel-coated polyester fabric (CNF) was bought from the 3 M company. Absolute alcohol ($\geq 99.5\%$, ACS reagent) was purchased from Sigma-Aldrich. AgNO_3 ($>99\%$), PVP ($M_w=1300000$), and FeCl_3 (98%) were

purchased from Aladdin Chemical Reagent. Ethylene glycol (>99%, GC) and PVA (1788) were purchased from Dieckmann. Na₂CO₃ (99%, AR) and LiBr (99%) were purchased from Macklin Co., Ltd. Polydimethylsiloxane (PDMS) precursors consisting of a PDMS-based elastomer and a curing agent was from Dow Corning (Sylgard 184). Dialysis membrane (MD77-14000) was purchased from Nantong Supin Equipment Co., Ltd. Fluoro-nylon was purchased from Shenma Group Co., Ltd., China. Deionized (DI) water was used in all experiments. All reagents and materials were commercially available without further purification.

5.2.2 Preparation of SF Solution

SF solution was prepared through the methods previously reported²²⁸. Silkworm cocoons were first cut into pieces and then degummed in 5 g/L sodium carbonate at 120 °C for 1.5 h to remove the binding SS. Then, the obtained degummed SF fibers were rinsed with DI water and dried under ambient conditions. Next, the degummed SF fibers were dissolved in 9.3 M lithium bromide (LiBr) solution at 60 °C for 6 h. The LiBr-SF mixture was then purified by dialysis against DI water with a dialysis membrane for 72 h to remove LiBr and obtain the preliminary SF solution. Finally, the SF solution was purified through microfiltration and stored at 4 °C before use. The whole process was conducted in room temperature (28 ~33 °C, summer, Hong Kong), the humidity was 70 %~90 % with a low-pressure area, and the air circulation is excellent in the chemistry lab. In addition, the prepared solution was immediately encapsulated without any dust particles.

5.2.3 Synthesis of AgNWs

AgNWs were synthesized following the approach reported previously²³⁴. Typically, ethylene glycol (EG) (45 mL) was preheated in a boiling flask-3-neck in an oil bath at 150 °C for around 1 h with continuous magnetic stirring. Then, 2 mL of FeCl₃ solution (0.004 M) was added to the flask. After 15 min, 15 mL of AgNO₃ solution (0.5 M) was injected into the flask using a syringe pump. Then, 45 mL of PVP solution (0.147 M) was added to the flask and left for 6 h. Afterward, the reaction was cooled down to room

temperature with a water bath. For the purification step, the synthesized AgNWs were dispersed in ethanol and acetone and centrifuged three times. Finally, the purified AgNWs were dispersed in ethanol (10 mg/mL) for use in TENG fabrication in the next step.

5.2.4 Preparation of SF/SS/PVA/AgNWs Membrane (SFPAG)

Water-soluble PVA precursor (1 g) was added to 10 mL of prepared SF solution. The resulting mixture was heated and stirred at 90 °C for 40 min, followed by natural cooling to 60 °C. Then, the optimized amount of SS powders was added into the mixture, with different amounts of AgNWs subsequently blended with the solution, which was then heated and stirred in an oil bath at 60 °C for 2 h. After that, the mixture was sonicated for 20 min to ensure complete dispersion of AgNWs. Finally, a petri dish was used to form the SFPAG membrane, as depicted in Fig.5. 1. The detailed composition and thickness of SFPAG membranes were supplied in Table 5. 1. The membranes are named SFPAG-Ag-0.21% or FSPAG-Ag-0.21%, SFPAG-Ag-0.37% or FSPAG-Ag-0.37%, SFPAG-Ag-0.48% or FSPAG-Ag-0.48%, SFPAG-Ag-0.57% or FSPAG-Ag-0.57%, and SFPAG-Ag-0.64% or FSPAG-Ag-0.64%, respectively.

Table 5. 1 Composition and thickness of the SFPAG membranes

membrane	SS (%/g)	SF (%/g)	PVA (%/g)	AgNWs (%/g)	Ethanol (%/g)	Water (%/g)	Thickness (mm)
SFP-S-3.39%	3.39(0.4)	3.39(0.4)	8.47(1)	0	0	84.75(10)	0.175±0.000
SFPAG-Ag-0.21%	2.81(0.4)	2.81(0.4)	7.03(1)	0.21(0.03)	16.87(2.4)	70.27(10)	0.183±0.003
SFPAG-Ag-0.37%	2.40(0.4)	2.41(0.4)	6.01(1)	0.37(0.06)	28.79(4.8)	60.03(10)	0.172±0.003
SFPAG-Ag-0.48%	2.10(0.4)	2.10(0.4)	5.24(1)	0.48(0.09)	37.71(7.2)	52.38(10)	0.185±0.005
SFPAG-Ag-0.57%	1.86(0.4)	1.86(0.4)	4.65(1)	0.57(0.12)	44.60(9.6)	46.47(10)	0.177±0.003
SFPAG-Ag-0.64%	1.67(0.4)	1.67(0.4)	4.18(1)	0.64(0.15)	50.09(12.0)	41.75(10)	0.170±0.001

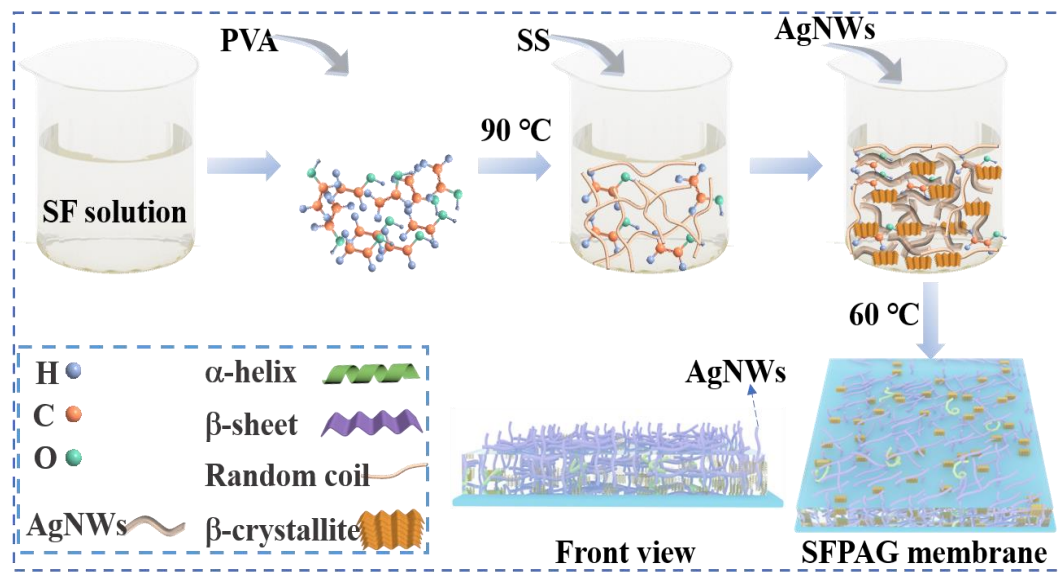


Fig.5. 1 Synthesis process of the SFPAG membranes

5.2.5 Fabrication of SFPAG/F-TENGs

The SFPAG/F-TENG was prepared, with the SFPAG composite membrane serving as the positive friction layer and commercial fluoro-nylon as the negative friction layer. Both tribolayers were then cut into 2 cm × 2 cm dimensions for optimal effectiveness.

5.2.6 Characterizations

Field Emission Scanning Electron Microscope (SEM, Tescan MIRA) was used to characterize the morphology of SFP and SFPAG membranes operating at an accelerating voltage of 5 kV. Energy Disperse Spectroscopy (EDS) data was acquired on a SEM (Tescan VEGA3) operating at 10 kV. X-ray diffraction (XRD) pattern (Rigaku SmartLab) was used to identify the crystalline phase in the fibroin fibril samples with scanning from 5 to 80° (2θ) at a speed of 0.04°/s ($\lambda = 0.154$ nm). The mechanical properties were measured with a universal material testing machine (3365, Instron, USA) in a room with constant temperature and humidity (20 °C, R.H. 65%). The test conditions were as follows: initial width × length, 2 × 4 cm²; tensile speed, 250 mm/min. Contact angle (CA) was characterized on an optical contact angle measuring device (SDC-350, Dynetech, Inc., China) by dropping DI water on the

sample surface. The thermal gravimetric analysis (TGA) was attained using a TGA (Perkinelmer) under a dynamic nitrogen atmosphere, with a sample of 1~5 mg heated from 30 to 800 °C at a rate of 25 °C/min. The simulation was conducted with COMSOL software. The dielectric constant was measured using a precision LCR meter (Keysight E4980A). The short-circuit current and short-circuit charge transfer were recorded on the electrometer (Keithley 6514, Tektronix). The output voltage was measured by an oscilloscope (Keysight InfiniiVision DSOX3024T).

5.3 Results and Discussion

5.3.1 Structure and Working Principle of Fabricated SFPAG/F-TENGs

The working principles of the fabricated SFPAG/F-TENG are both based on contact triboelectrification and electrostatic induction¹². Four working modes have been developed including vertical contact-separation mode, single-electrode mode, lateral-sliding mode, and freestanding layer mode²⁰⁸. SFPAG/F-TENG works in the form of the vertical contact-separation mode. In the first stage, two tribolayers are forced to be in contact with each other accompanied by the generation of equal electrons due to their different electron affinities, without electrons flowing because of contact equilibrium. The surfaces of fluoro-nylon and the composite membrane become excited by opposite static charges obtaining electrons on fluoro-nylon and losing electrons on the composite membrane. For the second stage, the two triboelectric layers begin to separate from each other, inducing a voltage potential (V) between the two friction layers with increased distance. Electrons flow through the external circuit, and the current increasingly reaches a peak value at the proper distance, then drops with the increase of distance²²⁹. In the third stage, when the applied force is completely released, the transferred charges reach an equilibrium state again without current in the external circuit. At the final stage, when they are pressed together again, the electrostatically induced charge flows back through the external load to compensate for the voltage potential, generating a converse current. This iterative process continuously generates the alternating current (AC) signal, as depicted in Fig.5. 2a. To gain a quantitative

understanding of the enhancement effect theoretically, the interrelated potential distribution on two dielectric layers was analyzed and simulated using COMSOL simulation software, as shown in Fig.5. 2b.

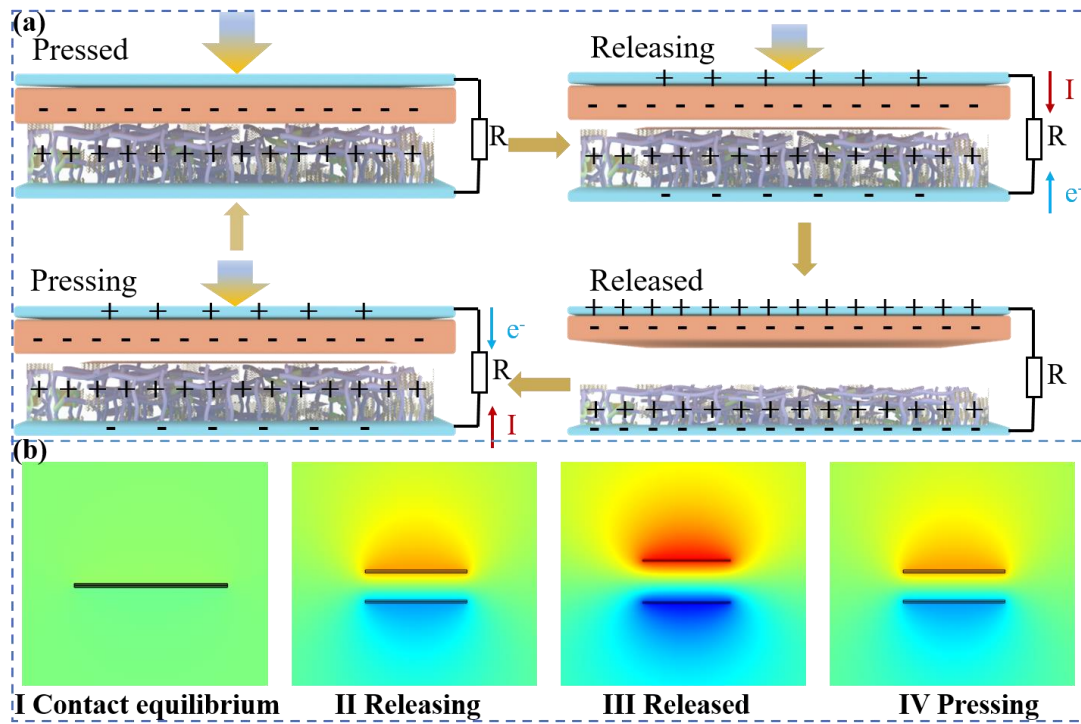


Fig.5. 2 Schematic illustration of the working mechanism of the designed SFPAG/F-TENG: a. Working mechanisms of SFPAG/F-TENG; b. COMSOL simulation results of the potential distribution on dielectric layers

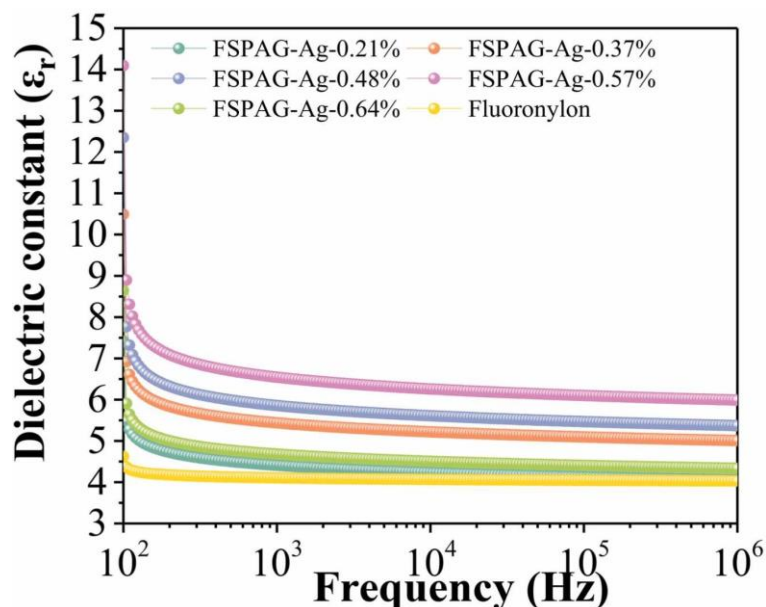


Fig.5. 3 Dielectric constant values of SFPAG membranes

Fig.5. 3 displays that SFPAG membranes doped with varying concentrations of AgNWs exhibit different dielectric constant, demonstrating a significant improvement in dielectric constant compared to pure SFP membranes. Noticeably, the dielectric constant increases with an increment in embedded AgNWs in the composite SFP membranes, which is due to two possible reasons. Firstly, the AgNWs were dispersed in an ethanol solution, which allowed the hydrophobic blocks to form micelles, resulting in a regular and stable β -sheet crystallite formation. These crystalline further form a highly crystalline network structure¹¹⁷. However, when the content of β -sheet crystallites reaches saturation, the additive of AgNWs would affect the β -sheet crystallite network, which is consistent with the reduction of dielectric constant of SFPAG-Ag-0.64% as depicted in Fig.5. 3. Secondly, AgNWs exhibit high electrical conductivity, making them suitable for fabricating stretchable conductive friction layers²³⁵.

5.3.2 Characterization of the Composite SFPAG Membrane

The usage of AgNWs as a conductive electrode platform is highly desirable owing to their exceptional properties, such as high electrical conductivity, good optical

transparency, and high mechanical flexibility²³⁵. Herein, AgNWs were incorporated into the SFP biomatrix to improve the triboelectric effect. The AgNWs formed a web-like structure after being deposited, with alternating horizontal and vertical arrangements across the SFP substrate, indicating the successful introduction of AgNWs (Fig.5. 4a). The distribution of AgNWs was confirmed through elemental mapping of the SFPAG membrane, as shown in Fig.5. 5.

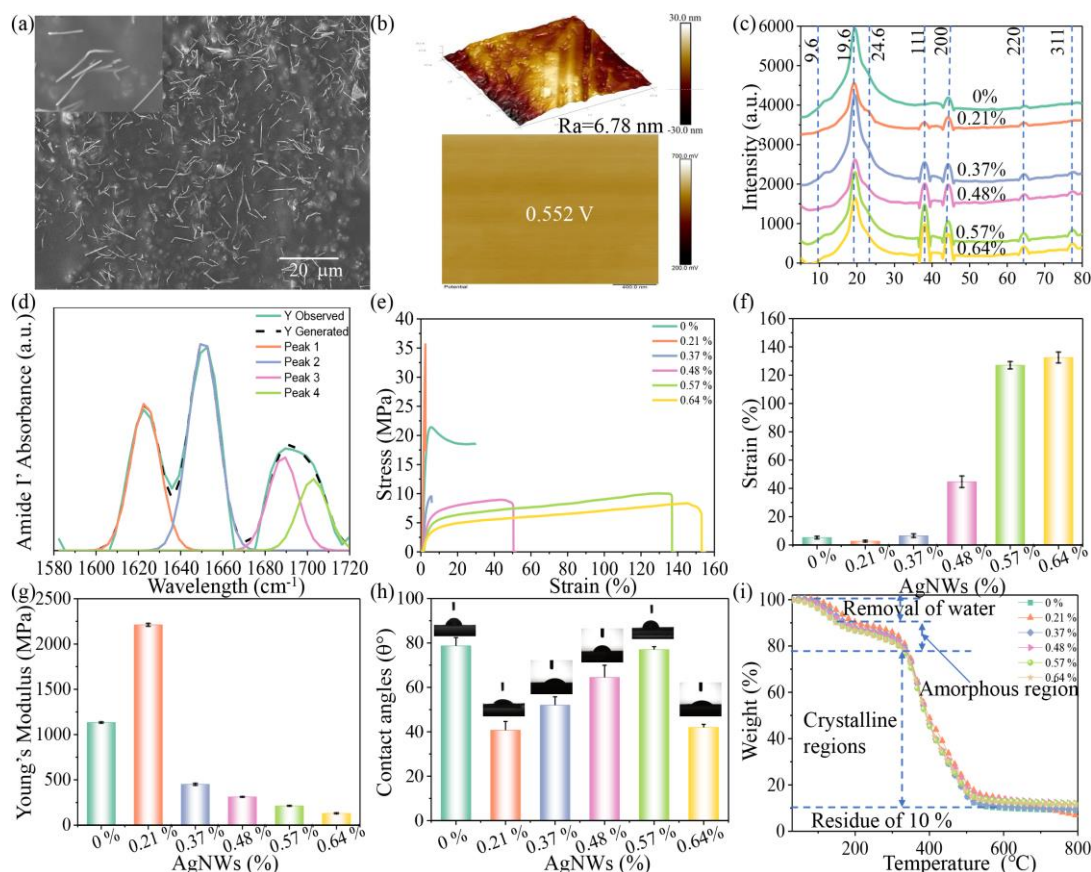


Fig.5. 4 Characterization of SFPAG membranes. a SEM images of SFPAG membranes; b The KPFM images and measured surface potentials of the SFPAG-Ag-0.57%; c XRD patterns of the composite SFPAG films; d Deconvolution of the amide I region (1,580~1,720) of FTIR spectra of SFPAG-Ag-0.57%; e Stress-strain curves of different SFPAG films; f Elongations at break and their vibration of different SFPAG membranes; g Young's modulus of different SFPAG films; h Hydrophilic properties of SFPAG membranes; i TGA results of SFPAG membranes

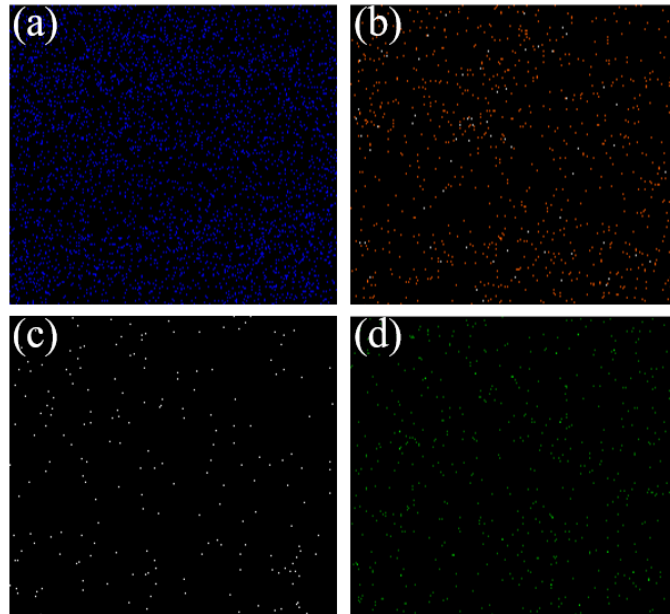


Fig.5. 5 EDS mapping of elemental a C; b N; c O; d Ag

The SFPAG-Ag-0.57% membrane exhibited positive surface potentials of 0.052 V (Fig.5. 4b), whereas the SFP-S-3.39% membrane demonstrated positive surface potentials of 0.437 V (Fig.5. 6), indicating an enhancement of electricity with the addition of AgNWs, which is owing to the high electrical conductivity of AgNWs²³⁵.

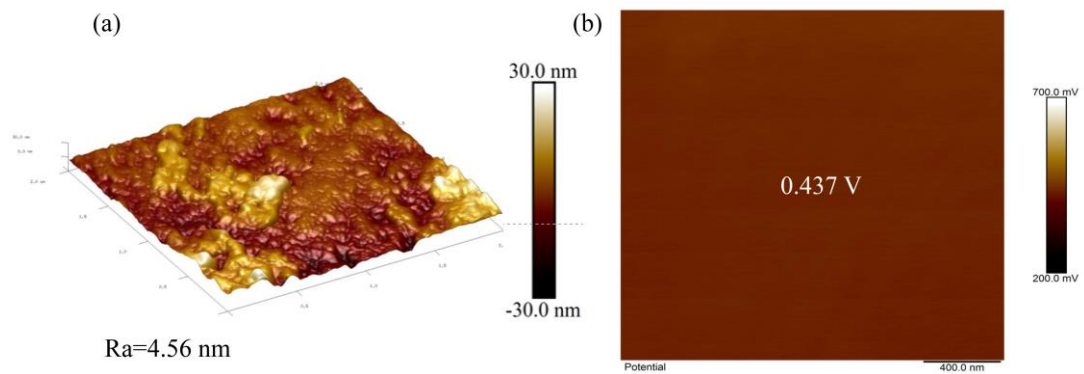


Fig.5. 6 a. KPFM images of SFP-S-3.39% membrane and b. Surface potential of SFP-S-3.39% membrane.

XRD was used to illustrate the secondary structure of the SFPAG membrane and the presence of AgNWs. Notably, the 2θ values of 9.6° , 19.6° , and a shoulder peak at 24.6° were observed due to the β -sheet crystallite of silk, while 11.8° and 24.02° were assigned to the α -helix or random coils²³⁶, as depicted in Fig.5. 4c. The observed diffraction peaks at 38° , 45° , 65° , and 75° were assigned to (111), (200), (220), and (311) crystallographic planes, confirming the presence of pure Ag.

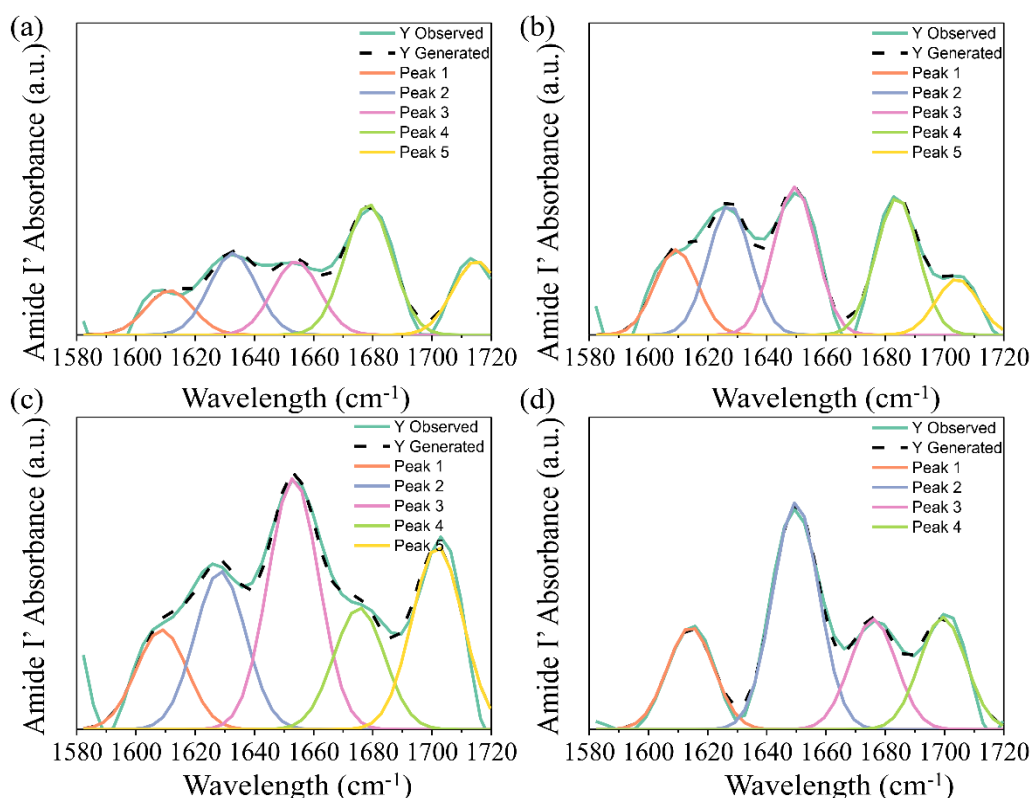


Fig.5. 7 Deconvolution of the amide I region (1580~1720) of FTIR spectra. a SFPAG-Ag-0.21%; b SFPAG-Ag-0.37%; c SFPAG-Ag-0.48%; d SFPAG-Ag-0.64%

By deconvolution of the amide I region (1,580~1,720) (Fig.5. 4d and Fig.5. 7), it was observed that there are four characteristic peaks, which are 1,623, 1,650, 1,688, 1,702, correspond to strong intermolecular β -sheets, random coil, β -turn and weak intermolecular β -sheets, respectively²³². The content of each secondary structure could be obtained by calculation of area ratio as illustrated in Table 5. 2. It is noticed the addition of AgNWs to the SFP membrane caused a change in its crystalline structure.

Initially, the membrane had a small amount of strong intramolecular β -sheets (SFPAG-Ag-0.21%). As more AgNWs were added, strong intermolecular β -sheets (SFPAG-Ag-0.37%) started to form, after which weak intermolecular β -sheets began to form alongside the strong ones (0.48%-0.57 %), which is attributed to the role of alcohol in promoting crystallization¹¹⁷. Eventually, the membrane contained only weak intermolecular β -sheets (SFPAG-Ag-0.64%), which was attributed to the high specific surface area of AgNWs, which impeded the motion of macromolecular chains, leading to the nanoconfined crystallization of SF and an increase in amorphous regions²³⁷.

Table 5. 2 Relative contents of SFPAG membrane's secondary structures

	Random coil	β -sheet	β -turn	Others
SFPAG-Ag-0.21%	18.22	20.21 sb	32.34	29.23
SFPAG-Ag-0.37%	26.60	23.34 sa	24.70	25.36
SFPAG-Ag-0.48%	30.88	19.46 sa + 22.45 wa	14.96	12.25
SFPAG-Ag-0.57%	40.27	28.14 sa+13.66 wa	17.93	0
SFPAG-Ag-0.64%	41.10	20.34 wa	19.99	18.56

wa: Weak Intermolecular beta-sheets; sb: Strong Intramolecular beta-sheets

Fig.5. 4e presents the tensile strength and elongation at the break of a single SFP-S-3.39% membrane and modified SFPAG films with varying AgNWs concentrations. The pure SFP film possessed a tensile strain of about 5.19 %, indicating a brittle property of the SFP membrane. However, after depositing AgNWs into the SFP matrix, there was a significant improvement in elongation, as revealed in Fig.5. 4f. It is worth noting that elongation first fell to 2.65 % with the introduction of AgNWs concentration from 0.21 % to 0.64 %, and then increased from 6.52 % (SFPAG-Ag-0.37%) to 132 % (SFPAG-Ag-0.64%) (Fig.5. 4f). This implies that a slight content of AgNWs is not helpful in enhancing elasticity, such as SFPAG-Ag-0.21%, while a proper AgNWs content is favorable for elasticity enhancement. This is because a small amount of AgNWs might be randomly stacked in the pristine SFP matrix or cause entanglement, leading to a lower-ordered structure. The improvement in tensile strength and stretchability with the additive of AgNWs can be ascribed to their orderly distribution in the SFP matrix.

Impressively, Young's modulus of SFPAG films increased first compared to the pure SFP membrane (from 0 % to 0.21 %) and then decreased with an increment of AgNWs (Fig.5. 4g), which is attributed to the better stretching of amorphous molecules.

Fig.5. 4h displays the results of dynamic contact angle tests conducted on five different component electrode films. The introduction of AgNWs and ethanol has been found to effectively promote surface hydrophilicity, resulting in a decrease in the contact angle as compared to the SFP membrane. This is likely due to the hydrophilic nature of ethanol which is rich in hydroxyl and can form hydrogen bonds with water molecules. The addition of ethanol increases the ratio of hydrophilic ingredients, ultimately leading to an enhancement of hydrophilicity. As more ethanol and AgNWs are added continuously, the contact angles increase while remaining hydrophilic due to an abundant polyhydroxy in PVA and a high content of hydrophilic amino acids in SS. This is because strong intermolecular beta-sheets are formed, as illustrated in Table 5. 2. However, when the AgNWs content reaches 0.64 %, the contact angles start to decrease, which is due to the reduction of intermolecular beta-sheet content as shown in Table 5. 2.

TGA was conducted to investigate the thermal stability of the composite SFPAG membrane, as shown in Fig.5. 4i. The results revealed three distinct transitions: the first at around 100 °C due to water evaporation, the second from 150~310 °C due to the degradation of α -helix and random coil structures²³⁸, and the third from 310 ~ 530 °C due to decomposition of the well-oriented crystalline region. Despite the curve doping AgNWs being similar to that of the pure SFP membrane, the residue of SFPAG-Ag-0.57% was higher, indicating greater thermal stability.

5.3.3 Electrical Characterization of the SFPAG/F-TENGs

To determine the ideal weight ratio of AgNWs to SFP membrane for optimal electrical performance of SFPAG/F-TENG, a series of SFPAG/F-TENGs were fabricated with varying weight ratios (wt% = 0.21%, 0.37%, 0.48%, 0.57%, and 0.64%). The triboelectric performance of the as-fabricated SFPAG/F-TENGs, which had a size of

2.0 cm × 2.0 cm, was evaluated at a frequency of 3 Hz and under a periodic vertical force of 5 N. Results showed that the SFPAG-Ag-0.57%/F-TENG achieved improved V_{oc} of 745 V (Supporting information Video S1), I_{sc} of 22.5 μ A, and Q_{sc} of 65 nC, as illustrated in Fig.5. 8a, b, and c. This may be due to the excellent electrical and thermal conductivities of silver and the flexible and stretchable conductive electrode platform of AgNWs, which can enhance the conductivity of composite SFPAG membrane. Incorporations of 0.21% AgNWs into silk biomatrix may provide a less conductivity path, and mutual entanglement possibly restrains the formation of crystal structures, causing inability to form a complete conductive network. However, increased concentration of AgNWs may result in a more uniform distribution throughout the SFP matrix, leading to improved mechanical contact and electrical outputs. Conversely, excessive AgNWs additions may cause the formation of nanowire agglomerates, leading to reduced mechanical contact area and decreased electrical outputs²³⁹. However, the dielectric constant of SFPAG (AgNWs=0.37 %, 0.48 %, 0.57 %, and 0.64 %) is 10.49005, 12.34842, 14.09315, and 8.63979, respectively. This is in agreement with the voltage trend of 655, 656, 748, and 479 V, confirming that a higher dielectric constant results in more electrostatic energy storage capacity in an electric field.

In addition, typically, alcohol treatment has been found to increase the crystalline domains of β -sheet in SF or SS^{117, 240}. The hydroxyl side chains of the Ser and Thr residues from the 38-amino acid repetitive region of β -sheet interact with adjacent side chains through hydrogen bonding to form β -sheet aggregates after hydration²⁴¹. During the synthesis of AgNWs, alcohol was utilized to disperse them. Afterward, ethanol was added to the SFP matrix, causing the hydrophobic blocks to assemble and form micelles. Thereby SFPAG-Ag-0.57 % possesses the highest dielectric constant, which corresponds to the best triboelectric performance^{239, 242}. Additionally, our PVA substrate and SS introduction have amorphous structures that provide a larger specific surface area and electron donors, confirming that SFPAG/F-TENG demonstrated high electrical outputs²³⁷.

The output performance of TENGs is strongly influenced by the applied compression force and frequency²²⁹. Thus, the effect of external compression force on the output performance of SFPAG/F-TENG was first experimentally analyzed (Fig.5. 8d). These studies indicated that the output voltage value of the SFPAG/F-TENG is directly dependent on the applied compression force. As the compression force increased from 1 to 9 N, the peak voltage values of the SFPAG/F-TENG device increased from approximately 400 V (1 N) to 880 V (9 N). This increase in performance is mainly ascribed to the larger surface contact area between the SFPAG membrane and fluoronylon layers when a stronger compression force is applied¹⁹².

The electrical output performance of SFPAG/F-TENG was examined with changed compression frequencies, as shown in Fig.5. 8e. During these measurements, the compression force of 3 N was kept constant while the compression frequencies were changed in the range of 1-4 Hz. The peak voltage values of SFPAG/F-TENG were observed to gradually rise from 250 V to 780 V as the frequency increased from 1 to 4 Hz. This voltage change is attributed to the alteration in the triboelectric surface contact-separation rate and effective contact-separation area as vibration frequency changes. The accumulation of surface charges is higher at higher frequencies because there is more contact in a short period of time, resulting in an increase in the output voltage.

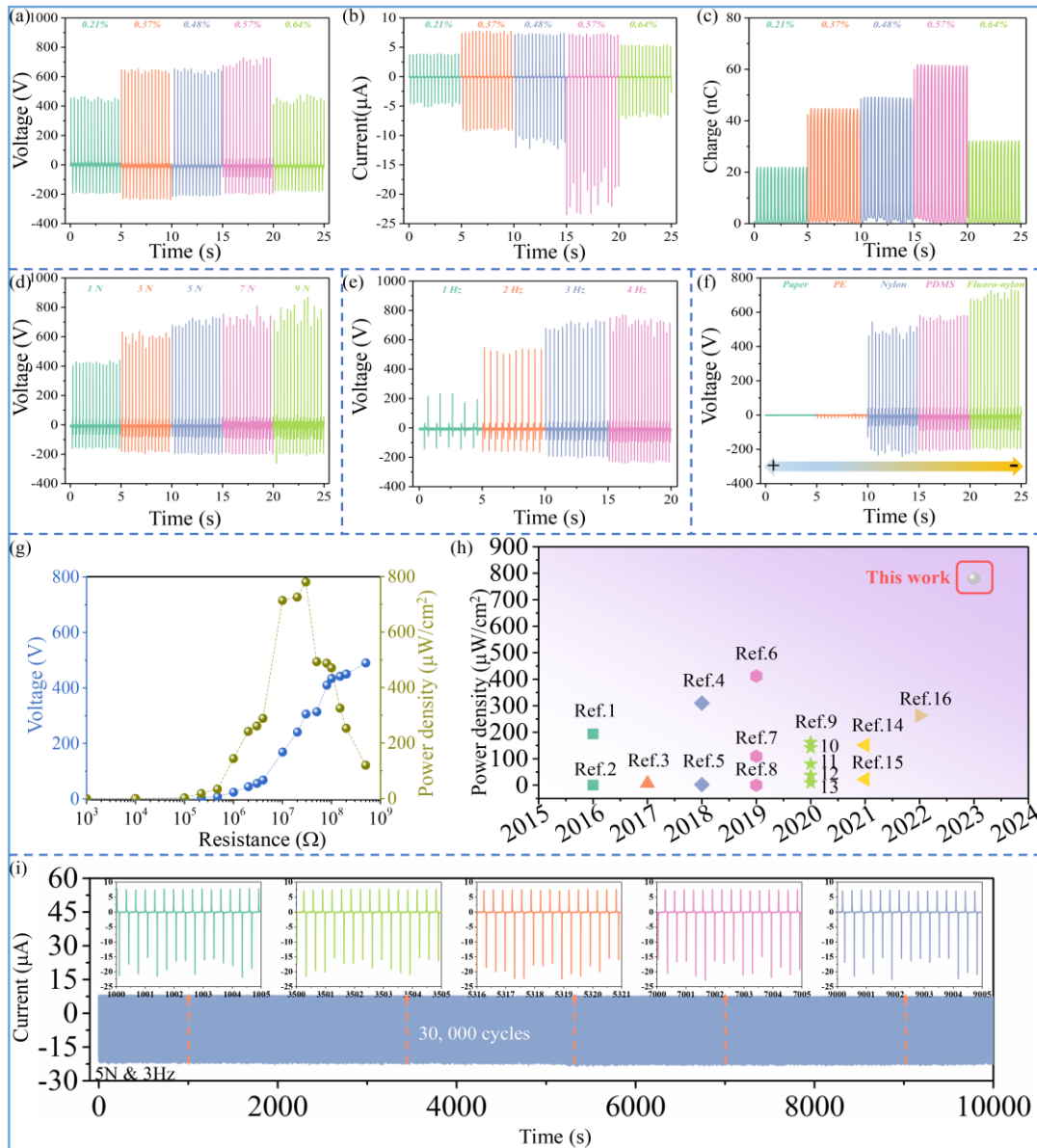


Fig.5. 8 Parametric analysis and design optimization of SFPAG/F-TENG: a. V_{oc} ; b. I_{sc} ; c. Q_{sc} ; d. V_{oc} of SFPAG/F-TENG with different pressures; e. V_{oc} of SFPAG/F-TENG with different frequencies; f. The SFPAG/F-TENG device with the respective triboelectric materials; g. Power density of the SFPAG/F-TENG; h. Electrical performance comparison with silk-based TENGs previously reported^{1, 24, 27-30, 33-38, 118, 122, 133, 134}. Detailed data are provided in Table 5. 3; i. The durability of SFPAG/F-TENG within 30,000 cycles

When two materials with different electron affinities come into contact and are

separated, it is known that they will drive different electrical output performances. Fig.5. 8f illustrates the voltage signals observed when the SFPAG membrane is in contact with different materials such as paper, polyethylene (PE), Nylon, and PDMS. The sequence of electronegativity of the materials determines the corresponding voltage signals, with paper (Copy paper) < PE (Polyethylene) < Nylon (Polyimide film) < PDMS (Polydimethylsiloxane) being the order. It is noteworthy that chemical-resistant viton® fluoroelastomer rubber exhibits the highest electronegativity, which may suggest that fluoro-nylon has higher electronegativity compared to other contrasting materials.

Table 5. 3 Electrical performance comparison of previously reported silk-based TENGs

Electrode	Triboelectric materials	Pressure (N)	Frequency (Hz)	Area (cm ²)	Voltage (V)	Current (μA)	Power density μW/cm ²	Ref.
CS D	Bio-silk/polyimide film/Al	16.8	3	28	15	2.5	0.43	24
CS D	e-silk/BiFeO ₃ -glass fiber fabric-PDMS	-	1	2 × 3	110	3.67 μA/cm ²	151.42	122
CS D	PET-silk fibroin (Spray-coating)	6	5	4 × 6	213.9	-	6.8	38
CS S	AgNW/e-silk	6	5	2.0 × 1.8	90	0.06	0.2	36
CS S	Fibroin/PDMS+ graphite	Hand pressure	7	6 × 3	666	174.6	412	37
CS D	Regenerated SF film/silk nanoribbons+Mg	50	5	2 × 1	41.64	0.5	8.67	133
CS D	Silk aerogels/PTFE Chitosan/albumin, egg-shell membrane (ESM) and silk fiber	-	5	2 × 1	52.8	5.2	37	134
CS D	Silk/PET	250	1.5	3 × 3	77	13	22.4	118
CS D	Silk/PET	-	5	2 × 4	268	5.78	193.6	33
CS D	PVA/MXene+ Electrospinning silk	10	10	3.14	118.4	-	108.76	28
CS D	PET/SF (electrospray-etching)+SiO ₂	18	1	2 × 2	260	6.2	161.5	34

CS D	MOFs+SF/PDMS	10	2	2×2.5	107.5	10	263	35
CS D	SF+CNT/PET	14	7	2×4	200	8	140.99	29
CS D	SF+PVDF	25.7	2	2×4	500	12	310	27
CS D	SF+Mg/bioresorbable polymers		1	1×2	55	0.6	2.16	30
CS S	PDMS/Ag NFs+SF	/	1	1×1	13	0.4	80	1
CS D	SF/SS/PVA/AgNWs+ Fluoro-nylon	5	3	2×2	745	22.5	760	This work

Higher power density indicates transferring large amounts of energy based on its mass and recharging quickly, rendering it one of the significant factors in deciding the quality of TENGs. The output power density (P) is calculated using the following Eq. (5-1)

$$P = \frac{U^2}{RA} \quad (5-1)$$

Where U , R , and A are the peak-to-peak output voltage, load resistance, and effective area, respectively. The maximum instantaneous power density of the SFPAG/F-TENG can reach $760 \mu\text{W}/\text{cm}^2$ based on Eq. (1) at a loading resistance of $30 \text{ M}\Omega$ (Fig.5. 8g), which provides guarantee for subsequent powering electronic devices. In order to provide a clear illustration of the TENG performance level devised in this work, recent research on the highly electrical properties of silk-based TENGs was compared as depicted in Fig.5. 8h. It is noteworthy that the instantaneous power density of the SFPAG/F TENG keeps above $760 \mu\text{W}/\text{cm}^2$, which presents higher level than most reported research results on modified silk-based TENG^{1,24,27-30,33-38,118,122,133,134} (Table 5. 3) and cellulose-based TENGs (Table 5. 4). The physical reliability of wearable TENGs during long-term operation is always a major concern for practical applications. However, it can be found that the output of our proposed SFPAG/F-TENG remains almost constant throughout 30,000 operating cycles (3 Hz), and even shows a slight improvement in I_{sc} after being exposed to 5,000 contact-separation cycles, which may

be attributed to the improved contact between the SFPAG membrane and the fluoro-nylon elastomer resulting from the persistent external force, as exhibited in Fig.5. 8i²⁴³.

Table 5. 4 Comparison of the electrical performance of cellulose-TENGs

Mode	Triboelectric materials	Pressure (N)	Frequency (Hz)	Area (cm ²)	Voltage (V)	Current (μA)	Power density μW/cm ²	Ref.
D-CS	Allicin-modified CNF membrane/PVDF	12	20	4	7.9	5.13	10.13	244
D-CS	Commercial polyamide film/PFOTES-CNF film	50	2	16	35	9.3	1.35	245
D-CS	ZIF-8@wood/PDMS@wood	50	2.5	7	24.3	0.32	1.04	246
D-CS	DF-CNF/PTFE	8	5	4.9	388	18.6	431	247
S-CS	PTFE+wood/Cu	20	1	9	81	1.8	5.7	248
D-CS	C-wood/F-wood	8.2	3	4	90.1	0.331	13.63	249
S-CS	Treated Wood+Cu	1	1	4	38	/	/	250
D-CS	CMCS membrane/CMC-Na membrane	/	2	9	3.5	0.02	12	251
D-CS	N ₃ HSC/F ₂₁ HSC	50	0.5	5	4.86	0.045	/	252
D-CS	SEBC fabric/PTFE	40	4	100	266.0	5.9	4.879	253
D-CS	SF/SS/PVA/AgNWs+Fluoro-nylon	5	3	2 × 2	745	22.5	760	This work

The electrical properties of the SFPAG/F-TENGs showed a decreasing trend with the increase of membrane thickness from 0.1 to 0.3 mm, as confirmed by Fig.5. 9. According to the formula:

$$C_{\max} = \epsilon_0 \epsilon_r \frac{A_{\text{effective}}}{d} \quad (5-2)$$

The ratio of the dielectric constant to the thickness (ϵ_r/d) of the friction layer directly determines the C_{\max} . In fact, when mixing AgNWs with an appropriate amount of SFP

membrane, the change in its dielectric properties is negligible, but the effective d value can be greatly reduced, thus increasing the maximum power output of the TENG. Therefore, with an increased d value, the electric outputs will be decreased²³³.

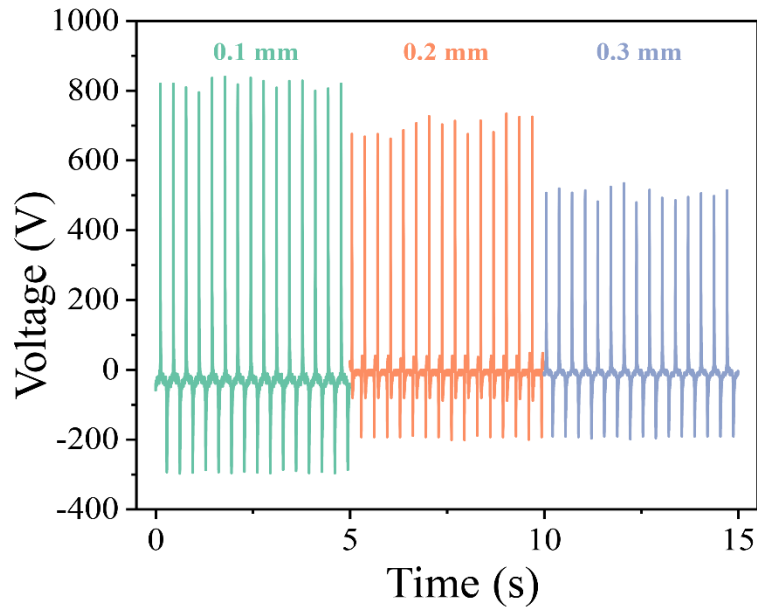


Fig.5. 9 V_{oc} of SFPAG/F-TENG with different thickness

5.3.4 Applications of SFPAG/F-TENG as Energy Harvesters

To explore the practicality of the fabricated SFPAG/F-TENG for energy harvesting, an equivalent working circuit was utilized to demonstrate its working principle (frequency of 3 Hz, pressure of 5 N), as exhibited in Fig.5. 10a. Based on the equivalent working circuit, SFPAG/F-TENG was able to power various electronics, such as a calculator, sports watch, and LED lights Fig.5. 10b illustrates a picture of the circuit being used to power a commercial electrical calculator. To achieve this goal, a capacitor of 10 μF and a rectifier were utilized to integrate the AC into DC and directly drive the commercial electronic calculator to operate normally. It can be viewed that the capacitor was charged swiftly from 0 to 4.5 V within 140 s of continuous tapping on the SFPAG/F-TENG, and the switch was turned on to power the calculator for about 10 s (Fig.5. 10c). The energy stored in the 10 μF capacitor could also be used to power a white sports watch (Fig.5. 10d). Additionally, by connecting 240 LED lights to the positive and

negative layers of the SFPAG/F-TENG, the LEDs could be easily illuminated (Fig.5. 10e). Finally, the charging ability of the SFPAG/F-TENG was summarized with various capacitors (1, 1.5, 10, and 22 μF). Notably, the small device can rapidly charge a 1, 1.5, 10, and 22 μF capacitor to 6.5, 6, 3.3, and 0.9 V in 100 s, respectively. All results demonstrate that the SFPAG/F-TENG is a reliable device that can power various commercial electronics in real-life situations.

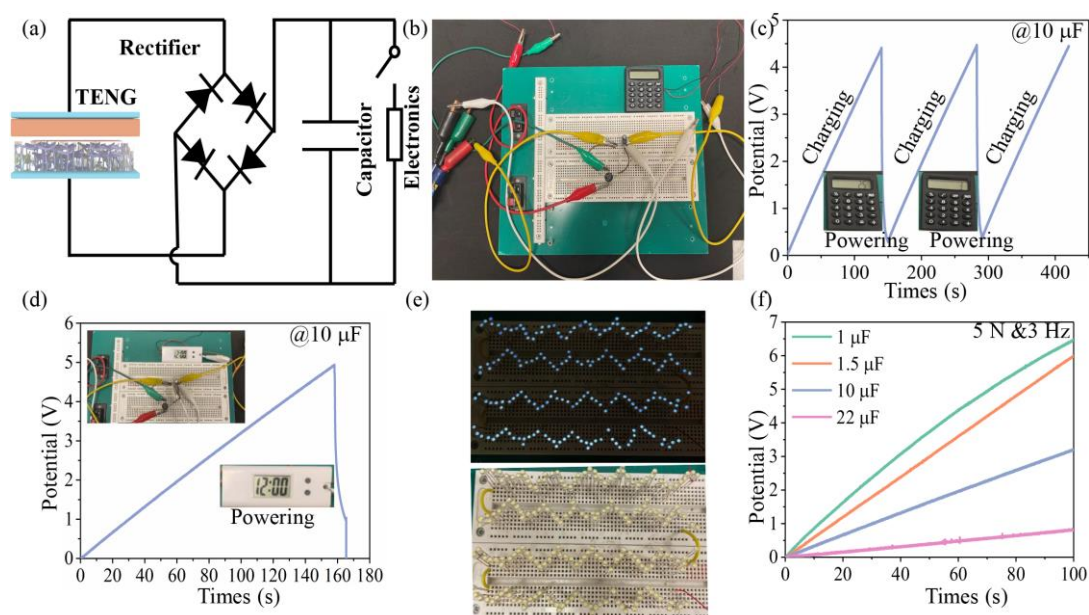


Fig.5. 10 The applications of SFPAG/F-TENG are energy harvesters. a The equivalent electrical circuit of the SFPAG/F-TENG; b Illustration of SFPAG/F-TENG drives a calculator with a 10 μF capacitor; c and d The illustration of charging and powering a calculator for calculation and a sports watch with a 10 μF capacitor ($2 \times 2 \text{ cm}^2$); e Images of the TENG lighting up 240 LEDs with an applied force of 5 N at 3 Hz; f Charging curves of various capacitors by the SFPAG/F-TENG

5.3.5 Applications of SFPAG/F-TENG as Sensors

Owing to the excellent flexibility, compressibility, and high sensitivity, the fabricated SFPAG/F-TENG can be viewed as smart sensors in wearable devices to detect body motion and gestures. As Fig.5. 8d shows, it is sensitive to the applied force, thereby, different numbers of finger pressing are utilized here to monitor changed electrical

signals (Fig.5. 11a). It is obvious that sharp AC voltage signals emerge with one finger, two fingers, and three fingers pressing. With more finger pressing, the voltage is higher, which is attributed to the larger effective areas between two tribolayers. The SFPAG/F-TENG can also be used to detect different bending angles of elbows by high flexibility as presented in Fig.5. 11b. The SFPAG/F-TENG sensor depicts a repeated characteristic peak with different bending angles, and it is apparent the increased bending angle generates the higher voltage outputs, which are ascribed to the surface contact area between the SFPAG membrane and fluoro-nylon layers²⁵⁴. In addition, with the stretchability of the small device, it can deform with the movement of the knee and retain its function, rendering it a good candidate to sense the bending angles of the knee as displayed in Fig.5. 11c. Typically, slight knee bending generates a V_{oc} with an estimated 30 V, moderate knee bending gives a voltage of about 50 V, while high knee bending shows a voltage of ~ 70 V, revealing the greater the bending amplitude of the knee, the greater the voltage signal output by the SFPAG/F-TENG. Various types of foot-related activities, such as walking, jumping, and running, could also be distinguished from the flexible device. It is evident that the voltage signals are distinctively different when humans are walking, jumping, and running, respectively, as embodied in Fig.5. 11d. It is a typical alternating voltage with the value of 90 V as walking, while the voltage signals change to be sharp with a delayed decline when jumping, which is pertaining to the longer time out of the ground compared with walking. However, when the foot conducts running, the voltage signal becomes plunged and delayed, which is attributed to out of the ground non-simultaneously.

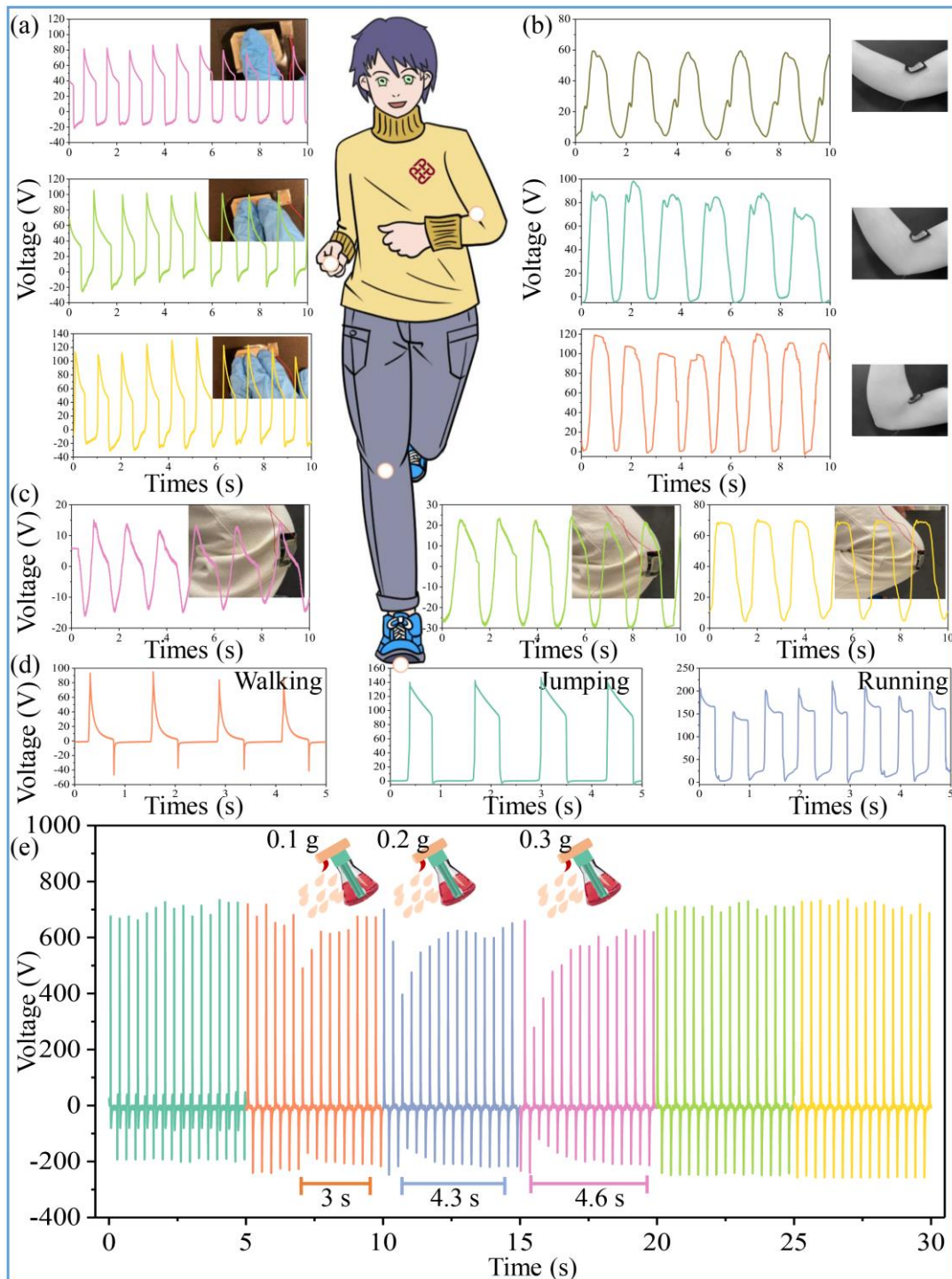


Fig.5. 11 The application of SFPAG/F-TENG being smart sensors. a SFPAG/F-TENG being pressure sensors for finger pressing; b Monitoring of elbow bending angles by pasting SFPAG/F-TENG on the elbow; c Knee-related activities monitoring by attaching SFPAG/F-TENG to the knee joint; d Foot-related activities detecting by

placing SFPAG/F-TENG in the shoes; e Humidity resistance of the fabricated SFPAG/F-TENG

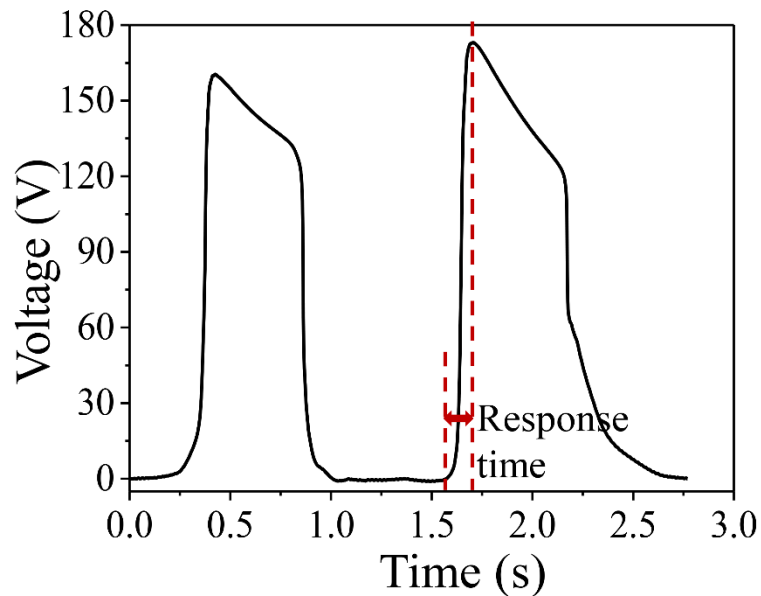


Fig.5. 12 Time sensitivity and response duration

In addition, the time response duration of SFPAG/F TENG was supplied in Fig.5. 12. The response time, corresponding to the time taken by the sensor output to change from its initial value to a final defined value, is considered as an important characteristic of any pressure sensor. As shown in Fig. S7, the response time of the SFPAG/F-TENG device was 0.16 s. All results demonstrate that the proposed SFPAG/F-TENG is suitable as an indicator for various physiological activity monitoring via a self-powered manner.

Apart from wearable sensors, the SFPAG/F-TENG shows excellent humidity sensitivity and resistance because of polyhydroxy polymer (PVA) and high content of hydrophilic amino acids (SS)²⁴¹ which provides high sensitivity for water functions, and repetitive hydrophobic crystalline regions presented in SF molecules²⁵⁵, which plays a significant role to evaporate quickly to achieve humidity resistance. During the contact-separation working mode, water droplets of different weights were sprayed on

the surface of two friction layers using a spray bottle as illustrated in Fig.5. 11e. When 0.1 g of water droplets were sprayed on the SFPAG/F-TENG, it showed a 25 % decrease in voltage and took 3 s to recover, implying its remarkable adsorption and desorption ability in response to water molecules. This is because moisture can cause the friction layers to dissipate surface charges and weaken the triboelectricity of TENGs^{192, 256}. With rapid evaporation of the SFPAG membrane, the SFPAG/F-TENG immediately returned to its initial voltage. It is pertinent to note that larger water droplets had a greater impact on the voltage, and it took longer to offset, rendering it a promising candidate for being humidity sensors. It should be emphasized after removing moisture, the SFPAG/F-TENG remained 99.99% of the initial electrical output, indicating its good humidity resistance property.

5.4 Summary

In summary, a highly flexible and durable silk-based triboelectric device is developed with enhanced electrical outputs by incorporating sericin powders and AgNWs into the SF/PVA matrix, inspired by the hierarchical architecture of silkworm cocoons. The modified SFPAG membrane, acting as a positive friction layer, exhibited attractive mechanical properties with an elongation of 132 %, good hydrophilic properties, and excellent thermal stability. Moreover, the proposed SFPAG/F-TENG achieved high electrical outputs, remarkable flexibility, stable durability, and distinguished adsorption and desorption ability simultaneously that can be used as humidity sensors and resistance. Under the applied force of 5 N and frequency of 3 Hz, the introduction of sericin and AgNWs has enabled the optimal SFPAG/F-TENG to achieve a voltage of 745 V, current of 22.5 μ A, transferred charge of 65 nC, and instantaneous power density of 760 μ W/cm², respectively, making it superior to most silk-based TENGs that have been reported recently. The mechanism of output performance enhancement is explained. The fabricated SFPAG/F-TENG demonstrated a stable output performance after the operation time of 30, 000 s, extended service life and strong anti-wearing performance. This special TENG can not only convert arbitrary low-frequency mechanical energy from human movements that can be deemed as human gesture

sensors, but also could be integrated through the rectifier bridge to continuously power electronic devices such as calculators, sports watches, and 240 LED lights. Except for the human sensing and energy storage functionalities, it can be viewed as humidity sensors and resistance since it has exceptional ability to adsorb and release water molecules. Overall, this idea provides an innovative and general strategy to facilitate the development of high-electrical output TENGs for sustainable and renewable energy applications.

CHAPTER 6 High-Performance Triboelectric Nanogenerators for Energy Harvesting and Sensing Based on MXene-Enhanced Silk Composite Membranes

6.1 Introduction

In the contemporary landscape marked by the proliferation of wearable smart electronics, driven by advancements in artificial intelligence and the Internet of Things (IoT), the priority to address challenges such as the finite availability of natural resources and the environmental degradation resulting from the overexploitation of petroleum resources has become increasingly critical²⁵⁷⁻²⁶⁰. The advent of TENGs has garnered extensive attention owing to their advantages such as lightweight construction, simple fabrication process, a broad range of material options, and versatile energy conversion capabilities at low frequency^{148, 261, 262}. Based on the principle of coupling effect of triboelectrification and electrostatic induction, TENGs have encompassed four working modes containing contact-separation mode, single-electrode mode, lateral-sliding mode, and freestanding mode^{208, 263}. Of note, the single-electrode mode, which involves only one tribolayer that can be positioned anywhere in space or directly on the ground, offers a highly optimized structural integration compared to the double-electrode working modes²⁶⁴.

As an innovative energy-harvesting technology, the evaluation of TENGs hinges critically on their electrical energy output. Nevertheless, the electrical charge output produced by the majority of single-electrode TENGs (SETENGs) is conspicuously insufficient to meet the energy demands requisite for commercial applications. This deficiency is attributable to the limited achievable saturated charge state, which stems from the insufficient influence of the dielectric layer on the primary electrode²⁶⁵. Theoretical analyses reveal that, while the maximum charge transfer efficiency (η_{CT}) for dielectric-to-dielectric contact-separation mode SETENGs is constrained to a ceiling of 50%, double-electrode TENGs can attain an η_{CT} approaching the ideal

threshold of 100%^{54, 265}. For instance, a recent study²⁶⁴ summarized the power density data of SETENGs reported in contemporary studies, revealing that the majority of these devices exhibit power densities ranging from milliwatts per square meter (mW/m²) to several watts per square meter (W/m²). Accordingly, enhancing the charge generation capability of SETENGs continues to be a formidable challenge.

To enhance the charge generation capability of SETENGs, a series of attempts have been made, such as the selection of high-performance tribo-materials²⁶⁶, charge-defect tuning²⁶⁷, the addition of conductive networks²⁶⁸, and surface physical/chemical modification¹. Among these methods, surface physical/chemical modification holds significant promise for scalable applications owing to its ease of operation, which improves contact intimacy by crafting microstructures on the surfaces of tribo-materials. With this method, the selection of tribo-materials is of paramount importance, ideally prioritizing materials that are distinguished by their biodegradability, biocompatibility, flexibility, mechanical stability, and environmental sustainability.

Silk, derived from silkworm cocoons (*B. mori*), is accepted as a renowned natural protein fiber consisting of intertwined hydrophobic silk fibroin (SF) filaments and a glue-like hydrophilic sericin (SS) acting as a binder to seamlessly connect both intralayer and interlayer SF to form a highly integrated hierarchical structure^{95, 269}. Owing to the favorable properties of silks, including flexibility, biocompatibility, and electron-donating capability, it has facilitated the development of many silk-based double-electrode TENGs, yet the exploration and proposition of SETENGs remain relatively limited^{32, 149}. For instance, He et al.⁴² ingeniously designed a stretchable conductive hydrogel-based SETENG by precisely blending SF with polyacrylamide, graphene oxide, and poly(3,4-ethylenedioxythiophene): poly(styrene sulfonate). It is an innovative approach to fabricate silk-based composited hydrogel, yet the resultant energy output is insufficient, illuminating only 20 commercial green lights. In addition, Gogurla et al.³⁶ presented a protein-based SETENG that employs silver nanowire (AgNW) electrodes embedded within a silk membrane to enable both energy harvesting and sensor monitoring. Nonetheless, the device exhibited a peak power density of 2

mW/m², which remains inadequate for a wide range of application scenarios. As a result, there is a pressing need for novel approaches to surmount the challenges associated with limited electrical outputs and to fabricate high-performance, stretchable silk-based SETENGs via facile and effective methods.

In this study, a SETENG device is designed and developed that is not only biocompatible but also environmentally sustainable, leveraging an innovative selection of materials including SF, which serves as a durable mechanical substrate; SS, which augments the matrix's stretchability through its high content of amorphous regions and aids in MXene dispersion via disaggregation effects; PVA, which synergistically interacts with SS to form a densely cross-linked architecture; and MXene, which significantly enhances the conductivity of the composite membrane. The meticulously engineered SF/SS/PVA/MXene (MFS) films function as the positive tribolayer, paired with F-Nylon connected to the ground, operating in a SE mode. With a facile solution blending approach, the hierarchical porous MFS/F-SETENG exhibits a prominent voltage of 748 V and a power density of 35.76 W/m² under an applied force of 5 N and a frequency of 3 Hz, surpassing the performance metrics of most silk-based double-electrode TENGs and SETENGs. Furthermore, the mechanical stability of the MFS/F-SETENG was evaluated, revealing consistent and stable performance even after enduring 15,000 operational cycles. The fabricated MFS/F-SETENG is endowed with electrical conductivity, stretchability, and dynamic stability, rendering it suitable for a wide range of applications, including serving as an energy harvester for powering small electronic devices such as digital calculators, timers, and clocks, as well as functioning as sensors for detecting human gestures and enabling multichannel sensing via computer interactions. This study provides valuable insights into the advancement of high-performance silk-based SETENGs, significantly contributing to the domains of flexible electronics, energy harvesting, and sensing technologies.

6.2 Experimental Section

6.2.1 Materials

Silkworm cocoons were purchased from the market. Silk sericin powder ($\geq 99.5\%$) was purchased from Macklin Co., Ltd. Copper/nickel-coated polyester fabric (CNF) was bought from the 3 M company. PVA (1788) was purchased from Dieckmann. Na_2CO_3 (99%, AR) and LiBr (99%) were purchased from Macklin Co., Ltd. Dialysis membrane (MD77–14000) was purchased from Nantong Supin Equipment Co., Ltd. Fluoro-nylon was obtained from Shenma Group Co., Ltd., China. Multilayer clay-like $\text{Ti}_3\text{C}_2\text{Tx}$ ($5\ \mu\text{m} \sim 10\ \mu\text{m}$) was purchased from Grahope New Materials Technologies Inc. All reagents and materials were commercially available without further purification.

6.2.2 Preparation of SF Solution

SF solution was prepared via previously studied methods²⁷⁰. Silkworm cocoons were cut into small pieces and then placed in 5 g/L sodium carbonate solutions at 120 °C for 1.5 h to remove the SS coating. The silk was then rinsed with DI water and dried in the oven for several hours. Next, the degummed SF fibers were dissolved in 9.3 M lithium bromide (LiBr) solution at 60 °C for 6 h, followed by purifying via dialysis against DI water for 72 h to remove LiBr and acquire the preliminary SF solution. Finally, the SF solution was purified through microfiltration and stored at 4 °C before use.

6.2.3 Preparation of SF/SS/PVA/MXene (MFS) Membrane

MFS membrane was gained through a solution blending method. Firstly, 1 g of water-soluble PVA precursor was added to 10 mL of SF solution. After heating and stirring at 90 °C for 40 minutes, the mixture was cooled down to 60 °C for the additive of SS powders (0.4 g) needed to retain biological Activity. Simultaneously, different content of MXene powders was added to the SF/PVA substrate to form composite membranes named SFP, MFS-0.08%, MFS-0.17%, MFS-0.25%, MFS-0.34%, and MFS-0.42%, respectively. To enhance the dispersion of MXene, all MFS membranes were subjected

to ultrasonication for 1 h. The specific parameters and proportions of each component inside the MFS membranes are exhibited in Table 6. 1.

Table 6. 1 Specific parameters and proportion of each component inside the MFS membranes

Material	SS (g/%)	SF (g/%)	PVA (g/%)	MXene (g/%)	Water (g/%)
SFP	0.4(3.39%)	0.4(3.39%)	1(8.47%)	0(0%)	10(84.75%)
MFS-0.08%	0.4(3.39%)	0.4(3.39%)	1(8.46%)	0.01(0.08%)	10(84.68%)
MFS-0.17%	0.4(3.39%)	0.4(3.39%)	1(8.46%)	0.02(0.17%)	10(84.59%)
MFS-0.25%	0.4(3.39%)	0.4(3.39%)	1(8.45%)	0.03(0.25%)	10(84.52%)
MFS-0.34%	0.4(3.39%)	0.4(3.39%)	1(8.45%)	0.04(0.34%)	10(84.43%)
MFS-0.42%	0.4(3.39%)	0.4(3.39%)	1(8.44%)	0.05(0.42%)	10(84.36%)

6.2.4 Fabrication of MFS/F-TENGs

The as-prepared MFS films were tailored into a square shape with a dimension of 2.0 cm × 2.0 cm as the positive tribolayers while the Fluoro-nylon as the negative one with the copper wire connecting to the ground working as a single electrode MFS/F-TENGs.

6.2.5 Characterizations

Basic characteristics: Morphology, microstructure, and elemental analysis of MFS films were assessed through Field Emission Scanning Electron Microscope (Tescan MIRA), Energy dispersive X-ray (EDX) spectroscopic mapping (Tescan MIRA), Fourier Transform Infrared Spectrometer (FTIR) (PerkinElmer FTIR Spectrum 100 + Autoimage IR Microscope), and Thermogravimetric analyzer (TGA) (Perkinelmer TGA 4000 System 100–240 V/50–60 Hz). To investigate the tensile strength of the MFS membranes, a universal material testing machine (3365, Instron, USA) was employed under constant temperature and humidity (20 °C, R.H. 65%). X-ray Diffractometer (XRD, Rigaku SmartLab 9kW) was used to detect the combination of MXene into the silk-based matrix at the 2θ ranging from 5° to 80° (4°/min). UV–vis (Hitachi UH5300) was used to measure the UV-visible absorption spectrum of MFS membranes. Contact angle (SDC-350, Dynetech, Inc., China) was utilized to confirm the water repellency of MFS films. AFM (Germany, Bruker Dimension Icon) was used

to measure the surface roughness, the surface potential difference, and the work functions of the MFS membranes. Electrical performance: The dielectric constant was tested by an LCR meter (E4980A, Keysight). The short-circuit currents (I_{sc}) and transferred charge (Q_{sc}) of the MFS/F TENGs were investigated by an electrometer (Keithley 6514 system) and the open-circuit voltages (V_{oc}) were measured by an oscilloscope. The operating frequency was kept at 3 Hz and 5 N during the TENG output tests without specific elucidation.

6.3 Results and Discussion

6.3.1 Structure and Characteristics of MFS Membrane as Friction Layer

The MFS membrane was synthesized by a three-step process clearly illustrated in Fig.6. 1: (1) dissolution of PVA in the SF Solution; (2) mutual dispersion of MXene and SS on the premise of retaining the activity of SS; (3) ultrasonication to obtain a homogeneous and stable composite solution. The materials and fabrication were detailed in the experimental section.

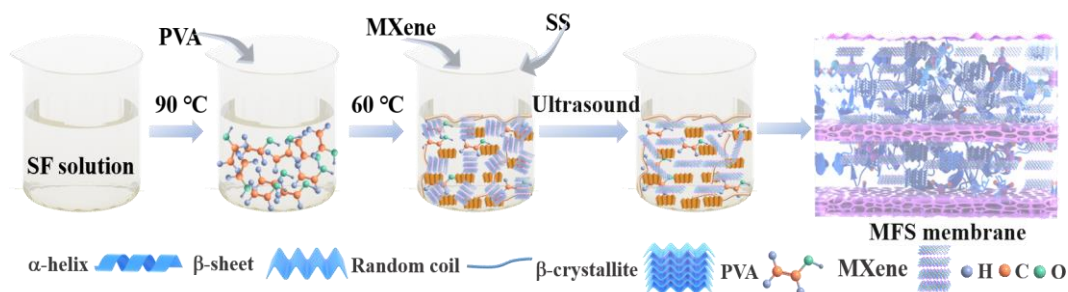


Fig.6. 1 Preparation process of the MFS membrane

As depicted schematically in Fig.6. 2a, a hierarchical MFS composite with diverse MXene loadings is attainable, ensuring a porous, wrinkled, and interlaced architecture via a facial method of blending, heating, and sonication. Notably, the MFS membranes manifested three distinctive features: coarse surface morphologies caused by distributed MXene nanosheets (Fig.6. 2b and c), a parallel alignment of homogeneous MXene sheets with interspersed small pores (Fig.6. 2d), and porous architecture on the

sidewalls predominantly appearing at the bottom of the MFS membranes (Fig.6. 2e).

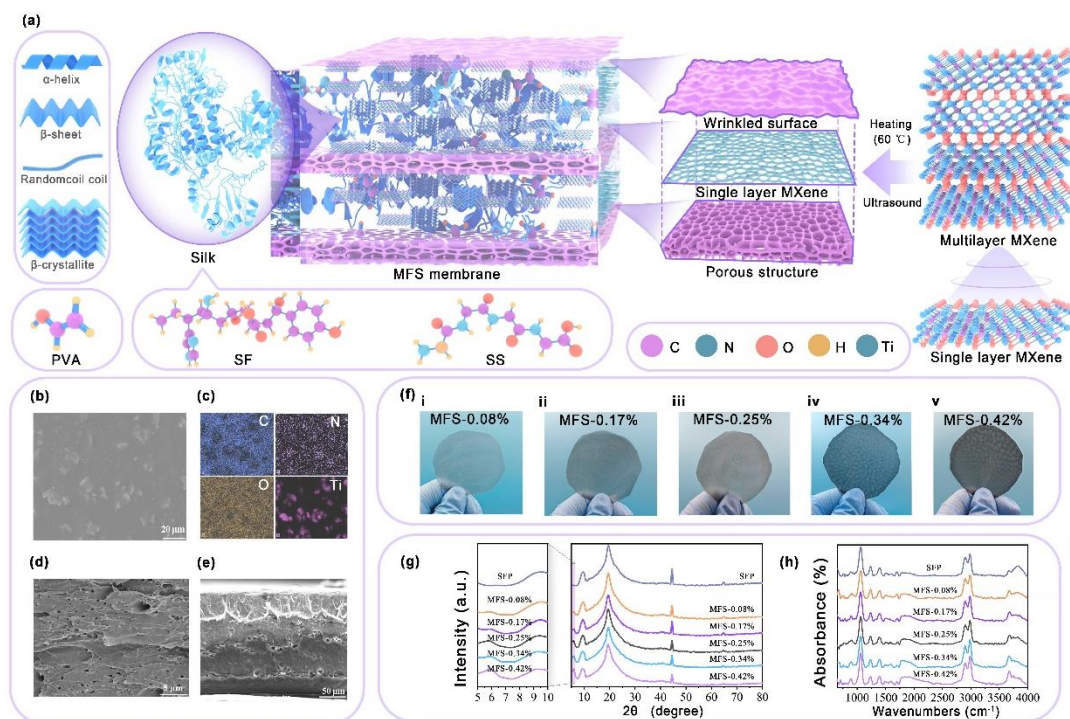


Fig.6. 2 Concept, fabrication, and characteristics of MFS films: a. Schematic illustration of the structure of the hierarchical porous MFS film; b. surface morphology of MFS-0.25% film; c. EDS of the MFS-0.25% film including C, N, O, and Ti element; d and e. Cross-sectional morphologies of the MFS-0.25% film; f. Digital photos of the fabricated MFS membranes with contrasting MXene content; g. XRD spectra of the MFS membranes; h. FTIR of diverse MFS membranes

Fig.6. 3 provides a series of MFS membranes with distinct MXene concentrations, showing the sectional view, magnified sectional enlargements, and surface morphologies. It is evident that excess MXene concentration leads to agglomeration in both the sectional and surface regions of the MFS films (Fig.6. 3 d1, e1, d2, and e2). Conversely, introducing a minimal amount of MXene primarily results in the formation of porous structures along the sides of the film (Fig.6. 3 b1 and c1). This phenomenon may be ascribed to the different evaporation rates of the solution's components, which lead to localized stress and structural reorganization during the drying process²⁷¹.

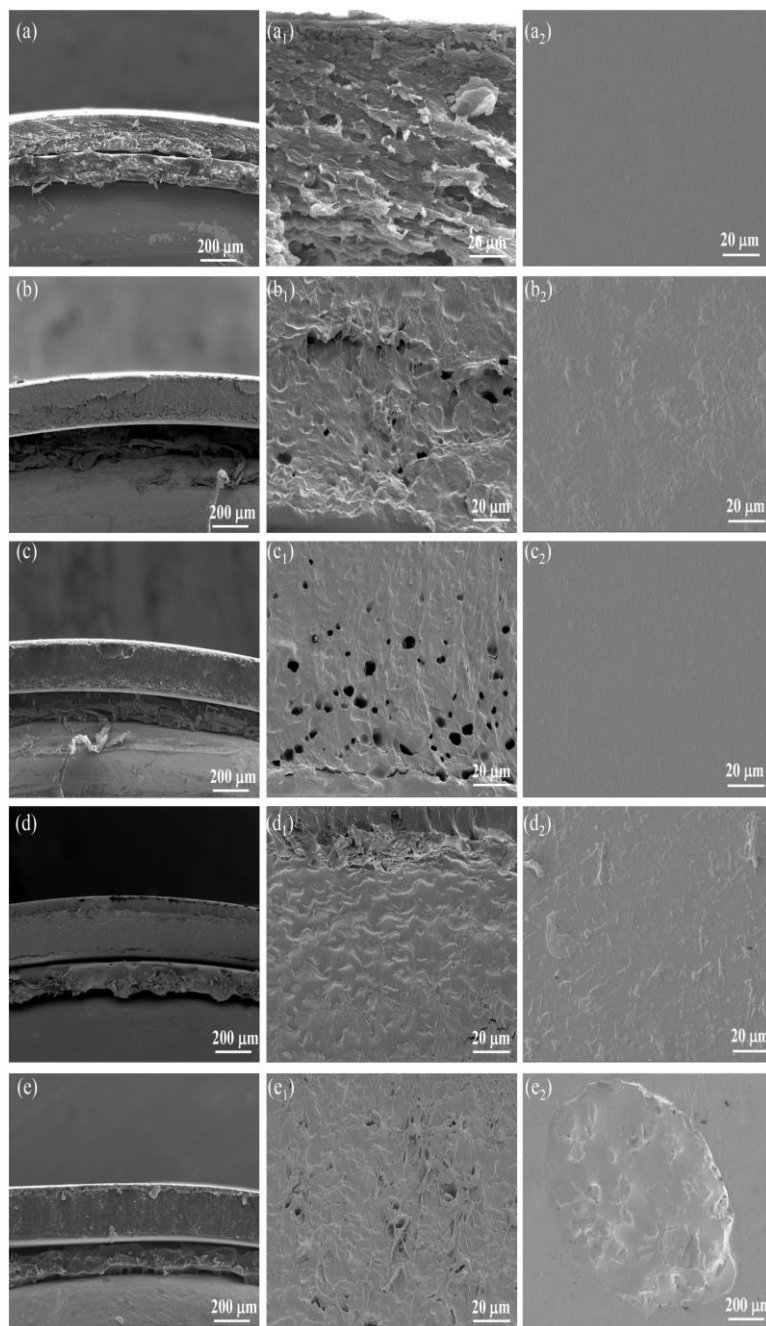


Fig.6. 3 Sectional view and surface morphologies of the MFS membranes: a. The sectional view of PVA/SF/SS membrane; a1. Partial enlargement of the sectional view of PVA/SF/SS membrane; a2. Surface morphology of PVA/SF/SS membrane; b. The sectional view of the MFS-0.08% membrane; b1. Partial enlargement of the sectional view of the MFS-0.08% membrane; b2. Surface morphology of the MFS-0.08% membrane; c. The sectional view of the MFS-0.17% membrane; c1. Partial enlargement

of the sectional view of the MFS-0.17% membrane; c2. Surface morphology of the MFS-0.17% membrane; d. The sectional view of the MFS-0.34% membrane; d1. Partial enlargement of the sectional view of the MFS-0.34% membrane; d2. Surface morphology of the MFS-0.34% membrane; e. The sectional view of the MFS-0.42% membrane; e1. Partial enlargement of the sectional view of the MFS-0.42% membrane; e2. Surface morphology of the MFS-0.42% membrane.

Additionally, the hierarchical configuration of the original MXene nanosheets, comprising at least 20 layers, is illustrated in Fig.6. 4a. The energy-dispersive spectroscopy (EDS) analysis of the MFS-0.08% sectional view further corroborates the successful integration of MXene nanosheets into the PVA/SF/SS (SFP) matrix, as displayed in Fig.6. 4b.

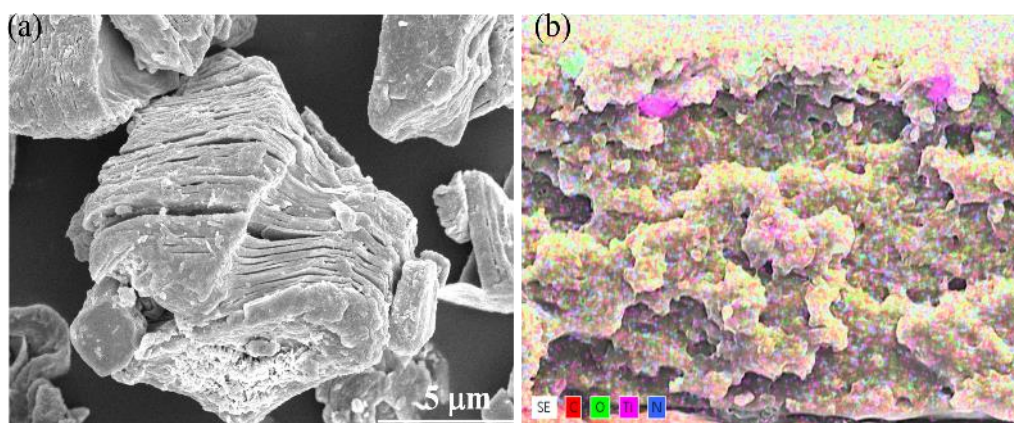


Fig.6. 4 a. SEM of MXene nanosheets; b. EDS of the MFS-0.08% membrane for the sectional view.

The photographs (Fig.6. 2f) illustrate the transition of the MFS membrane from transparent to opaque with increasing MXene content, in alignment with the UV transmittance spectra presented in Fig.6. 5. Notably, the surfaces of the MFS-0.34% and MFS-0.42% membranes display hexagonal light rings, which are possibly ascribed to the aggregation of surplus MXene, an observation further corroborated by the SEM images in Fig.6. 3 d1 and e1.

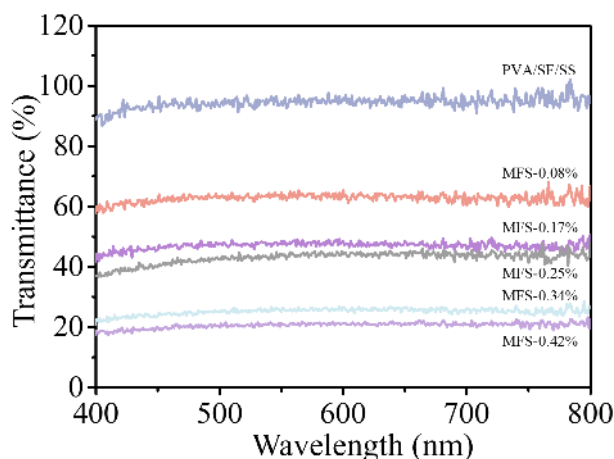


Fig.6. 5 UV Transmission of the MFS membranes

As clearly illustrated in Fig.6. 2g, upon the incorporation of MXene into the SFP matrix, the unaltered presence of the characteristic peak at 9.8° , in contrast to the original SFP matrix, suggested that this peak is pertained to the silk II structure instead of MXene. Conversely, the emergence of a distinct peak at 5.94° , absent in the original SFP matrix, indicated the potential characteristic peak of MXene. Furthermore, the anticipated characteristic peak of MXene, initially expected within the range of 8° - 10° , exhibited a noticeable shift^{272,273}. According to Bragg's law ($2d\sin\theta=n\lambda$), the decrease in θ indicated an increase in the spacing between the MXene nanosheets, suggesting that the SS interwoven within the MXene effectively hinders its aggregation²⁷⁴. The appearance of a peak at 20° corresponds to the β -sheet conformation, signifying that the inclusion of MXene does not affect the β -sheet structure²⁷⁵. Conversely, the attenuation of the broad peak at 24 – 25° in the original silk, attributed to silk I structure such as α -helix, random coil, and β -turn, implies the formation of a stable silk II structure.

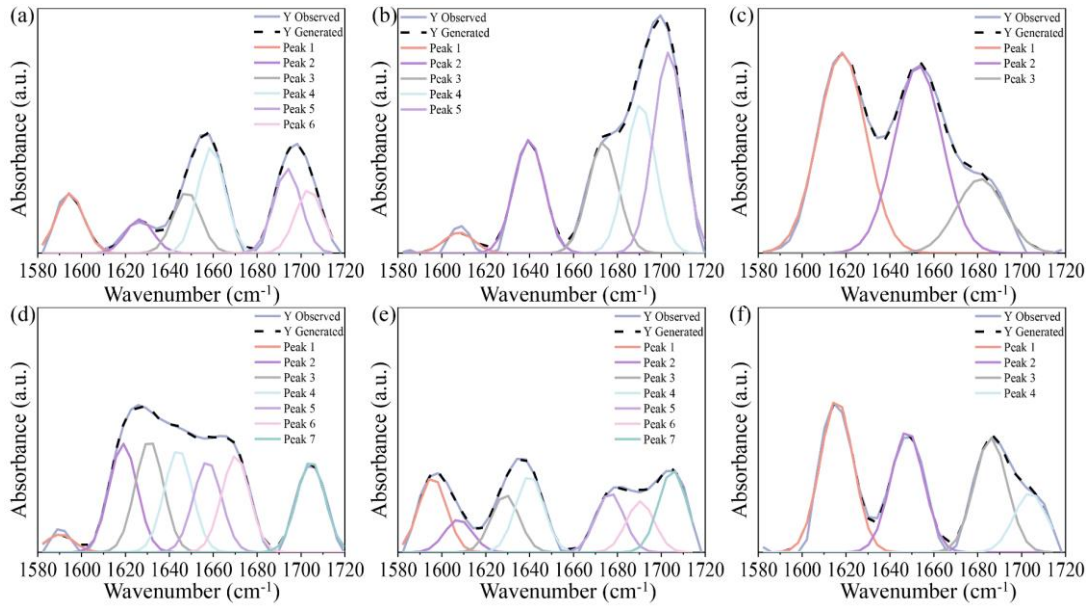


Fig.6. 6 Deconvolution of the amide I region (1580~1720) of FTIR spectra of MSF membranes. a PVA/SF/SS; b MFS-0.08%; c MFS-0.17%; d MFS-0.25%; e MFS-0.34%; f MFS-0.42%

FTIR was employed to qualitatively analyze the secondary structure of MFS membranes, as illustrated in Fig.6. 2h. To gain deeper insights into the secondary structure and molecular cross-linking, a quantitative analysis was performed through the deconvolution of the MFS membrane amide I band on FTIR (ranging from 1,580 to 1,720 cm^{-1}), as presented in Fig.6. 6 and Table 6. 2. The FTIR data revealed peaks at 1,605–1,615 cm^{-1} (Tyr side chains/aggregated strands), 1,616–1,621 cm^{-1} (aggregate β -strand/weak intermolecular β -sheets), 1,622–1,627 cm^{-1} (strong intermolecular β -sheets), 1,628–1,637 cm^{-1} (strong intramolecular β -sheets), 1,638–1,646 cm^{-1} (random coils/extended chains), 1,647–1,655 cm^{-1} (random coil), 1,656–1,662 cm^{-1} (α -helices), 1,663–1,696 cm^{-1} (β -turns), and 1,697–1,703 cm^{-1} (weak intermolecular β -sheets)²³². SFP membranes exhibit strong intermolecular β -sheets, while the incorporation of MXene transforms this conformation into intramolecular β -sheets (MFS-0.25% and MFS-0.34%), potentially due to the disaggregation effect of SS, which promotes cross-distribution within the inter-nanosheet spaces of MXene²⁷⁴. With the addition of a minimal amount of MXene (MFS-0.08%), SF and SS fibers

agglomerate, as evidenced by the appearance of aggregated strands illustrated in Table 6. 2. As the incorporation of MXene continues, two forms of β -sheets emerge: weak intermolecular β -sheets (MFS-0.17% and MFS-0.25%) and strong intramolecular β -sheets (MFS-0.25% and MFS-0.34%). An excessive amount of MXene (MFS-0.42%), however, inhibited the formation of any β -sheet structures, likely due to the agglomeration of MXene nanosheets, as indicated in Fig.6. 3 d1, e1, d2, and e2. Notably, inter- and intramolecular β -sheets are formed only in the MFS-0.25% membrane.

Table 6. 2 Relative contents of secondary structures through FTIR test

Membrane	β -sheet aggregate			(Tyr) side chains/ aggregated strands	Random coil	β -turn	α -helix	Others
	β -sheets sa	β -strand/ β -sheets wa	β -sheets sb					
SFP	8.28	0	0	0	15.05	20.61	25.86	30.20
MFS-0.08%	0	0	0	3.48	19.08	43.69	0	33.75
MFS-0.17%	0	43.34	0	0	40.59	16.07	0	0
MFS-0.25%	0	17.50	18.11	0	16.59	15.55	14.66	17.59
MFS-0.34%	0	0	13.22	7.52	17.71	25.37	0	36.18
MFS-0.42%	0	0	0	34.09	27.13	25.54	0	13.24

wa: Weak Intermolecular beta-sheets; sb: Strong Intramolecular beta-sheets

The tensile properties of synthetic composite films are paramount in ensuring its mechanical strength, durability, and performance across diverse applications. The tensile strength and strain curves are presented in Fig.6. 7a with its summarized statistics shown in Fig.6. 7b. As illustrated in Fig.6. 7a and b, as the MXene content increased, the tensile strength of the MFS films rose, reaching a peak at MFS-0.25% before declining. In contrast, the tensile strain of the MFS films was found to follow an inverse tendency. The strongest tensile strength observed in MFS-0.25% was mainly attributed to the formation of intermolecular and intramolecular β -crystalline structures, as detailed in Table 6. 2. Additionally, the reduction in tensile strength at higher MXene concentrations is likely due to the aggregation of MXene nanosheets, as depicted in Fig.6. 3 d1, d2, e1, and e2, alongside a decrease in β -sheets content and the emergence of aggregated strands, also noted in Table 6. 2.

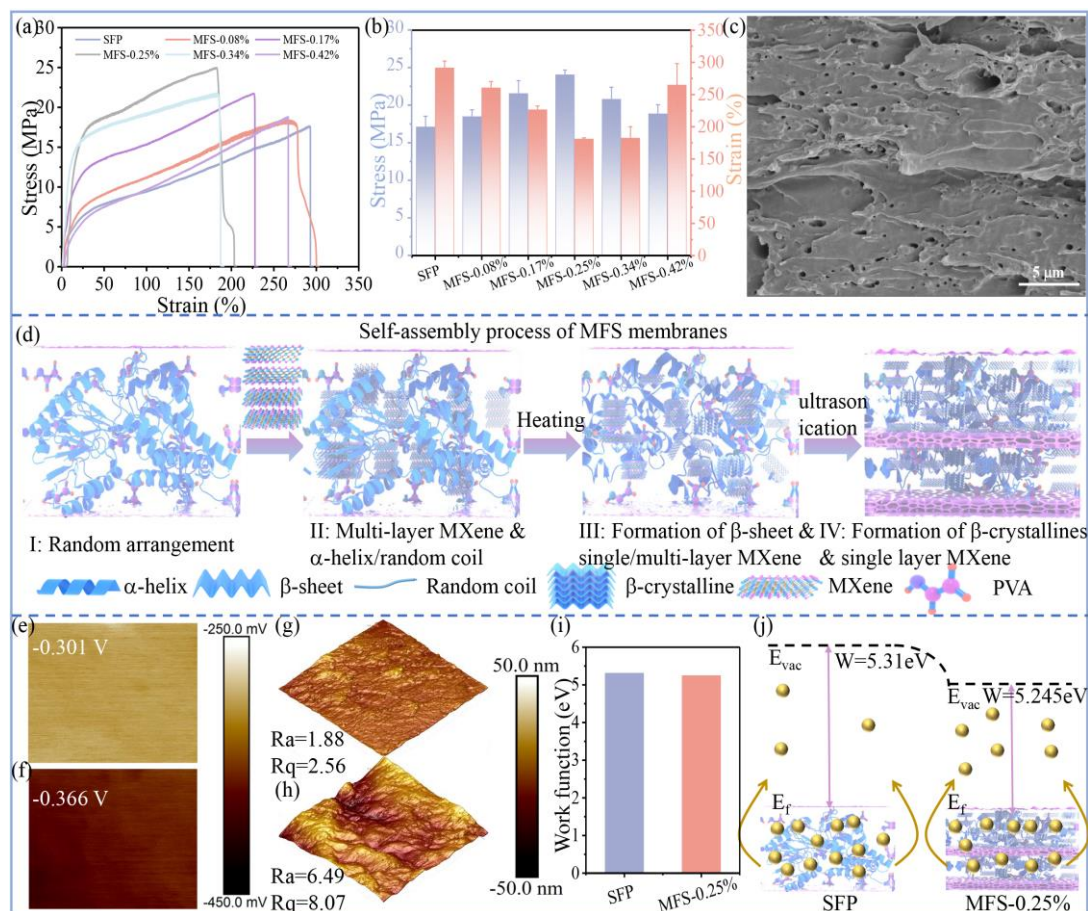


Fig.6. 7 Structural characteristics of the MFS membranes: a. Representative stress-strain curve of different MFS films; b. Summary of stress and strain of varied MFS membranes; c. The surface morphology of the MFS-0.25% membrane after the tensile fracture; d. The potential self-assembly process of the MFS membranes; e. The surface potential difference of the SFP membrane; f. The surface potential difference of the MFS-0.25% film; g. The roughness of the SFP membrane; h. The roughness of MFS-0.25% membrane; i. The work function of SFP membrane and MFS-0.25% membrane; j. Diagram of the work function changes for SFP membrane and MFS-0.25% membrane

The surface morphologies of the MSF membranes post-fracture were investigated to gain a profound understanding of the fracture process, as presented in Fig.6. 7c and Fig.6. 8. The pristine SFP membrane reveals a surface morphology characterized by silk fibers encapsulated within the PVA matrix. However, with the incorporation of MXene, the fracture surface predominantly exhibits parallel-aligned MXene

nanosheets, resulting in relatively smooth and orderly fracture planes. In conjunction with the stress-strain curve, this suggests that the MFS membranes undergo brittle fracture, indicative of a crystalline-dominated structure within the MFS membrane.

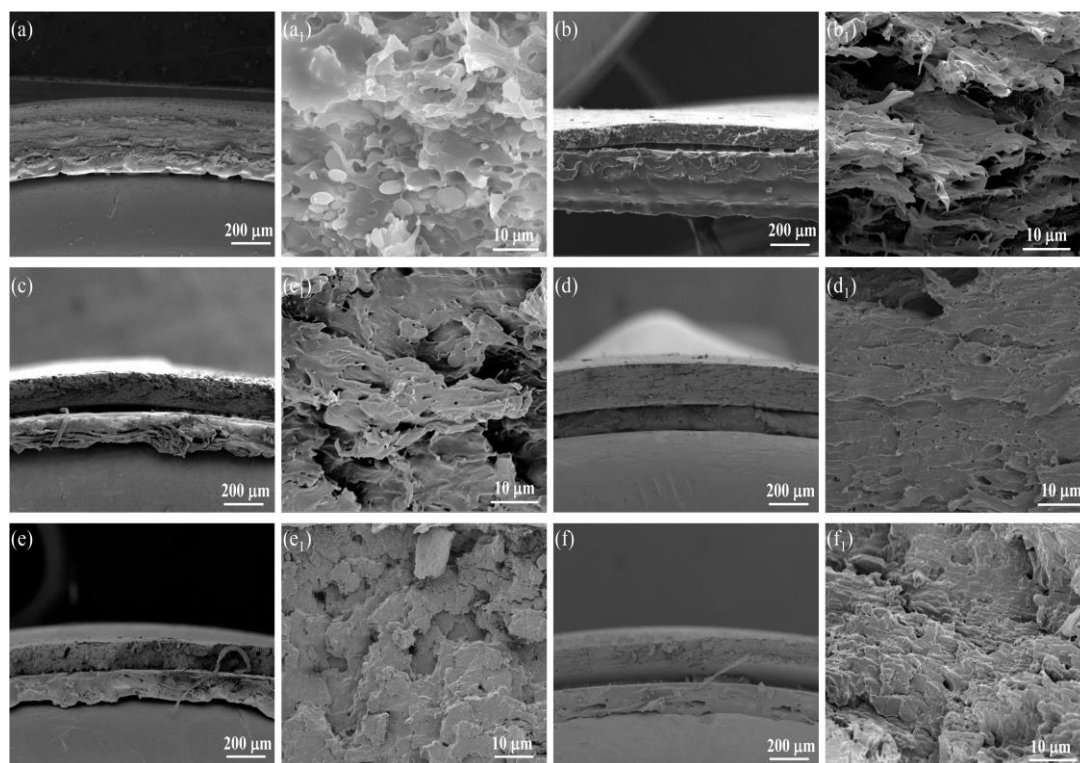


Fig.6. 8 Surface morphology of the MFS membranes after the tensile fracture: a and a₁: the surface morphology of the PVA/SF/SS membrane after the tensile fracture; b and b₁: the surface morphology of the MFS-0.08% membrane after the tensile fracture; c and c₁: the surface morphology of the MFS-0.17% membrane after the tensile fracture; d and d₁: the surface morphology of the MFS-0.25% membrane after the tensile fracture; e and e₁: the surface morphology of the MFS-0.34% membrane after the tensile fracture; f and f₁: the surface morphology of the MFS-0.42% membrane after the tensile fracture.

Fig.6. 7d provides a potential mechanism for forming β -crystalline and single MXene nanosheets. Initially, a substantial amount of amorphous structures such as α -helix, random coil, and β -turn were present in the SFP matrix i. With the addition of MXene, multilayered MXene was introduced into the solution, temporarily disrupting these amorphous regions without inducing the formation of crystalline structures, as

indicated by Table 6. 2 for MFS-0.08% (II). Under the influence of temperature, the multilayered MXene began to partially exfoliate into monolayers owing to the dispersive effect of SS, while the elevated temperature also facilitated the transition of amorphous structures into crystalline structures, forming a modest amount of β -sheets (III). Ultimately, ultrasonication dispersed the multilayered MXene into monolayers, thereby promoting the formation of a significant quantity of β -crystalline structures and achieving a highly ordered arrangement within the MFS membrane (IV).

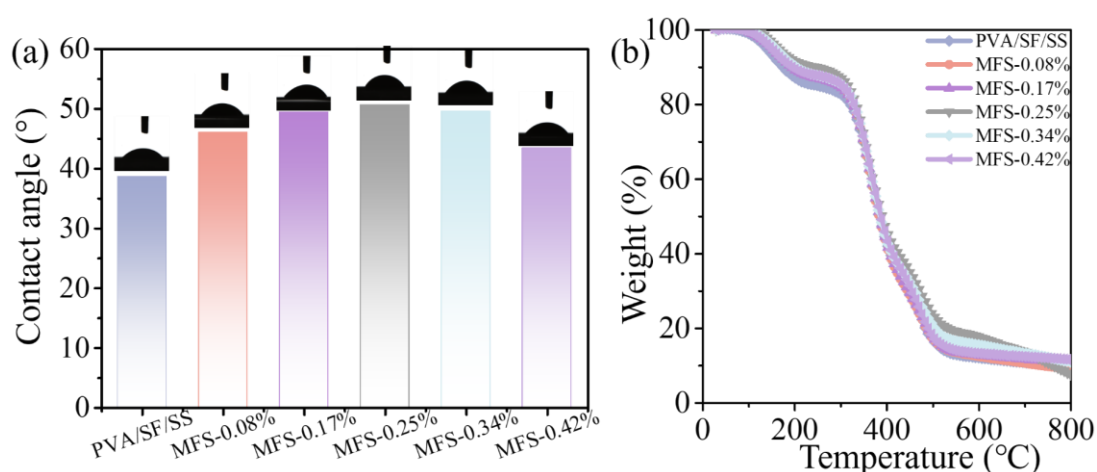


Fig.6. 9 a. Contact angles of the MFS membranes; b. TGA results of the MFS membranes.

The contact angle of the MFS membrane was measured to further elucidate its secondary structure alongside its hydrophilic and hydrophobic properties. As depicted in Fig.6. 9a, the pristine SFP membrane exhibited a contact angle of 38°. Following the introduction of MXene, the MFS-0.25% membrane reached the maximum contact angle of 52°, suggesting an increased crystalline content and hydrophilic properties, consistent with the results presented in Table 6. 2. The thermal stability of the MFS membrane was assessed through thermogravimetric analysis (TGA). The results revealed three distinct transitional phases (Fig.6. 9b): the initial phase, occurring around 100 °C, is attributed to water evaporation; the second phase, ranging from 150 to 310 °C, involves the degradation of α -helix and random coil structures; and the third phase, occurring between 310 and 530 °C, is associated with the decomposition of well-

oriented crystalline regions²³⁸. Notably, the MFS-0.25% membrane exhibited a higher content in the third phase, indicating a more stable structural configuration.

Based on the molecular mechanisms discussed previously, the subsequent analysis of the surface potential difference offers deeper insights into the structural characteristics influenced by the introduction of MXene nanosheets. As presented in Fig.6. 7e and f, the surface potential value of the MFS-0.25% membrane increased to 0.366 V, compared to 0.301 V for the SFP membrane. The enhancement may be ascribed to the conductivity of MXene, creating new pathways for electron transfer. Additionally, the elevated surface roughness of the MFS-0.25% membrane, with a roughness value of 6.59 (Fig.6. 7h) compared to 1.88 for the SFP membrane (Fig.6. 7g), may also contribute to the enhancement of surface potential²⁷⁶. The larger effective surface area enhances interactions between the membrane and its surrounding environment, potentially increasing the surface potential. Furthermore, the modified topography of the MFS membrane, characterized by enlarged peaks and valleys (Fig.6. 2b), creates localized areas of higher or lower potential, further contributing to the observed increase in surface potential.



Fig.6. 10 CPD of the Au

The alteration of surface topography is likely to affect the work function of the membrane, indicating changes in its electronic structure and surface energy. The work function denotes the minimum thermodynamic work necessary to extract an electron from the surface of a solid to a point in the vacuum just beyond that surface. It is calculated by the following formula²⁷⁷:

$$W = 5.1eV + e \times CPD(sample) - e \times CPD(Au) \quad (6-1)$$

Where CPD denotes the contact potential difference obtained by the KPFM, with CPD (Au) valued at -0.511 V (Fig.6. 10). Typically, electrons move from the material with a lower work function to one with a higher work function to minimize the system's overall energy. As displayed in Fig.6. 7i, the work function of the SFP film was measured at 5.3 eV and after the incorporation of MXene, the work function decreased to 5.25 eV, indicating a significant enhancement in the conductivity of the composite MFS film. In addition, a reduced work function implies that more electrons can overcome their binding energy, thus facilitating the electron transfer process, as depicted in Fig.6. 7j.

6.3.2 Mechanism of the MFS/F-SETENGs

The schematic working mechanism and simulation of potential distribution are presented to understand the charge-generating and transferring process better. Fig.6. 11a illustrates the electron generation process of our proposed MFS/F-SETENGs in the working cycles. Once the F-Nylon is in complete contact with the MFS membrane, negative triboelectric charges are seized by the F-Nylon layer owing to its negative tribo-polarity, whereas the MFS layer is positively charged. Upon experiencing a relative displacement between the F-Nylon layer and the MFS composite, negative electrostatic charges are generated on the CNF electrode to neutralize the triboelectric charges. This action creates a voltage differential between the CNF electrode and the ground, prompting a flow of electrons from the ground toward the CNF electrode via the external circuit (ii). The impermanent flow of external electrons continues until the device reaches a state of full separation (iii). As the F-Nylon membrane re-approaches the MFS layer, the negative electrostatic charges previously induced on the CNF electrode begin to wane, causing electrons to reverse their flow back towards the ground (iv). Through the periodical process of contact and separation within the MFS/F-SETENGs, an alternating current is consistently generated⁵⁴. To gain a more quantitative understanding of the operational mechanism of the constructed MFS/F-SETENGs, a corresponding COMSOL simulation was performed for the electric potential distribution, as shown in Fig.6. 11b.

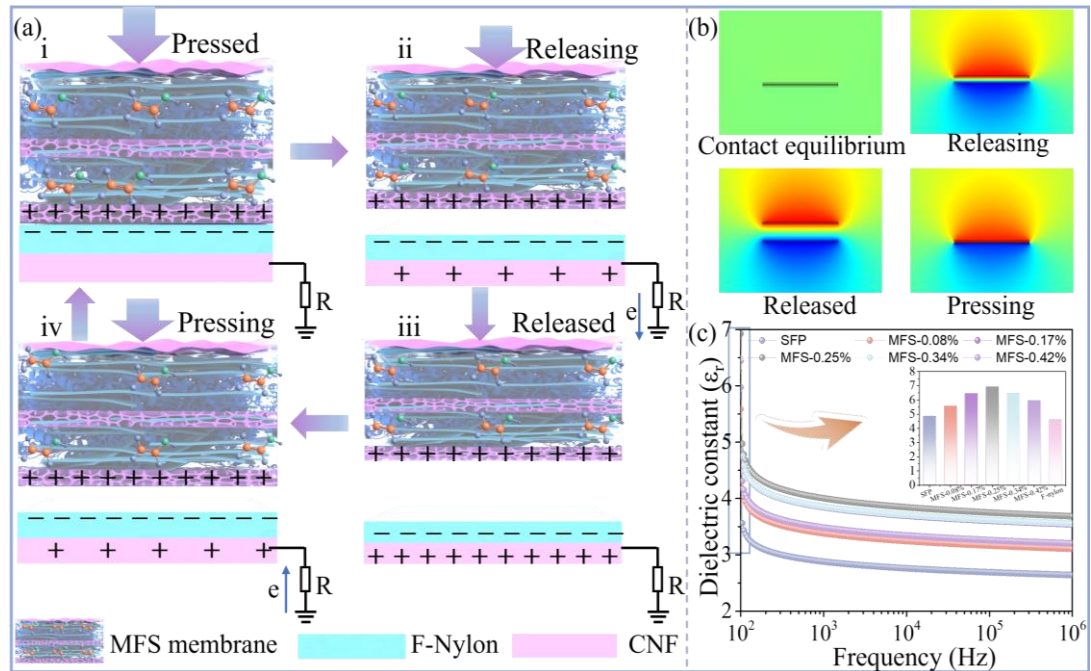


Fig.6. 11 The working mechanism of the MFS/F-SETENGs: a. The illustration of the electricity transferring process in a full cycle of the TENG; b. COMSOL simulation on the potential distribution in the TENG; c. The dielectric constant of different MFS membranes

Modifying the dielectric properties is recognized as an effective approach to increase the surface density of triboelectric charges and enhance charge retention, thereby amplifying the overall output efficiency. The two-dimensional MXene is considered a filler to boost the dielectric characteristics of the SFP composite owing to its substantial dielectric constant¹²⁵. As depicted in Fig.6. 11c, the inclusion of MXene into the SFP blend elevates the dielectric constant from 4.85 (for SFP) to 6.92 (for MFS-0.25%), but further addition of MXene results in a decrease to 4.62 (for MFS-0.25%) at a frequency of 100 Hz. This behavior can be attributed to several factors: primarily, the high dielectric constant of MXene is a consequence of its stratified structure and the presence of numerous surface functional groups, which endow it with superior polarization capabilities and thus markedly improve the dielectric constant of the composite²⁷⁰. The integration of MXene generates microscale dipoles and capacitor networks within the composite's dielectric layer, significantly amplifying the dielectric constant of the MFS

membranes. However, excessive concentration of MXene likely aggregates in the SFP matrix, as shown in Fig. 6. 3 d1, d2, e1, e2, and Table 6. 2, destroying the dielectric properties of MFS membranes¹²⁴.

6.3.3 Electrical Output Performance of MFS/F-SETENGs

A constant external force of 5 N at a frequency of 3 Hz was applied to all the fabricated MFS/F-SETENGs, which comprised MFS membranes with varying MXene content, operating in single-electrode mode. The electrical outputs generated by the MFS/F-SETENGs were measured, as illustrated in Fig. 6. 12a-c. It was observed that the pure SFP membrane showed an electrical output of $\approx 5.5 \mu\text{A}$, 260 V, and 39 nC, respectively. With the incorporation of MXene, the electric outputs of the MFS membranes consistently increased until the peak at MFS-0.25% with a value of 748 V, 12.5 μA , and 47 nC, followed by a subsequent decline. This phenomenon can be elucidated by considering the following factors, with the dielectric constant being a primary consideration. Ideally, the TENG is composed of a conductive medium and a dielectric medium; thus, it can be modeled as a parallel plate capacitor. Enhancing the dielectric constant of the composite membrane can potentially elevate the electrical output of the TENG. The dielectric constant is highest at MFS-0.25%, but it starts to decrease with further addition of MXene, consistent with the trend of the electric outputs of the MFS membranes. From a molecular structural perspective, the peak performance at MFS-0.25% is attributed to the formation of both inter- and intramolecular β -sheets, resulting in a highly ordered crystalline structure, as clarified in Table 6. 2. The subsequent decline in electrical output is due to the aggregation of MXene, which impedes electron transfer (Fig. 6. 3 d1, d2, e1, and e2, and Fig. 6. 2f). Additionally, the work function values align with the resultant tendency. The work function of the MFS-0.25% membrane is lower than that of the pristine membrane, indicating that electrons in MFS-0.25% require less energy to transfer into the air, signifying more electron transfer between the triboelectric materials and thus corresponding to higher electrical output performance (Fig. 6. 7i and j).

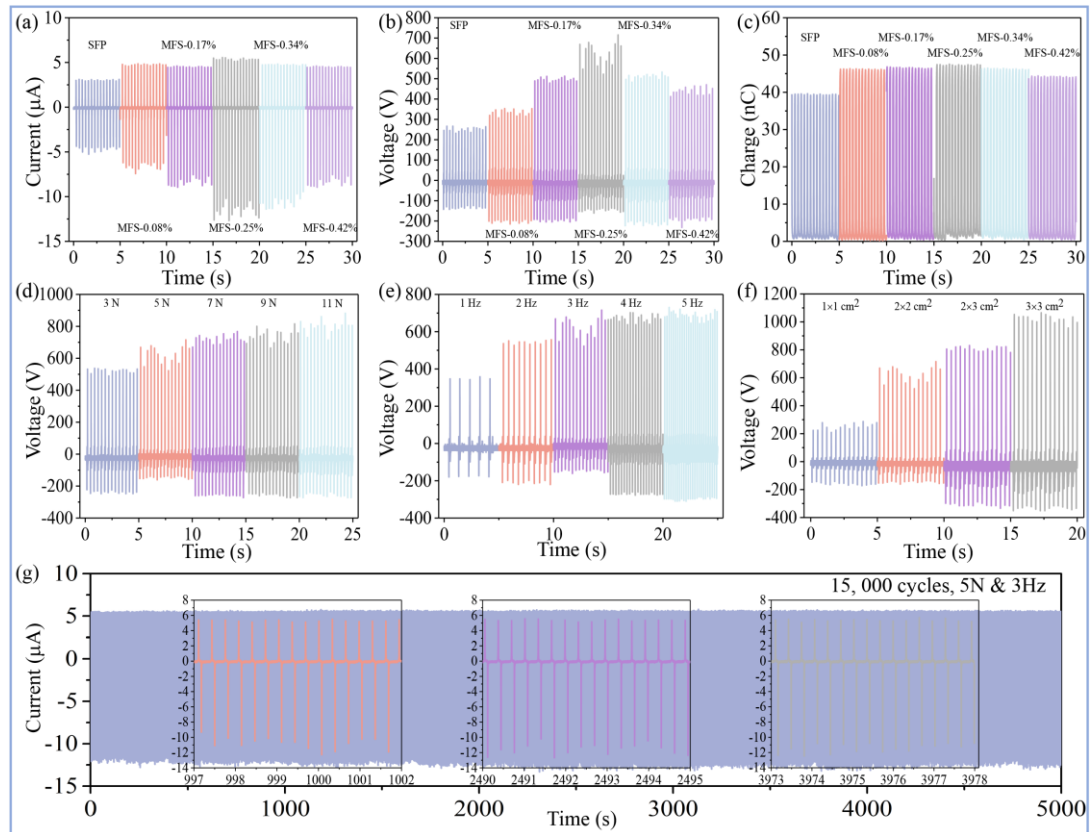


Fig.6. 12 Electrical output performance of the MFS/F-SETENGs: a. Current, b. Voltage, and c. Charge of the MFS/F-SETENGs under fixed frequencies of 3 Hz and applied force of 5 N; d. The voltage of the MFS-0.25% film applied different forces (3 N~11 N) with a fixed frequency of 3 Hz; e. Voltage of the MFS-0.25% film in various frequencies (1 Hz~5 Hz) with a fixed force of 5 N; f. Voltage of the MFS-0.25% film based on different areas (1, 4, 6, 9 cm²); g. Durability and stability test of MFS/F-SETENGs for 15,000 cycles. The insets exhibit detailed signals during the test cycles

Based on the optimized triboelectrification and dielectric properties, the operating conditions were subsequently investigated, including applied force and frequency, to further improve the output performance. The electric voltage values escalate from 570 V to 900 V with the augmentation of the applied force from 3 N to 11 N (Fig.6. 12d). This phenomenon can be attributed to the enhancement of induction electrification owing to the closer proximity of the friction layer resulting from the increased force²⁰⁷. Similarly, the voltage values of the MFS-0.25%/F-SETENG raised with an increased

frequency from 1 Hz to 5 Hz (Fig.6. 12e). The improved electric voltage can be attributed to three factors: the accelerated external electron flow, the incomplete neutralization of surface charges, and the facilitation of charge transfer coupled with the reduction in peak current duration, thereby contributing to a substantial increase in the magnitude of the short-circuit current²³³. In addition, the impact of the area on the electrical performance was evaluated. As demonstrated in Fig.6. 12f, when the contact area changed from 1 cm² to 9 cm², the voltages altered from 300 V to 1,100 V, indicating an effective way to improve the electrical properties of SETENGs. Durability plays a pivotal role in ensuring the adaptability and suitability of applications across diverse scenarios. The durability test was conducted, as depicted in Fig.6. 12g. It is observed that the voltage output of the MFS-0.25%/F-SETENG remained remarkably stable after 15,000 cycles of the beating test, indicating its exceptional wear resistance. This robustness underscores its potential for long-term application in real-world scenarios.

6.3.4 Application of MFS/F-SETENGs for Energy Harvesting

The effectiveness of MFS-0.25%/F-SETENG as a power source was also evaluated. Power density is an essential parameter for evaluating the TENG device in energy harvesting applications. By connecting the SETENG to various external loads ascending from 0.1 M Ω to 1,000 M Ω , the instantaneous power density can be achieved at 35.76 W/m² with the calculation of $P=U^2/RA$ at the matched resistance of 10 M Ω , as presented in Fig.6. 13a, where U represents the output voltage, R denotes the external load resistance, and A indicates the effective contact area. Our fabricated MFS-0.25%/F-SETENG demonstrates an elevated power density as compared to previously reported silk-based TENGs (SETENGs^{1, 36, 37, 123, 278} and double-electrode TENGs^{24, 29, 30, 33-35, 38, 117, 118, 122, 133, 134, 141, 142, 146, 147, 155, 229, 279, 280}), as displayed in Fig.6. 13b. Interestingly, the power density of our designed silk/F-SETENG is at least ten times higher than that of recently reported silk-based SETENGs, guaranteeing the further application of a swift charging process. With the high power density, various capacitors with different capacities were utilized to be charged by a rectifier, which converts the AC generated by the TENG into DC to power electronic devices. As shown in Fig.6.

13c, the MFS-0.25%/F-SETENG can charge a 0.22 μF capacitor to 15 V within only 30 seconds. The inset represents the equivalent electrical circuit that functions as the single-electrode TENG. Furthermore, the converted direct current can serve as a power supply for powering various electronic devices, such as an electronic calculator (Fig.6. 13d), a digital timer (Fig.6. 13e) and an electronic clock (Fig.6. 13f). Therefore, these findings highlight the substantial potential of our TENG for sustainable self-powered systems in wearable electronics.

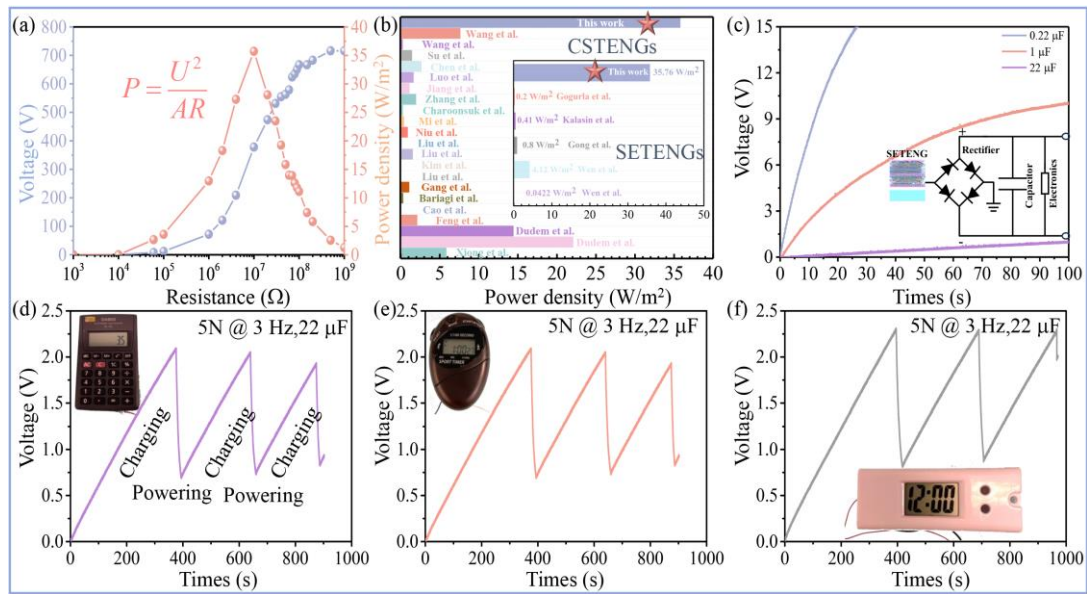


Fig.6. 13 Application of MFS/F-SETENGs considered as an energy harvester: a. Power density of MFS-0.25%/F-SETENG with different external load resistance; b. Comparison of the power density of our fabricated MFS-0.25%/F-SETENG with silk-based double-electrode TENGs^{24, 29, 30, 33-35, 38, 117, 118, 122, 133, 134, 141, 142, 146, 147, 155, 229, 279, 280}, and the inset is the comparison with other silk-based SETENGs^{1, 36, 37, 123, 278}; c. The MFS-0.25%/F-SETENG charging capacitors of different capacities, and the inset is the equivalent electrical circuit of MFS-0.25%/F-SETENG when working as a power supplier; Charging and powering small electronics of MFS-0.25%/F-SETENG: d. A calculator; e. A timer; and f. A clock

6.3.5 Application of MFS/F-SETENGs for Sensing

Owing to its excellent flexibility and extensibility (Fig.6. 2f), our MFS/F-SETENG is adept at monitoring a diverse range of hand gestures. By fixing the MFS/F-SETENG at the wrist, different bending angles of the wrist will generate distinct voltage signals, which can be used to monitor the wrist's flexion at various degrees, such as 30°, 45°, and 90° (Fig.6. 14a, b, and c). Specifically, a bending angle of 30° produces a voltage of 60 V, 45° results in 75 V, and 90° yields 90 V. Notably, the voltage peak at 30° is relatively broad. At the same time, the signal becomes increasingly sharper as the bending angle increases. This capability arises from the changes in bending angles, which affect the signal amplitude and shape. Our designed MFS/F-SETENG can also be applied to various parts of the human body, such as fingers, as illustrated in Fig.6. 14d, e, and f. Similar to wrist detection, varying the bending angles of the fingers results in distinct electrical signals. As the bending angle increases, the generated voltage signal correspondingly rises, which is attributed to the larger effective contact area that occurs with greater degrees of flexion. The sensitivity of our device to these subtle changes underscores its precision and efficacy in monitoring fine motor movements. Additionally, attaching our designed MFS/F-SETENG to the soles of shoes enables the detection of various movement patterns, including walking, running, and jumping. As illustrated in Fig.6. 14g, h, and i, the voltage signals generated during these activities exhibit distinct characteristics. Specifically, the signal produced during jumping is relatively sharp and pronounced, reflecting the abrupt and forceful nature of the motion. In contrast, the signal associated with walking is more gradual and smoother, indicative of steady and rhythmic movement. On the other hand, running generates a signal that is intermediate in sharpness, capturing the rapid yet continuous motion.

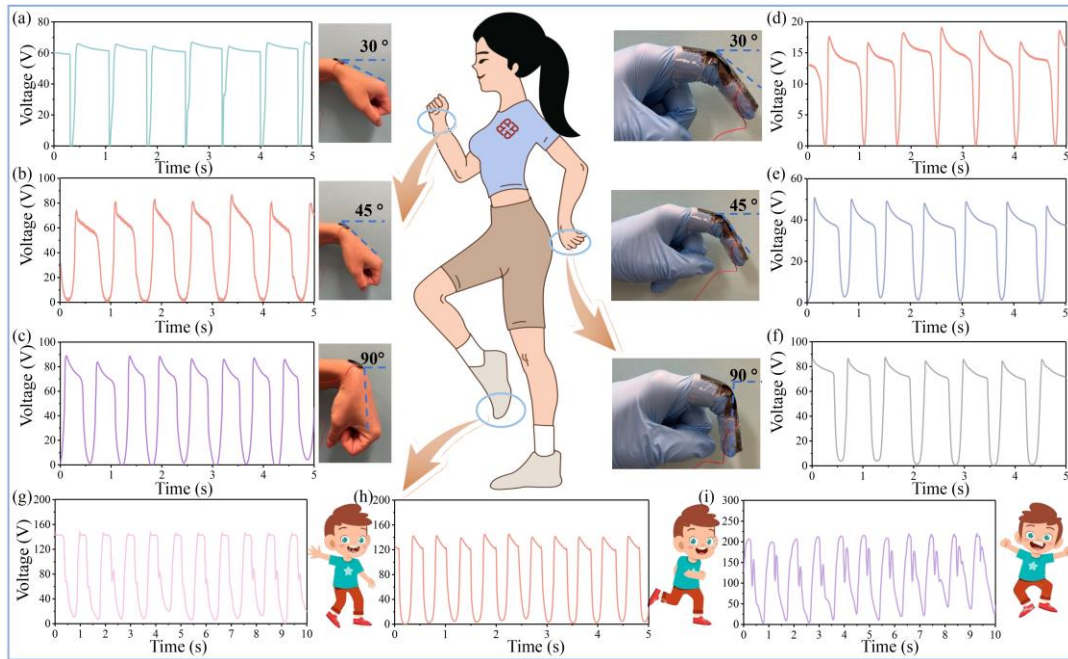


Fig.6. 14 The applications of MFS/F-SETENG as a self-powered wearable sensor for human motion monitoring: Wrist motion detection at different angles: a. 30°; b. 45°; c. 90°; Finger bending detection at varying angle d. 30°; e. 45°; f. 90°; The MFS/F-SETENG is applied for the detection of g. Walking; h. Running detection; i. Jumping

Apart from human gesture monitoring, the fabricated MFS/F-SETENG can be integrated with smartphones and multi-channel devices to enable real-time sensing. For instance, the MFS/F-SETENG device demonstrated the capability to facilitate Bluetooth signal transmission to a smartphone by affixing it to a finger. The tapping actions detected by the sensing device generate signals that are transmitted via a Bluetooth module to the smartphone, where they are instantaneously displayed (Fig.6. 15a). This capability demonstrates the feasibility of using the MFS/F-SETENG for portable motion monitoring and tracking of finger tapping, as well as its potential application in health-related alarm systems.

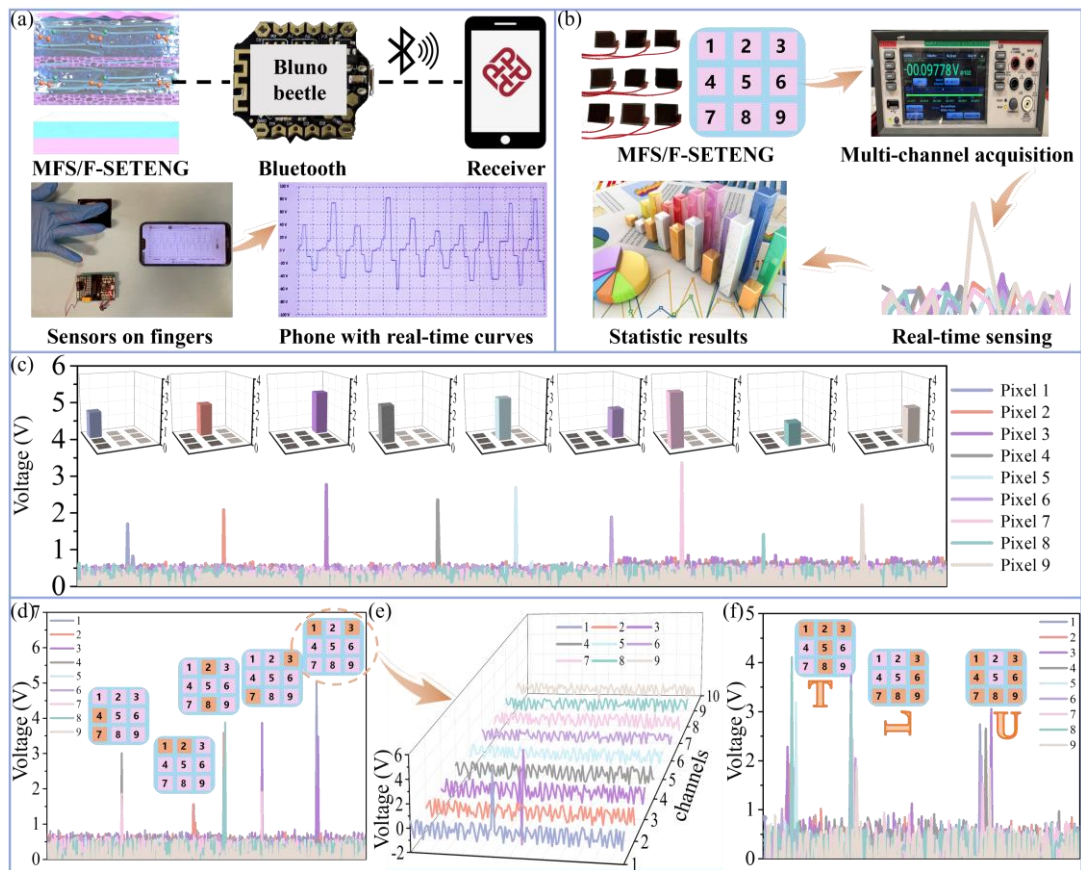


Fig.6. 15 Practical applications of the MFS/F-SETENG in self-powered sensing: a. The Bluetooth signal transmission system by tapping the MFS/F-SETENG; b. The schematic diagram of the pressure-sensing system includes the optical and schematic diagram with 3×3 channels, multichannel acquisition, real-time sensing, and statistic results; c. Real-time output voltage signals in tapping different pixels in the order of 1, 2, 3, 4, 5, 6, 7, 8, and 9; d. Real-time output voltage signals in tapping different channels in the order of 47, 12, 28, 37, and 13; e. Enlarged output voltage signals of 13 pixels; f. Pressure distribution of the MFS/F-SETENG sensor in sensing different letter located in the sensing arrays

In addition, the MFS/F-SETENG integrated into 3×3 arrays numbering from 1 to 9 could offer capabilities in recognizing tactile trajectories and detecting pressure distributions, as depicted in Fig.6. 15b. When fingers press various channels, distinct voltage signals corresponding to each channel are generated, enabling effective sensing and identification. Based on such a premise, a single-channel recognition was

conducted by pressing individual channel, enabling us to obtain voltage signals from all nine channels in the arrays and accurately identify the corresponding channels (Fig.6. 15c). The insets provide a detailed representation of the pressure distribution across the nine channels under continuous finger interaction. Furthermore, dual-channel recognition was investigated by simultaneously pressing two adjacent channels, such as channel 12 and 47. This approach not only facilitated the identification of these closely positioned channels but also enabled the detection of distant channels, such as 28, 13, and 37 (Fig.6. 15d). Additionally, Fig.6. 15e presents a detailed distribution of voltage signals, highlighting the signal output for each channel when dual-channel 13 was activated. It is apparent that the other channels remained inactive, whereas the channel subjected to pressure displayed a distinct pulsed signal output. The multi-channel sensor also possesses the capability to recognize various letters, facilitating simultaneous five-channel sensing or more. For example, it can accurately identify letters such as T, L, and U (Fig.6. 15f). This series of sensing capabilities indicates the sensor's potential applications in various sensing scenarios such as human healthcare monitoring and human-computer interaction.

6.4 Summary

In summary, an innovative MFS/F-SETENG has been designed and developed, featured with an MFS film acting as the positive tribolayer with meticulously engineered pore structures and rough surface morphology. By incorporating highly conductive two-dimensional MXene materials into the SFP matrix, the developed MFS/F-SETENG illustrates an exceptional instantaneous power density of 35.76 W/m^2 and generates a voltage of 748 V with an area of 4 cm^2 . The electrical performance of the MFS/F-TENG was comprehensively evaluated with varying MXene concentrations. Moreover, the dielectric constant and work function of the MFS membranes were analyzed in relation to their secondary structure. This MFS/F-SETENG efficiently powers small electronic devices, such as calculators, timers, and clocks, and functions as a sensor for detecting human gestures and facilitating multichannel sensing through computer interfaces. This study provides valuable insights into the advancement of

high-performance, silk-based SETENGs, thereby contributing to the domains of flexible electronics, energy harvesting, and sensing technologies.

CHAPTER 7 Conclusions and Suggestions for Future Research

7.1 Conclusions

With the research background of silk-based TENGs for energy harvesting, the current research challenges and gaps in this field were properly pointed out. Next, a comprehensive literature review on silk-based TENGs was presented, including natural fibrous-based TENG, an in-depth examination of silk's structure, the preparation method for fabricating silk-based TENG, and the diverse configurations of TENGs derived from silk, including those based on pure silk membranes and composite silk membranes, as well as methods like silk electrospinning, spraying, 3D printing, gel formation, and fibrous techniques. The applications of silk-based TENGs were also concluded, which encompass energy harvesters and sensors. Through identifying the existing challenges, corresponding strategies to respond to them were proposed. Firstly, a novel silk-based TENG design (SCLs/PDMS-TENG) was introduced that employed an SCL as the tribolayer through a facial and effective process. The SCLs are biodegradable, biocompatible, and eco-friendly, effectively alleviating concerns associated with the environmental issues caused by the usage of many current materials. Subsequently, an SFP/F-TENG was developed that incorporates PVA, SF, and SS powders, a discarded silk byproduct material inspired by the structural composition of silkworm cocoons. All materials exhibited biocompatibility and skin-friendliness, and the incorporation of SS mitigates material waste and prevents water oxidation. Afterward, an advanced SFPAG/F-Nylon TENG (SFPAG/F-TENG) is designed that introduces AgNWs into the SFP matrix to significantly enhance conductivity. Finally, an SFP/MXene (MFS)/F-Nylon single-electrode TENG (MFS/F-SETENG) is constructed with enhanced electrical performance by integrating MXene into the SFP substrate. The structural simplicity and optimized configuration enable it to be applied in various applications. The SFP/F-TENG, SFPAG/F-TENG, and MFS/F-SETENG displayed ultra-high electrical performance, significantly exceeding the instantaneous

power density of most existing silk-based TENG configurations reported previously.

(1) A novel TENG based on a natural biological structure was successfully designed and developed, utilizing a pristine silkworm cocoon layer integrated with polydimethylsiloxane (SCLs/PDMS). This design is characterized by its environmental compatibility and skin-friendly properties. The proposed SCLs/PDMS-TENG demonstrates a novel architecture resembling a nonwoven structure, achieved through a straightforward and effective peeling method. Benefiting from the natural structure disparities of the silkworm cocoon, the SCLs/PDMS devices exhibit diverse electrical performance, with the OL/PDMS-TENG attaining a voltage of 126 V. Furthermore, the proposed SCLs/PDMS-TENG maintain stable output voltage after 10,500 cycles. The engineered OL/PDMS TENG was utilized to power low-energy electronic devices and serve as effective sensors for monitoring physiological signals and joint movements.

(2) A novel bionic-inspired TENG was developed using an SFP membrane as the positive tribolayer and F-Nylon as the negative tribolayer (SFP/F-TENG), drawing inspiration from the intrinsic SF to SS ratio found in silkworm cocoons. The resulting SFP/F-Nylon-TENG exhibited enhanced electrical output by adjusting the SS proportion, achieving an impressive voltage of 494.47 V. The optimal SF to SS ratio of 3:1 was evaluated and discussed. These SFP membranes demonstrated an improved crystalline structure. The comprehension of SS-induced crystalline-enhancement mechanism on silk-based composites promises the potential of bionic design.

(3) A conductivity-enhanced composite membrane, designated as PVA/SF/SS/AgNWs (SFPAG), was synthesized by exploiting the superior conductivity of AgNWs and evaluated as the positive tribolayer. The tensile strain of the fabricated SFPAG membrane reached 132 %, conferring exceptional stretchability to the film. Additionally, all SFPAG membranes demonstrated hydrophilic properties, which facilitate excellent breathability, enhanced biocompatibility, and increased comfort in wearable applications. The resultant SFPAG/F-Nylon-TENG exhibited improved electrical performance, achieving a voltage of 745 V and an instantaneous power density of 7.6 W/m².

(4) An SFP/MXene (MFS)/F-Nylon single-electrode TENG (MFS/F-SETENG) was developed by incorporating the two-dimensional material MXene into the SFP substrate. The MFS membranes exhibited a decreased work function and enhanced coarse surface morphologies, elucidating the MXene-enhanced triboelectric performance mechanism. Benefiting from the benefits of structural simplicity and optimized configuration, this MFS/F-SETENG resulted in a voltage output of 745 V and an instantaneous power density of 35.76 W/m², significantly surpassing those achieved by more complex configurations. The MFS/F-SETENG exhibited excellent durability and stability after 15,000 cycles of the beating test, underscoring its exceptional wear resistance.

7.2 Limitations of the Study and Suggestions for Future Research

Although biocompatible, biodegradable, eco-friendly silk-based TENG devices have been successfully developed and fabricated, some potential challenges and limitations still need to be further addressed as follows:

(1) Limited fabrication methods like fiber and membrane are used to develop biocompatible, biodegradable, and eco-friendly silk-based TENG devices. To expand the versatility and functionality of these devices, other fabrication techniques such as gel formation, 3D printing, spraying, coating, and blended methods should be explored. For example, silk gel-based TENGs should be further developed and explored owing to their potential applications in next-generation energy solutions. These devices offer unique advantages, such as high flexibility, lightweight properties, and biocompatibility, making them ideal for integration into wearable electronics and biomedical devices.

(2) The secondary structure of the protein was discussed concerning the protein-enhanced mechanism of the triboelectric effect. However, the primary and tertiary structures are briefly discussed while the quaternary structures are even without being analyzed due to the time-intensive nature of computational simulations. It is suggested that Finite element simulation and COMSOL Simulation should be utilized to deeply explore the relationship between the electrical performance and the primary, tertiary, and quaternary structures, refining the understanding of silk-based TENG. In addition,

Orientation is another important aspect of fibers in determining their different properties; however, machine constraints and the scarcity of references addressing this factor have restricted our analysis. It is suggested that researchers should discuss the influence of the orientation of silk fibers on the electrical outputs.

(3) Limited AgNWs were utilized to explore the metal nanowires-enhanced triboelectric effect. It is suggested that a wider variety of metal materials, such as copper nanowires, gold nanowires, and aluminum nanowires, should be considered and incorporated. In addition, the synthesis time and temperature of nanowires, as well as the ratio between the matrix and precursor, and the impact of the formation of nanowires should be considered and explored. Selecting the appropriate metal materials should be matched to the specific characteristics of the matrix to optimize performance.

(4) This thesis concentrates on the limited structural design of silkworm cocoons. It is suggested that greater attention should be dedicated to the structural design to expand the applications of silk-based TENGs. The hierarchical structure of silk necessitates further structural design, including the arrangement of fibers within the initial silkworm cocoon and the use of fibers and binders to more accurately mimic these hierarchical structures.

(5) Future research should explicitly address the power efficiency of each device configuration. Understanding power efficiency is critical for evaluating the practical applicability of TENGs. This involves quantifying the energy conversion capabilities under various operating conditions. Systematic investigations should be conducted to assess the efficiency across different environmental conditions, loading scenarios, and operational modes.

Reference

1. Gong, H.; Xu, Z.; Yang, Y.; Xu, Q.; Li, X.; Cheng, X.; Huang, Y.; Zhang, F.; Zhao, J.; Li, S., Transparent, stretchable and degradable protein electronic skin for biomechanical energy scavenging and wireless sensing. *Biosensors and Bioelectronics* **2020**, *169*, 112567.
2. Wang, X.; Dong, L.; Zhang, H.; Yu, R.; Pan, C.; Wang, Z. L., Recent progress in electronic skin. *Advanced Science* **2015**, *2* (10), 1500169.
3. Chen, J.; Zhu, Y.; Chang, X.; Pan, D.; Song, G.; Guo, Z.; Naik, N., Recent progress in essential functions of soft electronic skin. *Advanced Functional Materials* **2021**, *31* (42), 2104686.
4. Zhao, J.; Wang, Y.; Song, X.; Zhou, A.; Ma, Y.; Wang, X., Flexible triboelectric nanogenerator based on polyester conductive cloth for biomechanical energy harvesting and self-powered sensors. *Nanoscale* **2021**, *13* (43), 18363-18373.
5. Han, S. T.; Peng, H.; Sun, Q.; Venkatesh, S.; Chung, K. S.; Lau, S. C.; Zhou, Y.; Roy, V., An overview of the development of flexible sensors. *Advanced Materials* **2017**, *29* (33), 1700375.
6. Gao, Y.; Li, Z.; Xu, B.; Li, M.; Jiang, C.; Guan, X.; Yang, Y., Scalable core–spun coating yarn-based triboelectric nanogenerators with hierarchical structure for wearable energy harvesting and sensing via continuous manufacturing. *Nano Energy* **2022**, *91*, 106672.
7. Radousky, H. B.; Liang, H., Energy harvesting: an integrated view of materials, devices and applications. *Nanotechnology* **2012**, *23* (50), 502001.
8. Callis, T. W.; Hu, K.; Al Jamal, H.; Tentzeris, M. M., Additively Manufactured, Flexible 5G Electronics for MIMO, IoT, Digital Twins, and Smart Cities Applications. *International Journal of High Speed Electronics and Systems* **2024**, 2440066.
9. Yun, J.; Jayababu, N.; Kim, D., Self-powered transparent and flexible touchpad based on triboelectricity towards artificial intelligence. *Nano Energy* **2020**, *78*, 105325.
10. Ma, Y.; Zhang, Y.; Cai, S.; Han, Z.; Liu, X.; Wang, F.; Cao, Y.; Wang, Z.; Li, H.; Chen, Y., Flexible hybrid electronics for digital healthcare. *Advanced Materials* **2020**, *32* (15), 1902062.
11. Fan, F.-R.; Tian, Z.-Q.; Wang, Z. L., Flexible triboelectric generator. *Nano Energy* **2012**, *1* (2), 328-334.

-
12. Niu, S.; Wang, S.; Lin, L.; Liu, Y.; Zhou, Y. S.; Hu, Y.; Wang, Z. L., Theoretical study of contact-mode triboelectric nanogenerators as an effective power source. *Energy & Environmental Science* **2013**, *6* (12), 3576-3583.
 13. Wang, Z. L., On Maxwell's displacement current for energy and sensors: the origin of nanogenerators. *Materials Today* **2017**, *20* (2), 74-82.
 14. Zhang, Z.; He, T.; Zhu, M.; Sun, Z.; Shi, Q.; Zhu, J.; Dong, B.; Yuce, M. R.; Lee, C., Deep learning-enabled triboelectric smart socks for IoT-based gait analysis and VR applications. *npj Flexible Electronics* **2020**, *4* (1), 1-12.
 15. Shi, J.; Liu, S.; Zhang, L.; Yang, B.; Shu, L.; Yang, Y.; Ren, M.; Wang, Y.; Chen, J.; Chen, W., Smart textile-integrated microelectronic systems for wearable applications. *Advanced Materials* **2020**, *32* (5), 1901958.
 16. Dong, K.; Peng, X.; Cheng, R.; Ning, C.; Jiang, Y.; Zhang, Y.; Wang, Z. L., Advances in High-Performance Autonomous Energy and Self-Powered Sensing Textiles with Novel 3D Fabric Structures. *Advanced Materials* **2022**, 2109355.
 17. Peng, X.; Dong, K.; Ye, C.; Jiang, Y.; Zhai, S.; Cheng, R.; Liu, D.; Gao, X.; Wang, J.; Wang, Z. L., A breathable, biodegradable, antibacterial, and self-powered electronic skin based on all-nanofiber triboelectric nanogenerators. *Science Advances* **2020**, *6* (26), eaba9624.
 18. Park, J.; Kang, D.-h.; Chae, H.; Ghosh, S. K.; Jeong, C.; Park, Y.; Cho, S.; Lee, Y.; Kim, J.; Ko, Y., Frequency-selective acoustic and haptic smart skin for dual-mode dynamic/static human-machine interface. *Science advances* **2022**, *8* (12), eabj9220.
 19. Dong, K.; Peng, X.; An, J.; Wang, A. C.; Luo, J.; Sun, B.; Wang, J.; Wang, Z. L., Shape adaptable and highly resilient 3D braided triboelectric nanogenerators as e-textiles for power and sensing. *Nature communications* **2020**, *11* (1), 1-11.
 20. Li, L.; Wang, X.; Hu, Y.; Li, Z.; Wang, C.; Zhao, Z., Understanding the Ferroelectric Polymer–Metal Contact Electrification for Triboelectric Nanogenerator from Molecular and Electronic Structure. *Advanced Functional Materials* **2022**, *32* (10), 2109949.
 21. Li, M.; Xu, B.; Li, Z.; Gao, Y.; Yang, Y.; Huang, X., Toward 3D double-electrode textile triboelectric nanogenerators for wearable biomechanical energy harvesting and sensing. *Chemical Engineering Journal* **2022**, *450*, 137491.
 22. Guan, X.; Xu, B.; Huang, J.; Jing, T.; Gao, Y., Fiber-shaped stretchable

triboelectric nanogenerator with a novel synergistic structure of opposite Poisson's ratios. *Chemical Engineering Journal* **2022**, 427, 131698.

23. Leem, J. W.; Fraser, M. J.; Kim, Y. L., Transgenic and diet-enhanced silk production for reinforced biomaterials: a metamaterial perspective. *Annual Review of Biomedical Engineering* **2020**, 22, 79-102.

24. Kim, H. J.; Kim, J. H.; Jun, K. W.; Kim, J. H.; Seung, W. C.; Kwon, O. H.; Park, J. Y.; Kim, S. W.; Oh, I. K., Silk nanofiber-networked bio-triboelectric generator: silk bio-TEG. *Advanced Energy Materials* **2016**, 6 (8), 1502329.

25. Zhang, J.; Kaur, J.; Rajkhowa, R.; Li, J.; Liu, X.; Wang, X., Mechanical properties and structure of silkworm cocoons: a comparative study of *Bombyx mori*, *Antheraea assamensis*, *Antheraea pernyi* and *Antheraea mylitta* silkworm cocoons. *Materials Science and Engineering: C* **2013**, 33 (6), 3206-3213.

26. Wang, C.; Xia, K.; Zhang, Y.; Kaplan, D. L., Silk-based advanced materials for soft electronics. *Accounts of Chemical Research* **2019**, 52 (10), 2916-2927.

27. Guo, Y.; Zhang, X.-S.; Wang, Y.; Gong, W.; Zhang, Q.; Wang, H.; Brugger, J., All-fiber hybrid piezoelectric-enhanced triboelectric nanogenerator for wearable gesture monitoring. *Nano Energy* **2018**, 48, 152-160.

28. Jiang, C.; Wu, C.; Li, X.; Yao, Y.; Lan, L.; Zhao, F.; Ye, Z.; Ying, Y.; Ping, J., All-electrospun flexible triboelectric nanogenerator based on metallic MXene nanosheets. *Nano Energy* **2019**, 59, 268-276.

29. Su, M.; Kim, B., Silk Fibroin-Carbon Nanotube Composites based Fiber Substrated Wearable Triboelectric Nanogenerator. *ACS Applied Nano Materials* **2020**, 3 (10), 9759-9770.

30. Jiang, W.; Li, H.; Liu, Z.; Li, Z.; Tian, J.; Shi, B.; Zou, Y.; Ouyang, H.; Zhao, C.; Zhao, L., Fully bioabsorbable natural-materials-based triboelectric nanogenerators. *Advanced Materials* **2018**, 30 (32), 1801895.

31. Mallineni, S. S. K.; Dong, Y.; Behlow, H.; Rao, A. M.; Podila, R., A wireless triboelectric nanogenerator. *Advanced Energy Materials* **2018**, 8 (10), 1702736.

32. Xu, Z.; Qiu, W.; Fan, X.; Shi, Y.; Gong, H.; Huang, J.; Patil, A.; Li, X.; Wang, S.; Lin, H., Stretchable, stable, and degradable silk fibroin enabled by mesoscopic doping for finger motion triggered color/transmittance adjustment. *ACS nano* **2021**, 15 (7), 12429-12437.

33. Zhang, X.-S.; Brugger, J.; Kim, B., A silk-fibroin-based transparent triboelectric

generator suitable for autonomous sensor network. *Nano Energy* **2016**, *20*, 37-47.

34. Luo, Y.; Li, Y.; Feng, X.; Pei, Y.; Zhang, Z.; Wang, L.; Zhao, Y.; Lu, B.; Zhu, B., Triboelectric nanogenerators with porous and hierarchically structured silk fibroin films via water electrospray-etching technology. *Nano Energy* **2020**, *75*, 104974.

35. Chen, Z.; Cao, Y.; Yang, W.; An, L.; Fan, H.; Guo, Y., Embedding in-plane aligned MOF nanoflakes in silk fibroin for highly enhanced output performance of triboelectric nanogenerators. *Journal of Materials Chemistry A* **2022**, *10* (2), 799-807.

36. Gogurla, N.; Roy, B.; Park, J.-Y.; Kim, S., Skin-contact actuated single-electrode protein triboelectric nanogenerator and strain sensor for biomechanical energy harvesting and motion sensing. *Nano Energy* **2019**, *62*, 674-681.

37. Wen, D.-L.; Liu, X.; Deng, H.-T.; Sun, D.-H.; Qian, H.-Y.; Brugger, J.; Zhang, X.-S., Printed silk-fibroin-based triboelectric nanogenerators for multi-functional wearable sensing. *Nano Energy* **2019**, *66*, 104123.

38. Liu, C.; Li, J.; Che, L.; Chen, S.; Wang, Z.; Zhou, X., Toward large-scale fabrication of triboelectric nanogenerator (TENG) with silk-fibroin patches film via spray-coating process. *Nano Energy* **2017**, *41*, 359-366.

39. Liu, C.; Zhang, N.; Li, J.; Dong, L.; Wang, T.; Wang, Z.; Wang, G.; Zhou, X.; Zhang, J., Harvesting ultralow frequency (< 1 Hz) mechanical energy using triboelectric nanogenerator. *Nano Energy* **2019**, *65*, 104011.

40. Liu, C.; Wang, Y.; Zhang, N.; Yang, X.; Wang, Z.; Zhao, L.; Yang, W.; Dong, L.; Che, L.; Wang, G., A self-powered and high sensitivity acceleration sensor with VQa model based on triboelectric nanogenerators (TENGs). *Nano Energy* **2020**, *67*, 104228.

41. Tan, X.; Wang, S.; You, Z.; Zheng, J.; Liu, Y., High performance porous triboelectric nanogenerator based on silk fibroin@ MXene composite aerogel and PDMS sponge. *ACS Materials Letters* **2023**, *5* (7), 1929-1937.

42. He, F.; You, X.; Gong, H.; Yang, Y.; Bai, T.; Wang, W.; Guo, W.; Liu, X.; Ye, M., Stretchable, biocompatible, and multifunctional silk fibroin-based hydrogels toward wearable strain/pressure sensors and triboelectric nanogenerators. *ACS applied materials & interfaces* **2020**, *12* (5), 6442-6450.

43. Hu, Y.; Li, X.; Gao, Y.; Zhao, Z.; Liu, X.; He, L.; Zhang, B.; Zhou, L.; Wang, Z. L.; Wang, J., A Combined Wind Harvesting and Speed Sensing System Based on Constant-Voltage Triboelectric Nanogenerator. *Advanced Energy Materials* **2024**, 2400672.

-
44. Feng, M.; Feng, Y.; Cheng, J.; Zhang, Z.; Yang, D.; Du, C.; Wang, D., Clothing comfort sensing system based on triboelectric and tribological behavior of fabrics. *Nano Energy* **2024**, *127*, 109721.
45. Lowell, J.; Rose-Innes, A., Contact electrification. *Advances in Physics* **1980**, *29* (6), 947-1023.
46. Yang, Y.; Zhou, Y. S.; Zhang, H.; Liu, Y.; Lee, S.; Wang, Z. L., A single-electrode based triboelectric nanogenerator as self-powered tracking system. *Advanced Materials (Deerfield Beach, Fla.)* **2013**, *25* (45), 6594-6601.
47. Chen, H.; Song, Y.; Cheng, X.; Zhang, H., Self-powered electronic skin based on the triboelectric generator. *Nano Energy* **2019**, *56*, 252-268.
48. Wang, Z. L.; Chen, J.; Lin, L., Progress in triboelectric nanogenerators as a new energy technology and self-powered sensors. *Energy & Environmental Science* **2015**, *8* (8), 2250-2282.
49. Liu, D.; Zhou, L.; Wang, Z. L.; Wang, J., Triboelectric nanogenerator: from alternating current to direct current. *Iscience* **2021**, *24* (1), 102018.
50. Dassanayaka, D. G.; Alves, T. M.; Wanasekara, N. D.; Dharmasena, I. G.; Ventura, J., Recent progresses in wearable triboelectric nanogenerators. *Advanced Functional Materials* **2022**, *32* (44), 2205438.
51. Maiti, S.; Karan, S. K.; Kim, J. K.; Khatua, B. B., Nature driven bio-piezoelectric/triboelectric nanogenerator as next-generation green energy harvester for smart and pollution free society. *Advanced Energy Materials* **2019**, *9* (9), 1803027.
52. Paosangthong, W.; Torah, R.; Beeby, S., Recent progress on textile-based triboelectric nanogenerators. *Nano Energy* **2019**, *55*, 401-423.
53. Chao, S.; Ouyang, H.; Jiang, D.; Fan, Y.; Li, Z., Triboelectric nanogenerator based on degradable materials. *EcoMat* **2021**, *3* (1), e12072.
54. Niu, S.; Liu, Y.; Wang, S.; Lin, L.; Zhou, Y. S.; Hu, Y.; Wang, Z. L., Theoretical investigation and structural optimization of single-electrode triboelectric nanogenerators. *Advanced Functional Materials* **2014**, *24* (22), 3332-3340.
55. Pan, S.; Zhang, Z., Fundamental theories and basic principles of triboelectric effect: A review. *Friction* **2019**, *7*, 2-17.
56. Updegraff, D. M., Semimicro determination of cellulose in biological materials. *Analytical biochemistry* **1969**, *32* (3), 420-424.

-
57. Toprak, T.; Anis, P., Textile industry's environmental effects and approaching cleaner production and sustainability, an overview. *Journal of Textile Engineering & Fashion Technology* **2017**, 2 (4), 429-442.
58. Zhang, Z.; Cai, J., High output triboelectric nanogenerator based on PTFE and cotton for energy harvester and human motion sensor. *CAP* **2021**, 22, 1-5.
59. Simpson, W.; Crawshaw, G., *Wool: Science and technology*. Elsevier: 2002.
60. Rippon, J. A., The structure of wool. *The coloration of wool and other keratin fibres* **2013**, 1-42.
61. Gurarlan, A.; Özdemir, B.; Bayat, İ. H.; Yelten, M. B.; Karabulut Kurt, G., Silver nanowire coated knitted wool fabrics for wearable electronic applications. *Journal of Engineered Fibers and Fabrics* **2019**, 14, 1558925019856222.
62. Shen, Y.; Chen, C.; Chen, L.; Shang, L.; Wang, T.; Wang, K.; Zhao, Y.; Hou, R.; Cong, H.; Jiang, G., Mass-production of biomimetic fur knitted triboelectric fabric for smart home and healthcare. *Nano Energy* **2024**, 125, 109510.
63. Torculas, M.; Medina, J.; Xue, W.; Hu, X., Protein-based bioelectronics. *ACS Biomaterials Science & Engineering* **2016**, 2 (8), 1211-1223.
64. Wen, D.-L.; Sun, D.-H.; Huang, P.; Huang, W.; Su, M.; Wang, Y.; Han, M.-D.; Kim, B.; Brugger, J.; Zhang, H.-X., Recent progress in silk fibroin-based flexible electronics. *Microsystems & nanoengineering* **2021**, 7 (1), 1-25.
65. Manikandan, G.; Murali, A.; Kumar, R.; Satapathy, D. K., Rapid moisture-responsive silk fibroin actuators. *ACS Applied Materials & Interfaces* **2021**, 13 (7), 8880-8888.
66. Song, K. Y.; Kim, S. W.; Nguyen, D. C.; Park, J. Y.; Luu, T. T.; Choi, D.; Baik, J. M.; An, S., Recent progress on nature-derived biomaterials for eco-friendly triboelectric nanogenerators. *EcoMat* **2023**, 5 (8), e12357.
67. Slabov, V.; Kopyl, S.; Soares dos Santos, M. P.; Kholkin, A. L., Natural and eco-friendly materials for triboelectric energy harvesting. *Nano-Micro Letters* **2020**, 12, 1-18.
68. He, E.; Sun, Y.; Wang, X.; Chen, H.; Sun, B.; Gu, B.; Zhang, W., 3D angle-interlock woven structural wearable triboelectric nanogenerator fabricated with silicone rubber coated graphene oxide/cotton composite yarn. *Composites Part B: Engineering* **2020**, 200, 108244.

-
69. Graham, S. A.; Dudem, B.; Mule, A. R.; Patnam, H.; Yu, J. S., Engineering squandered cotton into eco-benign microarchitected triboelectric films for sustainable and highly efficient mechanical energy harvesting. *Nano Energy* **2019**, *61*, 505-516.
70. Sahu, M.; Hajra, S.; Panda, S.; Rajaiitha, M.; Panigrahi, B. K.; Rubahn, H.-G.; Mishra, Y. K.; Kim, H. J., Waste textiles as the versatile triboelectric energy-harvesting platform for self-powered applications in sports and athletics. *Nano Energy* **2022**, *97*, 107208.
71. Li, M.; Pan, Y.; Wan, L.; Hao, X.; Huang, T.; Zhang, K.; Mai, W.; Chen, S.; Qin, A., Sisal cellulose paper based triboelectric nanogenerator with high performance for detection of chemical group substitution degree. *Nano Energy* **2022**, *104*, 107937.
72. Xia, K.; Xu, Z.; Hong, Y.; Wang, L., A free-floating structure triboelectric nanogenerator based on natural wool ball for offshore wind turbine environmental monitoring. *Materials Today Sustainability* **2023**, *24*, 100467.
73. Sarkar, L.; Mondal, M.; Bhattacharyya, T. K., From natural abundant silk to TENG; from biowaste to carbon supercap: A natural sustainable approach of active energy storage. *Journal of Energy Storage* **2024**, *97*, 112641.
74. Hu, L.; Pasta, M.; La Mantia, F.; Cui, L.; Jeong, S.; Deshazer, H. D.; Choi, J. W.; Han, S. M.; Cui, Y., Stretchable, porous, and conductive energy textiles. *Nano Letters* **2010**, *10* (2), 708-714.
75. Pasta, M.; La Mantia, F.; Hu, L.; Deshazer, H. D.; Cui, Y., Aqueous supercapacitors on conductive cotton. *Nano Research* **2010**, *3*, 452-458.
76. Gao, Y.; Hou, M.; Yang, R.; Zhang, L.; Xu, Z.; Kang, Y.; Xue, P., Highly porous silk fibroin scaffold packed in PEGDA/sucrose microneedles for controllable transdermal drug delivery. *Biomacromolecules* **2019**, *20* (3), 1334-1345.
77. Min, K.; Kim, S.; Kim, S., Deformable and conformal silk hydrogel inverse opal. *Proceedings of the National Academy of Sciences* **2017**, *114* (24), 6185-6190.
78. Zhang, S.; Zhou, Z.; Zhong, J.; Shi, Z.; Mao, Y.; Tao, T. H., Body - Integrated, Enzyme - Triggered Degradable, Silk - Based Mechanical Sensors for Customized Health/Fitness Monitoring and In Situ Treatment. *Advanced Science* **2020**, *7* (13), 1903802.
79. Wang, Q.; Ling, S.; Liang, X.; Wang, H.; Lu, H.; Zhang, Y., Self-healable multifunctional electronic tattoos based on silk and graphene. *Advanced Functional Materials* **2019**, *29* (16), 1808695.

-
80. Huang, J.; Xu, Z.; Qiu, W.; Chen, F.; Meng, Z.; Hou, C.; Guo, W.; Liu, X. Y., Stretchable and heat - resistant protein - based electronic skin for human thermoregulation. *Advanced Functional Materials* **2020**, *30* (13), 1910547.
81. Tao, H.; Hwang, S.-W.; Marelli, B.; An, B.; Moreau, J. E.; Yang, M.; Brenckle, M. A.; Kim, S.; Kaplan, D. L.; Rogers, J. A., Silk-based resorbable electronic devices for remotely controlled therapy and in vivo infection abatement. *Proceedings of the National Academy of Sciences* **2014**, *111* (49), 17385-17389.
82. Hwang, S.-W.; Tao, H.; Kim, D.-H.; Cheng, H.; Song, J.-K.; Rill, E.; Brenckle, M. A.; Panilaitis, B.; Won, S. M.; Kim, Y.-S., A physically transient form of silicon electronics. *Science* **2012**, *337* (6102), 1640-1644.
83. Karan, S. K.; Maiti, S.; Kwon, O.; Paria, S.; Maitra, A.; Si, S. K.; Kim, Y.; Kim, J. K.; Khatua, B. B., Nature driven spider silk as high energy conversion efficient bio-piezoelectric nanogenerator. *Nano Energy* **2018**, *49*, 655-666.
84. Wen, D.-L.; Deng, H.-T.; Liu, X.; Li, G.-K.; Zhang, X.-R.; Zhang, X.-S., Wearable multi-sensing double-chain thermoelectric generator. *Microsystems & nanoengineering* **2020**, *6* (1), 1-13.
85. Wang, C.; Xia, K.; Zhang, M.; Jian, M.; Zhang, Y., An all-silk-derived dual-mode e-skin for simultaneous temperature–pressure detection. *ACS applied materials & interfaces* **2017**, *9* (45), 39484-39492.
86. Jokisch, S.; Neuenfeldt, M.; Scheibel, T., Silk-based fine dust filters for air filtration. *Advanced Sustainable Systems* **2017**, *1* (10), 1700079.
87. Kook, G.; Jeong, S.; Kim, M. K.; Lee, S.; Choi, N.; Lee, H. J., Fabrication of highly dense silk fibroin biomemristor array and its resistive switching characteristics. *Advanced Materials Technologies* **2020**, *5* (4), 1900991.
88. Melikov, R.; Press, D. A.; Kumar, B. G.; Dogru, I. B.; Sadeghi, S.; Chirea, M.; Yilgör, İ.; Nizamoglu, S., Silk-hydrogel lenses for light-emitting diodes. *Scientific Reports* **2017**, *7* (1), 1-8.
89. Guidetti, G.; d'Amone, L.; Kim, T.; Matzeu, G.; Mogas-Soldevila, L.; Napier, B.; Ostrovsky-Snider, N.; Roshko, J.; Ruggeri, E.; Omenetto, F. G., Silk materials at the convergence of science, sustainability, healthcare, and technology. *Applied Physics Reviews* **2022**, *9* (1).
90. Zhang, B.; Ren, T.; Li, H.; Chen, B.; Mao, Y., Recent Progress of Nature Materials Based Triboelectric Nanogenerators for Electronic Skins and Human–Machine Interaction. *Advanced Energy and Sustainability Research* **2024**, *5* (4),

2300245.

91. Qiu, W.; Patil, A.; Hu, F.; Liu, X. Y., Hierarchical structure of silk materials versus mechanical performance and mesoscopic engineering principles. *Small* **2019**, *15* (51), 1903948.
92. Liu, R.; Deng, Q.; Yang, Z.; Yang, D.; Han, M. Y.; Liu, X. Y., "Nano-Fishnet" Structure Making Silk Fibers Tougher. *Advanced Functional Materials* **2016**, *26* (30), 5534-5541.
93. Koh, L.-D.; Cheng, Y.; Teng, C.-P.; Khin, Y.-W.; Loh, X.-J.; Tee, S.-Y.; Low, M.; Ye, E.; Yu, H.-D.; Zhang, Y.-W., Structures, mechanical properties and applications of silk fibroin materials. *Progress in Polymer Science* **2015**, *46*, 86-110.
94. Vepari, C.; Kaplan, D. L., Silk as a biomaterial. *Progress in Polymer Science* **2007**, *32* (8-9), 991-1007.
95. Ahmed, A.; Bain, S.; Prottoy, Z. H.; Morsada, Z.; Islam, M. T.; Hossain, M. M.; Shkir, M., Silk-templated nanomaterial interfaces for wearables and bioelectronics: advances and prospects. *ACS Materials Letters* **2021**, *4* (1), 68-86.
96. Shen, Y.; Johnson, M. A.; Martin, D. C., Microstructural characterization of Bombyx mori silk fibers. *Macromolecules* **1998**, *31* (25), 8857-8864.
97. Maleki, H.; Montes, S.; Hayati-Roodbari, N.; Putz, F.; Huesing, N., Compressible, thermally insulating, and fire retardant aerogels through self-assembling silk fibroin biopolymers inside a silica structure—an approach towards 3D printing of aerogels. *ACS applied materials & interfaces* **2018**, *10* (26), 22718-22730.
98. Sarkar, L.; Kandala, A.; Bonam, S.; Mohanty, S.; Singh, S.; Vanjari, S. K., Flexible polymer-based triboelectric nanogenerator using poly (vinylidene fluoride) and bombyx mori silk. *Materials Today Sustainability* **2022**, *20*, 100230.
99. Hsu P C, Li X. Photon-engineered radiative cooling textiles. *Science*, 2020, 370(6518): 784-785.
100. Li, X.; Hu, N.; Fan, Q.; Sun, M.; Hu, T.; Ni, Z., High-performance triboelectric nanogenerator based on natural silk fibroin and microstructured polytetrafluoroethylene for self-powered electronics and wearable sensing. *Materials Today Communications* **2024**, *38*, 108418.
101. Sarkar, L.; Karmakar, G.; Ghosh, S.; Bhattacharyya, T. K., Triboelectric nanogenerator as next generation traffic monitoring system: Concept and modelling. *Nano Energy* **2024**, *121*, 109212.

-
102. Su, M.; Brugger, J.; Kim, B., Simply structured wearable triboelectric nanogenerator based on a hybrid composition of carbon nanotubes and polymer layer. *International Journal of Precision Engineering and Manufacturing-Green Technology* **2020**, *7*, 683-698.
103. Liu, J.; Chen, J.; Dai, F.; Zhao, J.; Li, S.; Shi, Y.; Li, W.; Geng, L.; Ye, M.; Chen, X., Wearable five-finger keyboardless input system based on silk fibroin electronic skin. *Nano Energy* **2022**, *103*, 107764.
104. Shen, S.; Yi, J.; Sun, Z.; Guo, Z.; He, T.; Ma, L.; Li, H.; Fu, J.; Lee, C.; Wang, Z. L., Human machine interface with wearable electronics using biodegradable triboelectric films for calligraphy practice and correction. *Nano-Micro Letters* **2022**, *14* (1), 225.
105. Joshi, S. R.; Kim, S., High power triboelectric nanogenerator based on nanofibers of silk protein and PVBVA and its motion sensing applications. *Chemical Engineering Journal* **2024**, *489*, 151248.
106. Li, Y.; Zhu, J.; Cheng, H.; Li, G.; Cho, H.; Jiang, M.; Gao, Q.; Zhang, X., Developments of advanced electrospinning techniques: A critical review. *Advanced Materials Technologies* **2021**, *6* (11), 2100410.
107. Li, X.; Chen, W.; Qian, Q.; Huang, H.; Chen, Y.; Wang, Z.; Chen, Q.; Yang, J.; Li, J.; Mai, Y. W., Electrospinning-based strategies for battery materials. *Advanced Energy Materials* **2021**, *11* (2), 2000845.
108. Ling, S.; Zhang, Q.; Kaplan, D. L.; Omenetto, F.; Buehler, M. J.; Qin, Z., Printing of stretchable silk membranes for strain measurements. *Lab on a Chip* **2016**, *16* (13), 2459-2466.
109. Onder, O. C.; Batool, S. R.; Nazeer, M. A., Self-assembled silk fibroin hydrogels: From preparation to biomedical applications. *Materials Advances* **2022**, *3* (18), 6920-6949.
110. Li, P.; Chen, J.; Tang, S., Ionic liquid-impregnated covalent organic framework/silk nanofibril composite membrane for efficient proton conduction. *Chemical Engineering Journal* **2021**, *415*, 129021.
111. Arumugam, M.; Murugesan, B.; Pandiyan, N.; Chinnalagu, D. K.; Rangasamy, G.; Mahalingam, S., Electrospinning cellulose acetate/silk fibroin/Au-Ag hybrid composite nanofiber for enhanced biocidal activity against MCF-7 breast cancer cell. *Materials Science and Engineering: C* **2021**, *123*, 112019.
112. Zhou, L.; Wang, Z.; Chen, D.; Lin, J.; Li, W.; Guo, S.; Wu, R.; Zhao, X.; Lin, T.; Chen, G., An injectable and photocurable methacrylate-silk fibroin

hydrogel loaded with bFGF for spinal cord regeneration. *Materials & Design* **2022**, *217*, 110670.

113. Cai, H.; Wang, Y.; Xu, M.; Cheng, L.; Liu, Z.; Li, Z.; Dai, F., Low cost, green and effective preparation of multifunctional flexible silk fabric electrode with ultra-high capacitance retention. *Carbon* **2022**, *188*, 197-208.

114. Zou, H.; Zhang, Y.; Guo, L.; Wang, P.; He, X.; Dai, G.; Zheng, H.; Chen, C.; Wang, A. C.; Xu, C., Quantifying the triboelectric series. *Nature communications* **2019**, *10* (1), 1427.

115. Zhang, Y. J.; Zhou, Z. T.; Fan, Z.; Zhang, S. Q.; Zheng, F. M.; Liu, K. Y.; Zhang, Y. L.; Shi, Z. F.; Chen, L.; Li, X. X.; Mao, Y.; Wang, F.; Sun, Y. L.; Tao, T. H., Self-Powered Multifunctional Transient Bioelectronics. *Small* **2018**, *14* (35).

116. Candido, I. C.; Oliveira, G. d. S.; Ribeiro, S. J.; Cavicchioli, M.; Barud, H. S.; Silva, L. G.; de Oliveira, H. P., PVA-silk fibroin bio-based triboelectric nanogenerator. *Nano Energy* **2023**, *105*, 108035.

117. Dudem, B.; Dharmasena, R. I. G.; Graham, S. A.; Leem, J. W.; Patnam, H.; Mule, A. R.; Silva, S. R. P.; Yu, J. S., Exploring the theoretical and experimental optimization of high-performance triboelectric nanogenerators using microarchitected silk cocoon films. *Nano Energy* **2020**, *74*, 104882.

118. Charoonsuk, T.; Pongampai, S.; Pakawanit, P.; Vittayakorn, N., Achieving a highly efficient chitosan-based triboelectric nanogenerator via adding organic proteins: Influence of morphology and molecular structure. *Nano Energy* **2021**, *89*, 106430.

119. Dudem, B.; Graham, S. A.; Dharmasena, R. I. G.; Silva, S. R. P.; Yu, J. S., Natural silk-composite enabled versatile robust triboelectric nanogenerators for smart applications. *Nano Energy* **2021**, *83*, 105819.

120. Parandeh, S.; Kharaziha, M.; Karimzadeh, F.; Hosseinabadi, F., Triboelectric nanogenerators based on graphene oxide coated nanocomposite fibers for biomedical applications. *Nanotechnology* **2020**, *31* (38), 385402.

121. Gogurla, N.; Kim, S., Self-powered and imperceptible electronic tattoos based on silk protein nanofiber and carbon nanotubes for human-machine interfaces. *Advanced Energy Materials* **2021**, *11* (29), 2100801.

122. Liu, J.; Yu, D.; Zheng, Z.; Huangfu, G.; Guo, Y., Lead-free BiFeO₃ film on glass fiber fabric: Wearable hybrid piezoelectric-triboelectric nanogenerator. *Ceramics International* **2021**, *47* (3), 3573-3579.

-
123. Li, Y.; Xiao, S.; Zhang, X.; Jia, P.; Tian, S.; Pan, C.; Zeng, F.; Chen, D.; Chen, Y.; Tang, J., Silk inspired in-situ interlocked superelastic microfibers for permeable stretchable triboelectric nanogenerator. *Nano Energy* **2022**, *98*, 107347.
124. He, W.; Sohn, M.; Ma, R.; Kang, D. J., Flexible single-electrode triboelectric nanogenerators with MXene/PDMS composite film for biomechanical motion sensors. *Nano Energy* **2020**, *78*, 105383.
125. Salauddin, M.; Rana, S. S.; Sharifuzzaman, M.; Rahman, M. T.; Park, C.; Cho, H.; Maharjan, P.; Bhatta, T.; Park, J. Y., A novel MXene/Ecoflex nanocomposite-coated fabric as a highly negative and stable friction layer for high-output triboelectric nanogenerators. *Advanced Energy Materials* **2021**, *11* (1), 2002832.
126. Liu, Y.; Ping, J.; Ying, Y., Recent progress in 2D - nanomaterial - based triboelectric nanogenerators. *Advanced Functional Materials* **2021**, *31* (17), 2009994.
127. Wen, D.-L.; Huang, P.; Li, B.-Y.; Qiu, Y.; Wang, Y.-L.; Zhang, X.-R.; Deng, H.-T.; Zhang, X.-S., Silk fibroin/Ag nanowire-based multifunctional sensor for wearable self-powered wireless multi-sensing microsystems. *Nano Energy* **2023**, *113*, 108569.
128. Lee, J.-Y.; An, J.; Chua, C. K., Fundamentals and applications of 3D printing for novel materials. *Applied materials today* **2017**, *7*, 120-133.
129. Mahmud, M. P.; Zolfagharian, A.; Gharaie, S.; Kaynak, A.; Farjana, S. H.; Ellis, A. V.; Chen, J.; Kouzani, A. Z., 3D-Printed Triboelectric Nanogenerators: State of the Art, Applications, and Challenges. *Advanced Energy and Sustainability Research* **2021**, *2* (3), 2000045.
130. Chen, S.; Huang, T.; Zuo, H.; Qian, S.; Guo, Y.; Sun, L.; Lei, D.; Wu, Q.; Zhu, B.; He, C., A single integrated 3D-printing process customizes elastic and sustainable triboelectric nanogenerators for wearable electronics. *Advanced Functional Materials* **2018**, *28* (46), 1805108.
131. Zhang, M.; Zhao, M.; Jian, M.; Wang, C.; Yu, A.; Yin, Z.; Liang, X.; Wang, H.; Xia, K.; Liang, X., Printable smart pattern for multifunctional energy-management E-textile. *Matter* **2019**, *1* (1), 168-179.
132. Liu, H.; Zhang, H.; Han, W.; Lin, H.; Li, R.; Zhu, J.; Huang, W., 3D printed flexible strain sensors: from printing to devices and signals. *Advanced Materials* **2021**, *33* (8), 2004782.
133. Niu, Q.; Huang, L.; Lv, S.; Shao, H.; Fan, S.; Zhang, Y., Pulse-driven bio-triboelectric nanogenerator based on silk nanoribbons. *Nano Energy* **2020**, *74*, 104837.

-
134. Mi, H.-Y.; Li, H.; Jing, X.; He, P.; Feng, P.-Y.; Tao, X.; Liu, Y.; Liu, C.; Shen, C., Silk and silk composite aerogel-based biocompatible triboelectric nanogenerators for efficient energy harvesting. *Industrial & Engineering Chemistry Research* **2020**, *59* (27), 12399-12408.
135. Sun, L.; Chen, S.; Guo, Y.; Song, J.; Zhang, L.; Xiao, L.; Guan, Q.; You, Z., Ionogel-based, highly stretchable, transparent, durable triboelectric nanogenerators for energy harvesting and motion sensing over a wide temperature range. *Nano Energy* **2019**, *63*, 103847.
136. Lv, P.; Shi, L.; Fan, C.; Gao, Y.; Yang, A.; Wang, X.; Ding, S.; Rong, M., Hydrophobic ionic liquid gel-based triboelectric nanogenerator: next generation of ultrastable, flexible, and transparent power sources for sustainable electronics. *ACS applied materials & interfaces* **2020**, *12* (13), 15012-15022.
137. Gogurla, N.; Roy, B.; Kim, S., Self-powered artificial skin made of engineered silk protein hydrogel. *Nano Energy* **2020**, *77*, 105242.
138. Luo, Y.; Yu, M.; Zhang, Y.; Wang, Y.; Long, L.; Tan, H.; Li, N.; Xu, L.; Xu, J., Highly sensitive strain sensor and self-powered triboelectric nanogenerator using a fully physical crosslinked double-network conductive hydrogel. *Nano Energy* **2022**, *104*, 107955.
139. Xiong, Q.; Yang, Z.; Zhang, X., Flexible triboelectric nanogenerator based on silk fibroin-modified carbon nanotube arrays. *Chemical Engineering Journal* **2024**, *482*, 148986.
140. Tufan, Y.; Öztatlı, H.; Doganay, D.; Buyuksungur, A.; Cicek, M. O.; Döş, I. p. T. c. e.; Berberoglu, C.; Unalan, H. E.; Garipcan, B.; Ercan, B., Multifunctional Silk Fibroin/Carbon Nanofiber Scaffolds for In Vitro Cardiomyogenic Differentiation of Induced Pluripotent Stem Cells and Energy Harvesting from Simulated Cardiac Motion. *ACS Applied Materials & Interfaces* **2023**, *15* (36), 42271-42283.
141. Cao, Y.; Shao, H.; Wang, H.; Li, X.; Zhu, M.; Fang, J.; Cheng, T.; Lin, T., A full-textile triboelectric nanogenerator with multisource energy harvesting capability. *Energy Conversion and Management* **2022**, *267*, 115910.
142. Jian, G.; Meng, Q.; Jiao, Y.; Feng, L.; Shao, H.; Wang, F.; Meng, F., Hybrid PDMS-TiO₂-stainless steel textiles for triboelectric nanogenerators. *Chemical Engineering Journal* **2021**, *417*, 127974.
143. Choi, A. Y.; Lee, C. J.; Park, J.; Kim, D.; Kim, Y. T., Corrugated textile based triboelectric generator for wearable energy harvesting. *Scientific Reports* **2017**, *7* (1), 45583.

-
144. Cao, R.; Pu, X.; Du, X.; Yang, W.; Wang, J.; Guo, H.; Zhao, S.; Yuan, Z.; Zhang, C.; Li, C., Screen-printed washable electronic textiles as self-powered touch/gesture tribo-sensors for intelligent human-machine interaction. *ACS nano* **2018**, *12* (6), 5190-5196.
145. Wang, W.; Yu, A.; Liu, X.; Liu, Y.; Zhang, Y.; Zhu, Y.; Lei, Y.; Jia, M.; Zhai, J.; Wang, Z. L., Large-scale fabrication of robust textile triboelectric nanogenerators. *Nano Energy* **2020**, *71*, 104605.
146. Bairagi, S.; Khandelwal, G.; Karagiorgis, X.; Gokhool, S.; Kumar, C.; Min, G.; Mulvihill, D. M., High-Performance Triboelectric Nanogenerators Based on Commercial Textiles: Electrospun Nylon 66 Nanofibers on Silk and PVDF on Polyester. *ACS Applied Materials & Interfaces* **2022**, *14* (39), 44591-44603.
147. Feng, M.; Wu, Y.; Feng, Y.; Dong, Y.; Liu, Y.; Peng, J.; Wang, N.; Xu, S.; Wang, D., Highly wearable, machine-washable, and self-cleaning fabric-based triboelectric nanogenerator for wireless drowning sensors. *Nano Energy* **2022**, *93*, 106835.
148. He, L.; Zhang, C.; Zhang, B.; Gao, Y.; Yuan, W.; Li, X.; Zhou, L.; Zhao, Z.; Wang, Z. L.; Wang, J., A high-output silk-based triboelectric nanogenerator with durability and humidity resistance. *Nano Energy* **2023**, *108*, 108244.
149. Ye, C.; Dong, S.; Ren, J.; Ling, S., Ultrastable and high-performance silk energy harvesting textiles. *Nano-Micro Letters* **2020**, *12*, 1-15.
150. Sangkhun, W.; Wanwong, S., Natural textile based triboelectric nanogenerators for efficient energy harvesting applications. *Nanoscale* **2021**, *13* (4), 2420-2428.
151. Ge, D.; Mi, Q.; Gong, R.; Li, S.; Qin, C.; Dong, Y.; Yu, H. Y.; Tam, K. C., Mass-Produced 3D Hair Structure-Editable Silk-Based Electronic Skin for Multiscenario Signal Monitoring and Emergency Alarming System. *Advanced Functional Materials* **2023**, *33* (46), 2305328.
152. Zhu, J.; Yang, H.; Cao, L.; Dai, C.; Ren, J.; Liang, J.; Ling, S., Functionalization of structural materials through electro-blown spinning of ultrathin and transparent silk fibroin ionotronic nanofiber skin. *Nano Today* **2023**, *50*, 101873.
153. Cao, X.; Ye, C.; Cao, L.; Shan, Y.; Ren, J.; Ling, S., Biomimetic spun silk ionotronic fibers for intelligent discrimination of motions and tactile stimuli. *Advanced Materials* **2023**, *35* (36), 2300447.
154. Hu, H.; Shang, S.; Liu, J.; Zhu, P., Silk fibroin based flexible and self-powered sensor for real-time monitoring of abdominal respiration. *International Journal of Biological Macromolecules* **2024**, *254*, 127723.

-
155. Dudem, B.; Graham, S. A.; Dharmasena, R. D. I. G.; Silva, S. R. P.; Yu, J. S., Natural silk-composite enabled versatile robust triboelectric nanogenerators for smart applications. *Nano Energy* **2021**, *83*.
156. Fan, F. R.; Tian, Z. Q.; Wang, Z. L., Flexible triboelectric generator! *Nano Energy* **2012**, *1* (2), 328-334.
157. Niu, S.; Wang, S.; Lin, L.; Liu, Y.; Zhou, Y. S.; Hu, Y.; Wang, Z. L., Theoretical study of contact-mode triboelectric nanogenerators as an effective power source. *Energy & Environmental Science* **2013**, *6* (12), 3576–3583.
158. Zhang, Z.; He, T.; Zhu, M.; Sun, Z.; Shi, Q.; Zhu, J.; Dong, B.; Yuce, M. R.; Lee, C., Deep learning-enabled triboelectric smart socks for IoT-based gait analysis and VR applications. *npj Flexible Electronics* **2020**, *4* (1).
159. Shi, J.; Liu, S.; Zhang, L.; Yang, B.; Shu, L.; Yang, Y.; Ren, M.; Wang, Y.; Chen, J.; Chen, W.; Chai, Y.; Tao, X., Smart Textile-Integrated Microelectronic Systems for Wearable Applications. *Advanced Materials* **2020**, *32* (5), e1901958.
160. Yuanyuan Gao, Z. L., Bingang Xu, Meiqi Li, Chenghanzhi Jiang, Xiaoyang Guan, Yujue Yang, Scalable core–spun coating yarn-based triboelectric nanogenerators with hierarchical structure for wearable energy harvesting and sensing via continuous manufacturing. *Nano Energy* **2022**.
161. Dong, K.; Peng, X.; Cheng, R.; Ning, C.; Jiang, Y.; Zhang, Y.; Wang, Z. L., Advances in High-Performance Autonomous Energy and Self-Powered Sensing Textiles with Novel 3D Fabric Structures. *Advanced Materials* **2022**, e2109355.
162. Peng, X.; Dong, K.; Ye, C.; Jiang, Y.; Zhai, S.; Cheng, R.; Liu, D.; Gao, X.; Wang, J.; Wang, Z. L., A breathable, biodegradable, antibacterial, and self-powered electronic skin based on all-nanofiber triboelectric nanogenerators. *Science Advances* **2020**, *6* (26), eaba9624.
163. Park, J.; Kang, D. H.; Chae, H.; Ghosh, S. K.; Jeong, C.; Park, Y.; Cho, S.; Lee, Y.; Kim, J.; Ko, Y.; Kim, J. J.; Ko, H., Frequency-selective acoustic and haptic smart skin for dual-mode dynamic/static human-machine interface. *Sci Adv* **2022**, *8* (12), eabj9220.
164. Dong, K.; Peng, X.; An, J.; Wang, A. C.; Luo, J.; Sun, B.; Wang, J.; Wang, Z. L., Shape adaptable and highly resilient 3D braided triboelectric nanogenerators as e-textiles for power and sensing. *Nature Communications* **2020**, *11* (1), 2868.
165. Li, L.; Wang, X.; Hu, Y.; Li, Z.; Wang, C.; Zhao, Z., Understanding the

Ferroelectric Polymer–Metal Contact Electrification for Triboelectric Nanogenerator from Molecular and Electronic Structure. *Advanced Functional Materials* **2021**, 32 (10).

166. Meiqi Li, B. X., Zihua Li, Yuanyuan Gao, Yujue Yang, Xinxin Huang, Toward 3D double-electrode textile triboelectric nanogenerators for wearable biomechanical energy harvesting and sensing. *Chemical Engineering Journal* **2022**.

167. Guan, X.; Xu, B.; Huang, J.; Jing, T.; Gao, Y., Fiber-shaped stretchable triboelectric nanogenerator with a novel synergistic structure of opposite Poisson's ratios. *Chemical Engineering Journal* **2022**, 427.

168. Leem, J. W.; Fraser, M. J.; Kim, Y. L., Transgenic and Diet-Enhanced Silk Production for Reinforced Biomaterials: A Metamaterial Perspective. *Annual Review of Biomedical Engineering* **2020**, 22, 79-102.

169. Kim, H.-J.; Kim, J.-H.; Jun, K.-W.; Kim, J.-H.; Seung, W.-C.; Kwon, O. H.; Park, J.-Y.; Kim, S.-W.; Oh, I.-K., Silk Nanofiber-Networked Bio-Triboelectric Generator: Silk Bio-TEG. *Advanced Energy Materials* **2016**, 6 (8).

170. Zhang, J.; Kaur, J.; Rajkhowa, R.; Li, J. L.; Liu, X. Y.; Wang, X. G., Mechanical properties and structure of silkworm cocoons: A comparative study of *Bombyx mori*, *Antheraea assamensis*, *Antheraea pernyi* and *Antheraea mylitta* silkworm cocoons. *Materials Science and Engineering: C* **2013**, 33 (6), 3206-3213.

171. Chengmei Jianga, C. W., Xunjia Lia, Yao Yaoa, Lingyi Lana, Fengnian Zhaoa, Zunzhong Yea, Yibin Yinga,b, Jianfeng Pinga,*, All-electrospunflexible triboelectric nanogenerator based on metallic MXene nanosheets. *Nano Energy* **2019**, 59, 268-276.

172. Jiang, W.; Li, H.; Liu, Z.; Li, Z.; Tian, J.; Shi, B.; Zou, Y.; Ouyang, H.; Zhao, C.; Zhao, L.; Sun, R.; Zheng, H.; Fan, Y.; Wang, Z. L.; Li, Z., Fully Bioabsorbable Natural-Materials-Based Triboelectric Nanogenerators. *Advanced Materials* **2018**, 30 (32), e1801895.

173. Mallineni, S. S. K.; Dong, Y.; Behlow, H.; Rao, A. M.; Podila, R., A Wireless Triboelectric Nanogenerator. *Advanced Energy Materials* **2018**, 8 (10).

174. Xu, Z.; Qiu, W.; Fan, X.; Shi, Y.; Gong, H.; Huang, J.; Patil, A.; Li, X.; Wang, S.; Lin, H.; Hou, C.; Zhao, J.; Guo, X.; Yang, Y.; Lin, H.; Huang, L.; Liu, X. Y.; Guo, W., Stretchable, Stable, and Degradable Silk Fibroin Enabled by Mesoscopic Doping for Finger Motion Triggered Color/Transmittance Adjustment. *ACS Nano* **2021**, 15(7): 12429-12437.

175. Zhang, X. S.; Brugger, J.; Kim, B., A silk-fibroin-based transparent triboelectric generator suitable for autonomous sensor network. *Nano Energy* **2016**, 20, 37-47.

-
176. Luo, Y.; Li, Y. T.; Feng, X. M.; Pei, Y. C.; Zhang, Z. F.; Wang, L.; Zhao, Y. L.; Lu, B. H.; Zhu, B. C., Triboelectric nanogenerators with porous and hierarchically structured silk fibroin films via water electrospray-etching technology. *Nano Energy* **2020**, *75*.
177. Chen, Z., Cao, Y., Yang, W., An, L., Fan, H., & Guo, Y. , Embedding in-plane aligned MOF nanoflakes in silk fibroin for highly enhanced output performance of triboelectric nanogenerator. *Journal of Materials Chemistry. A, Materials for Energy and Sustainability, Journal of materials chemistry. A, Materials for energy and sustainability* **2021**, *10*(2): 799-807.
178. Wen, D.-L.; Liu, X.; Deng, H.-T.; Sun, D.-H.; Qian, H.-Y.; Brugger, J.; Zhang, X.-S., Printed silk-fibroin-based triboelectric nanogenerators for multi-functional wearable sensing. *Nano Energy* **2019**, *66*.
179. He, F.; You, X.; Gong, H.; Yang, Y.; Bai, T.; Wang, W.; Guo, W.; Liu, X.; Ye, M., Stretchable, Biocompatible, and Multifunctional Silk Fibroin-Based Hydrogels toward Wearable Strain/Pressure Sensors and Triboelectric Nanogenerators. *ACS Applied Materials & Interfaces* **2020**, *12* (5), 6442-6450.
180. Dudem, B.; Dharmasena, R. D. I. G.; Graham, S. A.; Leem, J. W.; Patnam, H.; Mule, A. R.; Silva, S. R. P.; Yu, J. S., Exploring the theoretical and experimental optimization of high-performance triboelectric nanogenerators using microarchitected silk cocoon films. *Nano Energy* **2020**, *74*.
181. Charoonsuk, T.; Pongampai, S.; Pakawanit, P.; Vittayakorn, N., Achieving a highly efficient chitosan-based triboelectric nanogenerator via adding organic proteins: Influence of morphology and molecular structure. *Nano Energy* **2021**, *89*.
182. Sparkes, J.; Holland, C., The rheological properties of native sericin. *Acta Biomaterialia* **2018**, *69*, 234-242.
183. Yuxin Tang, J. D., Wenlong Li, Oleksandr I. Malyi, Yanyan Zhang, Xinran Zhou, Shaowu Pan, Jiaqi Wei, Yurong Cai, Zhong Chen, and Xiaodong Chen, Water-Soluble Sericin Protein Enabling Stable Solid Electrolyte Interphase for Fast. *Advanced Materials* **2017**, *29*, 1701828.
184. Lee, B. Y. Z., Jinxing; Zueger, Chris; Chung, Woo-Jae; Yoo, So Young; Wang, Eddie; Meyer, Joel; Ramesh, Ramamoorthy; Lee, Seung-Wuk, Virus-based piezoelectric energy generation. *Nature Nanotechnology* **2012**, *7* (6), 351-356.
185. Chen, F.; Porter, D.; Vollrath, F., Silk cocoon (*Bombyx mori*): multi-layer structure and mechanical properties. *Acta Biomaterialia* **2012**, *8* (7), 2620-7.
186. Chen, F.; Porter, D.; Vollrath, F., Silk cocoon (*Bombyx mori*): multi-layer

structure and mechanical properties. *Acta Biomaterialia* **2012**, 8 (7), 2620-2627.

187. Kunz, R. I.; Brancalhão, R. M. C.; Ribeiro, L. d. F. C.; Natali, M. R. M., Silkworm sericin: Properties and biomedical applications. *Biomedical Research International* **2016**, 2016.

188. Li, S.; Liu, G.; Wen, H.; Liu, G.; Wang, H.; Ye, M.; Yang, Y.; Guo, W.; Liu, Y., A Skin-Like Pressure-and Vibration-Sensitive Tactile Sensor Based on Polyacrylamide/Silk Fibroin Elastomer. *Advanced Functional Materials* **2022**, 32 (19), 2111747.

189. Huang, W.; Ling, S.; Li, C.; Omenetto, F. G.; Kaplan, D. L., Silkworm silk-based materials and devices generated using bio-nanotechnology. *Chemical Society Reviews* **2018**, 47 (17), 6486-6504.

190. Pereira, R. F.; Silva, M. M.; de Zea Bermudez, V., Bombyx mori silk fibers: an outstanding family of materials. *Macromolecular Materials and Engineering* **2015**, 300 (12), 1171-1198.

191. Wang, L.; Liu, W.; Yan, Z.; Wang, F.; Wang, X., Stretchable and shape-adaptable triboelectric nanogenerator based on biocompatible liquid electrolyte for biomechanical energy harvesting and wearable human-machine interaction. *Advanced Functional Materials* **2021**, 31 (7), 2007221.

192. Li, Z.; Xu, B.; Han, J.; Huang, J.; Chung, K. Y., Interfacial polarization and dual charge transfer induced high permittivity of carbon dots-based composite as humidity-resistant tribomaterial for efficient biomechanical energy harvesting. *Advanced Energy Materials* **2021**, 11 (30), 2101294.

193. Wang, Z. L., Triboelectric nanogenerators as new energy technology for self-powered systems and as active mechanical and chemical sensors. *ACS nano* **2013**, 7 (11), 9533-9557.

194. Yang, Y.; Xu, B.; Gao, Y.; Li, M., Conductive composite fiber with customizable functionalities for energy harvesting and electronic textiles. *ACS Applied Materials & Interfaces* **2021**, 13 (42), 49927-49935.

195. Yu, A.; Zhu, Y.; Wang, W.; Zhai, J., Progress in triboelectric materials: toward high performance and widespread applications. *Advanced Functional Materials* **2019**, 29 (41), 1900098.

196. Wang, J.; Wu, C.; Dai, Y.; Zhao, Z.; Wang, A.; Zhang, T.; Wang, Z. L., Achieving ultrahigh triboelectric charge density for efficient energy harvesting. *Nature communications* **2017**, 8 (1), 1-8.

-
197. Lee, B. Y.; Zhang, J.; Zueger, C.; Chung, W.-J.; Yoo, S. Y.; Wang, E.; Meyer, J.; Ramesh, R.; Lee, S.-W., Virus-based piezoelectric energy generation. *Nature nanotechnology* **2012**, *7* (6), 351-356.
198. Wang, Y.; Shim, E.; He, N.; Pourdeyhimi, B.; Gao, W., Modeling the Triboelectric Behaviors of Elastomeric Nonwoven Fabrics. *Advanced Materials* **2022**, *34* (2), 2106429.
199. Zhao, D.; Yu, X.; Wang, J.; Gao, Q.; Wang, Z.; Cheng, T.; Wang, Z. L., A standard for normalizing the outputs of triboelectric nanogenerators in various modes. *Energy & Environmental Science* **2022**, *15* (9), 3901-3911.
200. Tcho, I.-W.; Kim, W.-G.; Jeon, S.-B.; Park, S.-J.; Lee, B. J.; Bae, H.-K.; Kim, D.; Choi, Y.-K., Surface structural analysis of a friction layer for a triboelectric nanogenerator. *Nano Energy* **2017**, *42*, 34-42.
201. Cheng, G.-G.; Jiang, S.-Y.; Li, K.; Zhang, Z.-Q.; Wang, Y.; Yuan, N.-Y.; Ding, J.-N.; Zhang, W., Effect of argon plasma treatment on the output performance of triboelectric nanogenerator. *Applied Surface Science* **2017**, *412*, 350-356.
202. Zhou, J.; Zhang, Y.; Yang, Y.; Chen, Z.; Jia, G.; Zhang, L., Silk fibroin-graphene oxide functionalized melamine sponge for efficient oil absorption and oil/water separation. *Applied Surface Science* **2019**, *497*, 143762.
203. Pan, C.-T.; Yen, C.-K.; Hsieh, M.-C.; Wang, S.-Y.; Chien, C.-H.; Huang, J. C.-C.; Lin, L.; Shiue, Y.-L.; Kuo, S.-W., Energy harvesters incorporating silk from the Taiwan-native spider *nephila pilipes*. *ACS Applied Energy Materials* **2018**, *1* (10), 5627-5635.
204. Karan, S. K.; Bera, R.; Paria, S.; Das, A. K.; Maiti, S.; Maitra, A.; Khatua, B. B., An approach to design highly durable piezoelectric nanogenerator based on self-poled PVDF/AlO-rGO flexible nanocomposite with high power density and energy conversion efficiency. *Advanced Energy Materials* **2016**, *6* (20), 1601016.
205. Rahman, M. T.; Rana, S. S.; Zahed, M. A.; Lee, S.; Yoon, E.-S.; Park, J. Y., Metal-organic framework-derived nanoporous carbon incorporated nanofibers for high-performance triboelectric nanogenerators and self-powered sensors. *Nano Energy* **2022**, *94*, 106921.
206. Huang, J.; Xu, B.; Gao, Y.; Jiang, C.; Guan, X.; Li, Z.; Han, J.; Chung, K. Y., Surface Microstructural Engineering of Continuous Fibers as One-dimensional Multifunctional Fiber Materials for Wearable Electronic Applications. *Chemical Engineering Journal* **2022**, 137192.

-
207. Li, Z.; Xu, B.; Han, J.; Huang, J.; Fu, H., A polycation-modified nanofillers tailored polymer electrolytes fiber for versatile biomechanical energy harvesting and full-range personal healthcare sensing. *Advanced Functional Materials* **2022**, *32* (6), 2106731.
208. Wen, J.; Pan, X.; Fu, H.; Xu, B., Advanced designs for electrochemically storing energy from triboelectric nanogenerators. *Matter* **2023**, *6* (7), 2153-2181.
209. Lu, H.; Hu, J.; Wei, X.; Zhang, K.; Xiao, X.; Zhao, J.; Hu, Q.; Yu, J.; Zhou, G.; Xu, B., A recyclable biomass electrolyte towards green zinc-ion batteries. *Nature Communications* **2023**, *14* (1), 4435.
210. Lv, X.; Liu, Y.; Yu, J.; Li, Z.; Ding, B., Smart fibers for self-powered electronic skins. *Advanced Fiber Materials* **2023**, *5* (2), 401-428.
211. Zhu, M.; Yu, J.; Li, Z.; Ding, B., Self - healing fibrous membranes. *Angewandte Chemie* **2022**, *134* (41), e202208949.
212. Zhu, M.; Li, J.; Yu, J.; Li, Z.; Ding, B., Superstable and intrinsically self-healing fibrous membrane with bionic confined protective structure for breathable electronic skin. *Angewandte Chemie International Edition* **2022**, *61* (22), e202200226.
213. Yang, Y.; Guo, X.; Zhu, M.; Sun, Z.; Zhang, Z.; He, T.; Lee, C., Triboelectric nanogenerator enabled wearable sensors and electronics for sustainable internet of things integrated green earth. *Advanced Energy Materials* **2023**, *13* (1), 2203040.
214. Gao, Y.; Xu, B.; Tan, D.; Li, M.; Wang, Y.; Yang, Y., Asymmetric-elastic-structure fabric-based triboelectric nanogenerators for wearable energy harvesting and human motion sensing. *Chemical Engineering Journal* **2023**, *466*, 143079.
215. Basset, P.; Beeby, S. P.; Bowen, C.; Chew, Z. J.; Delbani, A.; Dharmasena, R.; Dudem, B.; Fan, F. R.; Galayko, D.; Guo, H., Roadmap on nanogenerators and piezotronics. *APL Materials* **2022**, *10* (10).
216. Li, J.; Cai, J.; Yu, J.; Li, Z.; Ding, B., The rising of fiber constructed piezo/triboelectric nanogenerators: from material selections, fabrication techniques to emerging applications. *Advanced Functional Materials* **2023**, 2303249.
217. Wen, D.-L.; Sun, D.-H.; Huang, P.; Huang, W.; Su, M.; Wang, Y.; Han, M.-D.; Kim, B.; Brugger, J.; Zhang, H.-X., Recent progress in silk fibroin-based flexible electronics. *Microsystems & Nanoengineering* **2021**, *7* (1), 35.
218. Niu, Q.; Peng, Q.; Lu, L.; Fan, S.; Shao, H.; Zhang, H.; Wu, R.;

Hsiao, B. S.; Zhang, Y., Single molecular layer of silk nanoribbon as potential basic building block of silk materials. *ACS nano* **2018**, *12* (12), 11860-11870.

219. Shi, C.; Hu, F.; Wu, R.; Xu, Z.; Shao, G.; Yu, R.; Liu, X. Y., New silk road: from mesoscopic reconstruction/functionalization to flexible meso - electronics/photronics based on cocoon silk materials. *Advanced Materials* **2021**, *33* (50), 2005910.

220. Chen, Z.; Zhang, H.; Lin, Z.; Lin, Y.; van Esch, J. H.; Liu, X. Y., Programming performance of silk fibroin materials by controlled nucleation. *Advanced Functional Materials* **2016**, *26* (48), 8978-8990.

221. Duan, Q.; Lu, Y., Silk sericin as a green adhesive to fabricate a textile strain sensor with excellent electromagnetic shielding performance. *ACS Applied Materials & Interfaces* **2021**, *13* (24), 28832-28842.

222. Liang, X.; Zhu, M.; Li, H.; Dou, J.; Jian, M.; Xia, K.; Li, S.; Zhang, Y., Hydrophilic, breathable, and washable graphene decorated textile assisted by silk sericin for integrated multimodal smart wearables. *Advanced Functional Materials* **2022**, *32* (42), 2200162.

223. Mu, X.; Agostinacchio, F.; Xiang, N.; Pei, Y.; Khan, Y.; Guo, C.; Cebe, P.; Motta, A.; Kaplan, D. L., Recent advances in 3D printing with protein-based inks. *Progress in Polymer Science* **2021**, *115*, 101375.

224. Dong, X.; Liu, Q.; Liu, S.; Wu, R.; Ma, L., Silk fibroin based conductive film for multifunctional sensing and energy harvesting. *Advanced Fiber Materials*. **2022**, *4* (4), 885-893.

225. Rana, S. S.; Rahman, M. T.; Salauddin, M.; Sharma, S.; Maharjan, P.; Bhatta, T.; Cho, H.; Park, C.; Park, J. Y., Electrospun PVDF-TrFE/MXene nanofiber mat-based triboelectric nanogenerator for smart home appliances. *ACS applied materials & interfaces* **2021**, *13* (4), 4955-4967.

226. Gong, J.; Xu, B.; Yang, Y.; Wu, M.; Yang, B., An adhesive surface enables high-performance mechanical energy harvesting with unique frequency - insensitive and pressure - enhanced output characteristics. *Advanced Materials* **2020**, *32* (14), 1907948.

227. Uzabakiriho, P. C.; Haider, Z.; Emmanuel, K.; Ahmad, R. U. S.; Haleem, A.; Farooq, U.; Uwisengyimana, J. D. D.; Mbogba, M. K.; Fareed, A.; Memon, K., High-Performance, Mechanically and Thermally Compliant Silica-Based Solid Polymer Electrolyte for Triboelectric Nanogenerators Application. *Advanced Materials Technologies* **2020**, *5* (7), 2000303.

-
228. Guo, C.; Li, C.; Vu, H. V.; Hanna, P.; Lechtig, A.; Qiu, Y.; Mu, X.; Ling, S.; Nazarian, A.; Lin, S. J., Thermoplastic moulding of regenerated silk. *Nature materials* **2020**, *19* (1), 102-108.
229. Wang, Q.; Xu, B.; Huang, J.; Tan, D., Natural silkworm cocoon-based hierarchically architected composite triboelectric nanogenerators for biomechanical energy harvesting. *ACS Applied Materials & Interfaces* **2023**, *15* (7), 9182-9192.
230. He, H.; Cai, R.; Wang, Y.; Tao, G.; Guo, P.; Zuo, H.; Chen, L.; Liu, X.; Zhao, P.; Xia, Q., Preparation and characterization of silk sericin/PVA blend film with silver nanoparticles for potential antimicrobial application. *International journal of biological macromolecules* **2017**, *104*, 457-464.
231. Lee, K. H., Silk sericin retards the crystallization of silk fibroin. *Macromol. Rapid Communications* **2004**, *25* (20), 1792-1796.
232. Hu, X.; Kaplan, D.; Cebe, P., Determining beta-sheet crystallinity in fibrous proteins by thermal analysis and infrared spectroscopy. *Macromolecules* **2006**, *39* (18), 6161-6170.
233. Tang, Y.; Xu, B.; Gao, Y.; Li, Z.; Tan, D.; Li, M.; Liu, Y.; Huang, J., Ultrastrong-polar polyacrylonitrile organic-inorganic architected nanogenerators with synergistic triboelectric behavior for efficient biomechanical energy harvesting and self-powered sensing. *Nano Energy* **2022**, *103*, 107833.
234. Ho, M. D.; Ling, Y.; Yap, L. W.; Wang, Y.; Dong, D.; Zhao, Y.; Cheng, W., Percolating network of ultrathin gold nanowires and silver nanowires toward “invisible” wearable sensors for detecting emotional expression and apexcardiogram. *Advanced Functional Materials* **2017**, *27* (25), 1700845.
235. Kang, H.; Kim, H.; Kim, S.; Shin, H. J.; Cheon, S.; Huh, J. H.; Lee, D. Y.; Lee, S.; Kim, S. W.; Cho, J. H., Mechanically robust silver nanowires network for triboelectric nanogenerators. *Advanced Functional Materials* **2016**, *26* (42), 7717-7724.
236. Lu, P.-W.; Wu, Y.-T.; Chang, L.-Y.; Lu, T.-W.; Jaihao, C.; Huang, C.-S.; Chuang, M.-F. M.; Lin, C.; Chen, I.; Brangule, A., The biocompatibility and hemostatic efficacy of silk fibroin nanofibrils fabricated by Shear-Induced phase separation process. *Chemical Engineering Journal* **2023**, *474*, 145731.
237. Xia, X.; Zhou, Z.; Shang, Y.; Yang, Y.; Zi, Y., Metallic glass-based triboelectric nanogenerators. *Nature Communications* **2023**, *14* (1), 1023.
238. Xu, Z.; Shi, L.; Yang, M.; Zhang, H.; Zhu, L., Fabrication of a novel blended membrane with chitosan and silk microfibers for wound healing: characterization, in

vitro and in vivo studies. *Journal of Materials Chemistry B* **2015**, 3 (17), 3634-3642.

239. Cheon, S.; Kang, H.; Kim, H.; Son, Y.; Lee, J. Y.; Shin, H. J.; Kim, S. W.; Cho, J. H., High-performance triboelectric nanogenerators based on electrospun polyvinylidene fluoride–silver nanowire composite nanofibers. *Advanced Functional Materials* **2018**, 28 (2), 1703778.

240. Ryu, S.; Kim, H.; Park, Y.; Lin, C.-C.; Um, I.; Ki, C., Dual mode gelation behavior of silk fibroin microgel embedded poly (ethylene glycol) hydrogels. *Journal of Materials Chemistry B* **2016**, 4 (26), 4574-4584.

241. Kundu, S. C.; Dash, B. C.; Dash, R.; Kaplan, D. L., Natural protective glue protein, sericin bioengineered by silkworms: potential for biomedical and biotechnological applications. *Progress in Polymer Science* **2008**, 33 (10), 998-1012.

242. Kim, M. P.; Um, D.-S.; Shin, Y.-E.; Ko, H., High-performance triboelectric devices via dielectric polarization: a review. *Nanoscale Research Letters* **2021**, 16, 1-14.

243. Li, R.; Xu, Z.; Li, L.; Wei, J.; Wang, W.; Yan, Z.; Chen, T., Breakage-resistant hydrogel electrode enables ultrahigh mechanical reliability for triboelectric nanogenerators. *Chemical Engineering Journal* **2023**, 454, 140261.

244. Roy, S.; Ko, H.-U.; Maji, P. K.; Kim, J., Large amplification of triboelectric property by allicin to develop high performance cellulosic triboelectric nanogenerator. *Chemical Engineering Journal* **2020**, 385, 123723.

245. Nie, S.; Fu, Q.; Lin, X.; Zhang, C.; Lu, Y.; Wang, S., Enhanced performance of a cellulose nanofibrils-based triboelectric nanogenerator by tuning the surface polarizability and hydrophobicity. *Chemical Engineering Journal* **2021**, 404, 126512.

246. Sun, J.; Tu, K.; Büchele, S.; Koch, S. M.; Ding, Y.; Ramakrishna, S. N.; Stucki, S.; Guo, H.; Wu, C.; Keplinger, T., Functionalized wood with tunable tribopolarity for efficient triboelectric nanogenerators. *Matter* **2021**, 4 (9), 3049-3066.

247. Rajabi-Abhari, A.; Kim, J.-N.; Lee, J.; Tabassian, R.; Mahato, M.; Youn, H. J.; Lee, H.; Oh, I.-K., Diatom bio-silica and cellulose nanofibril for bio-triboelectric nanogenerators and self-powered breath monitoring masks. *ACS Applied Materials & Interfaces* **2020**, 13 (1), 219-232.

248. Luo, J.; Wang, Z.; Xu, L.; Wang, A. C.; Han, K.; Jiang, T.; Lai, Q.; Bai, Y.; Tang, W.; Fan, F. R., Flexible and durable wood-based triboelectric nanogenerators for self-powered sensing in athletic big data analytics. *Nature*

communications **2019**, *10* (1), 5147.

249. Bang, J.; Moon, I. K.; Jeon, Y. P.; Ki, B.; Oh, J., Fully wood-based green triboelectric nanogenerators. *Applied Surface Science* **2021**, *567*, 150806.

250. Shi, X.; Luo, J.; Luo, J.; Li, X.; Han, K.; Li, D.; Cao, X.; Wang, Z. L., Flexible wood-based triboelectric self-powered smart home system. *ACS nano* **2022**, *16* (2), 3341-3350.

251. Yan, K.; Li, X.; Wang, X.-X.; Yu, M.; Fan, Z.; Ramakrishna, S.; Hu, H.; Long, Y.-Z., A non-toxic triboelectric nanogenerator for baby care applications. *Journal of Materials Chemistry A* **2020**, *8* (43), 22745-22753.

252. Chen, Q.; Li, W.; Yan, F.; Maniar, D.; van Dijken, J.; Rudolf, P.; Pei, Y.; Loos, K., Lightweight triboelectric nanogenerators based on hollow stellate cellulose films derived from *Juncus effusus* L. aerenchyma. *Advanced Functional Materials* **2023**, 2304801.

253. Chen, K.; Li, Y.; Yang, G.; Hu, S.; Shi, Z.; Yang, G., Fabric-Based TENG Woven with Bio-Fabricated Superhydrophobic Bacterial Cellulose Fiber for Energy Harvesting and Motion Detection. *Advanced Functional Materials* **2023**, 2304809.

254. Huang, J.; Xu, B.; Gao, Y.; Jiang, C.; Guan, X.; Li, Z.; Han, J.; Chung, K. Y., Surface microstructural engineering of continuous fibers as one-dimensional multifunctional fiber materials for wearable electronic applications. *Chemical Engineering Journal* **2022**, *446*, 137192.

255. Meng, L.; Shao, C.; Cui, C.; Xu, F.; Lei, J.; Yang, J., Autonomous self-healing silk fibroin injectable hydrogels formed via surfactant-free hydrophobic association. *ACS applied materials & interfaces* **2019**, *12* (1), 1628-1639.

256. Wang, N.; Feng, Y.; Zheng, Y.; Zhang, L.; Feng, M.; Li, X.; Zhou, F.; Wang, D., New hydrogen bonding enhanced polyvinyl alcohol based self-charged medical mask with superior charge retention and moisture resistance performances. *Advanced Functional Materials* **2021**, *31* (14), 2009172.

257. Yu, Y.; Li, H.; Zhang, X.; Gao, Q.; Yang, B.; Wang, Z. L.; Cheng, T., Substantially boosting performance of triboelectric nanogenerators via a triboelectrification enhancement effect. *Joule* **2024**.

258. Xu, Z.; Chen, L.; Zhang, Z.; Han, J.; Chen, P.; Hong, Z.; Jiang, T.; Wang, Z. L., Durable Roller-Based Swing-Structured Triboelectric Nanogenerator for Water Wave Energy Harvesting. *Small* **2024**, *20* (15), 2307288.

-
259. Yang, Y.; Xu, B.; Yin, X.; Liu, X.; Tan, D.; Wang, Q., Flexible hybrid nanogenerator coupling of triboelectric and photovoltaic effects based on fluoride dielectric regulation for energy harvesting. *Nano Energy* **2024**, *126*, 109707.
260. Chung, K. Y.; Xu, B.; Tan, D.; Yang, Q.; Li, Z.; Fu, H., Naturally Crosslinked Biocompatible Carbonaceous Liquid Metal Aqueous Ink Printing Wearable Electronics for Multi-Sensing and Energy Harvesting. *Nano-Micro Letters* **2024**, *16* (1), 149.
261. Li, C.; Luo, R.; Bai, Y.; Shao, J.; Ji, J.; Wang, E.; Li, Z.; Meng, H.; Li, Z., Molecular Doped Biodegradable Triboelectric Nanogenerator with Optimal Output Performance. *Advanced Functional Materials* **2024**, 2400277.
262. Han, J.; Li, Z.; Fang, C.; Liu, X.; Yang, Y.; Wang, Q.; Zhang, J.; Xu, B., Hierarchically porous architected stretchable fibrous materials in energy harvesting and self-powered sensing. *Nano Energy* **2024**, *129*, 110080.
263. Tang, Y.; Fu, H.; Xu, B., Advanced design of triboelectric nanogenerators for future eco-smart cities. *Advanced Composites and Hybrid Materials* **2024**, *7* (3), 102.
264. Akram, W.; Chen, Q.; Xia, G.; Fang, J., A review of single electrode triboelectric nanogenerators. *Nano Energy* **2023**, *106*, 108043.
265. Niu, S.; Wang, Z. L., Theoretical systems of triboelectric nanogenerators. *Nano Energy* **2015**, *14*, 161-192.
266. Guo, H.; Li, T.; Cao, X.; Xiong, J.; Jie, Y.; Willander, M.; Cao, X.; Wang, N.; Wang, Z. L., Self-sterilized flexible single-electrode triboelectric nanogenerator for energy harvesting and dynamic force sensing. *ACS nano* **2017**, *11* (1), 856-864.
267. Sasmal, A.; Seetharaman, A.; Maiti, P.; Sudhakar, S.; Arockiarajan, A., Charge-defect tuned PVDF based ternary biocompatible composite as skin touch actuated single electrode triboelectric nanogenerator for wireless healthcare monitoring. *Chemical Engineering Journal* **2024**, *487*, 150573.
268. Sun, Q.; Ren, G.; He, S.; Tang, B.; Li, Y.; Wei, Y.; Shi, X.; Tan, S.; Yan, R.; Wang, K., Charge Dispersion Strategy for High-Performance and Rain-Proof Triboelectric Nanogenerator. *Advanced Materials* **2024**, *36* (8), 2307918.
269. Reizabal, A.; Costa, C. M.; Pérez-Álvarez, L.; Vilas-Vilela, J. L.; Lanceros-Méndez, S., Silk fibroin as sustainable advanced material: material properties and characteristics, processing, and applications. *Advanced Functional Materials* **2023**, *33* (3), 2210764.

-
270. Krecker, M. C.; Bukharina, D.; Hatter, C. B.; Gogotsi, Y.; Tsukruk, V. V., Bioencapsulated MXene flakes for enhanced stability and composite precursors. *Advanced Functional Materials* **2020**, *30* (43), 2004554.
271. Zhang, Z.; Xu, W.; Wang, J.; Hu, M.; Zhang, D.; Jia, L.; Kang, A.; Xi, Y.; Ye, X.; Cheng, S., Improving solar vapor generation by eliminating the boundary layer inhibition effect of evaporator pores. *ACS Energy Letters* **2023**, *8* (5), 2276-2283.
272. Chen, C.; Xie, X.; Anasori, B.; Sarycheva, A.; Makaryan, T.; Zhao, M.; Urbankowski, P.; Miao, L.; Jiang, J.; Gogotsi, Y., MoS₂ - on - MXene heterostructures as highly reversible anode materials for lithium - ion batteries. *Angewandte Chemie International Edition* **2018**, *57* (7), 1846-1850.
273. Naguib, M.; Kurtoglu, M.; Presser, V.; Lu, J.; Niu, J.; Heon, M.; Hultman, L.; Gogotsi, Y.; Barsoum, M. W., Two-dimensional nanocrystals: two-dimensional nanocrystals produced by exfoliation of Ti₃AlC₂ (Adv. Mater. 37/2011). *Advanced Materials* **2011**, *23* (37), 4207-4207.
274. Wang, J.; Liu, H.; Shi, X.; Qin, S.; Liu, J.; Lv, Q.; Liu, J.; Li, Q. s.; Wang, Z.; Wang, L., Development and Application of an Advanced Biomedical Material-Silk Sericin. *Advanced Materials* **2024**, 2311593.
275. Liu, H.; Wei, W.; Zhang, L.; Xiao, J.; Pan, J.; Wu, Q.; Ma, S.; Dong, H.; Yu, L.; Yang, W., Shape-engineerable silk fibroin papers for ideal substrate alternatives of plastic electronics. *Advanced Functional Materials* **2021**, *31* (52), 2104088.
276. Jing, T.; Wang, S.; Yuan, H.; Yang, Y.; Xue, M.; Xu, B., Interfacial roughness enhanced gel/elastomer interfacial bonding enables robust and stretchable triboelectric nanogenerator for reliable energy harvesting. *Small* **2023**, *19* (12), 2206528.
277. Wu, Z.; Zhang, B.; Zou, H.; Lin, Z.; Liu, G.; Wang, Z. L., Multifunctional sensor based on translational -rotary triboelectric nanogenerator. *Advanced Energy Materials* **2019**, *9* (33), 1901124.
278. Kalasin, S.; Sangnuang, P.; Surareungchai, W., Wearable Triboelectric Sensors with Self-Powered Energy: Multifunctional Laser-Engraved Electrets to Activate Satellite Communication for Life-Emergency Alert in Pandemics. *ACS Applied Electronic Materials* **2021**, *3* (12), 5383-5392.
279. Wang, Q.; Xu, B.; Tan, D.; Hu, X.; Yang, Y.; Huang, J.; Gao, Y.; Liu, X., Nature-inspired scalable high-performance triboelectric nanogenerators for energy

harvesting and sensing. *Nano Energy* **2024**, *121*, 109217.

280. Liu, J.-H.; Li, W.-D.; Jia, J.; Tang, C.-Y.; Wang, S.; Yu, P.; Zhang, Z.-M.; Ke, K.; Bao, R.-Y.; Liu, Z.-Y., Structure-regenerated silk fibroin with boosted piezoelectricity for disposable and biodegradable oral healthcare device. *Nano Energy* **2022**, *103*, 107787.